Spectral Imprints from Electromagnetic Cascades in Blazar Jets

Dissertation zur Erlangung des naturwissenschaftlichen Doktorgrades der
Julius-Maximilians-Universität Würzburg

vorgelegt von
Christoph Wendel
aus Würzburg

Würzburg 2022

Eingereicht bei der Fakultät für Physik und Astronomie am ....

1. Gutachter der Dissertation: Prof. Dr. Karl Mannheim

2. Gutachter der Dissertation: Prof. Dr. Jörn Wilms

3. Gutachter der Dissertation: ....

Vorsitzende(r):

1. Prüfer im Promotionskolloquium: Prof. Dr. Karl Mannheim

2. Prüfer im Promotionskolloquium: Prof. Dr. Jörn Wilms

3. Prüfer im Promotionskolloquium: ....

Datum des Promotionskolloquiums: ....

Doktorurkunde ausgehändigt am: ....

Zusammenfassung

Beobachtet man das Firmament im Licht der Gammastrahlung, stellen Blasare die Mehrzahl extragalaktischer Objekte dar. Blasare sind aktive Galaxienkerne mit einem relativistischen Jet, der entlang der Sichtlinie ausgerichtet ist. Galaxien haben einen aktiven Kern, wenn das zentrale supermassereiche Schwarze Loch große Mengen an Umgebungsmaterie und magnetischem Fluss akkretiert. Die nach Innen strömende Masse sammelt sich nahe der Ebene an, die senkrecht zum Drehimpuls des Akkretionsflusses steht. Das akkretierte Material wird durch viskose Reibung aufgeheizt und ein Teil der freigesetzten Energie wird als Schwarzkörper- oder nicht-thermische Strahlung abgestrahlt, deren Leuchtkraft die gesamte stellare Leuchtkraft der Wirtsgalaxie übertreffen kann. Ein Teil der Leuchtkraft des Akkretionsflusses wird in einem umgebenden Feld von ionisierten Gaswolken reprozessiert. Diese Wolken, die um das zentrale Schwarze Loch kreisen, emittieren Doppler-verbreiterte Emissionslinien. Den Teil des aktiven Galaxienkerns, in dem sich diese Wolken befinden, bezeichnet man als BLR (englisch: broad-line region). Ihr Abstand zum zentralen Schwarzen Loch beträgt typischerweise etwa 0,1 pc.

Etwa einer von zehn aktiven Galaxienkernen bildet einen Ausfluss von Strahlung und relativistischen Teilchen aus, einen sogenannten relativistischen Jet. Dies wird gemäß dem Blandford-Znajek-Mechanismus durch elektromagnetische Prozesse in den Magnetosphären rotierender Schwarzer Löcher bewerkstelligt. Letztere induzieren einen poloidalen magnetosphärischen Stromkreis, der ein abbremsendes Drehmoment auf das Schwarze Loch ausübt und ein toroidales Magnetfeld erzeugt. Folglich wird die Rotationsenergie des Schwarzen Lochs in Poynting-Fluss umgewandelt, der hauptsächlich entlang der Rotationsachse abfließt und den Jet entstehen lässt. Durch Prozesse, die noch nicht eindeutig identifiziert wurden, werden geladene Teilchen in der Nähe der Jetbasis beschleunigt. Eine Möglichkeit dafür ist Teilchenbeschleunigung in magnetosphärischen Vakuum-Lücken. Dies sind Regionen, die vorübergehend nahezu frei von Plasma sind, sodass zeitweise ein elektrisches Feld parallel zu den Magnetfeldlinien entsteht, das die Teilchenbeschleunigung ermöglicht und zur Aufladung der Jets mit massebehafteten Teilchen beiträgt.

Magnetisierte Strukturen, die relativistische Elektronen enthalten, bewegen sich entlang der Jets vom Galaxienkern weg. Unter der Annahme, dass diese Elektronen Synchrotronstrahlung aussenden und dass sie vorhandenen weichen Photonen, die entweder die Synchrotronphotonen selbst oder Photonen von externen Emittern sein können, durch inverse Compton-Streuung höhere Energien verleihen, kann das emittierte Spektrum berechnet werden. Berücksichtigt man zusätzlich, dass sich diese Emissionsgebiete selbst relativistisch bewegen und dass die Emission Doppler-verstärkt ist und bevorzugt in Vorwärtsrichtung abgestrahlt wird, erhält man die typische zweihöckrige spektrale Energieverteilung von Blasaren.

Es gibt jedoch Erkenntnisse, die dieses bewährte Modell in Frage stellen. Kurzzeit-Variabilität, die bei sehr hochenergetischer Gammastrahlung bis zu Minuten-Skalen hinunterreicht, ist ein weit verbreitetes Phänomen bei Blasaren und setzt sehr kompakte Emissionsregionen voraus. In den meisten Modellen für solche optisch dicken Emissionsregionen wird der Gammastrahlenfluss durch Paarbildung lediglich exponentiell absorbiert, ohne die Kaskade zu berücksichtigen, die sich durch die erzeugten Elektronen entwickelt. Aus den Beobachtungen wird oft gefolgert, dass die Emission aus optisch dünnen Regionen bei größeren Entfernungen stammt, insbesondere von außerhalb der BLR. Nur bei wenigen Blasaren wurde eine Abschwächung der Gammastrahlung durch Absorption

in der BLR eindeutig nachgewiesen.

Durch moderne Gammastrahlen-Detektoren, wie das Fermi Large Area Telescope oder den Major Atmospheric Gamma-ray Imaging Cherenkov Teleskopen, wurden neben der Kurzzeit-Variabilität auch spektrale Merkmale gefunden, die nicht durch konventionelle Modelle, die die zweihöckrigen spektralen Energieverteilungen wiedergeben können, erklärt werden können. Zwei solcher besonderen spektralen Merkmale werden in dieser Arbeit diskutiert. Für den Blasar Markarian 501 wurden bei einer im Juli 2014 durchgeführten Multiwellenlängenkampagne Hinweise auf einen schmalen Buckel bei 3 TeV gefunden, während für 3C 279 in Daten von 2018 eine Mulde im Spektrum gefunden wurde, die mit oft verwendeten Fit-Funktionen nur schlecht beschrieben werden kann. In dieser Arbeit wird untersucht, ob diese spektralen Besonderheiten der Blasar-Jet-Emission erklärt werden können, wenn die vollständige Reprozessierung der Strahlung durch eine inverse Compton-Paar-Kaskade berücksichtigt wird.

Eine solche Kaskade ist die mehrfache Aneinanderreihung von inverser Compton-Streuung und Paarproduktion. Bei den in dieser Arbeit allgemein betrachteten Kaskaden werden relativistische Elektronen und hochenergetische Photonen in eine Region mit niederenergetischen Photonen konstanter Dichte injiziert. Auf der Grundlage von Vorarbeiten wird eine mathematische Beschreibung für lineare inverse Compton-Paar-Kaskaden mit Entweichtermen ausgearbeitet. Es werden die zeitunabhängigen kinetischen Gleichungen für Elektronen und Photonen hergeleitet, wobei auf eine vollständige Formulierung und auf die Begründung der korrekten Integrationsgrenzen aller Integrale durch die kinematischen Vorgaben geachtet wird. Bei der Bestimmung des potentiell beobachtbaren Gammastrahlenflusses werden sowohl der teilweise absorbierte, injizierte Fluss als auch der Fluss, der sich als Effekt der inversen Compton-Streuung, der Paar-Absorption und des Entweichens ergibt, einbezogen, was den entstehenden Spektren charakteristische Formen aufprägt.

Die kinetische Gleichung der Elektronen wird durch iterative Vorgehensweisen numerisch gelöst. Es wird erklärt, warum eine punktweise Iteration von höheren zu niedrigeren Lorentz-Faktoren effizienter ist als die Iteration des gesamten Satzes von Stützstellen. Der Algorithmus wird an zwei Stellen parallelisiert. Erstens können mehrere Prozessor-Kerne gleichzeitig punktweise Iterationen durchführen. Zweitens wird das rechenintensivste Integral in mehrere Teilintegrale zerlegt, die von mehreren Kernen berechnet werden können. Durch diese Maßnahmen kann der Python-Code zur Simulation von zeitunabhängigen inversen Compton-Paar-Kaskaden eingesetzt werden.

Im Fall von Markarian 501 wird folgendes Modell bemüht. Der aktive Galaxienkern hat einen advektionsdominierten Akkretionsfluss mit einer normalisierten Akkretionsrate von mehreren 10^{-4} und einer Elektronentemperatur um 10^{10} K. Einerseits bestrahlt der Akkretionsfluss die wenigen umgebenden Gaswolken mit ungefährem Radius von 10^{11} m, die einen Faktor 0,01 der Leuchtkraft in Form von Wasserstoff- und Helium-Emissionslinien wieder abstrahlen. Andererseits erzeugen die vom Akkretionsfluss stammenden Gammaphotonen in einer zeitweise aktiven Vakuum-Lücke in der Magnetosphäre des Schwarzen Lochs Elektronen und Positronen. In der geöffneten Lücke wird dem rotierenden Schwarzen Loch durch einen Potentialunterschied von mehreren 10^{18} V eine Leistung von etwa 0,001 der Blandford-Znajek-Leistung entzogen, wodurch ultra-relativistische Elektronen erzeugt werden, die anschließend durch Wechselwirkung mit den Photonen des Akkretionsflusses um einen Faktor von etwa 10^6 multipliziert werden. Dieser Elektronenstrahl verlässt die Magnetosphäre und trifft auf das Photonenfeld einer vorbeiziehenden ionisierten Wolke. Die daraus resultierende inverse Compton-Paar-Kaskade wird simuliert und das sich ergebende Gammastrahlenspektrum wird berechnet. Unmittelbar oberhalb der durch die Wasserstofflinien verursachten Absorptionströge erscheint bei rund 3 TeV ein schmaler Höcker. Wenn die Strahlung der Kaskade der aus größerer Entfernung stammenden Strahlung überlagert wird, wird die gesamte spektrale Energieverteilung einschließlich des scharfen Buckels bei 3 TeV reproduziert. Das bedeutet, dass schmale spektrale Merkmale für die Relevanz von Strahlungsprozessen sprechen, die über konventionelle Modelle hinausgehen.

Der Trog im Spektrum von 3C 279 wird mit einem ähnlichen Kaskadenmodell untersucht. Es werden drei Fälle der Injektion betrachtet, die sich im Verhältnis der Photonen-Anzahl zur Elektronen-

Anzahl und im spektralen Verlauf unterscheiden. Es wird angenommen, dass die Kaskade entweder im dichten Photonenfeld der BLR mit einer Leuchtkraft von mehreren 10^{37} W und einer radialen Ausdehnung von einigen 10^{14} m oder im ausgedünnten Photonenfeld außerhalb der BLR stattfindet. Das letztgenannte Szenario muss jedoch verworfen werden, da die spektrale Steigung bei einigen 100 MeV und der Absorptionstrog bei einigen 10 GeV innerhalb dieses Modells nicht miteinander in Einklang gebracht werden können. Die innerhalb der BLR kaskadierte Strahlung kann die Beobachtungsdaten unabhängig von der angenommenen Injektionsrate erklären. Daraus folgt, dass die Gammastrahlung während dieses Emissionsereignisses am Rande der BLR von 3C 279 produziert wird.

Beide Untersuchungen zeigen, dass inverse Compton-Paar-Kaskaden Feinstrukturen in der spektralen Energieverteilung von Blasaren erklären können. Es reicht nicht aus, den Strahlungstransport auf reine exponentielle Absorption eines Injektionsterms zu beschränken. Paarbildung und inverse Compton-Streuung im optisch dicken Bereich und über alle Generationen von Photonen und Elektronen hinweg prägen die entstehenden Spektren entscheidend. Da künftige, verbesserte Detektoren detailliertere Spektren liefern werden, darf man weitere Berichte über schmale spektrale Merkmale erwarten. Es erscheint daher empfehlenswert, die Kaskadierung in konventionelle Modelle der Strahlungsproduktion mit einzubeziehen oder das in dieser Arbeit entwickelte Modell um Synchrotronstrahlung zu erweitern.

Summary

The extragalactic gamma-ray sky is dominated by blazars, active galactic nuclei (AGN) with a relativistic jet that is closely aligned with the line of sight. Galaxies develop an active nucleus if the central supermassive black hole (BH) accretes large amounts of ambient matter and magnetic flux. The inflowing mass accumulates around the plane perpendicular to the accretion flow's angular momentum. The flow is heated through viscous friction and part of the released energy is radiated as blackbody or non-thermal radiation, with luminosities that can dominate the accumulated stellar luminosity of the host galaxy. A fraction of the accretion flow luminosity is reprocessed in a surrounding field of ionised gas clouds. These clouds, revolving around the central BH, emit Doppler-broadened atomic emission lines. The region where these broad-line-emitting clouds are located is called broad-line region (BLR).

About one in ten AGN forms an outflow of radiation and relativistic particles, called a relativistic jet. According to the Blandford-Znajek mechanism, this is facilitated through electromagnetic processes in the magnetosphere of a spinning BH. The latter induces a magnetospheric poloidal current circuit, generating a decelerating torque on the BH and inducing a toroidal magnetic field. Consequently, rotational energy of the BH is converted to Poynting flux streaming away mainly along the rotational axis and starting the jet. One possibility for particle acceleration near the jet base is realised by magnetospheric vacuum gaps, regions temporarily devoid of plasma, such that an intermittent electric field arises parallel to the magnetic field lines, enabling particle acceleration and contributing to the mass loading of the jets.

Magnetised structures, containing bunches of relativistic electrons, propagate away from the galactic nucleus along the jets. Assuming that these electrons emit synchrotron radiation and that they inverse-Compton (IC) up-scatter abundant target photons, which can either be the synchrotron photons themselves or photons from external emitters, the emitted spectrum can be theoretically determined. Additionally taking into account that these emission regions move relativistically themselves and that the emission is Doppler-boosted and beamed in forward direction, the typical two-hump spectral energy distribution (SED) of blazars is recovered.

There are however findings that challenge this well-established model. Short-time variability, reaching down to minute scales at very high energy gamma rays, is today known to be a widespread phenomenon of blazars, calling for very compact emission regions. In most models of such optically thick emission regions, the gamma-ray flux is usually pair-absorbed exponentially, without considering the cascade evolving from the pair-produced electrons. From the observed flux, it is often concluded that emission emanates from larger distances where the region is optically thin, especially from outside of the BLR. Only in few blazars gamma-ray attenuation associated with pair absorption in the BLR was clearly reported.

With the advent of sophisticated high-energy or very high energy gamma-ray detectors, like the Fermi Large Area Telescope or the Major Atmospheric Gamma-ray Imaging Cherenkov telescopes, besides the extraordinarily fast variability, spectral features have been found that cannot be explained by conventional models reproducing the two-hump SED. Two such narrow spectral features are discussed in this work. For the nearby blazar Markarian 501, hints to a sharp peak around 3 TeV have been reported from a multi-wavelength campaign carried out in July 2014, while for 3C 279 a

spectral dip was found in 2018 data, that can hardly be described with conventional fitting functions. In this work it is examined whether these spectral peculiarities of blazar jet emission can be explained, if the full radiation reprocessing through an IC pair cascade is accounted for.

Such a cascade is the multiple concatenation of IC scattering events and pair production events. In the cascades generally considered in this work, relativistic electrons and high-energy photons are injected into a fixed soft target photon field. A mathematical description for linear IC pair cascades with escape terms is delivered on the basis of preliminary works. The steady-state kinetic equations for the electrons and for the photons are determined, whereby it is paid attention to an explicit formulation and to motivating the correct integration borders of all integrals from kinematic constraints. In determining the potentially observable gamma-ray flux, both the attenuated injected flux and the flux evolving as an effect of IC up-scattering, pair absorption and escape are incorporated, giving the emerging spectra very distinct imprints.

Much effort is dedicated to the numerical solution of the electrons' kinetic equation via iterative schemes. It is explained why pointwise iteration from higher to lower Lorentz factors is more efficient than iterating the whole set of sampling points. The algorithm is parallelised at two positions. First, several workers can perform pointwise iterations simultaneously. Second, the most demanding integral is cut into a number of part integrals which can be determined by multiple workers. Through these measures, the Python code can be readily applied to simulate steady-state IC pair cascades with escape.

In the case of Markarian 501 the developed framework is as follows. The AGN hosts an advection-dominated accretion flow with a normalised accretion rate of several 10^{-4} and an electron temperature near 10^{10} K. On the one hand, the accretion flow illuminates the few ambient gas clouds with approximate radius 10^{11} m, which reprocess a fraction 0.01 of the luminosity into hydrogen and helium emission lines. On the other hand, the gamma rays from the accretion flow create electrons and positrons in a sporadically active vacuum gap in the BH magnetosphere. In the active gap, a power of roughly 0.001 of the Blandford-Znajek power is extracted from the rotating BH through a gap potential drop of several 10^{18} V, generating ultra-relativistic electrons, which subsequently are multiplied by a factor of about 10^{6} through interaction with the accretion flow photons. This electron beam propagates away from the central engine and encounters the photon field of one passing ionised cloud. The resulting IC pair cascade is simulated and the evolving gamma-ray spectrum is determined. Just above the absorption troughs due to the hydrogen lines, the spectrum exhibits a narrow bump around 3 TeV. When the cascaded emission is added to the emission generated at larger distances, the observed multi-wavelength SED including the sharp peak at 3 TeV is reproduced, underlining that radiation processes beyond conventional models are motivated by distinct spectral features.

The dip in the spectrum of 3C 279 is addressed by a similar cascade model. Three types of injection are considered, varying in the ratio of the photon density to the electron density and varying in the spectral shape. The IC pair cascade is assumed to happen either in the dense BLR photon field with a luminosity of several 10^{37} W and a radial size of few 10^{14} m or in the diluted photon field outside of the BLR. The latter scenario is however rejected as the spectral slope around several 100 MeV and the dip at few 10 GeV cannot be reconciled within this model. The radiation cascaded in the BLR can explain the observational data, irrespective of the assumed injection rate. It is therefore concluded that for this period of gamma-ray emission, the radiation production happens at the edge of the BLR of 3C 279.

Both investigations show that IC pair cascades can account for fine structure seen in blazar SEDs. It is insufficient to restrict the radiation transport to pure exponential absorption of an injection term. Pair production and IC up-scattering by all generations of photons and electrons in the optically thick regime critically shape the emerging spectra. As the advent of future improved detectors will provide more high-precision spectra, further observations of narrow spectral features can be expected. It seems therefore recommendable to incorporate cascading into conventional radiation production models or to extend the model developed in this work by synchrotron radiation.

Contents

1 Introduction 11

2 Active Galactic Nuclei 14
- 2.1 The Structure of Active Galactic Nuclei 15
  - 2.1.1 The Central Supermassive Black Hole 15
  - 2.1.2 The Accretion Flow 17
    - 2.1.2.1 Standard Disks 17
    - 2.1.2.2 Advection-Dominated Accretion Flows 18
      - 2.1.2.2.1 Analytical Integration 20
      - 2.1.2.2.2 Numerical Integration 20
  - 2.1.3 The Corona 20
  - 2.1.4 The Broad-Line Region 22
  - 2.1.5 The Equatorial Torus 24
  - 2.1.6 The Narrow-Line Region 24
  - 2.1.7 The Relativistic Jet 24
- 2.2 The Unification Scheme 26
- 2.3 Jetted Active Galactic Nuclei 27
- 2.4 Blazars 29
  - 2.4.1 Overview 29
  - 2.4.2 Modelling of Blazar Broadband Spectral Energy Distributions 30
  - 2.4.3 Two Exemplary Blazars 32
    - 2.4.3.1 The Flat-Spectrum Radio Quasar 3C 279 32
    - 2.4.3.2 The BL Lacertae Object Markarian 501 32
  - 2.4.4 Variability 33
  - 2.4.5 Gamma Rays from Blazars 33
  - 2.4.6 The Location of the Gamma-Ray Emitting Region 34
- 2.5 Magnetospheric Particle Acceleration 37

3 Inverse-Compton Pair Cascades with Escape Terms 40
- 3.1 Basic Radiation Processes 41
  - 3.1.1 Inverse-Compton Scattering 41
  - 3.1.2 Pair Production 44
- 3.2 Inverse-Compton Pair Cascades 47
  - 3.2.1 Qualitative Description 47
  - 3.2.2 Quantitative Description 48
    - 3.2.2.1 Derivation of the Kinetic Equations 49
    - 3.2.2.2 Conceptual Solution Scheme 51

4 Numerical Solution Procedure 55
- 4.1 Overview about the Code 55
- 4.2 Integrations 57
- 4.3 The Iterative Scheme 59

4.3.1 Scheme 1: Iteration as a Whole 60
4.3.2 Scheme 2: Pointwise Iteration 61
4.3.3 Iterating in the Thomson Regime 63
4.4 Multi-Core Implementation 63
4.4.1 Multiple Workers in the Iteration 64
4.4.2 Parallelisation of Integrations 65

5 Vacuum Gap Activity in Markarian 501 66
5.1 Hints to a Narrow Spectral Component in Markarian 501 66
5.2 Description of the Modelled Physical Setting 68
5.2.1 An Electron Beam from a Vacuum Gap 68
5.2.2 Emission-Line Photons from an Ionised Cloud 69
5.3 Results of the Modelling 72
5.4 Inferences about the Physical Constitution of Markarian 501 76
5.4.1 Emission-Line Clouds in Markarian 501 76
5.4.2 Illumination of the Clouds by the Accretion Flow 77
5.4.3 Particle Multiplication in and behind the Gap 77
5.4.4 The Energetical Point of View 79
5.5 Discussion 80

6 A Peculiar Gamma-Ray Spectrum of 3C 279 from the Broad-Line Region 82
6.1 A Cascade on Broad-Line Region Photons 82
6.2 Results of the Modelling 85
6.3 Inferences about the Location of the Gamma-Ray Emission 87
6.4 Discussion 90

7 Conclusion 92
7.1 Radiation Processes beyond Conventional Models 92
7.2 Drawbacks and Advantages of the Numerical Approach 94
7.3 Outlook 95

List of Physical Constants, Quantities and Variables 97

List of Abbreviations 104

References 106

Acknowledgements 121

Publications in Context with this Work 122

Statutory Declaration of Authorship 123

Chapter 1

Introduction

"Um in unserem Denken mit der Wirklichkeit in Übereinstimmung zu bleiben, müssen wir unseren Blick auf den Himmel, auf die Erde und auf die vergitterten Fenster einer Irrenanstalt gerichtet halten. Auf den Himmel: dass wir gegenwärtig haben, wie klein die Erde in der Unendlichkeit der Welten ist; auf die Erde: damit wir uns Rechenschaft davon geben, wie wenig der Mensch auf ihr bedeutet; auf die vergitterten Fenster einer Irrenanstalt: dass wir der furchtbaren Tatsache der Zerstörbarkeit des geistigen Wesens des Menschen eingedenk bleiben."

Schweitzer, Günzler and Zürcher (2017)

Albert Schweitzer, a 20th century physician, philosopher, philanthropist and a friend of Albert Einstein, thinks we should look upward to the sky, peer at the Earth and cast a glance to the cross-barred windows of a psychiatry to attain a complete perception of reality. The latter in order to be aware of the potential destructibility of the human intellect. By this, one can appreciate the various positive products of human culture like art, literature, science and welfare and one can realise that all these achievements can be fugacious and volatile.

The study of the Earth via disciplines like biology, chemistry or geology is beneficial to realise the position of mankind in the multifarious realm of life and to understand the interrelations between mankind and animate nature. These attempts to get a sight of the big picture are, however, incomplete without studying the inanimate nature via physics and mathematics and without discovering the world outside of Earth through space science, astronomy and astrophysics. By looking to the sky, as Schweitzer recommends, and by exploring the physical universe, it can one day be possible to get a nearly full and unbiased picture of nature, of the vantage point of mankind and about the evolution of life and the cosmos. This is also reflected in many Nobel laureates being astrophysicists and explicitly in the awarding of the 2019 Nobel Prize in Physics to the cosmologist Jim Peebles as well as to the exoplanet pioneers Michel Mayor and Didier Queloz "for contributions to our understanding of the evolution of the universe and Earth's place in the cosmos" (The Nobel Committee for Physics, 2021a).

Observing the sky in visible light with the unaided eye is indeed one of the oldest sciences. Since the dawn of human culture, people have tried to explain what they have observed, even though these explanations were often intertwined with religious, mythological or even astrological beliefs. Today, we still use observations, detections or measurements to acquire knowledge and to develop our conception of the world with help of the scientific method. Observational astronomy forms a symbiosis with theoretical astrophysics. The purpose of the latter is to build physical models that describe the object under consideration, in other words to formulate hypotheses being subject to certain assumptions. The laws of physics permit to deduce predictions or logical consequences of the model. By comparing the observations to the theoretical predictions, the model or parts of it can be falsified and the assumptions can be discarded, revised or refined. Such an approach is also taken in the course of the present PhD thesis.

Today, by performing in-situ measurements by space probes, by detecting electromagnetic or gravitational waves as well as by registering mass-carrying particles like cosmic rays or neutrinos, we obtain a multitude of information about the structure, the state, the composition and the prevailing conditions of the universe as well as about its history and future. We can even learn about the most extreme environments, like e.g. the early universe, neutron stars or the luminous, active centres of galaxies. The latter objects, generally called active galactic nuclei (AGN), are study subject of this work. Therefore, an impressive artist's illustration of an AGN is shown in figure 1.1. In these objects that are not much bigger than our Solar System, the release of gravitational energy of matter infalling onto a supermassive black hole (SMBH) leads to radiation emission over the whole electromagnetic spectrum with luminosities exceeding the stellar power output of entire galaxies, and probably also to cosmic ray and neutrino production.

Figure 1.1: An artist's illustration of our concept of an AGN. A spinning SMBH is situated in the centre, digging a deep gravitational well. It is surrounded by a rotating accretion disk of infalling matter, whose temperature increases the more it is approaching the BH. The disk is surrounded by a cooler, inflated structure of dust clouds. In the background behind this dusty torus, the stars of the surrounding host galaxy can be seen. The SMBH itself does not emit radiation. Its rotational energy can however be extracted and propels an outflow of Poynting flux and particles. As shown in the picture, this relativistic jet is directed perpendicular to the accretion disk. For the sake of simplicity, several additional features like e.g. general relativistic light bending effects or the BLR are neglected in this picture. Image courtesy: National Aeronautics and Space Administration / Jet Propulsion Laboratory-Caltech.

Some crucial aspects about AGN will be introduced in chapter 2. There, the structure and the way of functioning of these most energetic, persistent engines known as well as their observational characteristics and their classification will be outlined. It will in particular be shown in section 2.3 that relativistic outflows of matter and radiation, called jets, are often produced by AGN. If such a jet is directed to the observer, the AGN is classified as a blazar (see section 2.4). A typical, observed blazar multi-wavelength spectral energy distribution (SED) basically extends from the radio to the very high energy (VHE) gamma-ray regime and exhibits two wide humps. Theoretical models to explain this radiation output of AGN jets, in particular the traditional synchrotron-self-Compton (SSC) and external-Compton (EC) models, will be introduced in section 2.4.2. These are often brought forth to explain the two-humped broadband SEDs of blazars. It will also be stressed that these models cannot account for all observational characteristics of blazars. For example, hints to fine structure in blazar spectra on top of the two wide humps have been found with the advent of cutting-edge gamma-ray detectors. However, such additional spectral features cannot be explained by conventional SSC or EC models. Furthermore, temporal fluctuations of the radiation output have often been registered. Especially in the VHE gamma-ray band variability timescales go down to several minutes, pointing to compact emission regions beyond conventional SSC and EC scenarios (section 2.4.4). Therefore additional, refined radiation processes appear to be operating in blazars. Besides the lack of explanations for narrow spectral imprints and the uncertainty about the cause of short-time variability, the spatial origin of gamma rays from blazars is a debated question, as addressed in section 2.4.6.

The aim of this work is to develop a model of radiation emission in blazar jets that can provide answers to the issues of spectral fine structure and short-time variability. This is the subject of the chapters 3 and 4.

In chapter 3 the radiation processes that are relevant in the context of this work will be addressed, namely inverse-Compton (IC) scattering and pair production (PP), in section 3.1.1 and section 3.1.2, respectively. The repeated interaction of relativistic electrons, low-energy (LE) and high-energy (HE) photons via the interplay of IC scattering and PP causes the evolution of an IC pair cascade (section 3.2). Cascade processes go beyond the usual SSC and EC scenarios. They take the radiation reprocessing, the internally produced pairs and the up-scattered gamma rays into account and can therefore be applied to the optically thick regime. Furthermore, the radiation reaction on the electron distribution is taken into account. After a qualitative introduction of IC pair cascades with escape terms in section 3.2.1, the exact mathematical description of such cascades is given in section 3.2.2. The numerical procedure to determine the steady-state electron and photon distributions of the cascades are elucidated in chapter 4. In the subsequent chapters, the cascade model is applied to explain gamma-ray observations of the blazars Markarian (Mrk) 501 and 3C 279 and to address the open issues raised above.

In chapter 5, a peculiar, transient feature in an observed SED of the blazar Mrk 501 will be explained theoretically. Within the framework of this explanation, an electron beam emanating from a vacuum gap in the innermost region of Mrk 501 is interacting with emission-line photons in the surroundings of the AGN. Through this interaction, an IC pair cascade develops and forms a distinct gamma-ray emission feature. For the observed SED feature to be explainable by the theoretical gamma-ray emission, certain physical conditions have to be satisfied in the AGN. It will be shown that these conditions are indeed possibly realised in Mrk 501 with conclusions outlined in section 5.4. Within this model, the intermittency of the vacuum gap activity provides a natural explanation of the transient appearance of the additional SED feature.

Cascade scenarios are also applied to a high-activity period of the blazar 3C 279 (chapter 6). Radiation production in and outside of the broad-line region (BLR) will be considered, but to achieve agreement with the observed gamma-ray spectrum, the scenario happening outside of the BLR will be ruled out. It will also become evident how a dip in the gamma-ray spectrum can arise through a cascade in the BLR. A conclusion about the essentials of this work will be presented in the final chapter 7.

All mathematical symbols, physical quantities, constants and variables used in the course of this thesis are explained in a list on page 97. If one sign has various meanings, each meaning has its own entry in the list. The reader is encouraged to consult this list each time a new symbol appears during reading, because it is beneficial to catch the correct meaning of every quantity. Acronyms that are used more than once are explained in the list of abbreviations on page 104.

Chapter 2

Active Galactic Nuclei

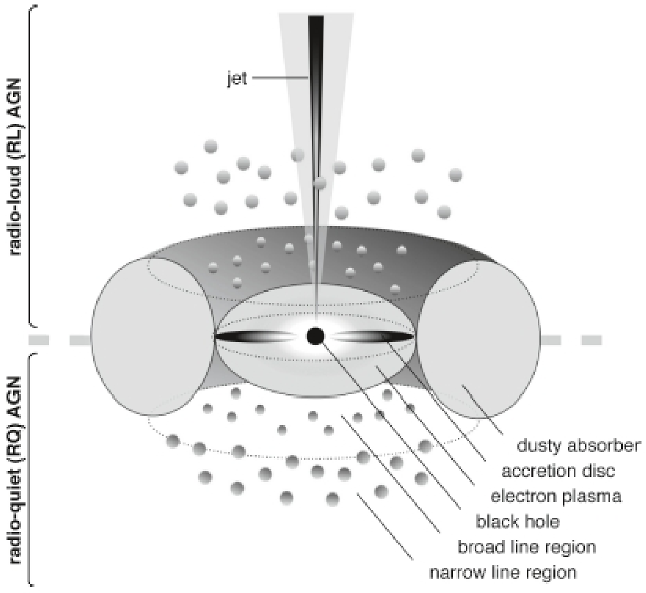

Figure 2.1: Schematic structure of a typical AGN, drawn not to scale. An SMBH is located in the centre (see section 2.1.1). It is accreting matter through the AF (section 2.1.2), which can be a vertically collapsed accretion disk or a geometrically thick inflow. Immediately above and below the AF, there is a hot, dilute electron plasma, called the corona (section 2.1.3). Above and below the corona, there is the BLR (section 2.1.4) and at bigger distances there is the NLR (section 2.1.6). The central engine and the BLR are surrounded by an equatorial, toroidal, dusty absorber (section 2.1.5), introducing a degree of anisotropy. These are the components of radio-quiet or non-jetted AGN. In addition to these components, a bipolar relativistic jet (section 2.1.7) directed perpendicular to the equatorial plane is present in about 10 % of all AGN and provides an additional degree of anisotropy. Such jetted objects are also called radio-loud AGN. Image courtesy: Beckmann and Shrader (2012): Active Galactic Nuclei. Page 5. Copyright Wiley-Verlag Chemie. Reproduced with permission.

The first documented observation of an extragalactic jet, a feature that is today known to be genuinely caused by an AGN, goes back to Heber Curtis. In a description of the elliptical galaxy Messier 87 he noted that a "curious straight ray lies in a gap in the nebulosity [...], apparently connected with the nucleus by a thin line of matter." (Curtis, 1918). At that time, Curtis did not know about the origin of the jet, and he did not know that an AGN is located at the jet base in the centre of Messier 87.

Nearly 100 years later the Event Horizon Telescope Collaboration et al. (2019) presented an unprecedented image of the very central portion of Messier 87. By interconnecting radio telescopes around the globe, observing at mm wavelengths and exploiting the technique called very long baseline interferometry (VLBI), the international collaboration could image for the first time the "shadow" of a black hole (BH), fascinating not only scientists, but also thrilling the interested publicity. In this image, a gravitationally distorted and beamed accretion flow of heated matter is discernible as a ring around the dark BH "shadow", inside of which photons cannot escape from the gravitational well (Event Horizon Telescope Collaboration et al., 2019). The spinning SMBH is accreting magnetised matter, by this converting gravitational potential energy mainly into heat, electromagnetic radiation and bipolar, relativistic particle outflows. Such a relativistic outflow, called jet, is the ray that has been observed a century ago by Curtis.

In this chapter, the phenomenon of AGN will be introduced. The structure of AGN according to the AGN unification scheme as well as the AGN energetics will be explained. The wealth of observational characteristics, classes and peculiarities will be briefly outlined and nearly explained by the unification scheme. The prominent role of blazars, which are AGN with a jet that is pointing towards us, and their ability to emit radiation up to energies of several TeV will also be discussed.

2.1 The Structure of Active Galactic Nuclei

Soon after the description of Seyfert galaxies as a peculiar class of galaxies (Seyfert, 1943), after association of discrete radio sources with certain galaxies (Baade and Minkowski, 1954a; Baade and Minkowski, 1954b) and after the identification of quasi-stellar radio sources (quasars) with extragalactic objects (Schmidt, 1963) with typical redshifts of $z \approx 1.8$ (Véron-Cetty and Véron, 2010), it was realised (Salpeter, 1964; Zel'dovich, 1964; Lynden-Bell, 1969) that accretion of matter onto a central compact object is the only possible measure to release bolometric luminosities up to 10^{41} W (Onken et al., 2020) from regions that could be constrained to be smaller than 100 pc (Woltjer, 1959). Today this view has been manifested in the AGN unification scheme (Antonucci, 1993; Urry and Padovani, 1995). According to this paradigm, all classes of AGN are intrinsically similar objects, and differing only in a few parameters. The basic building blocks of AGN are sketched in figure 2.1 and are discussed now.

2.1.1 The Central Supermassive Black Hole

BHs are objects whose mass is concentrated into a point-like or ring-shaped singularity due to the own gravitational attraction of the mass. Inherently connected to this is the property of BHs to be surrounded by an event horizon, which is a one-way membrane that separates its interior from its exterior. Information cannot be transmitted from inside the event horizon to the universe outside of it. Hence, events in the exterior cannot be causally affected by events in the interior.

It has been speculated for centuries about the existence of objects whose gravitational attraction is so large that even light cannot escape from them (Michell, 1784). It is indeed difficult if not impossible to undoubtedly proof the existence of astrophysical BHs because gain of information is limited to the exterior of the event horizon. Nevertheless, today there is a rich variety of indirect evidence for the existence of astrophysical BHs, which culminated recently in the 2017 Nobel Prize-awarded detection of gravitational waves from BH merger events (Abbott et al., 2021), in the above mentioned imaging of the BH "shadow" in Messier 87 (Event Horizon Telescope Collaboration et al., 2019) and in the 2020 Nobel Prize-honoured theoretical work on the formation of BHs and the observations of stellar kinematics around the SMBH in the Milky Way centre (The Nobel Committee for Physics, 2021b). The occurrence of AGN itself is a strong argument for the existence of BHs.

According to the no-hair conjecture, BHs are completely described by three classical parameters, namely by the mass M_{BH}, the angular momentum J and the electric charge Q of the BH (Israel, 1968; Carter, 1971). The angular momentum is usually parametrised via the dimensionless quantity $a = c\,J/(G\,M_{\mathrm{BH}}^2)$ which can attain values in the range $-1 < a < 1$ of the Kerr bound (see however Thorne, 1974, for the more stringent Thorne limit $|a| \leq 0.998$). For astrophysical BHs it is usually assumed that the BH charge is negligible due to charged matter accretion from the surroundings neutralising any initial charge. However, the rotation of the BH can drag an external magnetic field, by this inducing a magnetic-field-parallel electric field component that causes the accumulation of a net BH charge (Wald, 1974; King and Pringle, 2021). While it is still debated whether a potential net charge can render electromagnetic extraction of energy from the BH (via the Blandford-Znajek (BZ) mechanism, see section 2.1.7) impossible or at least intermittent (King and Pringle, 2021), a net charge has negligible effect on the general relativistic spacetime geometry (Zajaček et al., 2018; Zajacek and Tursunov, 2019).

Therefore, the spacetime geometry of astrophysical BHs is usually described by that one of spinning, non-charged BHs, given by the Kerr metric (Kerr, 1963; Boyer and Lindquist, 1967). The radius of the event horizon from the singularity is then given by

$$r_\mathrm{h} = \frac{r_\mathrm{S}}{2}\left(1+\sqrt{1-a^2}\right) \tag{2.1}$$

where the Schwarzschild radius

$$r_\mathrm{S} = \frac{2\,G\,M_\mathrm{BH}}{c^2} \approx \frac{M_\mathrm{BH}}{10^9 M_\odot} 20\,\mathrm{au} \approx \frac{M_\mathrm{BH}}{M_\odot} 3\,\mathrm{km} \tag{2.2}$$

is a characteristic length for BH physics. For spinning BHs, r_h decreases towards $r_\mathrm{S}/2$. Furthermore, general relativity predicts the frame-dragging effect, according to which the spacetime is forced to co-rotate with the rotating BH at an angular velocity that decreases with increasing distance. In other words, a locally non-rotating object (called a Bardeen observer) will rotate around the BH, if seen from a distant observer. Inside of a surface called the static limit, located at

$$r_\mathrm{stat} = \frac{r_\mathrm{S}}{2}\left(1+\sqrt{1-a^2\cos^2\theta}\right) \tag{2.3}$$

where θ is the polar angle, the frame dragging is fast enough that neither particles nor photons can be stationary with respect to the distant observer. The region between the event horizon and the static limit is called ergosphere, as energy can be extracted in this region from the BH via Penrose processes (Penrose, 1969; Tursunov et al., 2020). Ergospheric particles can attain trajectories with negative redshifted energy (which is the energy as measured by a very distant observer). When such negative-redshifted-energy particles are created through particle interactions in the ergosphere and plunge into the BH, the rotational energy of the BH decreases. The second particle involved in the interaction correspondingly gains energy and can carry it away.

Another important surface in the BH vicinity is the outer light surface (sometimes also called light cylinder, in analogy to pulsar magnetospheres). This is the surface where the rotational velocity of a co-rotating test particle equals c. In the case of a rotating plasma-filled BH magnetosphere, charged particles act like a bead on a wire. For causal reasons, such particles can cross the light surface only from the inside towards the outer magnetosphere, hence the light surface also acts like a one-way membrane for charged particles. Additionally, an inner light surface appears inside of the static limit, due to the frame-dragging effect, and it acts as a one-way membrane in the opposite direction. These most important surfaces around a spinning BH are shown in figure 2.5.

Astrophysical BHs appear in at least three classes. Stellar-mass BHs are the remnants of massive stars, forming when the gravitational attraction of the stellar matter can neither be supported by radiation pressure nor by quantum mechanical degeneracy pressure, and have masses in the approximate range $3\,M_\odot - 100\,M_\odot$. Intermediate-mass BHs are thought to be the results of mergers of stellar-mass BHs. SMBHs have masses of $> 10^5\,M_\odot$ and are located in the centres of massive galaxies. They render galactic activity possible mainly via two qualities:

First, due to their high mass, the created potential well is extraordinarily deep. As a result of their compactness, a test mass can approach from infinity up to few r_S and release energy with an efficiency η of several percent up to 42 % (Bambi, 2018) before plunging into the event horizon. Precisely, the matter approaching a BH is thought to accumulate in an accretion flow (AF). In this flow, the particles have a small radially inward-directed velocity. Additionally, they revolve around the BH on nearly Keplerian orbits. However, unlike to Newtonian gravity, in general relativity there is an innermost stable circular orbit (ISCO), also called marginally stable circular orbit (Bardeen, Press and Teukolsky, 1972). There exist circular orbits inside of the ISCO, but a small perturbation of a test particle on an orbit inside of the ISCO will inevitably cause the particle to cross the event horizon. Therefore, the inner boundary of an AF is usually assumed to be located at the ISCO. Its radial location is dependent on M_BH, on a and on the revolution direction of the test particle. For a Schwarzschild BH ($a = 0$), for an extreme-Kerr BH ($a = 1$) with prograde particle orbit and for an extreme-Kerr BH with retrograde particle orbit, the ISCO is located at $r_\mathrm{ISCO} = 3\,r_\mathrm{S}$, $0.5\,r_\mathrm{S}$ and $4.5\,r_\mathrm{S}$, respectively. For a prograde orbit, r_ISCO decreases monotonically with increasing a.

The second important feature is the rotation of the BH. Without it jets can most probably not be launched. The rotational energy of the BH can be tapped either via Penrose processes or together with the co-rotating ambient magnetic field through the Blandford-Znajek mechanism or via the Blandford-Payne mechanism (Blandford and Znajek, 1977; Blandford and Payne, 1982), as will be explained in section 2.1.7.

2.1.2 The Accretion Flow

Material from the surrounding host galaxy is gravitationally attracted by the SMBH. The stream of infalling matter is called the AF, while the mass that is infalling per unit time is called the accretion rate $\dot{M}$.

The gravitational potential energy of the particles is transformed into kinetic energy. The latter is dissipated through viscous heating, resulting in an increase of thermal energy, such that the matter in AFs around BHs is ionised. Eventually, a part of the thermal energy is transformed through emission of radiation into electromagnetic energy. The resulting temperature arises from the balance of heating and cooling via radiation emission.

Releasing energy with an efficiency η, the luminosity of the AF is given by

$$L = \eta\, \dot{M} c^2. \tag{2.4}$$

Although the accretion process can be extremely efficient ($\eta = 0.42$) for extreme-Kerr BHs and prograde orbits, a moderate radiative efficiency $\eta = 0.1$ is usually assumed in approximative AF models (Esin, McClintock and Narayan, 1997; Frank, King and Raine, 2002). Notice that $\eta = 0.1$ is valid for standard (geometrically thin) disks, but that η can be orders of magnitude smaller in the case of advection-dominated accretion flows (ADAFs) (Narayan, Mahadevan and Quataert, 1998).

A characteristic luminosity of spherically symmetric AFs consisting out of protons and electrons is the Eddington luminosity

$$L_{\mathrm{Edd}} = \frac{4\pi\, G\, M_{\mathrm{BH}}\, m_{\mathrm{p}}\, c}{\sigma_{\mathrm{T}}} \approx 1.3 \cdot 10^{40} \frac{M_{\mathrm{BH}}}{10^9\, M_\odot} \mathrm{W}. \tag{2.5}$$

It is obtained by equating the outward-directed radiation force on the electrons (which is mediated electromagnetically to the protons) with the inward directed gravitational force of the central BH on the protons. If the luminosity exceeds L_{Edd}, the accretion flow is eroded by its own radiation. By eq. 2.4, one can assign an Eddington accretion rate

$$\dot{M}_{\mathrm{Edd}} = \frac{L_{\mathrm{Edd}}}{\eta\, c^2} \approx 22 \frac{M_{\mathrm{BH}}}{10^9\, M_\odot} \frac{M_\odot}{\mathrm{a}}. \tag{2.6}$$

Then, the dimensionless accretion rate is $\dot{m} = \dot{M}/\dot{M}_{\mathrm{Edd}}$ and the accretion ceases for $\dot{m} > 1$.

2.1.2.1 Standard Disks

Interstellar matter has a non-vanishing angular momentum. Therefore, the AF is generally not spherically symmetric. Relative velocities of particle encounters are bigger for motions with a component parallel to the rotation axis than for motions whose orbital angular momentum is parallel to the total angular momentum. Consequently, dissipation of kinetic energy is stronger for motions parallel to the rotation axis, at least if the accretion rate is high enough. As a result, the AF collapses to a differentially rotating disk, which stretches from the ISCO up to a distance of order $10^3\, r_{\mathrm{S}}$. Due to the differential rotation of the plasma and due to a magnetic field frozen into the plasma, the magnetorotational instability leads to angular momentum transport towards larger radii (Balbus and Hawley, 1991). Only by this, a particle's centrifugal barrier is shifted inwards and the particle can drift towards the accretor.

Additionally, a disk whose angular momentum is tilted with respect to the BH angular momentum becomes warped as a result of radially dependent precession velocities due to the frame-dragging effect. In such warped disks, viscous torques achieve an alignment of the disk angular momentum with the BH angular momentum, which is known as the Bardeen-Petterson effect (Bardeen and Petterson, 1975).

Standard accretion disks are optically thick and geometrically thin, meaning that their height h at a given radius r is much smaller than r (Shakura and Sunyaev, 1973; Novikov and Thorne, 1973). For $r/r_\mathrm{S} \gg 3$ the plasma temperature increases with decreasing r according to $T \sim \frac{\dot{M}^{0.25}}{M_\mathrm{BH}^{0.5}}(r/r_\mathrm{S})^{-0.75}$ (Kato, Fukue and Mineshige, 2008). Locally, a standard disk emits thermal radiation at temperature T. The composite disk spectrum is a multi-colour blackbody spectrum. As the radiative cooling is very efficient, typical disk temperatures are in the range of several $10^4\,\mathrm{K}$. Hence, the standard disks mainly emit in the ultraviolet (UV) regime and their spectrum is observationally called a big blue bump. This type of AFs is present if the accretion rate $\dot{m} \gtrapprox \dot{m}_\mathrm{crit}$ is bigger than a critical value in the range $0.01 \lessapprox \dot{m}_\mathrm{crit} \lessapprox 0.1$ (Esin, McClintock and Narayan, 1997; Mahadevan, 1997; Narayan, Mahadevan and Quataert, 1998).

2.1.2.2 Advection-Dominated Accretion Flows

The ADAF is an analytical solution for radiatively inefficient AFs (Narayan and Yi, 1994). ADAFs are thought to be present if the accretion rate is either very high (super-Eddington) or very low with $\dot{m} \lessapprox \dot{m}_\mathrm{crit}$ (Esin, McClintock and Narayan, 1997; Narayan, Mahadevan and Quataert, 1998, for an excellent review). In the latter case, the AF is dilute and optically thin. Therefore, cooling of the plasma is inefficient, meaning that elements of the AF cannot radiate their thermal energy away before they are deposited in the BH. Instead of cooling via emission of thermal radiation, the thermal energy is advected with the flow. As a result, ADAFs are hot in comparison to standard disks and geometrically thick ($h(r) \approx r$) or even almost spherical AFs. The typical inward-directed particle velocity is comparable in size to the radial velocity, which is sub-Keplerian.

The viscous heating of the flow mainly acts on the protons (and/or ions) due to their higher inertial mass, whereas the electron viscous heating is reduced by $m_\mathrm{e}/m_\mathrm{p}$. Electrons are additionally heated by energy transfers from Coulomb interactions with the protons. Cooling through radiation emission is happening for the electrons, while it is reduced for the protons. Therefore, a two-temperature plasma is evolving in the central portion in ADAFs with the electron temperature T_e being several $10^9\,\mathrm{K}$ and constant along r and the proton temperature $T_\mathrm{p} \sim r^{-1}$ and being of the order $10^{12}\,\mathrm{K}$ (Narayan and Yi, 1995; Narayan, Mahadevan and Quataert, 1998).

ADAF spectra are non-thermal ones. They are comprised of synchrotron radiation, IC scattered radiation and bremsstrahlung. Based on the self-similar ADAF model by Narayan and Yi (1995), Mahadevan (1997) has derived analytic expressions for the contributions of the spectral ADAF luminosity

$$L_\mathrm{ADAF}(\epsilon) = L_\mathrm{ADAF,\,sync}(\epsilon) + L_\mathrm{ADAF,\,IC}(\epsilon) + L_\mathrm{ADAF,\,brems}(\epsilon) \tag{2.7}$$

as a function of the photon energy ϵ. To determine the synchrotron radiation contribution $L_\mathrm{ADAF,\,sync}$ of the ADAF spectrum, Mahadevan (1997) assumes an isotropic relativistic Maxwellian electron distribution of constant T_e and determines the transition energy $\epsilon_\mathrm{trans}(r)$ (corresponding to ν_c in Mahadevan (1997)), at which the optically thin synchrotron radiation becomes self-absorbed, as a function of the radial coordinate r. It is assumed that at a given r, the ADAF is radiating monochromatic synchrotron radiation at ϵ_trans and that the spectrum at this transition energy is described by the Rayleigh-Jeans law. The synchrotron spectrum is then obtained from the superposition of all the monochromatically approximated contributions from different r in the range $r_\mathrm{ADAF,\,in} \leq r \leq r_\mathrm{ADAF,\,out}$ as $L_\mathrm{ADAF,\,sync}(\epsilon) \sim \epsilon^{2/5}$. Outside of $r_\mathrm{ADAF,\,out}$, a one-temperature plasma with $T_\mathrm{e} \sim r^{-1}$ is assumed, yielding a dependency $L_\mathrm{ADAF,\,sync}(\epsilon) \sim \epsilon^{22/13}$ below the transition energy

$\epsilon_{\text{trans}}(r_{\text{ADAF, out}})$ corresponding to $r_{\text{ADAF, out}}$. Precisely, Mahadevan (1997) obtains:

$$\begin{aligned}
&\text{If } \epsilon_{\text{trans}}(r_{\text{ADAF, out}}) \leq \epsilon \leq \epsilon_{\text{trans}}(r_{\text{ADAF, in}}) : \\
&L_{\text{ADAF, sync}}(\epsilon) = L_{\text{ADAF, sync, 1}}(\epsilon) = \\
&= 1.05 \cdot 10^{-31}\, (s_1(\alpha,\, \beta)\, s_2)^{1.6} \left(\frac{M_{\text{BH}}}{M_\odot}\right)^{1.2} \dot{m}^{0.8} \left(\frac{T_{\text{e}}}{\text{K}}\right)^{4.2} \left(\frac{\epsilon}{h_{\text{Pl}}\,\text{Hz}}\right)^{0.4} \text{W}\,\text{Hz}^{-1} \qquad (2.8\text{a})
\end{aligned}$$

$$\begin{aligned}
&\text{If } \epsilon \leq \epsilon_{\text{trans}}(r_{\text{ADAF, out}}) : \\
&L_{\text{ADAF, sync}}(\epsilon) = L_{\text{ADAF, sync, 2}}(\epsilon) = \\
&= L_{\text{ADAF, sync, 1}}(\epsilon_{\text{trans}}(r_{\text{ADAF, out}})) \left(\frac{\epsilon}{\epsilon_{\text{trans}}(r_{\text{ADAF, out}})}\right)^{22/13} \qquad (2.8\text{b})
\end{aligned}$$

$$\begin{aligned}
&\text{If } \epsilon \geq \epsilon_{\text{trans}}(r_{\text{ADAF, in}}) : \\
&L_{\text{ADAF, sync}}(\epsilon) = 0
\end{aligned}$$

where s_1 and s_2 are dimensionless quantities. $s_1(\alpha,\, \beta)$ is prescribed by parameters of the self-similar ADAF solution, namely by the viscosity parameter $\alpha = 0.3$ and by the gas pressure to total pressure ratio $\beta = 0.5$ (meaning equipartition between magnetic and gas pressure, Narayan and Yi, 1995; Mahadevan, 1997). s_2 is dependent on the above-mentioned transition energy and is determined either approximately analytically or numerically (Mahadevan, 1997, see appendix B therein).

For the Comptonised spectral luminosity, Mahadevan (1997) applies standard treatments (based on e.g. Rybicki and Lightman (1979) and Ghisellini (2013)), approximates the target photons as being monochromatic at the energy $\epsilon_{\text{trans}}(r_{\text{ADAF, in}})$, employs an electron scattering optical depth τ which is half of the optical depth used by Narayan and Yi (1995), uses the mean amplification factor A of Comptonisation and finally gets:

$$\begin{aligned}
&\text{If } \epsilon_{\text{trans}}(r_{\text{ADAF, in}}) \leq \epsilon \leq 3\, k_{\text{B}}\, T_{\text{e}} : \\
&L_{\text{ADAF, IC}}(\epsilon) = L_{\text{ADAF, sync, 1}}(\epsilon_{\text{trans}}(r_{\text{ADAF, in}})) \cdot \left(\frac{\epsilon_{\text{trans}}(r_{\text{ADAF, in}})}{\epsilon}\right)^{-\frac{\ln \tau(\dot{m},\, \alpha,\, r_{\text{ADAF, in}})}{\ln A(T_{\text{e}})}} \qquad (2.8\text{c})
\end{aligned}$$

For the bremsstrahlung spectral luminosity involving electron-proton as well as electron-electron interactions, expressions derived by Svensson (1982) are used to obtain:

$$L_{\text{ADAF, brems}}(\epsilon) = 9.2 \cdot 10^{17} \ln\left(\frac{r_{\text{ADAF, out}}}{r_{\text{ADAF, in}}}\right) F(T_{\text{e}}) \frac{M_{\text{BH}}}{M_\odot} \frac{\dot{m}^2}{\alpha^2} \frac{\text{K}}{T_{\text{e}}} \exp\left(-\frac{\epsilon}{k_{\text{B}}\, T_{\text{e}}}\right) \text{W}\,\text{Hz}^{-1} \qquad (2.8\text{d})$$

Here, $F(T_{\text{e}})$ is the auxiliary function 28 by Mahadevan (1997) that depends solely on the temperature.

Henceforth, in all computations it is used $r_{\text{ADAF, in}} = 3\, r_{\text{S}}$ (motivated from r_{ISCO}) and $r_{\text{ADAF, out}} = 1000\, r_{\text{S}}$ (in agreement with literature values). Then, the spectral luminosity essentially is dependent on the energy ϵ and on the parameters M_{BH}, $\dot{m}$ and T_{e}.

Several ADAF spectra determined with the equations 2.8a-2.8d are exemplarily shown in figure 2.2. The bremsstrahlung spectral luminosity becomes negligible above $\epsilon_{\text{ADAF, 0}} = 300\, k_{\text{B}}\, T_{\text{e}}$, which is therefore used as an upper cutoff of the ADAF spectra (and as an upper integration border in the numerical integrations) henceforth. To obtain the total ADAF luminosity, the integration of $L_{\text{ADAF}}(\epsilon)$ has to be performed:

$$L_{\text{ADAF, tot}}(M_{\text{BH}}, \dot{m}, T_{\text{e}}) = \int_0^\infty L_{\text{ADAF}}(\epsilon, M_{\text{BH}}, \dot{m}, T_{\text{e}})\, \mathrm{d}\epsilon \qquad (2.11)$$

To estimate the spectral number density of photons around the AF, one has to estimate the total surface area A_{ADAF}. In this work, the ADAF height is assumed to be $h(r) = r$. Then, the radiating ADAF surface is approximated as the sum of the inner cylindrical lateral area, the outer cylindrical lateral area and two times the outer conical lateral area minus two times the inner conical lateral area. Thus, it is

$$A_{\mathrm{ADAF}} = 2\,\pi\,\left(r_{\mathrm{ADAF,\,in}}^2 + r_{\mathrm{ADAF,\,out}}^2 + r_{\mathrm{ADAF,\,out}}^2\,\sqrt{1.25} - r_{\mathrm{ADAF,\,in}}^2\,\sqrt{1.25}\right) \tag{2.12}$$

Then, the spectral number density of ADAF photons is

$$n_{\mathrm{ADAF}}(\epsilon, M_{\mathrm{BH}}, \dot{m}, T_{\mathrm{e}}) = L_{\mathrm{ADAF}}(\epsilon, M_{\mathrm{BH}}, \dot{m}, T_{\mathrm{e}})/(h_{\mathrm{Pl}}\,c\cdot\epsilon\cdot A_{\mathrm{ADAF}}). \tag{2.13}$$

The division by h_{Pl} is due to the fact that L_{ADAF} is differential in $\mathrm{d}\nu$, whereas n_{ADAF} is differential in $\mathrm{d}\epsilon$. The total number density is then obtained by integration of $n_{\mathrm{ADAF}}(\epsilon)$ along ϵ.

$$n_{\mathrm{ADAF,\,tot}}(M_{\mathrm{BH}}, \dot{m}, T_{\mathrm{e}}) = \int_0^\infty n_{\mathrm{ADAF}}(\epsilon, M_{\mathrm{BH}}, \dot{m}, T_{\mathrm{e}})\,\mathrm{d}\epsilon \tag{2.14}$$

In the course of this work, the integrations of the ADAF spectra (equations 2.11, 2.14 and 2.18) are performed analytically as well as numerically.

2.1.2.2.1 Analytical Integration First, equation 2.14 is determined analytically. The analytical integrations of the piecewise power laws (PLs) involving equations 2.8a, 2.8b and 2.8c are straightforward. The bremsstrahlung contribution 2.8d is integrated by applying the exponential integral. To do this, notice first that the integration is internally performed along the frequency ν instead of along ϵ. The lower integration border 0 is replaced by 1 Hz, which produces an error, that is negligible as the bremsstrahlung spectrum contributes far above 1 Hz in the X-ray regime. By this, the integral is (up to a coefficient) an exponential integral $E_1(z)$ (Abramowitz and Stegun, 1968) with argument $z = h_{\mathrm{Pl}}/(k_{\mathrm{B}}\,T_{\mathrm{e}})$, which is determined with help of the `Python`-implemented exponential integral `scipy.special.exp1`.

2.1.2.2.2 Numerical Integration Second, the integration is executed with the `Python` function `scipy.integrate.quad` described in section 4.2. This function can be used easily to integrate the spectral number densities based on equation 2.8a and 2.8b. Direct integration of the spectral number density based on 2.8c with `scipy.integrate.quad` and with the integration borders (in energy space) being $b_{\mathrm{l}} = \epsilon_{\mathrm{trans}}(r_{\mathrm{ADAF,\,in}})$ and $b_{\mathrm{0}} = 3\,k_{\mathrm{B}}\,T_{\mathrm{e}}$, often raises a `Python` warning and produces a negative, thus obviously erroneous result. This error occurs because the integration range stretches over several orders of magnitude along which the integrand is strongly changing. This problem appears several times in the course of this work. Therefore, in section 4.2 it is described in a general way and a procedure called integral splitting approach (ISA) is developed that prevents the warning and produces correct results.

Applying the ISA with $n = 3$, the spectral number density based on 2.8c can easily be integrated with `scipy.integrate.quad`. The numerical integration of the spectral number density based on 2.8d is performed with the ISA with $n = 4$. To obtain a result comparable to the analytical computation, the same lower integration border $b_{\mathrm{l}} = 1\,\mathrm{Hz}$ is used. As an upper border (in frequency space), $b_{\mathrm{0}} = \epsilon_{\mathrm{ADAF,\,0}}/h_{\mathrm{Pl}}$ is used instead of infinity, guaranteeing that the upper border is well above the exponential cutoff.

During all integrations of the ADAF photon distributions in this work, it is always made sure that the analytical and the numerical integration of both the synchrotron contributions and of the IC contribution and of the bremsstrahlung contribution, respectively, yield equal results.

2.1.3 The Corona

Above and below the equatorial plane, a hot and dilute plasma is surrounding the AF. It is called corona in analogy to the solar corona. Thermal electrons in the corona IC up-scatter the radiation from the AF, producing a PL in the X-ray regime with exponential cutoff around $\approx 100\,\mathrm{keV}$ (Haardt, Maraschi and Ghisellini, 1994). A part of this X-ray radiation is emitted in direction away from the

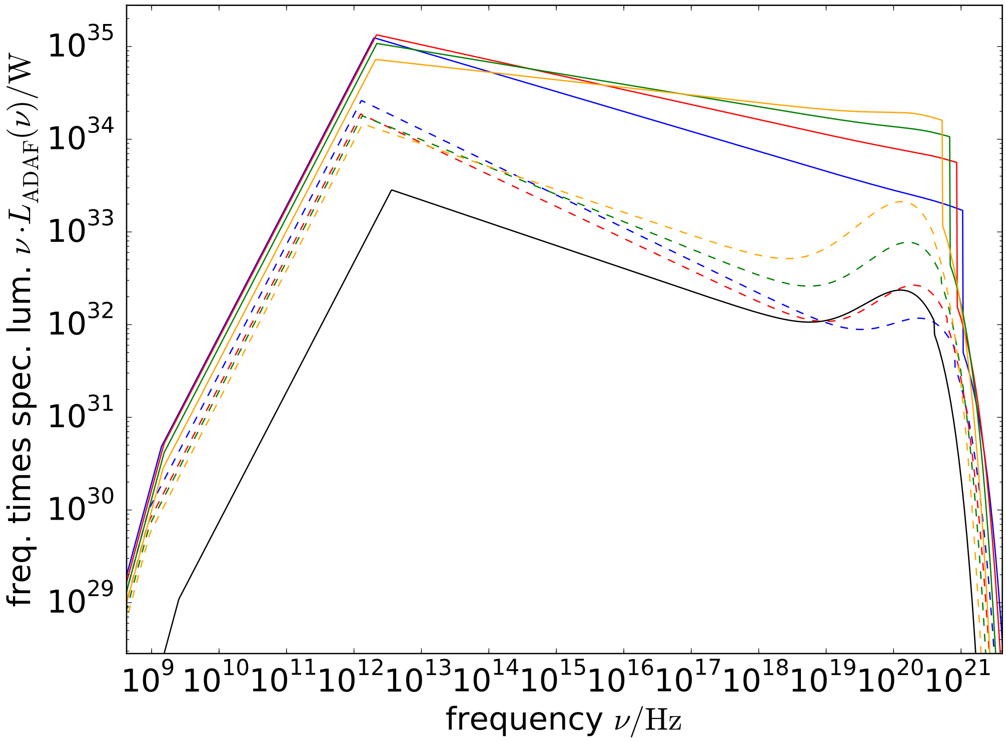

Figure 2.2: Exemplary ADAF spectra determined with equation 2.7. Plotted is the product $\nu\, L_{\mathrm{ADAF}}(\nu)$ of the frequency and the spectral luminosity versus the frequency. The colour coding is as follows: The blue, red, green, orange lines are determined with $M_{\mathrm{BH}} = 10^9\, M_\odot$ and with $\dot{m} = 1.0 \cdot 10^{-4}$, $2.0 \cdot 10^{-4}$, $4.0 \cdot 10^{-4}$, $8.0 \cdot 10^{-4}$, respectively. The solid, dashed coloured lines are for the values of T_{e} given in the second (higher temperatures in the $\xi = 0.01$ case), third line (lower temperatures in the $\xi = 0.1$ case) of table 5.4, respectively. For instruction, the black solid line is determined with $M_{\mathrm{BH}} = 10^8\, M_\odot$, $\dot{m} = 8.0 \cdot 10^{-4}$ and $T_{\mathrm{e}} = 6.4 \cdot 10^9\,\mathrm{K}$ and shows in comparison to the orange dashed line the dependence on M_{BH}. In all spectra, the peak at infrared (IR) wavelengths, corresponding to synchrotron radiation from $r_{\mathrm{ADAF,\,in}}$, is clearly seen. For decreasing M_{BH}, the peak moves to higher frequencies, as the ISCO approaches the BH. Emission below the peak is due to synchrotron emission from larger radii, until the self-absorbed part shapes another kink at $\nu \approx 10^9\,\mathrm{Hz}$. Above the synchrotron part, the Comptonised emission extends up to the soft gamma-ray regime. It is strongly dependent on T_{e} (on the one hand through the varying slope and on the other hand through the normalisation ensuring the continuity to the synchrotron part (see equation 2.8c)). The bremsstrahlung spectral luminosity can be dominating the X-ray output if T_{e} is not that high that it is overwhelmed by the Comptonised part.

disk. Another part is irradiating the disk, with two consequences: First, the radiation is Compton scattered by the disk electrons and thus back-reflected, by this producing a bump around several tens of keV (Fabian and Miniutti, 2005). Second, the radiation from the corona is exciting or ionising metals of the disk matter, by this causing fluorescent lines like e.g. the iron Kα lines. In some physical properties (high temperature, optical thinness, X-ray emission via IC scattering, inflated geometry) coronae are similar to ADAFs. Thus, coronae can be understood as ADAFs that are sandwiching standard disks.

2.1.4 The Broad-Line Region

Above and below the AF and the corona, there is a region called the BLR. The matter in this region is illuminated by the visible, UV and X-ray radiation of the AF and the corona. By this, gas particles become excited and the gas becomes partly ionised and attains a temperature of $\approx 10^4\,\mathrm{K}$ (see e.g. Netzer, 1990; Goad and Koratkar, 1998). During de-excitation of the matter in this region, allowed emission lines are emitted. By this, a fraction ξ of the continuum luminosity from the AF (and the corona) is reprocessed into the emission line luminosity. Notice that for optically thick BLR material, this reprocessing fraction ξ is identical to the more geometrically motivated covering factor of a BLR (Davidson and Netzer, 1979). A widely used value for the reprocessing fraction is $\xi \approx 0.1$.

The emission lines are observationally found to be Doppler-broadened by $10^3 - 2.5 \cdot 10^4\,\mathrm{km/s}$ (Peterson, 2006), motivating the designation BLR. These line widths cannot be explained by thermal broadening. Instead, they can be explained by bulk motion of the broad-line-emitting material around the central BH. For example, if the BLR material is concentrated in discrete gas clouds that are moving on Keplerian orbits and if the orbital planes are randomly oriented in space, then the superposition of the emission lines from all the clouds can cause the observed line widths.

The geometric structure of the BLR is still debated. It is often assumed to be a spherical ensemble of ionised gas clouds, as would be the case if the clouds' Keplerian orbits were isotropically oriented with a wide range of semi-major axes, but there is also evidence for BLRs having thin, shell-like or ring-formed structure (Jarvis and McLure, 2006; Decarli, Dotti and Treves, 2011; Fian et al., 2021), or bowl-shaped geometry (Goad, Korista and Ruff, 2012; Bentz et al., 2021). The typical electron density inside the clouds is $\approx 10^{15}\,\mathrm{m}^{-3}$. The total number N_{cl} of clouds is usually found to be higher than 10^6 in prominent BLRs, but it can also be smaller than several 10^3 (Peterson, 2006) in low-luminosity AGN. The nature and origin of the clouds is uncertain, too. Envelopes of supergiant stars (e.g. Scoville and Norman, 1988; Alexander and Netzer, 1997), gas flows from tidal disruption of stars (Roos, 1992), from star-AF interaction (Vilkoviskij and Czerny, 2002) or from gravitationally unstable disks (Collin and Huré, 2001) as well as overdensities due to shocks in the AF (Fromerth and Melia, 2001) have been suggested as the origin of the BLR clouds. Another possibility is that the BLR is a more continuous radiatively or hydromagnetically driven wind from the accretion disk (Shlosman, Vitello and Shaviv, 1985; Konigl and Kartje, 1994; Czerny, 2019; Vietri et al., 2020).

Typical radial sizes r_{BLR} of BLRs are between 0.01 pc and 1 pc but they can also be as low as 10^{-4} pc (Peterson et al., 2005). The radial extent can be determined empirically with reverberation mapping. At this observational technique, an AGN is monitored for several weeks up to many months. It is often found, that time variations in the continuum emission from the AF (e.g. due to changes in the accretion rate) are followed by time variations of the broad emission lines. This tracing variability of the lines is interpreted as the causal response to variations of the illuminating AF radiation. The AF radiation reverberates with the BLR material. Consequently, the time delay between variations of the continuum and the corresponding variations of the lines must be the light-travel time r_{BLR}/c from the AF, assumed to be in the central portion of the AGN, to the BLR matter. With help of reverberation mapping, the sizes of some dozens of (mostly low-luminosity) AGN have been determined. It was additionally found, that the sizes depend on the emission lines considered. This is a hint to a stratification of the BLR material according to atomic mass or ionisation state.

Furthermore, dependencies of the radial BLR size r_{BLR} on the luminosity in certain bands of the ionising continuum have been found and relations $r_{\mathrm{BLR}} \sim L^{\alpha}$ with $\alpha \approx 0.5$ have been compiled (see Kilerci Eser et al., 2015, and references therein). For example, Kaspi et al. (2007) have conducted a reverberation mapping campaign of eleven high-redshift, high-luminosity AGN of quasar type. Incorporating their own measurements as well as those from Peterson et al. (2005), they obtained the widely used empirical relation

$$r_{\mathrm{BLR}} = 2.2 \cdot 10^{14} \cdot \left(\frac{L_{135\,\mathrm{nm}}}{10^{37}\,\mathrm{W}}\right)^{0.55} \mathrm{m}. \tag{2.15}$$

This determines the C IV time-lag radius r_{BLR} of the BLR from the 135 nm continuum luminosity. The latter is, according to Kilerci Eser et al. (2015), a better proxy for the ionising continuum radiation than e.g. bands in the optical. Nevertheless, it is uncertain whether the 135 nm luminosity is correlated with the ionising continuum. An updated relationship between the C IV time-lag radius and the 135 nm luminosity was presented very recently by Kaspi et al. (2021):

$$r_{\mathrm{BLR}} = 2.5 \cdot 10^{14} \cdot \left(\frac{L_{135\,\mathrm{nm}}}{10^{37}\,\mathrm{W}}\right)^{0.45} \mathrm{m}. \tag{2.16}$$

It was obtained by incorporation of a total of 38 AGN spanning eight orders of magnitude in luminosity. The objects were compiled from their own reverberation mapping campaign of high-redshift quasars, which lasted more than a decade and includes the objects already considered by Kaspi et al. (2007), and from samples of other authors.

Using adaptive-optics-assisted telescopes together with interferometry, it is today possible to achieve high sensitivity and an angular resolution of the order of 10 μas at near-IR wavelengths. With the General Relativity Analysis via Very Large Telescope Interferometry (GRAVITY) instrument of the four Very Large Telescope detectors, the BLRs of three AGN could be directly imaged (Gravity Collaboration et al., 2021, and references therein). The blueshifted part (approaching along the line of sight) of the BLR could be resolved from the redshifted part (escaping along the line of sight). Thus, the rotation of a disk-like BLR was confirmed and radii in agreement with those obtained from reverberation mapping were yielded. A similar, spectroastrometric approach was pursued by Bosco et al. (2021) using the single Gemini North 8 m telescope. These authors obtained a BLR radius of few pc for the quasar J 2123-0050, in accordance with radius-luminosity relations, and strengthened the rotating-disk BLR models.

Another sophisticated approach to study the BLR geometry is to analyse spectra of AGN that are multiply gravitationally lensed. Broad emission line strengths and their line profiles can differ between the images of the same lensed AGN. These variations are (besides other causes like extinction or an inhomogeneous matter distribution in the lens galaxy) due to microlensing events affecting certain images. Compact objects in the lens galaxy magnify the flux of the AGN emission region. Thereby, a compact emission region is generally stronger affected by microlensing than an extended region. Therefore, high-ionisation lines and lines from clouds with high orbital velocity are magnified in comparison to low-ionisation lines and lines with low orbital velocity. Statistically evaluating emission line profiles from five epochs of 27 lensed AGN, Fian et al. (2021) could infer typical emission-region radii of three broad lines in agreement with reverberation mapping results and confirming the stratification of the BLR.

The broad emission lines are clearly observable in certain AGN types and their presence in unpolarised light is in particular one of the defining criteria of Seyfert 1 galaxies or more generally of type 1 AGN. They are also observed in the blazar-type AGN. Observational composite spectra, that reflect a typical visible-to-UV spectrum of AGN with emission lines, have e.g. been compiled by Telfer et al. (2002) and Pian, Falomo and Treves (2005). These will be used later, in chapter 5 and 6 to model a set of broad emission lines of the blazars Mrk 501 and 3C 279. Additionally, typical line strengths can be obtained theoretically from photoionisation codes like Cloudy (Ferland et al., 2017; Abolmasov and Poutanen, 2017) and Chianti (Dere et al., 1997; Landi et al., 2012) as well as from the Harvard-Smithsonian Center for Astrophysics atomic line database by R. L. Kelly (see `https://lweb.cfa.harvard.edu/ampcgi/kelly.pl`).

2.1.5 The Equatorial Torus

Around the AF, the corona and the BLR, there is a toroidal structure lying in the plane of the AF (Antonucci and Miller, 1985; Urry and Padovani, 1995). It is thought to be an outer, cloudy extension of the AF (Markowitz, Krumpe and Nikutta, 2014) with temperatures below the sublimation temperature ($< 2000\,\mathrm{K}$) of the accreted material, which is therefore present in molecular state. Therefore, it is also called dusty torus or molecular torus.

The torus is located at pc-scale distances from the central BH (see e.g. Burtscher et al., 2013; Markowitz, Krumpe and Nikutta, 2014). However, it was found that the inner torus boundary as determined by the sublimation edge increases with increasing luminosity of the central engine (Lawrence, 1991). With increasing luminosity the radiation pressure from the centre increases. By this, the torus recedes to bigger distances.

The torus absorbs the visible and UV emission from the AF, the corona and the BLR. The optical depth decreases in the X-ray regime, such that hard X-rays are absorbed less than soft X-rays. If the AGN is seen edge-on, the torus obscures the central engine, which gives rise to observational differences between edge-on seen objects (type 2 AGN) and more face-on seen sources (type 1 AGN). The dusty torus re-emits the incoming radiation thermally in the IR regime as well as in the form of molecular lines.

2.1.6 The Narrow-Line Region

Outside of the BLR and the equatorial torus, there is a region which is emitting lines that are Doppler-broadened by several $100\,\mathrm{km/s}$, and which is therefore called the narrow-line region (NLR). Like the BLR it is thought to consist of cloudy material with temperature of few $10^4\,\mathrm{K}$. The cause of the smaller line widths is the smaller orbital velocity of the clouds around the central BH. This points to the greater distances of the NLR material, which can indeed extend up to few kpc (Beckmann and Shrader, 2012). However unlike to the BLR, the density of clouds is smaller and the electron density inside the clouds is only $\approx 10^9\,\mathrm{m}^{-3}$ (Ghisellini, 2013) so that collisional de-excitations are improbable. Consequently, the NLR lines are forbidden emission lines.

2.1.7 The Relativistic Jet

The SMBH, the AF (with its corona), the BLR and the NLR as well as the equatorial torus are component parts of all AGN, even so they appear in varying strength or distinctness. About 10 % of all AGN have one additional feature, a relativistic jet. This is an outflow of electromagnetic fields and relativistic particles away from the accreting object. Jets are collimated, usually bipolar and oppositely directed along the symmetry axis of the AGN (usually coincident with the rotation axis of the BH and the AF). Relativistic AGN jets can have a length of several 100 kpc up to few Mpc, meaning that they reach out of the AGN's host galaxy. The jets usually emanate from a radio core, which is associated with the AGN centre, and terminate in diffuse structures called plumes or in extended radio lobes which can be dominated by smaller hot spots of radio emission.

The total jet luminosity can be up to $\approx 10^{39}\,\mathrm{W}$. This power is transported by electromagnetic radiation, Poynting flux and plasma. The latter is probably a mixture of electron positron pair plasma and of electron proton plasma. Radiation is produced mainly by the charged leptons while they propagate downstream. The jet inertia is mainly provided by the protons.

Relativistic jets emit non-thermally in two main emission zones: The blazar zone, which will be discussed in more detail in 2.3, is a relativistically moving region (or several regions) near the active nucleus or at the jet base and emits both highly variable in time and along the whole electromagnetic spectrum up to TeV energies. As the bulk of the emitting, relativistic particles is itself streaming with relativistic speed, the emission from the blazar zone is both Doppler-boosted to higher frequencies and flux densities and beamed due to relativistic aberration into a small solid angle directed in forward direction along the jet axis. This introduces a high degree of anisotropy concerning the observational appearance of jets.

The second emission zone is comprised by the two lobes (with their hotspots), which have an order of magnitude extent of $\approx 100\,\mathrm{kpc}$ and a magnetic flux density of $\approx 10^{-9}\,\mathrm{T}$. Here, the particles cool via emitting synchrotron radiation in the radio regime. As the lobes are typically much more extended than the jet diameter or than the radio core, the lobe emission is sometimes also called extended emission. This extended emission is isotropic and consequently, the observational appearance is not biased by the observer's viewing angle.

The mechanism of jet formation is not entirely understood yet, but it appears to be a scale-free phenomenon. In any case, three criteria have to be fulfilled to produce an astrophysical jet: First, a central object accretes matter in a gravitational well. Second, the accreted matter supplies angular momentum. Third, the AF is magnetised.

The magnetic field of the accretion disk at large distances r from the centre is mainly toroidal (Blandford and Payne, 1982), but becomes increasingly poloidal with decreasing r, due to magnetorotational instabilities in a turbulent dynamo (Brandenburg et al., 1995; Liska, Tchekhovskoy and Quataert, 2020). If the magnetic field lines are inclined at more than 30° against the rotation axis, the AF or coronal plasma can (driven by centrifugal forces in the rotating magnetosphere) stream away from the equatorial plane along the field lines (Blandford and Payne, 1982). If the field lines are tilted at less than 30°, additional radiation pressure is necessary to push the outflow over the effective potential barrier. Through this process, known as Blandford-Payne mechanism, sub-relativistic, matter-loaded outflows (disk winds) with radii of several r_S can be generated.

The AF advects the frozen-in poloidal magnetic field towards the BH. Wald (1974) has found that as an effect of general relativity, a BH rotating in an uniformly aligned magnetic field (with the magnetic field chosen without loss of generality to be parallel to the angular momentum) induces a quadrupole electric field. This effect can be considered analogous to a perfectly conducting sphere rotating in an aligned magnetic field. In this case, the Lorentz force redistributes charge carriers on the surface of the sphere in such a way that a quadrupole electric field arises and that positive, negative charges accumulate around the equator, near the poles, respectively. Provided that the BH environment is filled with plasma, the Wald field around a BH drives the following magnetospheric current system. Positrons, electrons stream towards the BH across the event horizon at the poles, in the equatorial region, respectively. Additionally positrons, electrons stream in outward direction away from the BH in the equatorial region, at the poles, respectively. The resulting electric current flows outward at low latitudes, then pole-ward through the magnetosphere, then inwards to the BH and then equator-ward. This electric circuit has two effects (Blandford and Znajek, 1977; Hirotani et al., 2021): First, the electric current flowing on the event horizon towards the equator experiences a toroidally directed Lorentz force in the poloidal magnetic field. This force creates a torque on the BH in opposite direction to the angular momentum. Thus, the BH is spun down and loses rotational energy. Second, the poloidal current system creates a toroidal magnetic field. The toroidal component is additionally enhanced due to the rotation of the AF and due to the frame dragging in the vicinity of the spinning BH. As an effect of the non-vanishing poloidal electric field and the non-vanishing toroidal magnetic field, a non-vanishing poloidal Poynting flux arises. This outflow of Poynting flux together with the spin down of the BH as results of the current system driven by the rotating BH is known as the BZ mechanism.

Effectively, the BZ mechanism extracts energy from the spinning BH and converts it into Poynting flux. For rapidly rotating BHs (with spin parameter a) and large ambient magnetic fields (with typical flux density B) threading the event horizon, the extracted BZ power can be estimated via

$$P_\mathrm{BZ} = 10^{38}\, a^2\, \frac{M_\mathrm{BH}}{10^9\, M_\odot} \left(\frac{B}{\mathrm{T}}\right)^2 \mathrm{W} \tag{2.17}$$

according to Hirotani et al. (2016). This can be several times larger than the power inflowing in form of the accreted matter (Tchekhovskoy, Narayan and McKinney, 2011; Ghisellini et al., 2014).

If the poloidal currents flow continuously, energy can be extracted permanently. In contrast, King and Pringle (2021) argue that the currents flow in such a way that a net BH charge accumulates with exactly that amount that nullifies the magnetic-field-parallel electric field. By this, the currents cease and BZ energy extraction is stopped. These authors infer that the BZ mechanism is at best an intermittent phenomenon, working in addition to Blandford-Payne-like disk winds.

The ergospheric outflow created through the BZ mechanism is with radii of few r_{S} much narrower than the one due to the Blandford-Payne mechanism. And while the Blandford-Payne mechanism creates a matter-dominated wind, the BZ jet base is initially Poynting-flux-dominated (Romero and Gutiérrez, 2020).

In the strong magnetic field (of order of magnitude $0.1-1\,\mathrm{T}$) of the magnetosphere, the gyroradii of charged particles are much smaller than the jet base. Therefore, charged particles cannot propagate directly from the AF into the jet, which is magnetically shielded. Matter loading might instead be mediated via gamma-ray photons or neutrons from an ADAF or a disk corona. Gamma-ray photons can, after penetrating from the AF into the jet funnel, interact with background photons to pair produce electrons and positrons (Levinson and Rieger, 2011). Neutrons, that have been produced in the hot AF either by proton self interactions or by proton photon inelastic interactions, can also penetrate into the jet and either decay or produce photo-mesons on background photons (Romero and Gutiérrez, 2020). Further mass load is possible through entrainment of BLR material, of disk wind particles or of intruding stellar matter. The pair content appears to dominate over the electron proton content in the majority of objects. In any case, a BZ jet is at first a Poynting-flux-dominated outflow. Because of the non-negligible inertia of the charge carriers constituting the magnetospheric circuit, the poloidal currents are not entirely parallel to the magnetic field lines. The currents have a poloidal component perpendicular to the field lines. With the toroidal magnetic field component, a Lorentz force along the poloidal field ensues. By this, charge carriers can be accelerated and the Poynting flux can be converted to kinetic particle energy. After the jet launching, it is additionally loaded with protons and leptons (electrons, positrons and neutrinos). They are accelerated by various processes (e.g. Blandford, Meier and Readhead, 2019; Matthews, Bell and Blundell, 2020) while propagating along the jet and cool by emitting radiation.

2.2 The Unification Scheme

Since the first systematic observations of galaxies whose SED is distinct from that of common non-active galaxies (shining via stars' and dust emission), a whole zoo of classifications for active galaxies has accumulated. Mainly based on morphological and spectral features, the objects are divided into a number of classes and sub-classes (and transitional objects), that cannot be addressed in completeness here (see e.g. Tadhunter, 2008; Dermer and Giebels, 2016, for precise summaries). According to the AGN unification scheme (Antonucci, 1993; Urry and Padovani, 1995), all AGN are thought to consist out of the component parts described in section 2.1. The overall AGN structure is sketched in figure 2.1. The physical constitution of an AGN is influenced by only few physical parameters, possibly the mass of the central SMBH, its angular momentum, the accretion rate and the environment of the galactic nucleus. For example, the angular momentum is thought to be the main influencing variable about the presence (high spin) or absence (low spin) of a jet, while the AGN power (luminosity) is mostly affected by the BH mass and by the accretion rate. Consequently, all these parameters affect the observational appearance, too, and lead to the multitude of classes. However, due to two features, AGN are anisotropic objects. Therefore, the appearance of an AGN is also influenced by the viewing angle of the observer with respect to the AGN symmetry axis. The same object would appear different and would be categorised into another class if it was observed from a different viewing angle.

The first feature causing an anisotropy is the presence of the equatorial torus, which absorbs radiation from the AF, the corona and the BLR, if the line of sight is crossing the torus. The latter will be the case, if the viewing angle θ measured against the symmetry axis (usually coincident with the angular momentum vector of the disk and of the SMBH) is near 90°, in other words for edge-on seen objects. Such AGN are called type 2 objects. Their continuum emission in visible, UV and soft-X-ray light is strongly absorbed. In unpolarised light they only show narrow emission lines, as the BLR is hidden behind the torus in contrast to the NLR. Radiation from the BLR is however scattered on free electrons surrounding the BLR and the torus. By this, broad emission lines can periscopically be seen in polarised light even for type 2 AGN (Antonucci and Miller, 1985). In contrast, type 1 AGN show broad emission lines also in unpolarised light and their continuum emission is unabsorbed, as the central engine is not (or far less) obscured by the torus.

A second anisotropising feature is the presence of a relativistic jet. As mentioned in section 2.1.7, because emission zones are themself moving with bulk Lorentz factor Γ along the jet, the jet emission is relativistically boosted and beamed into a narrow cone along the jet axis (Blandford and Rees, 1978; Scheuer and Readhead, 1979; Barthel, 1989). Therefore, from an observational point of view, the radiation from the jet will be most prominent if the jet is directed exactly towards the observer. Such AGN, from which the amplified blazar-zone emission is observationally dominating over the extended radio-lobe emission, are called blazars or type 0 AGN. An AGN is a blazar, if $\theta < 1/\Gamma$ is approximately satisfied (Dermer and Giebels, 2016). With increasing viewing angle, the jet emission from the blazar zone becomes less prominent. If $\theta > \arccos(\sqrt{(\Gamma-1)/(\Gamma+1)})$, the emission is even de-amplified, causing that jets observed from such viewing angles are observationally suppressed. The extended, un-beamed radio emission from the lobes is observable irrespective of θ. Therefore, misaligned jetted AGN, whose jet is detectable mainly by the extended radio emission, are called radio galaxies. These radio galaxies can again appear as type 1 or type 2 objects.

The explanation of the galactic nuclei taxonomy by the unification scheme is depicted in figure 2.3. At low BH spin and very low accretion rate, the nucleus is inactive, like in the case of Sagittarius A*, the central SMBH of our Milky Way. At low spin and high accretion rate, Seyfert galaxies exist at moderate luminosity and quasi-stellar objects (also called radio-quiet quasars) exist at high luminosity. AGN with high BH spin are addressed in the subsequent section.

2.3 Jetted Active Galactic Nuclei

Recall from section 2.1.7, that jets are thought to be created only by rapidly spinning BHs. At high spin (see right-hand side of figure 2.3) and low accretion rate, the AF, the torus and the line-emitting clouds are not prominent. Therefore, the non-thermal jet emission is dominating. Depending on the viewing angle, these objects are classified as Fanaroff-Riley I radio galaxies (Fanaroff and Riley, 1974) for a more edge-on view and as a blazar of sub-class BL Lac object for a face-on orientation. Similarly, at high angular momentum and high accretion rate, AGN are called Fanaroff-Riley II radio galaxies for a misaligned view and are designated as a blazar of sub-class flat-spectrum radio quasar (FSRQ) for a face-on alignment.

The strength of the relativistic jet correlates with the radio luminosity of the AGN. Until today, a strict division into radio-loud objects and radio-quiet objects is widely used. However, according to Padovani (2017) and Foschini (2017) applying this empirical nomenclature synonymously to jetted and non-jetted objects can be misleading and is therefore considered obsolete. First, the discrimination between radio-loud and radio-quiet, which is due to Sandage (1965), is historically motivated by the limitations of radio telescopes at that time. Since then, it turned out that radio-quiet-called AGN can indeed be faint radio emitters and jetted objects (Sbarrato et al., 2021). Second, the radio loudness basically is radio flux divided by optical flux. This is a valid definition only if the optical emission comes from the AF. Absorption of optical light leads to overestimation of the radio loudness, while boosted jet emission leads to underestimation. Therefore, the radio loudness is a reasonable definition and may be used for type 1 objects (unobscured and weakly or non-beamed AGN), but it should not be used with type 2 objects, blazars or radio galaxies. Third,

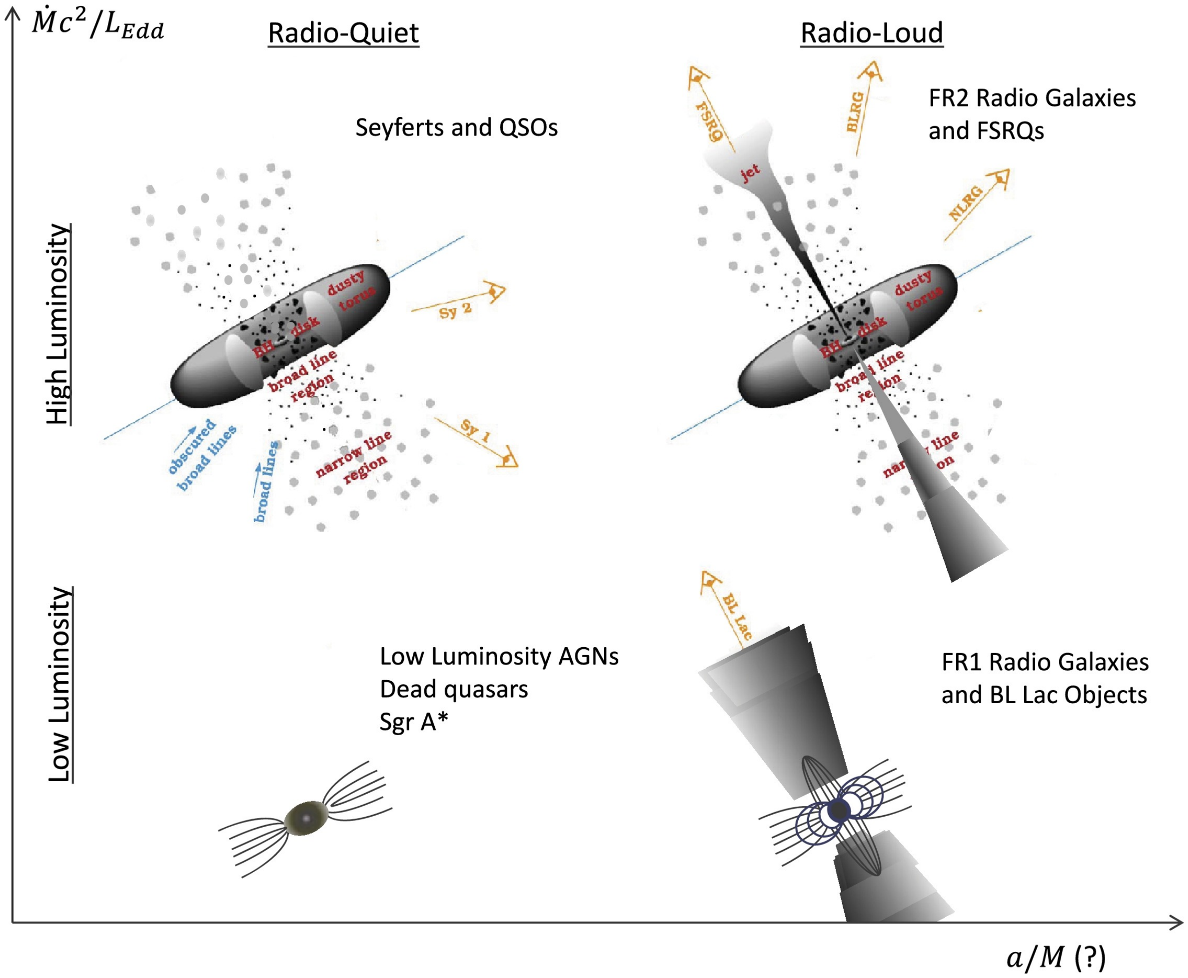

Figure 2.3: Depiction of the AGN unification scheme. The physical appearance of a galactic nucleus is sketched in the parameter space spanned by the BH spin (x-axis) and the accretion rate in units of the Eddington luminosity (y-axis). Be aware that the quantity drawn on the x-axis is equivalent to the dimensionless BH spin a used in the text. Non-jetted (radio-quiet) objects reside at low BH spins. If they have a low accretion rate, the galactic nucleus is inactive. If they have a moderate accretion rate, they are active and (depending on the viewing angle θ) observable as a Seyfert (1 or 2) galaxy. At very high accretion rate or very low viewing angle, they are called quasi-stellar objects. Galactic nuclei with high BH spin are forming relativistic jets. At high accretion rate, they appear as an FSRQ if seen face-on or as a Fanaroff-Riley II radio galaxy. The latter can appear as a narrow-line radio galaxy (a type 2 object) or as a broad-line radio galaxy (a type 1 object), depending again on θ. At low accretion rate, the AGN is appearing as a BL Lacertae (BL Lac) object if seen face-on or as a Fanaroff-Riley I radio galaxy. Notice however that it is still under debate whether the physical parameter assigned with the x-axis is really the BH angular momentum, or possibly some other quantity like the BH mass or even a combination of several parameters. Reproduced from Dermer and Giebels (2016) with kind permission by Prof. Dr. Charles Dermer; Copyright © 2021 Elsevier Masson SAS. All rights reserved.

the radio loudness can vary with the spatial resolution of the used telescopes. Fourth, the labelling as radio-loud and -quiet is misleading, because it wrongly connotes that the main difference between these objects is in the radio regime (Padovani, 2017).

Jetted AGN can be directly identified if the jet morphology can be resolved, e.g. with aid of VLBI. Apparent superluminal motion of emitting regions, a geometric effect of objects moving relativistically with small angle θ to the line of sight, is also an indicator of a relativistic jet. While non-jetted objects emit mainly thermally in IR to X-rays from the torus, the AF, the corona, the BLR and the NLR, jetted AGN emit mainly non-thermally over the entire electromagnetic spectrum. Therefore, distinct SEDs are undeniable indicators of relativistic jets, too, as will be explained in the subsequent section. For example, almost all non-jetted AGN lack in gamma-ray emission, while jetted ones and especially the blazars are usually gamma-ray emitters.

2.4 Blazars

2.4.1 Overview

Because of the strong Doppler boosting and relativistic beaming, blazars are from an observational point of view the most extreme AGN. Main characteristics are superluminal motion, a high degree of polarisation, a non-thermal, two-humped continuum SED that spans over up to 20 orders of magnitude along frequency, and variability on timescales that decrease down to minutes with increasing frequency of the emitted radiation.

The classical defining difference between the two sub-classes of blazars, FSRQs and BL Lac objects, is based on the strength of optical emission lines. A blazar is of type FSRQ, if the typical equivalent widths are $> 0.5\,\mathrm{nm}$, and of type BL Lac object otherwise (Urry and Padovani, 1995). Notice however that (despite what is suggested by this definition) optical and UV emission lines are actually present in BL Lac objects (Moles, Masegosa and del Olmo, 1987; Stocke, Danforth and Perlman, 2011; Becerra González et al., 2021). There is no consensus about whether the lines in BL Lac objects are intrinsically weak (e.g. due to weak illumination by the AF or due to the environment being starved in ambient gas clouds) or whether they are outshined by the jet emission.

Beside this defining difference via the equivalent width, there are other marked spectral differences as well as commonalities between FSRQs and BL Lac objects. Typical blazar broadband SEDs are shown in figure 2.4. In a $\nu\, L_\nu$ plot, they usually show two wide humps. The first hump (often called LE hump or synchrotron hump) peaks in the far-IR to optical range for FSRQs and in the mid-IR to soft-X-ray regime for BL Lac objects (Abdo et al., 2010). The second hump (often called HE hump or IC hump) peaks in the HE gamma-ray regime ($100\,\mathrm{MeV} - 100\,\mathrm{GeV}$) for FSRQs and in the very high energy (VHE) regime ($100\,\mathrm{GeV} - 100\,\mathrm{TeV}$) for BL Lac objects. Statistical correlations known as the observational blazar sequence find that with increasing bolometric luminosity, first there is a transition from BL Lac objects to FSRQs, second blazar SEDs become redder (meaning that the peak frequencies of the two humps decrease) and third the Compton dominances (which are the ratios of the HE hump luminosity to the LE hump luminosity) increase (Fossati et al., 1998). These observational findings have recently been confirmed (Mao et al., 2016; Ghisellini et al., 2017), explained as a mere selection effect (e.g. Giommi et al., 2012) as well as disproved and refined (Meyer et al., 2011; Keenan et al., 2021).

While all blazars are thought to host SMBHs with M_{BH} of the order of $10^8 - 10^{10}\, M_\odot$ (Ghisellini, Maraschi and Tavecchio, 2009) and with a high spin, prominent physical differences can be condensed as follows: FSRQs are, in comparison to BL Lac objects, high-luminosity objects with jets that are more powerful but have lower bulk Lorentz factors (Böttcher et al., 2013). They are surrounded by a dense and gas-rich environment, by a highly magnetised standard disk with high $\dot{m}$ and by a strong BLR. In contrast, the environment of BL Lac objects is depleted in gas supplies and they are consequently thought to have a lower accretion rate in a weakly magnetised, radiatively inefficient AF (Ghisellini, Maraschi and Tavecchio, 2009; Ghisellini et al., 2011; Ghisellini, 2012; Foschini, 2017; Liodakis, 2018). The reason for the weakness or absence of emission lines in BL Lac objects is either the intrinsic faintness of the BLR and/or the outshining of the lines by the boosted jet emission (Giommi et al., 2012).

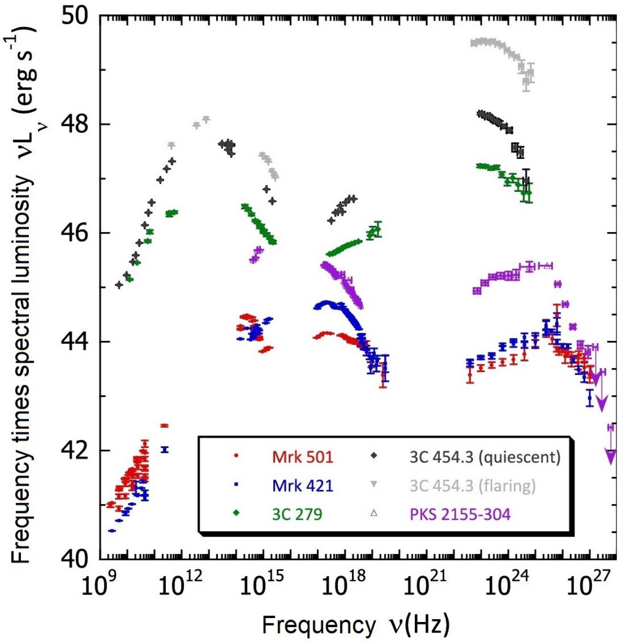

Figure 2.4: Exemplary quasi-simultaneous, multi-wavelength SEDs of well-known blazars. Shown is the product νL_ν of frequency times spectral luminosity versus frequency. The objects Mrk 501, Mrk 421 and PKS 2155-304 are BL Lac objects, while 3C 279 and 3C 454.3 are FSRQs. The typical two-hump structure and the trends described by the observational blazar sequence can clearly be recognised. Reproduced from Dermer and Giebels (2016) with kind permission by Prof. Dr. Charles Dermer; Copyright © 2021 Elsevier Masson SAS All rights reserved.

There is an additional AGN sub-class that is associated with jetted AGN and especially related to blazars, the sub-class of gamma-ray-emitting, narrow-line Seyfert 1 galaxies. These objects are characterised by small BH mass ($M_{\mathrm{BH}} < 10^8\,M_\odot$), close-to-Eddington accretion, strong but comparatively narrow optical emission lines, low jet power, gamma-ray emission with intra-day variability, superluminal knot motion and enhanced star forming activity and are thus seen as juvenile blazars (Foschini, 2017; Rieger, 2017; Gokus et al., 2021). The evolution of AGN with jets pointing towards us therefore corresponds to the transition from gamma-ray-emitting, narrow-line Seyfert 1 galaxies (low-mass and highly accreting objects, thought to be young objects), over FSRQs (high-mass and highly accreting objects, adult objects), to BL Lac objects (high-mass and low-accreting objects, aged objects) (Böttcher and Dermer, 2002; Foschini, 2017).

2.4.2 Modelling of Blazar Broadband Spectral Energy Distributions

The two SED humps of the blazar emission are due to the beamed and boosted emission from the blazar zone, an approximately spherical, homogeneous region (called a blob) that is filled with an isotropically distributed population of relativistic particles and permeated with a randomly oriented magnetic field. It is widely accepted that the nature of the LE hump is synchrotron radiation of electrons (and possibly positrons) spiralling in the magnetic field. This is why the LE hump is also called synchrotron hump. The nature of the second hump is not entirely clear. Two non-mutually exclusive families of explanations are debated, leptonic models and hadronic models.

According to leptonic models, the origin of the HE hump radiation is IC scattering of LE target photons by the relativistic electrons in the blob. Therefore, the HE hump can also be called IC hump. If the target photons are the synchrotron photons that are emitted by the electron population in the blob, the model is called an SSC model (Maraschi, Ghisellini and Celotti, 1992), while the model is called an EC model if the target photons are of external origin (Dermer, Schlickeiser and Mastichiadis, 1992), e.g. from the AF, the torus, the BLR or from the cosmic microwave background. Within most leptonic models, the blob radius R, the magnetic flux density B, the blob's bulk Lorentz factor Γ and the electron energy distribution (EED) have to be specified. Additionally to synchrotron radiation and IC scattering, synchrotron self absorption is usually implemented. Internal or external absorption of gamma rays due to PP and further reprocessing of the created pairs in electromagnetic cascades is often neglected. Furthermore, in most cases the EED $N(\gamma)$ is prescribed ad hoc, instead of determining it via balancing energy gains and energy losses. For example, in the SSC model by Tavecchio, Maraschi and Ghisellini (1998) which was also used by

MAGIC Collaboration et al. (2020) and Wendel et al. (2021b), $N(\gamma)$ is a broken PL, whose break and cutoff energies as well as spectral indices are parameters free within physically reasonable borders but not attained self-consistently by taking radiation reaction into account. Nevertheless, SSC models, EC models or hybrid models can copiously explain a multitude of blazar SEDs. SSC models are especially successful in describing the SEDs of BL Lac objects. In these AGN the EC contribution is sub-dominant because the external target photon fields are weak due to the less-marked and gas-depleted environment. In contrast, in FSRQs EC models typically give the main contribution to reproduce SEDs, because in these objects the BH surroundings are prominent and well-marked. Within leptonic models the observational blazar sequence (see section 2.4.1) can be explained by the physical blazar sequence (Ghisellini et al., 1998): A transition from BL Lac objects to FSRQs corresponds to an increasing density and strength of the circumnuclear environment and to an increasing $\dot{m}$. This increasing prominence of the AF, of the BLR and of the torus causes an increasing energy density of external photon fields. These act as target fields in the EC process, causing an increasing Compton dominance and stronger radiative cooling of the electrons. The latter causes a decreasing maximum electron energy and hence decreasing peak frequencies of the two SED humps.

In hadronic models, protons (or even heavier ions) are accelerated to energies high enough for the protons to significantly contribute to the radiative output and to serve as an explanation for the HE hump (Mannheim and Biermann, 1992; Mücke and Protheroe, 2001; Cerruti et al., 2021). First, protons directly emit synchrotron radiation, and second protons can undergo pion production. The latter can happen through interaction with soft target photons (photo-pion production) as well as through proton self interactions. By this, neutrons, neutral pions and charged pions are created and the pions subsequently decay into gamma-ray photons, muons, electrons, neutrinos (and their anti-particles). The muons and electrons can in turn emit synchrotron radiation or IC up-scatter target photons. The pion decay products can also initiate pair cascades as a result of pair absorption (absorption due to PP). All these gamma-ray production channels contribute to the HE hump. Furthermore, the decay of the charged pions and of the muons inevitably produces a neutrino flux. Therefore, the detection of neutrinos from blazars, like the tentative association of PeV neutrino events with Tracking Active Galactic Nuclei with Austral Milliarcsecond Interferometry (TANAMI) blazars (Krauß et al., 2014) or the $3\,\sigma$ association of a 290 TeV muon neutrino with a multi-wavelength flare of the blazar TXS 0506+056 (IceCube Collaboration et al., 2018), is a smoking gun (unambiguous evidence) for hadronic models (Mannheim, 1993).

In most leptonic and hadronic models, the blob itself is moving relativistically with velocity $\beta\,c$ and Lorentz factor $\Gamma = (1-\beta^2)^{-1/2}$ along the jet, which is tilted by θ towards the line of sight. This causes several effects (see e.g. Urry and Padovani, 1995; Boettcher, Harris and Krawczynski, 2012; Ghisellini, 2013):

- All timescales are reduced by $1/D$ when transforming them from the comoving frame to the AGN frame.
- Furthermore, Doppler boosting takes place, meaning that photon frequencies are blueshifted by the relativistic Doppler factor $D = (\Gamma\,(1-\beta\,\cos\theta))^{-1}$ which has its maximum value $D = 2\,\Gamma$ at $\theta = 0$, and that the bolometric intensity (as well as the flux density and the luminosity if the emission emanates from one spherical blob) is enhanced by D^4.
- As mentioned earlier, the emitted radiation is beamed due to relativistic aberration into a cone of approximate half opening angle $1/\Gamma$, giving rise to the anisotropic appearance of the jet emission.
- Another effect is that blobs appear to be moving superluminally along the jet with apparent velocity $D\,\Gamma\,\beta\,\sin\theta$.

Regardless of whether one is dealing with leptonic or hadronic models, the respective scenario is called a one-zone, two-zone or multi-zone model, if one blob, two blobs or several blobs are present and responsible for radiation production. Hybrid models involving features of both leptonic and hadronic models are called lepto-hadronic models.

2.4.3 Two Exemplary Blazars

In the course of this work, the two blazars 3C 279 and Mrk 501 will be the study subjects. Therefore, their basic properties will be briefly examined now.

2.4.3.1 The Flat-Spectrum Radio Quasar 3C 279

The blazar 3C 279 is considered to be an archetypal FSRQ. It is situated at redshift $z = 0.54$ (Marziani et al., 1996) with a corresponding luminosity distance $D = 3.1\,\mathrm{Gpc}$ and can thus be considered as a rather nearby FSRQ. For almost 50 years, it is especially known to exhibit superluminal motion of radio blobs. In the year 1991, gamma-ray emission was first detected from this object by the Energetic Gamma Ray Experiment Telescope (EGRET) (Hartman et al., 1992). Today, 3C 279 is known as one of the brightest and (due to evidence for minute-scale variability in HE gamma rays) as one of the most variable gamma-ray sources in the sky (Ackermann et al., 2016; Shukla and Mannheim, 2020). An exemplary quasi-simultaneous SED is depicted by the green markers in figure 2.4. A recent record was the best-resolved image of 3C 279: In the year 2017, the sub-pc-scale jet was imaged at mm wavelengths with an angular resolution of $\approx 20\,\mu\mathrm{as}$ (Kim et al., 2020), showing a structured or bend inner jet. The originating region of gamma-ray radiation from 3C 279 is, however, still poorly known and cannot be determined by direct imaging. This point will be addressed in the course of this work. While the majority of studies finds that gamma rays originate from outside of the BLR (section 2.4.6), it will be found in chapter 6 that a certain gamma-ray flare might emanate from the BLR of 3C 279.

2.4.3.2 The BL Lacertae Object Markarian 501

With $D = 149.4\,\mathrm{Mpc}$ (equivalent to $z = 0.034$), the BL Lac object Mrk 501 is a blazar in the local universe. It was detected in the VHE regime in the year 1996 (Quinn et al., 1996) and is the apparently brightest source above 100 GeV. Even during periods of low VHE emission, Mrk 501 can be detected with state-of-the-art imaging atmospheric Cherenkov telescopes (IACTs) in short observation times, making it an ideal target of long-term monitoring campaigns. Contributing to the wealth of unbiased observational data is the fact that Mrk 501 is in the sample of TeV blazars regularly observed by the First Geiger-mode Avalanche Photodiodes Cherenkov Telescope (FACT), a monitoring remote telescope enabling variability studies and providing flaring alerts to the community (Dorner et al., 2015). A multi-wavelength SED is shown by the red markers in figure 2.4. As the frequency of the peak of the synchrotron hump is situated above $10^{15}\,\mathrm{Hz}$, it is sub-classified as a high-synchrotron-peaked BL Lac object. On top of the almost featureless UV spectrum, the Lyman α broad emission line was recently observed by Stocke, Danforth and Perlman (2011) with a luminosity of $L_{\mathrm{Ly}\,\alpha,\,\mathrm{obs}} = 5.2 \cdot 10^{33}\,\mathrm{W}$, showing that a BLR is present in Mrk 501, even if it is weak. Short-time variability (down to minute scales) is also common for Mrk 501 (Albert et al., 2007; Ahnen et al., 2018; MAGIC Collaboration et al., 2020) and suggests that pure one-zone SSC models are not sufficient as an explanation of the emission. In the course of this work (chapter 5) it will be seen that an additional emission component is sporadically emanating from the central regions of this AGN.

A peculiarity in the one-sided jet of Mrk 501 is a 90° bending, that is observed in radio maps about 30 mas away from the radio core. The origin of this kink can be the interaction of the jet with an obstacle like a star or a gas cloud from the surrounding host galaxy.

Despite its proximity, the SMBH mass is not very well constrained. Estimates range from several $10^7\,M_\odot$ (based on variability in non-thermal X-rays and VHE gamma-rays during a flaring period in 1997, de Jager, 1999) up to $3.4 \cdot 10^9\,M_\odot$ (based on the correlation between the SMBH mass and the velocity dispersion of stars in the host galaxy, Barth, Ho and Sargent, 2002). Although

Rieger and Mannheim (2003) have suggested that this mass estimate discrepancy can be resolved by postulation of a binary SMBH whose companions have largely differing masses, the usage of values around $10^9\,M_\odot$ has established in the literature in the recent years. Therefore, the mass $M_\mathrm{BH} = 10^9\,M_\odot$ is used in the course of this text.

2.4.4 Variability

Assume a stationary ($\Gamma = 1 \;\rightarrow\; D = 1$), isotropically emitting, causally connected emission region of size R in an AGN at redshift z, that is switching off its emission. In this case, the intrinsic minimum variability timescale is the light-crossing time of the source $2\,R/c$. The detected minimum variability timescale is the redshift-corrected and Doppler-corrected timescale $2\,R\,(1+z)/(c\,D)$. Consequently, if z is known, an observed variability timescale can be used to obtain an upper limit of R if D is known, or a lower limit of D if R is known.

Variability of blazar emission was known as long as blazars are known. However today, variability with timescales down to minutes is observed in the HE and VHE gamma-ray regime (Aharonian et al., 2007; Albert et al., 2007; MAGIC Collaboration et al., 2008; Foschini et al., 2013; Aleksić et al., 2014a; Pittori et al., 2018; Shukla et al., 2018; Liao, 2018; Rieger, 2019; Glawion and Wierzcholska, 2021), implying either values D of several 10, which are however often exceeding those values D measured by radio VLBI (e.g. Giroletti et al., 2004, for the case of Mrk 501), or very compact emission regions of sizes even smaller than r_S, denoted as sub-horizon scales. Sub-horizon variability timescales are not even achieved by the violent and seemingly extremely rapid gamma-ray bursts occurring during the final stages of massive stars, because in this case $r_\mathrm{S}/c \approx 0.3\,\mathrm{ms}$ is below the shortest variability timescales of few ms (MacLachlan et al., 2013). A high compactness of an emission region however causes the emission region to be optically thick for gamma rays due to pair absorption. The gamma-ray photons should not be able to escape, but they are detected. This contradiction can be resolved by again assuming relativistic bulk motion ($\Gamma > 1 \;\rightarrow\; D > 1$) of the blob, as described in section 2.4.2, as this relaxes the constraint on R for a given timescale. Correlation of variability between different observational bands can also be used to infer information about the spatial origin of the emission, as will be described in the subsequent section.

2.4.5 Gamma Rays from Blazars

In the late 1970s, the first detection of an AGN, namely of the FSRQ 3C 273, in gamma rays around 100 MeV was achieved by the spaceborne spark chamber detector Cosmic Ray Satellite B (Swanenburg et al., 1978). The first AGN detection at TeV energies followed in the early 1990s by the ground-based 10-m Whipple Telescope, an IACT, with the BL Lac object Mrk 421 (Punch et al., 1992). Today, more than 3000 blazars have been detected by the Fermi Large Area Telescope (LAT) (Abdollahi et al., 2020). The LAT is a pair-conversion gamma-ray detector with a field of view of size 2.5 sr on board the Fermi satellite (Atwood et al., 2009). Currently, it is the most sensitive HE gamma-ray telescope below ≈ 100 GeV. As of 2021, more than 70 blazars have been detected in the VHE regime, according to the TeVCat (Wakely and Horan, 2008).

In most cases, the detected gamma-ray emission and the spectra from blazars can be explained within the above presented SSC and EC models. In limited energy ranges, like e.g. in the range probed by the LAT, the SEDs can usually be described by simple fitting functions like a PL (possibly with an exponential cutoff), a broken PL or a log parabola (LP). There are, however, cases where hints to additional emission components have been found, which manifest in sub-structure on top of the two-hump SEDs or as deviations from a PL or LP (Abdo et al., 2011; Ahnen et al., 2017b; Ahnen et al., 2018; MAGIC Collaboration et al., 2020; MAGIC Collaboration et al., 2021; Acciari et al., 2021; Wendel, Shukla and Mannheim, 2021). Such features are often connected with flaring periods exhibiting short-time variability and therefore point to transient events in compact emission regions. Such findings call for emission models beyond conventional SSC or EC scenarios. The development of a more refined scenario involving IC scattering, PP and escape with incorporation of the radiation feedback on the EED is done in the present work. An IC pair cascade on BLR photons will be applied in chapters 5 and 6 to the blazars Mrk 501 and 3C 279, respectively, to offer an explanation for the peculiar gamma-ray spectral components presented by the MAGIC Collaboration et al. (2020) and Wendel, Shukla and Mannheim (2021).

The location of gamma-ray emission within a blazar is unclear, too. Suggestions range from the smallest distances (in other words from inside of the BH magnetosphere) over sub-pc distances (the typical extent of the BLR) and pc-scale distances (equivalent to the extent of the torus IR radiation field) up to distances of more than 10 pc (where the AGN radiation fields from outside of the jet are diluted) (Dermer and Giebels, 2016). Of course, the gamma-ray emission from one blazar can also emanate from multiple, simultaneously existing emission regions at varying distance to the AGN centre (Stern and Poutanen, 2011; Stern and Poutanen, 2014; Aleksić et al., 2014b; Lei and Wang, 2015; Finke, 2016; Rani et al., 2018; Patiño-Álvarez et al., 2019; Shukla and Mannheim, 2020; Acharyya, Chadwick and Brown, 2021). Moreover, the emission regions and processes need not to be the same for different objects.

In contrast to detectors at optical or mm wavelengths, whose angular resolution is intrinsically better and can additionally be enhanced with interferometric imaging techniques, the resolution of current HE and VHE instruments is far from being able to image the morphology of distant AGN and blazars in gamma rays. Therefore, to determine the spatial origin of the gamma rays from blazars, it is necessary to pursue indirect diagnostics, as outlined subsequently.

2.4.6 The Location of the Gamma-Ray Emitting Region

One possibility to obtain information about the location of the gamma-ray emission region is to consider the HE or VHE spectra of blazars. Consider gamma-ray photons of energy x_γ that are emitted from the inside of a field of soft photons of energy x. Pair absorption of the gamma rays on the soft photons leads to a decrease in the SED above the PP threshold energy, i.e. at $x_\gamma \geq x^{-1}$, or as a rule of thumb at $\epsilon_\gamma/\mathrm{TeV} \geq \mathrm{eV}/\epsilon$. Assuming an intrinsically smooth or PL-like gamma-ray spectrum, the detection of a spectral break or of attenuation at energy x_γ in an SED therefore points to the interaction of gamma rays with soft photons of energy $x \geq x_\gamma^{-1}$. The energy of the soft photons gives evidence about their origin. Attenuation at several TeV points to pair absorption on IR photons whose origin is the equatorial torus, whereas gamma-ray attenuation in the GeV regime signals interaction with the optical to soft-X-ray photons from the BLR (Donea and Protheroe, 2003).

Liu and Bai (2006) modelled a BLR photon field as a spherical shell of photons. They included a blackbody continuum (which constitutes the reprocessed disk emission) as well as emission lines known from observational spectra. By computing the pair-absorption optical depth of gamma rays in this BLR photon field in the case of 3C 279 and other FSRQs they found that if gamma rays are detected at energies 10 GeV to several 100 GeV, the gamma-ray emission must originate from a distance of some 10^{15} m away from the SMBH, i.e. from outside of the BLR. Otherwise, gamma rays would be completely absorbed in the BLR photon field.

A similar model was considered by Tavecchio and Mazin (2009) and Tavecchio and Ghisellini (2012), who constructed their soft photon spectrum with help of the Cloudy photo-ionisation code and for a varying geometry. They determined the PP opacity in dependence of the location of the gamma-ray injection and found that steps in the opacity are clearly visible for the H and He II Lyman α line, but their strengths, shapes and precise locations depend on the geometry and on the disk luminosity. Reimer (2007) applied a model with only two absorbing emission lines but pronounced the dependence on the redshift of the AGN. Depending on z, the attenuation steps or breaks in the SED are redshifted by differing amounts. Britto, Razzaque and Lott (2015) used the six brightest UV emission lines to model the BLR of FSRQs. They fitted LAT-detected FSRQ spectra by three functions (broken PL, PL with exponential cutoff, LP, each multiplied with an absorption term due to the extragalactic background light) once with and once without an absorption term due to the BLR photon field. In these four works the PP optical depth of gamma rays, that are injected inside of the BLR in an FSRQ comparable to 3C 279, is $\tau \approx 10$ for ϵ_γ above few 10 GeV, most widely confirming the conclusions of Liu and Bai (2006). Böttcher and Els (2016) obtained less stringent results. These authors obtained an optically thick BLR only for $\epsilon_\gamma > 50$ GeV and only for injection inside of the inner border of the BLR shell.

In their inquiry of the strongest LAT-detected flares of 3C 279, Meyer, Scargle and Blandford (2019) did not find significant hints of pair absorption. Likewise, the H. E. S. S. Collaboration et al. (2019) did not find evidence for pair absorption in the BLR of 3C 279 during a HE and VHE flaring period in 2015 and estimated the distance of the emission region to be $> 10^{15}$ m. From variability timescales, Meyer, Scargle and Blandford (2019) obtained an upper limit of the blob size, and together with knowledge about the jet geometry from radio observations an approximation of the emission distance was yielded. These authors could constrain the distance of the gamma-ray emitting region to $> 10^{14}$ m, but estimates based on the comparison of the distance-dependent IC cooling timescales with measured decay timescales of flares found pc-scales to be plausible. Measured time lags between radio core and gamma-ray emission can be converted into spatial displacements between the radio and the gamma-ray emission region. With these displacements and with the position of the radio core, the location of the gamma-ray emission region can be yielded. For 3C 279, Meyer, Scargle and Blandford (2019) obtained inconclusive results. Distances of several pc were obtained for three other FSRQs, but within the errors the findings are compatible with sub-pc distances.

Flares with an even shorter minute-scale sub-flare on top have recently been reported in the Fermi LAT data of 2018 of 3C 279 (Shukla and Mannheim, 2020). Emission from within the BLR is, however, excluded, via the argument of missing pair-absorption imprints. As origin for these flares, the jet-in-a-jet scenario from Giannios, Uzdensky and Begelman (2010) is invoked. At sub-pc distance, the Poynting-dominated, ordered jet becomes subject to the kink instability and the magnetic field gets twisted, leading to magnetic reconnection events, which create plasmoids (magnetised, compact emitting regions that are moving relativistically in the jet comoving frame) that are responsible for the longer flares, as well as a monster plasmoid that is responsible for the brief, strong flare (Giannios, 2013; Petropoulou, Giannios and Sironi, 2016). In a larger context it was found that the ensemble of plasmoids from magnetic reconnection can indeed account for the Fermi lightcurve properties of FSRQs and in particular for their variability behaviour (Shukla et al., 2018; Meyer, Petropoulou and Christie, 2021; Wagner et al., 2021).

The emission region can also be estimated by modelling multi-wavelength SEDs of blazars. Tan et al. (2020) compiled quasi-simultaneous SEDs of Fermi-detected FSRQs and fitted a one-zone SSC plus EC model to these SEDs. The modelled SEDs are sensitive to the emission region distance via the distance dependency of the external photon field in the EC model. By this, they inferred emission region distances between $3.1 \cdot 10^{15}$ m and $3.1 \cdot 10^{17}$ m for their sample, and a distance of $5.0 \cdot 10^{16}$ m for 3C 279. Emission from dusty torus scales was also found by Shah et al. (2019), who fitted an EC model to an X-ray and HE gamma-ray 2018 flare of 3C 279, and by Harvey, Georganopoulos and Meyer (2020), who analysed FSRQ SED shapes statistically and found compatibility with electron cooling in dusty tori, but no compatibility with the BLR EC scenario.

There is, however, also evidence for gamma-ray emission from BLR or even smaller scales. With leptonic model fits to quasi-simultaneous SEDs of four epochs of 3C 279 and with the assumption of equipartition between the magnetic field energy density and the non-thermal leptonic energy density, Dermer et al. (2014) obtained emission distances of $> 3.3 \cdot 10^{15}$ m, equivalent to the outer edge of the BLR.

Poutanen and Stern (2010) compiled a BLR spectrum containing the most important emission lines obtained by the photo-ionisation code XSTAR. They fitted a PL multiplied with an exponential term due to pair absorption on this BLR photon field to Fermi LAT data of nine FSRQs. GeV breaks in these spectra could be attributed to pair absorption on H I Lyman continuum and He II Lyman continuum photons. For three objects, however not including 3C 279, a fit with a PL multiplied with a double-absorber term was preferred with respect to a broken PL fit, thus pointing to gamma-ray attenuation inside the BLR. Emission from within the BLR of 3C 279 was found during a state of high activity in 2011, whose HE emission was explained by an EC model with BLR external photons (Aleksić et al., 2014b), as well as during a Fermi-detected flare in 2013 (Hayashida et al., 2015) and during a flare in 2015 detected by the Astro-Rivelatore Gamma a Immagini Leggero (AGILE) (Pittori et al., 2018). The corresponding multi-wavelength SEDs could be modelled with an SSC + EC one-zone approach under the assumption of emission from the inside of the BLR.

Acharyya, Chadwick and Brown (2021) compiled lightcurves of nine Fermi-detected FSRQs and obtained variability timescales of flaring periods, which were converted to emission-region sizes (see section 2.4.4), which in turn were converted to a distance under the assumption of a given, constant jet opening angle whose cross section is comparable to the emission region size (see also Ackermann et al., 2016). Most emission distances were found to be inside of the BLR. Furthermore, LP cutoffs in the flare spectra were interpreted as evidence for pair absorption inside the BLR. For 3C 279, in a December 2013 flare pair absorption was not found. Pair absorption was found in a June 2015 flare and this was substantiated by the scarcity of detected VHE photons. Moreover, the spectra were separated into a sub-GeV part ($0.1-1\,\mathrm{GeV}$) and a super-GeV part ($1-300\,\mathrm{GeV}$), for both of which a lightcurve was compiled. For each source, it was checked whether a delay is present in one lightcurve with respect to the other one. A delay would be expected for cooling of electrons in the torus photon field, as IC scattering happens in the Thomson regime here. In this case, higher energetic electrons have smaller cooling times than lower energetic electrons, thus the sub-GeV component would be delayed in comparison to the super-GeV component. For cooling in the BLR, scattering happens in the Klein-Nishina (KN) regime and this would lead to weakly energy-dependent cooling timescales. For the June 2015 flare no achromatic cooling was found, therefore pointing to inside-BLR emission in 3C 279.

The approach to search for pair absorption in the BLR by fitting incident spectra multiplied with an exponential absorption term to the observed spectra underlies two main assumptions. First, the intrinsic spectra are usually described by a PL, a broken PL or an LP. These functions usually have no immediate justification because in most works the original acceleration and gamma-ray production processes remain unconsidered. However, PL-like EEDs and photon spectra are motivated from various astrophysical acceleration processes and radiation mechanisms. Therefore, this assumption can be regarded as plausible.

Second, it is assumed that the reprocessing of the pair-absorbed gamma rays is negligible. This is expressed by the multiplication of the incident spectrum with an $\exp(-\tau)$ term. This is the correct solution of the radiation transport equation for a vanishing source function, hence in the case of no internal emission, but only absorption. However, Marcowith, Henri and Pelletier (1995) and Vuillaume, Henri and Petrucci (2018) have pointed out that the internally produced gamma rays are neglected in such approaches. In order to correctly compute the emerging flux from the blazar zone, it is necessary to include the term $\sim (1-\exp(-\tau))/\tau$ instead of the pure exponential absorption. This is the result of radiation transport if the source function dominates over the incident intensity. Additionally to this, exponential absorption outside of the blazar zone can be present, if there are external photon fields (Marcowith, Henri and Pelletier, 1995; Vuillaume, Henri and Petrucci, 2018). To follow the advice by these authors to also implement internal radiation production, a complete IC pair cascade is treated in the present work. Gamma-ray photons are not only pair absorbed, but the produced pairs IC up-scatter soft ambient photons, generating an additional gamma-ray component, that can escape or in turn be pair absorbed. By this, an IC pair cascade evolves, whose emission can account for fine-structure gamma-ray components on top of the two-humped blazar SED. In chapter 3, the physical framework for IC pair cascades with escape terms is constructed and the resulting equations are solved numerically in chapter 4. In chapter 6 it will be shown how Wendel, Shukla and Mannheim (2021) took this approach to explain a Fermi-LAT observation of 3C 279 during a flaring period by radiation cascaded in the BLR photon field, setting constraints on the distance of the gamma-ray emission region. In chapter 5, it will be discussed how the MAGIC Collaboration et al. (2020) and Wendel et al. (2021b) attributed a very narrow peak observed in the SED of Mrk 501 as a signature of a cascade induced by an electron beam stemming from a magnetospheric particle accelerator near the SMBH.

2.5 Magnetospheric Particle Acceleration

As mentioned in the previous section, the jet-in-a-jet scenario proposing plasmoids triggered by reconnection events to be potential regions of HE and VHE emission with short-time variability has attained much attention in the last decade. Beside the jet-in-a-jet scenario and the possibility of gamma-ray production in collision events of stars and the relativistic jet (Barkov, Aharonian and Bosch-Ramon, 2010; Aharonian, Barkov and Khangulyan, 2017), emission from magnetospheric vacuum gaps was suggested to be responsible for minute-scale flaring events. Vacuum gaps are spatially confined regions that exhibit a strong magnetic-field-parallel electric field and were first considered to explain the pulsed gamma-ray emission from rotating, inclined, magnetised neutron stars called pulsars (Cheng, Ho and Ruderman, 1986; Hirotani, 2005).

AGN magnetospheres are the rotating, plasma-filled regions around the SMBH where the influence of the magnetic field on charged particles must not be neglected. The rotating magnetic field induces a poloidal electric field (Wald, 1974). Its radial as well as polar components would be non-vanishing, if the magnetosphere was devoid of charge carriers (Hirotani and Okamoto, 1998). Potential drops of the electric field can reach values of $10^{21}\,\mathrm{V}$ for typical SMBH magnetospheres (Levinson and Rieger, 2011).

However as mentioned earlier, the inner regions of AGN are generally far from being completely evacuated. Particles intrude either directly from the AF or are pair created in collisions of gamma rays from the AF. In the case of an ADAF, it is straightforward to estimate the number density of photons, that can interact via PP. As described in section 2.1.2.2, the upper cutoff of the ADAF spectrum is located at the energy $\epsilon_{\mathrm{ADAF},0}$. Consequently, the lowest energy of photons, that can just barely interact via PP on other ADAF photons, is given by the PP threshold $\epsilon_{\mathrm{ADAF,th}} = m_\mathrm{e}^2 c^4/\epsilon_{\mathrm{ADAF},0}$. The total number density of ADAF photons, that are capable of undergoing PP via self interactions, is then given in analogy to equation 2.14 by

$$n_{\mathrm{PP},1}(M_\mathrm{BH}, \dot{m}, T_\mathrm{e}) \approx \int_{\epsilon_{\mathrm{ADAF,th}}}^{\epsilon_{\mathrm{ADAF},0}} n_\mathrm{ADAF}(\epsilon, M_\mathrm{BH}, \dot{m}, T_\mathrm{e})\,\mathrm{d}\epsilon. \tag{2.18}$$

Based on analytic approximations for several ADAF quantities from Narayan and Yi (1995) and assuming equipartition between gas and magnetic pressure, Levinson and Rieger (2011) estimate the total number density of ADAF photons that are reaching the magnetosphere and have MeV energies and are thus able to pair produce electrons and positrons to

$$n_{\mathrm{PP},2}(M_\mathrm{BH}, \dot{m}) \approx 1.4 \cdot 10^{17}\, \dot{m}^2\, \frac{10^9 M_\odot}{M_\mathrm{BH}}\,\mathrm{m}^{-3}. \tag{2.19}$$

Both expressions will be used in chapter 5 to estimate the number density n_PP of photons in the magnetosphere that are capable of undergoing PP via self interaction. So, in realistic scenarios, mobile charge carriers are filling the magnetosphere. These electrons and positrons can readily move along magnetic field lines, but they can hardly stream perpendicular to them due to the Lorentz force. The particles will arrange in such a way that the magnetic-field-parallel component of the electric field drops to zero and only the component perpendicular to the magnetic field remains non-zero. The resulting distribution of the charge density is called the Goldreich-Julian (GJ) charge density, named after Goldreich and Julian (1969) who developed this concept in the case of pulsar magnetospheres. The ensuing electric field configuration and the state of the magnetosphere are called force-free, as the net electromagnetic force on electric charges vanishes in this case. Gas pressure and inertial terms can be neglected in force-free states. If there are abundant pair-producing photons and thus a sufficient supply of charge carriers, the magnetosphere is force-free and the component of the electric field parallel to the magnetic field is screened.

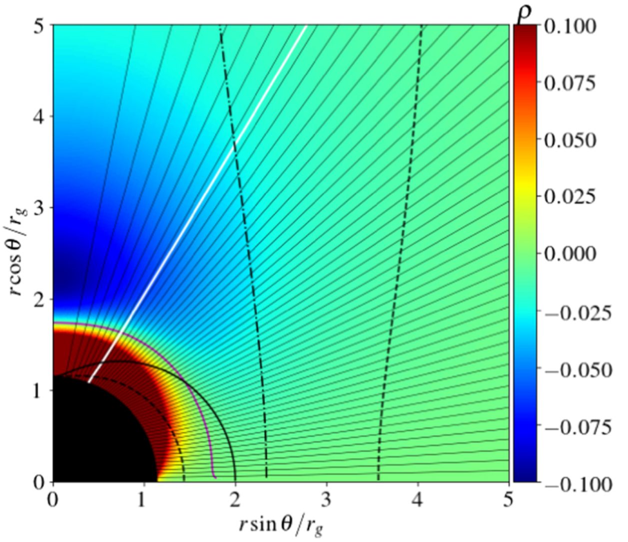

Figure 2.5: Depiction of the inner portion of a split-monopole, force-free magnetosphere around a BH rotating with $a = 0.99$. A split-monopole field is an approximation of the field that is sustained by toroidal currents flowing in an equatorial disk. The x-axis, y-axis is the coordinate perpendicular, parallel to the rotation axis, respectively. The black disk, black solid line is the BH event horizon, the static limit, respectively. The thin black lines (and the white line) show surfaces of constant enclosed magnetic flux. The inner and outer light surfaces are drawn by the black dashed lines. The stagnation surface is marked by the black dash-dotted line. The colour scale shows the charge density (normalised to its maximum value, and as measured in a locally non-rotating frame) which is equal to the GJ charge density. The lilac line is the null surface. Reproduced from Chen and Yuan (2020) with kind permission by Dr. Alexander Chen; © American Astronomical Society. Reproduced with permission.

If there is a deficit or excess of charge carriers, an imbalance between the GJ charge density and the actual one can result. Then, a non-vanishing magnetic-field-parallel electric field ensues. Such regions are called vacuum gaps (or electrostatic gaps, spark gaps or briefly gaps) because the deviation between the GJ charge density and the actual one is thought to be usually realised by a lack (evacuation) of electrons and positrons. In these magnetospheric vacuum gaps, intruding charged particles can be efficiently accelerated and the particles can tap the BH's rotational energy (Levinson, 2000).

The existence of vacuum gaps in BH magnetospheres was found both in analytical treatments as well as in one- and two-dimensional numerical simulations (Beskin, Istomin and Parev, 1992; Hirotani and Okamoto, 1998; Hirotani et al., 2017; Chen and Yuan, 2020; Kisaka, Levinson and Toma, 2020; Katsoulakos and Rieger, 2020). Gaps can open as soon as the replenishment of screening charges is insufficient to supply the GJ charge density. This is usually the case, if on the one hand the magnetic field is high enough to generate a high GJ charge density and on the other hand if the accretion rate is low enough such that the AF cannot provide enough pair-producing gamma rays. While it was assumed in earlier works, that vacuum gaps can exist steadily and that their properties are time-independent, Levinson and Segev (2017), Chen, Yuan and Yang (2018), Chen and Yuan (2020), Levinson and Cerutti (2018), Kisaka, Levinson and Toma (2020) and Hirotani et al. (2021) could show that gaps are inherently transient phenomena or possibly cyclically appearing during oscillations of the charge density. If strong electric fields are unscreened, charge carriers are accelerated and induce pair cascades, which supply additional charge carriers that discharge the potential drop and screen the gap. After the gap is screened, the cascade ceases and the magnetospheric current system can again evacuate the gap, resulting in a new cycle.

There is however no consensus about the location of vacuum gaps in BH magnetospheres. In analogy to pulsar's outer gaps, Beskin, Istomin and Parev (1992), Hirotani and Okamoto (1998), Ptitsyna and Neronov (2016), Hirotani et al. (2016), Levinson and Segev (2017), Ford, Keenan and Medvedev (2018), Chen and Yuan (2020) and Kisaka, Levinson and Toma (2020) argue that gaps appear near the null surface, which is the set of points where the GJ charge density is zero. The precise shape of the null surface is dependent on the magnetic field geometry and on a, but in all considered cases it is located between the BH horizon and the outer light surface (see figure 2.5). Near the null surface, a lack of free charge carriers can arise as particles can only be washed out from this region (but not flow into it), because the BH horizon and the outer light surface act as one-way membranes. The lack of charge carriers causes the inability to redistribute charges to facilitate the screening. Simulations by Hirotani et al. (2016), Hirotani et al. (2017), Song et al. (2017) and Ford, Keenan and Medvedev (2018) especially show that a gap forms near the magnetospheric poles

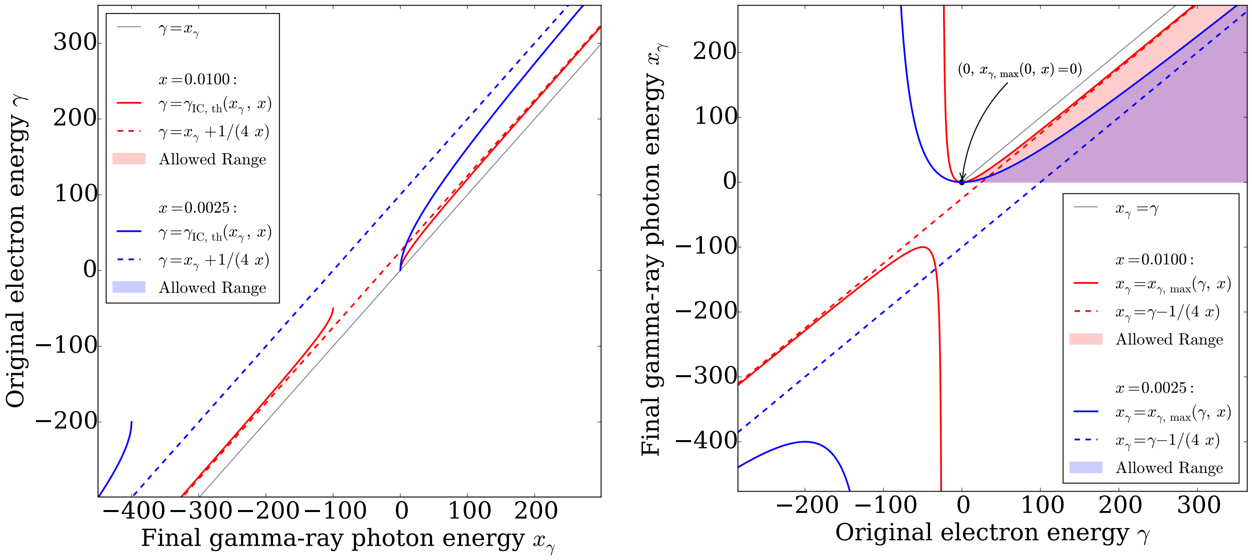

Figure 2.6: Plot of the functions $\gamma_{\mathrm{IC,\,th}}$ and $x_{\gamma,\,\mathrm{max}}$ involved in IC scattering kinematics. Left-hand side panel: Plot of the x_γ-γ plain. For two exemplary values of the soft target photon energy x, the function $\gamma_{\mathrm{IC,\,th}}(x_\gamma,\, x)$, its asymptote for very high (and very low) x_γ and the kinematically allowed range is depicted. Right-hand side panel: Equivalent plot, but in the γ-x_γ plain, i.e. flipped along the identical relation (grey line). The inverse functions are shown.

($\theta < 45°$) around the null surface. Another possibility for the gap location is the stagnation surface, which is a prolate-shaped divide of the magnetohydrodynamical fluid flow located at a distance of several r_{S} where the gravitational, centrifugal and Lorentz forces compensate each other (Vincent and Lebohec, 2010; Broderick and Tchekhovskoy, 2015; Hirotani and Pu, 2016; Aharonian, Barkov and Khangulyan, 2017). In contrast, simulations by Crinquand et al. (2020) find that a gap can also develop around the inner light surface.

Exhibiting a strong magnetic-field-parallel electric field, gaps are powerful particle accelerators and consequently possible sites of gamma-ray emission through the processes of IC scattering and curvature radiation emission. Estimates for the gap extent along the magnetic field lines range from few $0.001\,r_{\mathrm{S}}$ to several $0.1\,r_{\mathrm{S}}$. Due to these sub-horizon scales, intermittent activity of vacuum gaps was suggested to be a natural origin of both the observed short-time VHE gamma-ray variability of blazars (Levinson and Rieger, 2011; Wendel et al., 2017; Aharonian, Barkov and Khangulyan, 2017; Wendel et al., 2021b) and radio galaxies (Aleksić et al., 2014a; MAGIC Collaboration et al., 2018; Ahnen et al., 2017a) and of PeV cosmic rays (Ptitsyna and Neronov, 2016; Katsoulakos, Rieger and Reville, 2020).

In the course of the present work, electrons accelerated in a vacuum gap in the magnetosphere of Mrk 501 will be assumed to interact with emission line photons from an ionised gas cloud surrounding the central SMBH. Wendel et al. (2021b) have shown that the evolving IC pair cascade reprocesses the injected energy into TeV gamma rays with a very peculiar spectral imprint. It will further be shown how the MAGIC Collaboration et al. (2020) has associated this reprocessed emission with an observed, transient, narrow spectral feature in the SED of Mrk 501. This application of an electron-beam-induced IC pair cascade in Mrk 501 will be discussed in chapter 5. However, first, the physical description of IC pair cascades with escape terms is considered.

Chapter 3

Inverse-Compton Pair Cascades with Escape Terms

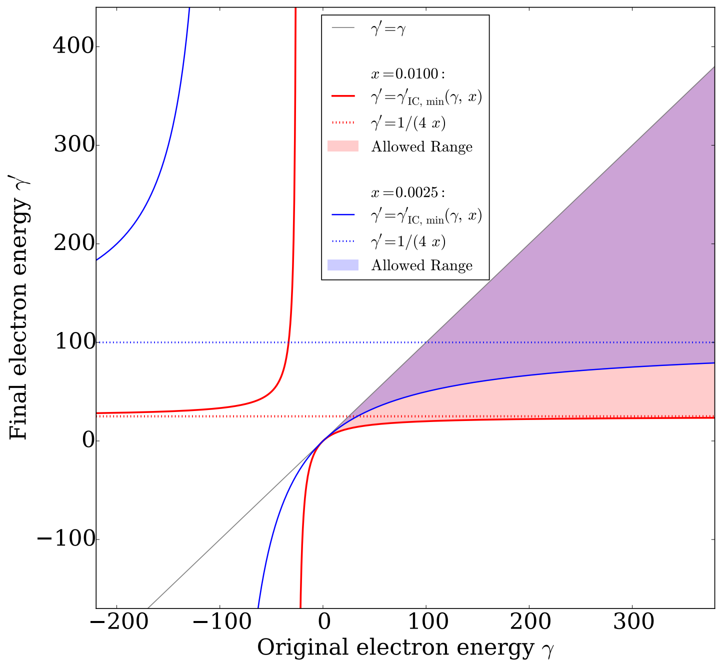

Figure 3.1: Plot of the function $\gamma'_{\mathrm{IC,\,min}}(\gamma,\, x)$ involved in IC scattering kinematics in the γ-γ' plain. For two exemplary values of the soft target photon energy x, the function $\gamma'_{\mathrm{IC,\,min}}$, its asymptote for very high (and very low) γ, the kinematically allowed range and the singularity is depicted. The dotted lines depict the approximate border between the Thomson and the KN regime. An equivalent plot showing the γ'-γ plain with the function $\gamma_{\mathrm{IC,\,max}}(\gamma',\, x)$ is not shown, but can be obtained by flipping the chart along the identical relation (grey line).

As stated in sections 2.4.6 and 2.5 of the preceding chapter, the objective of this work is to invoke IC pair cascades on emission line photons in AGN centres to explain transient SED features that cannot be explained straightforwardly in the context of conventional SSC or EC models. This will be done in chapter 5 for the case of Mrk 501 and in chapter 6 for 3C 279. To be able to compute the emitted gamma-ray spectrum, the cascade has to be solved numerically, which is done in a taylored algorithm described in chapter 4. To be able to perform this numerical treatment, the physics of IC pair cascades have to be grasped first, which is the aim of the present chapter.

A region filled with soft background photons will be considered. Relativistic electrons as well as HE photons are injected into this region. The electrons IC up-scatter the soft photons, producing additional HE photons. At the same time, the HE photons interact with the soft ones to pair produce new electrons (and positrons, which are not mentioned separately from now on, because they behave identically in the radiation processes considered). All the while, both electrons and HE photons escape from the interaction region. The emanating HE photons constitute the observable gamma rays. This entire cascade is described in section 3.2 through setting up two coupled kinetic equations that contain the physical processes of particle escape, IC scattering and PP. To achieve this, the physical processes will be discussed separately in sections 3.1.1 and 3.1.2.

In the present chapter, cascades are considered in a very general context to be able to apply the physical mechanism and the numerical solution scheme to a wide range of astrophysical scenarios. Therefore, the discussion in this chapter is detached from the AGN-specific context.

3.1 Basic Radiation Processes

Before the cascade as an interplay of IC scattering and PP is discussed, the single processes are considered separately. Thereby, instead of repeating the standard literature by Blumenthal and Gould (1970), Rybicki and Lightman (1986), Longair (2011), Ghisellini (2013) and Viganò et al. (2015), the aspects relevant for the present work are brought into focus. To keep consistency, the nomenclature of the quantities introduced by Zdziarski (1988) is used (except for cases where his naming seems misleading). In most cases, this also agrees with Wendel et al. (2017) and Wendel et al. (2021b). Especially, to be in line with these authors, upper cutoffs of any distribution are indexed with $_0$ henceforth, whereas lower cutoffs have the index $_\mathrm{l}$, which should not be confused with the index $_1$, which is the first element of a running/counting index. Notice also that the energies of the LE photons, HE photons and electrons are expressed in units of $m_\mathrm{e}c^2$.

3.1.1 Inverse-Compton Scattering

Now, an electron with original energy $\gamma \gg 1$ interacting with a soft photon of energy $x \ll 1$ is considered. The electron and the photon interact via IC scattering. By this, the electron gets down-scattered to the final energy γ', transferring its energy to the photon, whose final energy x_γ is now above $m_\mathrm{e}c^2$. Energy is conserved in this process, yielding

$$\gamma \approx \gamma + x = \gamma' + x_\gamma. \tag{3.1}$$

Based on the kinematics of IC scattering events (Jones, 1968; Blumenthal and Gould, 1970), Zdziarski (1988) obtained the relationship

$$\gamma\, x > E_\mathrm{IC} = \frac{\gamma/\gamma' - 1}{4}. \tag{3.2}$$

Several inequalities follow from this:

- First, for given x and x_γ, the original electron energy γ has to exceed a threshold energy defined by

  $$\gamma_{\mathrm{IC,\,th}}(x_\gamma, x) = \frac{x_\gamma}{2}\left(1 + \sqrt{1 + \frac{1}{x_\gamma x}}\right) \tag{3.3}$$

  and shown in the left-hand side panel of figure 2.6. Briefly written, it is

  $$\gamma > \gamma_{\mathrm{IC,\,th}}(x_\gamma, x). \tag{3.4}$$

  Furthermore, it is $\gamma_{\mathrm{IC,\,th}} > x_\gamma$ for all reasonable values of x_γ. The cause of this condition is that an incident electron cannot transfer all of its energy to the photon. The electron always keeps an amount of kinetic energy. In other words, γ must exceed x_γ by the final electron energy γ' (in accordance with equation 3.1). From equation 3.1 and inequality 3.4, it follows that γ' can never be smaller than $\gamma_{\mathrm{IC,\,th}}(x_\gamma, x) - x_\gamma$.

  It is easy to show that with increasing x and constant x_γ, the function $\gamma_{\mathrm{IC,\,th}}(x_\gamma, x)$ decreases. Therefore, if the LE photon population $n_0(x)$ is distributed along x and has an upper cutoff x_0, then $\gamma_{\mathrm{IC,\,th}}(x_\gamma, x_0)$ is smaller than any $\gamma_{\mathrm{IC,\,th}}(x_\gamma, x)$ with x in the range where n_0 is non-vanishing. Consequently, IC scattering events to the HE photon energy x_γ set in as soon as $\gamma > \gamma_{\mathrm{IC,\,th}}(x_\gamma, x_0)$.

  For later purpose, it is especially useful to realise that (for physically reasonable values and) for certain x, the function $\gamma_{\mathrm{IC,\,th}}(x_\gamma, x)$ increases monotonically with increasing x_γ towards the asymptote $x_\gamma + 1/(4x)$. This can be shown by Taylor developing $\gamma_{\mathrm{IC,\,th}}$ around small $1/x_\gamma$ and is illustrated in figure 2.6 by the dashed lines.

- Second, the fact that the original electron cannot give its total energy to the photon yields the condition

  $$x_\gamma < x_{\gamma,\,\mathrm{max}}(\gamma, x) \tag{3.5}$$

  with the definition

  $$x_{\gamma,\,\mathrm{max}}(\gamma, x) = \frac{4\gamma^2 x}{1 + 4\gamma x}, \tag{3.6}$$

  which is depicted in the right-hand side panel of figure 2.6. Inequality 3.5 follows from 3.2, too. For all sensible values of γ, it is $x_{\gamma,\,\mathrm{max}} < \gamma$, as is visible in the figure. Furthermore, notice that for given x, the function $x_\gamma = x_{\gamma,\,\mathrm{max}}(\gamma, x)$ is the inverse function of $\gamma = \gamma_{\mathrm{IC,\,th}}(x_\gamma, x)$. Moreover, it is not difficult to show that $x_{\gamma,\,\mathrm{max}}(\gamma, x)$ increases both when γ increases with constant x and when x increases with constant γ. Therefore, if the electron spectral number density $N(\gamma)$ is extended and non-zero along γ up to an upper cutoff γ_0 but is equal to zero everywhere above γ_0 and the soft photons' spectral number density $n_0(x)$ is non-zero only up to the upper cutoff x_0, then IC scattering events cannot reach energies above $x_{\gamma,\,\mathrm{max}}(\gamma_0, x_0)$.

- Due to the scattering kinematics 3.2, the value of γ' that is minimally allowed for given x and γ is bigger than 1, reflecting again that the electron always keeps a finite amount of kinetic energy. Quantitatively it is

  $$\gamma' > \gamma'_{\mathrm{IC,\,min}} \tag{3.7}$$

  with the lower limit

  $$\gamma'_{\mathrm{IC,\,min}}(\gamma, x) = \frac{\gamma}{1 + 4x\gamma} \tag{3.8}$$

  shown in figure 3.1. It is $\lim_{\gamma\to\pm\infty} \gamma'_{\mathrm{IC,\,min}}(\gamma, x) = 1/(4x)$ (dotted lines), meaning that scattering events that take place in the KN regime, always result in electrons that are still not in the Thomson regime yet. Obviously, $\gamma'_{\mathrm{IC,\,min}}(\gamma, x)$ decreases when x increases. Therefore, if the LE photon distribution is not mono-energetic, but $n_0(x)$ is distributed in energy with upper cutoff x_0, the minimally possible value of γ' after an IC scattering event with incident electron energy γ is $\gamma'_{\mathrm{IC,\,min}}(\gamma, x_0)$.

- For final electron energies $\gamma' \geq 1/(4x)$ (scattering events from the KN regime into the KN regime), the incident electron energy γ has no upper limit. But it ensues from inequality 3.2, that for $\gamma' < 1/(4x)$ (electron is scattered into the Thomson regime), a certain γ' cannot result from any incident electron energy γ. Instead, it has to be

  $$\gamma < \gamma_{\mathrm{IC,\,max}}(\gamma', x) \tag{3.9}$$

  where it was convenient to define

  $$\gamma_{\mathrm{IC,\,max}}(\gamma', x) = \begin{cases} \frac{\gamma'}{1-4x\gamma'} & \text{for } \gamma' < \frac{1}{4x}, \\ +\infty & \text{for } \gamma' \geq \frac{1}{4x}. \end{cases} \tag{3.10}$$

  It should be mentioned that for fixed x, the function $\gamma = \gamma_{\mathrm{IC,\,max}}(\gamma', x)$ (in the range $\gamma' < \frac{1}{4x}$) is the inverse of $\gamma' = \gamma'_{\mathrm{IC,\,min}}(\gamma, x)$. The course of $\gamma_{\mathrm{IC,\,max}}$ can be seen from flipping figure 3.1 along the line $\gamma = \gamma'$. Again, it is easy to show that with increasing x, the function $\gamma'/(1 - 4x\gamma')$ increases, too. Therefore, for an extended $n_0(x)$ which is zero everywhere above the upper cutoff x_0, the value $\gamma'/(1 - 4x_0\gamma')$ is bigger than any other $\gamma'/(1 - 4x\gamma')$ with x in the non-zero range of n_0. Consequently, IC scattering events with final electron energy γ' in the Thomson regime on the distribution n_0, condition an upper limit of γ at $\gamma'/(1 - 4x_0\gamma')$.

Based on findings by Jones (1968), the spectral interaction rate for IC scattering events on a soft photon field with spectral number density n_0 was approximated and rephrased by Zdziarski (1988):

$$C(\gamma, \gamma') = \int_{\max(x_1,\, \frac{E_{\mathrm{IC}}}{\gamma})}^{x_0} n_0(x)\, \frac{3\sigma_{\mathrm{T}} c}{4\gamma^2 x} \left[r_{\mathrm{IC}} + (2 - r_{\mathrm{IC}}) \frac{E_{\mathrm{IC}}}{\gamma x} - 2\left(\frac{E_{\mathrm{IC}}}{\gamma x}\right)^2 - 2\frac{E_{\mathrm{IC}}}{\gamma x} \ln \frac{\gamma x}{E_{\mathrm{IC}}} \right] \mathrm{d}x \tag{3.11}$$

Rearranging inequality 3.2 directly yields the second argument of the max function in the lower integration border. Here it is

$$r_{\mathrm{IC}}(\gamma,\gamma') = \frac{\gamma/\gamma' + \gamma'/\gamma}{2}. \tag{3.12}$$

If n_0, x_1 and x_0 are known, C is fully determined via equation 3.11.

In the computational implementation, the following caveat has to be considered. In the case $\gamma' = \gamma$, an evaluation of C according to equation 3.11 returns not a number. This is the case because for $\gamma' \to \gamma$, it is $E_{\mathrm{IC}} \to 0$ and the argument of the logarithm diverges. However, with $E_{\mathrm{IC}} \to 0$ and with an appropriate power series representation of the natural logarithm it is easy to show that

$$\frac{E_{\mathrm{IC}}}{\gamma x} \ln \frac{\gamma x}{E_{\mathrm{IC}}} \to 0 \quad \text{for} \quad \gamma' \to \gamma. \tag{3.13}$$

Additionally, it is $r_{\mathrm{IC}} \to 1$ for $\gamma' \to \gamma$. Consequently, the part in the squared brackets converges to 1 for $\gamma' \to \gamma$. This has to be stated explicitly in the computational implementation of the integrand of C.

Several quantities can be obtained with help of $C(\gamma,\gamma')$ and with the spectral electron number density $N(\gamma)$:

- $N(\gamma)C(\gamma,\gamma')$ denotes the number of IC scattering events per unit time, per unit space volume, per unit incident energy and per unit final energy, which scatter the electron with incident energy γ to the final energy γ'.
  - Based on this, for given final electron energy γ', the number of scattering events with any allowed original energy γ per unit time, per unit space volume and per unit final energy can be written as

    $$\int_{\gamma'}^{\gamma_{\mathrm{IC,\,max}}(\gamma',x_0)} N(\gamma)C(\gamma,\gamma')\,\mathrm{d}\gamma. \tag{3.14}$$

    Here, the limit 3.9 is used to constrain the permitted range of γ via the upper integration border, which contrasts to the integration border used in the third term of the right-hand side of equation 1 of Zdziarski (1988). Expression 3.14 denotes the number density of electrons, which are down-scattered (from higher energies) into the energy interval $[\gamma', \gamma' + \mathrm{d}\gamma']$ of the electron distribution per unit time and per unit γ'-interval.

    If N has an upper cutoff at γ_0, the upper integration border has to be refined to $\min(\gamma_0,\, \gamma_{\mathrm{IC,\,max}}(\gamma', x_0))$ in the computational implementation of expression 3.14. For later purpose, it is useful to realise that for $\gamma' > \gamma_0 > \min(\gamma_0,\, \gamma_{\mathrm{IC,\,max}}(\gamma', x_0))$, expression 3.14 is surely equal to zero. When expression 3.14 is used in the kinetic equation later on, γ and γ' have to be exchanged in this term, as the kinetic equation is formulated using γ as independent variable.
  - Second, for given original electron energy γ, the number of scattering events with any permitted final electron energy γ' per unit time, per unit space volume and per unit γ-interval can be expressed as

    $$N(\gamma) \cdot \int_{\gamma'_{\mathrm{IC,\,min}}(\gamma,x_0)}^{\gamma} C(\gamma,\gamma')\,\mathrm{d}\gamma'. \tag{3.15}$$

    Again, to allow for the kinematic constraints, the limit 3.7 is used for the lower integration border, which is in contrast to the border of the second term of the right-hand side in equation 1 of Zdziarski (1988) as well as to the border of the first integral in equation A21 of Zdziarski (1988). Expression 3.15 denotes the number density of electrons, which are removed from the energy interval $[\gamma, \gamma + \mathrm{d}\gamma]$ per unit time, and per unit γ-interval and are IC down-scattered to lower energies. Henceforth, the integral appearing in 3.15 is called spectral IC down-scattering rate.

- Substituting γ' from equation 3.1 into C, one arrives at $C(\gamma, \gamma - x_\gamma)$, which determines the probability per unit time and per unit x_γ-interval that an incident electron with energy γ produces an HE photon with energy x_γ.

  Drawing on this, $N(\gamma)C(\gamma, \gamma - x_\gamma)$ describes the number of scattering events per unit time, per unit space volume, per unit γ-interval and per unit x_γ-interval, which produce an HE photon with energy x_γ out of an original electron with energy γ.

  Now, for given HE photon energy x_γ, the number of scattering events with any kinematically permitted incident electron energy per unit time, per unit space volume and per unit x_γ-interval is quantified through

  $$\dot{n}_{\gamma,\,\mathrm{IC}}(x_\gamma) = \int_{\gamma_{\mathrm{IC,\,th}}(x_\gamma, x_0)}^{\infty} N(\gamma)C(\gamma, \gamma - x_\gamma)\,\mathrm{d}\gamma. \tag{3.16}$$

  The kinematic condition 3.4 is used here to obtain the correct lower integration border. $\dot{n}_{\gamma,\,\mathrm{IC}}$ describes the number density of photons with energy x_γ, which are IC up-scattered into the energy interval $[x_\gamma, x_\gamma + \mathrm{d}x_\gamma]$ of the HE photon distribution per unit time and per unit x_γ-interval and is therefore called spectral photon production rate.

  In the computational implementation of $\dot{n}_{\gamma,\,\mathrm{IC}}$, the upper integration border has to be restricted to γ_0, which is the Lorentz factor above which N is zero. Due to this upper cutoff, $\dot{n}_{\gamma,\,\mathrm{IC}}$ also has an upper cutoff. $\dot{n}_{\gamma,\,\mathrm{IC}}$ vanishes above $x_{\gamma,\,\max}(\gamma_0, x_0)$.

3.1.2 Pair Production

Here, the Breit-Wheeler process, i.e. the creation of an electron and a positron from the interaction of two photons is considered. The situation is restricted to the collision of an HE photon with energy $x_\gamma > 1$ with a soft photon with energy $x \ll 1$. The resulting electron and positron are energetically interchangeable and both particles are therefore comprisingly called electrons. The dimensionless energy of one particle is denoted by γ and the dimensionless energy of the other particle is γ'. From energy conservation it is

$$x_\gamma \approx x_\gamma + x = \gamma + \gamma'. \tag{3.17}$$

Consequently, γ' is determined, as soon as x_γ and γ are known. On the basis of the work by Agaronyan, Atoyan and Nagapetyan (1983), Zdziarski (1988) has rephrased the kinematic constraints of PP to

$$x_\gamma x > E_{\mathrm{PP}} = \frac{x_\gamma^2}{4\gamma(x_\gamma - \gamma)} > 1. \tag{3.18}$$

Similarly to the case of IC scattering, two important limitations follow from 3.18:

- For fixed x and x_γ, the maximum reachable electron energy γ is of course finite. There is, however, also a lower limit of γ, which is bigger than 1. Both limitations can be obtained from the kinematical relationship 3.18. Quantitatively expressed, the electron energy obeys

  $$\gamma_{\mathrm{PP,\,min}}(x_\gamma, x) < \gamma < \gamma_{\mathrm{PP,\,max}}(x_\gamma, x) \tag{3.19}$$

  where the limits are defined by

  $$\gamma_{\mathrm{PP,\,min}}(x_\gamma, x) = \frac{x_\gamma}{2}\left(1 - \sqrt{1 - \frac{1}{x_\gamma x}}\right) \tag{3.20}$$

  as shown by the solid lines in the left-hand side panel of figure 3.2 and by

  $$\gamma_{\mathrm{PP,\,max}}(x_\gamma, x) = \frac{x_\gamma}{2}\left(1 + \sqrt{1 - \frac{1}{x_\gamma x}}\right) \tag{3.21}$$

  as shown by the dashed lines in the figure. These limits are the correct integration borders of the first integral in equation B11 of Zdziarski (1988). Some properties should be noticed:

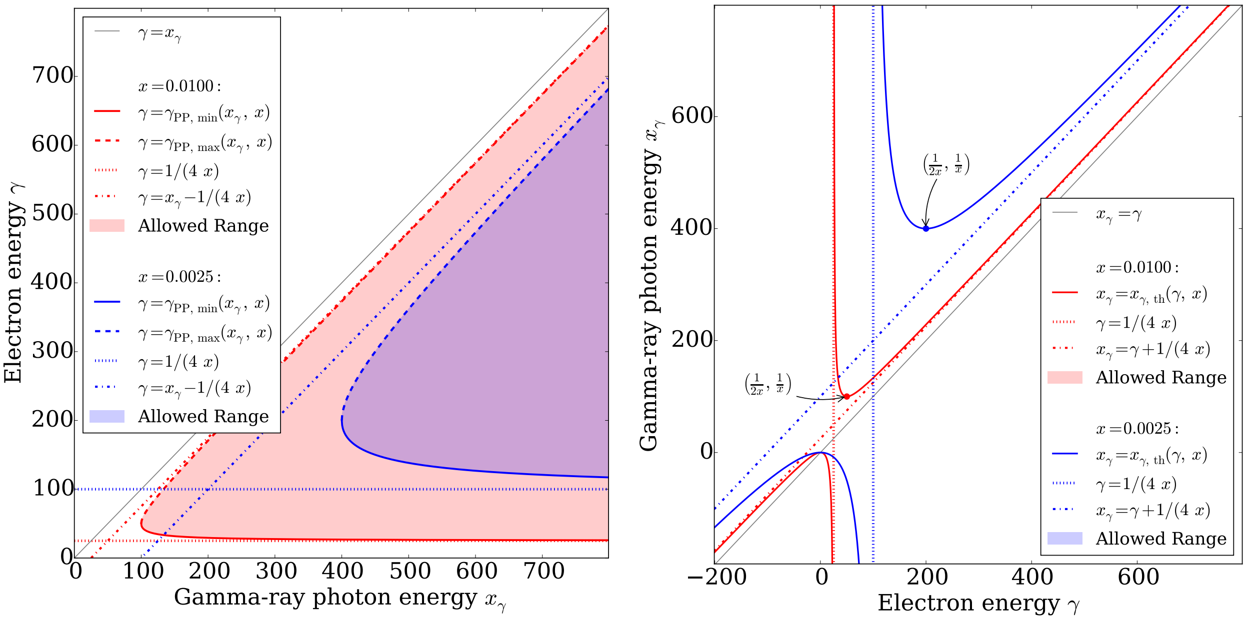

Figure 3.2: Plot of the functions $\gamma_{\mathrm{PP,\,min}}(x_\gamma,\, x)$, $\gamma_{\mathrm{PP,\,max}}(x_\gamma,\, x)$ and $x_{\gamma,\,\mathrm{th}}(\gamma,\, x)$ involved in PP kinematics. Left-hand side panel: Plot of the x_γ-γ plain. For two exemplary values of the soft target photon energy x, the functions $\gamma_{\mathrm{PP,\,min}}$ and $\gamma_{\mathrm{PP,\,max}}$, their asymptotes for very high (and very low) x_γ and the kinematically allowed range are depicted. Right-hand side panel: Equivalent plot, but in the γ-x_γ plain, i.e. flipped along the identical relation (grey line). Shown are the respective inverse functions as well as the location of the PP threshold.

  - When x increases, the limit $\gamma_{\mathrm{PP,\,min}}(x_\gamma, x)$ decreases, whereas $\gamma_{\mathrm{PP,\,max}}(x_\gamma, x)$ increases. Thus, if $n_0(x)$ is extended along x but non-zero only below an upper cutoff x_0, then the kinematically allowed electron energy is bounded according to $\gamma_{\mathrm{PP,\,min}}(x_\gamma, x_0) < \gamma < \gamma_{\mathrm{PP,\,max}}(x_\gamma, x_0)$.
  - It is easy to show, that for given x the minimum value $1/(4\,x)$ of $\gamma_{\mathrm{PP,\,min}}$ is reached asymptotically for $x_\gamma \to \infty$ (see Zdziarski, 1988), briefly written it is $\lim_{x_\gamma \to \pm\infty} \gamma_{\mathrm{PP,\,min}}(x_\gamma, x) = 1/(4x) > 1$ as shown by the dotted lines. This means that electrons cannot be created in the Thomson regime.
  - The function $\gamma_{\mathrm{PP,\,max}}(x_\gamma, x)$ grows monotonically for increasing x_γ with the asymptote $x_\gamma - 1/(4x)$ shown by the dash-dotted lines. Consequently, it is $\gamma_{\mathrm{PP,\,max}}(x_\gamma, x) < x_\gamma$.

- Consider a fixed soft photon energy x and a fixed electron energy γ. Such PP events are possible only if x_γ exceeds a threshold:

$$x_\gamma > x_{\gamma,\,\mathrm{th}}(\gamma, x) \tag{3.22}$$

The PP threshold is defined by

$$x_{\gamma,\,\mathrm{th}}(\gamma, x) = \frac{\gamma}{1 - 1/(4\gamma x)} \tag{3.23}$$

and is drawn in the right-hand side panel of figure 3.2. The condition 3.22 with 3.23 can be obtained from inequality 3.18. Three features of $x_{\gamma,\,\mathrm{th}}$ should be mentioned:

  - It is again instructive to notice that for given x, the functions $\gamma = \gamma_{\mathrm{PP,\,min}}(x_\gamma, x)$ and $\gamma = \gamma_{\mathrm{PP,\,max}}(x_\gamma, x)$ (expressions 3.20 and 3.21) are the inverse functions of the two branches of $x_\gamma = x_{\gamma,\,\mathrm{th}}(\gamma, x)$.
  - It is not difficult to show, that for given x, the function $x_{\gamma,\,\mathrm{th}}(\gamma, x)$ in dependence on γ gets positive and finite values only for $\gamma > 1/(4x)$ (dotted lines in the figure). This

expresses that electrons can be pair produced only with energies above $1/(4x)$. In the range $\gamma > 1/(4x)$, the function $x_{\gamma,\mathrm{th}}(\gamma, x)$ adopts a minimum at $\gamma = 1/(2x)$ shown by the heavy dots in the figure. The value at this minimum is $x_{\gamma,\mathrm{th}}(1/(2x), x) = 1/x$. This is widely called "the PP threshold", see sections 2.4.6 and 2.5.

- Moreover, for fixed γ the function $x_{\gamma,\mathrm{th}}(\gamma, x)$ decreases when x increases. Therefore, if the soft photons are distributed along x with the spectral number density $n_0(x)$ being non-zero only up to an upper cutoff x_0, then $x_{\gamma,\mathrm{th}}(\gamma, x_0)$ is the lowest of all thresholds and consequently PP sets in as soon as $x_\gamma > x_{\gamma,\mathrm{th}}(\gamma, x_0)$.

The spectral interaction rate of PP has a structure very similar to the IC scattering rate in equation 3.11. It was rewritten by Zdziarski (1988) on the basis of the work of Agaronyan, Atoyan and Nagapetyan (1983). The spectral PP interaction rate of an HE photon with energy x_γ in a soft photon field $n_0(x)$ with lower and upper cutoff x_l and x_0 is

$$P(x_\gamma, \gamma) = \int_{\max\left(x_\mathrm{l},\, \frac{E_\mathrm{PP}}{x_\gamma}\right)}^{x_0} n_0(x) \frac{3\sigma_\mathrm{T} c}{4x_\gamma^2 x} \left[r_\mathrm{PP} - (2 + r_\mathrm{PP}) \frac{E_\mathrm{PP}}{x_\gamma x} + 2\left(\frac{E_\mathrm{PP}}{x_\gamma x}\right)^2 + 2\frac{E_\mathrm{PP}}{x_\gamma x} \ln \frac{x_\gamma x}{E_\mathrm{PP}} \right] \mathrm{d}x. \tag{3.24}$$

It is

$$r_\mathrm{PP} = \frac{\gamma/(x_\gamma - \gamma) + (x_\gamma - \gamma)/\gamma}{2}. \tag{3.25}$$

Again, the second argument of the max function in the lower integration border is resulting from the kinetic constraints expressed by the first inequality in expression 3.18. The rate P is entirely determined, as soon as n_0, x_l and x_0 have been specified. Drawing from this and assuming that $n_\gamma(x_\gamma)$ is the spectral number density of the HE photons, some useful quantities can be obtained.

It is helpful to realise that $n_\gamma(x_\gamma)P(x_\gamma, \gamma)$ is the number per unit time, per unit space volume, per unit x_γ-interval and per unit γ-interval of such events that pair produce an electron with energy γ (and its anti-particle with energy $x_\gamma - \gamma$) out of an incident photon with energy x_γ.

- Now, applying the threshold condition 3.22 for the kinematically allowed range of x_γ and integrating along this variable, one obtains $\int_{x_{\gamma,\mathrm{th}}(\gamma,x_0)}^{\infty} n_\gamma(x_\gamma)P(x_\gamma, \gamma)\,\mathrm{d}x_\gamma$. This describes the number of interaction events per unit time, per unit space volume and per unit γ-interval, that produce an electron with energy γ out of an HE photon with any kinematically permitted energy. However, in each PP event, two electrons are created. Therefore,

  $$2 \cdot \int_{x_{\gamma,\mathrm{th}}(\gamma,x_0)}^{\infty} n_\gamma(x_\gamma)P(x_\gamma, \gamma)\,\mathrm{d}x_\gamma \tag{3.26}$$

  specifies the corresponding number of pair-produced electrons, that are inserted into the interval $[\gamma, \gamma + \mathrm{d}\gamma]$ of the energy distribution per unit time, per unit space volume and per unit electron energy interval.

  In the computational implementation of expression 3.26, the upper integration border has to be restricted to $x_{\gamma,0}$, which is the Lorentz factor above which n_γ is zero. Due to this upper cutoff, the integral 3.26 also has an upper cutoff, which is located at $\gamma_{\mathrm{PP,\,max}}(x_{\gamma,0}, x_0)$.

- Furthermore, paying attention to the limitation 3.19 for the possible electron energies,

  $$\int_{\gamma_{\mathrm{PP,\,min}}(x_\gamma,x_0)}^{\gamma_{\mathrm{PP,\,max}}(x_\gamma,x_0)} n_\gamma(x_\gamma)P(x_\gamma, \gamma)\,\mathrm{d}\gamma \tag{3.27}$$

  quantifies the number of HE photons with energy x_γ per unit time, per unit space volume and per unit x_γ-interval, that interact via PP, produce an electron with any kinematically allowed energy and are removed from the interval $[x_\gamma, x_\gamma + \mathrm{d}x_\gamma]$ of the photon distribution. Later on, this term will be called spectral pair-absorption rate.

3.2 Inverse-Compton Pair Cascades

Now, the described processes are brought together and the ensuing cascade is elaborated, first only qualitatively and quantitatively in section 3.2.2.

3.2.1 Qualitative Description

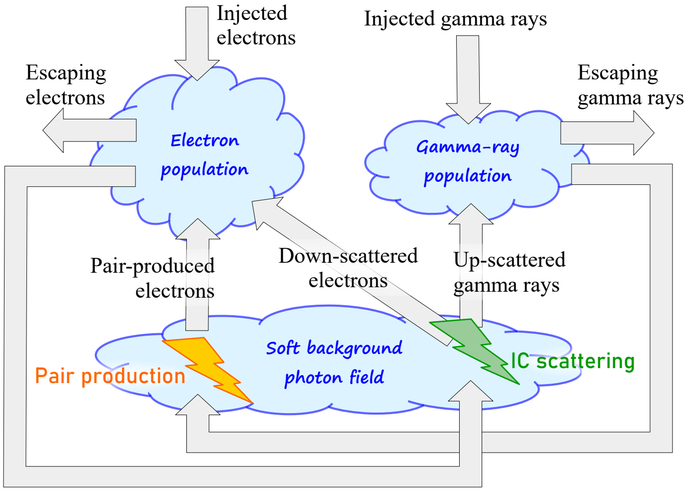

Figure 3.3: Depiction of the considered IC pair cascade. For an explanation, see section 3.2.1.

Pair cascades have been considered and analysed in a very wide range (see e.g. Lovelace, MacAuslan and Burns, 1979; Akharonian, Kririllov-Ugriumov and Vardanian, 1985; Svensson, 1987; Aharonian and Plyasheshnikov, 2003). The present treatment is mainly based on the work of Zdziarski (1988). The physical scenario is depicted in figure 3.3 and can be described as follows (Wendel et al., 2021b). There is a homogeneous and isotropic interaction region. In this region, relativistic electrons and HE photons interact repeatedly with soft, i.e. LE, photons. Thus, three particle species reservoirs are present:

- There is a pool of relativistic electrons. Their normalised energy (Lorentz factor) is denoted by γ. Their energy distribution is quantified through $N(\gamma)$ and has an upper cutoff at γ_0.
- There is a pool of HE photons, whose normalised energy is x_γ. Their spectral number density is $n_\gamma(x_\gamma)$ and has an upper cutoff at $x_{\gamma,0}$.
- There is a background of LE photons, whose normalised energy is x and whose spectral number density is denoted by $n_0(x)$. The biggest, smallest value of x, where n_0 is still non-vanishing is denoted by x_0, by x_1, respectively. Below x_1 and above x_0, n_0 is assumed to vanish and $x_0 \ll 1$ is required. This soft photon pool serves as the target photon population in the interaction processes involved, as it was already assumed in sections 3.1.1 and 3.1.2.

N, n_γ and n_0 are assumed to be time-independent, isotropic and homogeneous. IC scattering and photon-photon PP are included as possible interaction processes.

Electrons IC up-scatter soft photons, which has two effects:

- The electrons are down-scattered, i.e. they lose energy. Nevertheless, they remain in the electron pool and are still available for subsequent IC scattering events.
- New HE photons are produced and supplied to the HE photon pool. These photons can take part in PP in a next step.

Through PP, an HE photon and a soft one react and produce two electrons. The original HE photon is removed from its pool, while the created electrons replenish the electron pool and are available for additional IC scattering events. Electron self interactions (electron-positron annihilation, Møller scattering, Bhabha scattering), HE photon self interactions, synchro-curvature radiation, elastic photon-photon scattering, triplet PP, or PP processes of higher order are neglected in the present consideration.

The evolution of an IC pair cascade ensues from the repeated interaction of PP and IC scattering. The cascade modifies both the electron pool and the HE photon reservoir through annihilation and replenishment of the respective particles. Four additional processes acting as particle sources and sinks are included:

- HE photons are injected into the interaction region. The corresponding spectral injection rate is $\dot{n}_{\gamma,\,\mathrm{i}}(x_\gamma)$. It is required that $\dot{n}_{\gamma,\,\mathrm{i}}$ is non-zero only in an energy range between $x_{\gamma,\,\mathrm{i,\,l}}$ and $x_{\gamma,\,\mathrm{i,\,0}}$ with $x_{\gamma,\,\mathrm{i,\,l}} \gg 1$, thus the name HE photons. Furthermore, it is demanded that the HE photon energy exceeds the PP threshold on all the soft photons, i.e. $x_\gamma > 1/x_\mathrm{l}$.

- Electron injection is allowed, too, and the corresponding spectral injection rate is $\dot{N}_\mathrm{i}(\gamma)$. Again, $\dot{N}_\mathrm{i}$ is required to be non-zero only inside of an energy range from $\gamma_{\mathrm{i,\,l}}$ to $\gamma_{\mathrm{i,\,0}}$ with $\gamma_{\mathrm{i,\,l}} \gg 1$, in other words the electrons are highly relativistic. The finite values of $x_{\gamma,\,\mathrm{i,\,0}}$ and $\gamma_{\mathrm{i,\,0}}$ are necessary to keep the problem numerically manageable and are physically reasonable as infinitely energetic photons/particles are not existent. Furthermore, for the injected electrons $\gamma > 1/x_\mathrm{l}$ is demanded. This means that the primary IC events happen in the KN regime. Such cascades are called IC KN pair cascades (Zdziarski, 1988).

- Additionally, HE photon escape from the interaction region is incorporated. The escape happens on a timescale $T_{\mathrm{esc\,ph}}(x_\gamma)$ that is generally energy-dependent.

- Similarly, electron escape happens on an energy-dependent timescale $T_{\mathrm{esc\,e}}(\gamma)$.

The implementation of finite escape timescales (which is equivalent to a spatially bounded interaction region) is one of the main differences of the present work in comparison to the treatments by Zdziarski (1988) and Wendel et al. (2017). These authors did not take escape into account, which is equivalent to the usage of infinitely long escape timescales (and an infinitely large interaction volume), meaning that they dealt with saturated cascades. A cascade is called saturated, if the background photon field is dense enough for all HE photons above the PP threshold to be pair absorbed as well as for all electrons in the KN regime to get IC scattered before escaping from the interaction region (Zdziarski, 1988). Hence, in saturated KN cascades, all the injected energy is transformed into HE photons with energy below the PP threshold. In the present approach, finite escape timescales are used and the cascade is not necessarily saturated, but may be unsaturated. Through this generalisation introduced by Wendel et al. (2021b), the considered setting becomes more realistic.

For an unsaturated cascade, it is valid to assume that the reservoir of target photons is not modified by the cascade. Thus, n_0 is assumed to stay constant. This means that the considered cascades are linear (Zdziarski, 1988). In the context of electromagnetic cascades, linearity is the feature that only the LE photons act as targets. Self interactions of the HE photons, self interactions of the electrons and electron-HE photon interactions are negligible. Only interactions between HE and LE photons and interactions between electrons and LE photons have to be taken into account. In this case, the PP rate is direct proportional to the HE photon injection rate and the photon production rate is direct proportional to the electron injection, motivating the term "linear". Through the comparison of cross sections, Zdziarski (1988) has shown that KN cascades are always linear, if the LE photon energy density is similar to or bigger than the HE photon energy density (sufficient condition). In the course of this work, linearity of the cascades considered is assumed but the validity of this assumption has to be checked a posteriori. As the cascading goes on, electrons are successively IC down-scattered to lower energies, until scatterings finally happen in the Thomson regime ($\gamma\, x < 1$). Pair cascades are never linear in the Thomson regime, because $x_\gamma\, x < 1$ means that PP on the soft photons is impossible and consequently PP can happen only through HE photon self interactions.

3.2.2 Quantitative Description

In sections 3.1.1 and 3.1.2, all the relevant spectral interaction rates of IC scattering and of PP were derived. In section 3.2.1 it was outlined how these processes (together with injection and escape) play together and constitute a cascade. The corresponding kinetic equations are derived now. A conceptual approach to solve them is outlined in section 3.2.2.2.

3.2.2.1 Derivation of the Kinetic Equations

The net rates of change of the density of the electrons and of the HE photons, respectively, are now obtained by summarising all the source and sink terms as described in Zdziarski (1988) and Wendel et al. (2021b). Thereafter, steady state is assumed, making it possible to rewrite the kinetic equations in a numerically manageable form.

First, the contributions to the rate of change $\dot{N}$ of the electron spectral number density N are considered:

- There is the electron spectral injection rate $\dot{N}_\mathrm{i}(\gamma)$ as a source term of the energy distribution.
- There is escape with a finite timescale $T_\mathrm{esc\,e}$. The corresponding sink is $N(\gamma)/T_\mathrm{esc\,e}(\gamma)$.
- Via IC scattering, electrons are down-scattered. The electrons that are inserted into the electron distribution at the energy γ originate from higher values $\gamma' > \gamma$ in energy space. The corresponding source term is the expression 3.14 (just up to an exchange of the variables γ and γ', because in the consideration of the entire cascade, the Lorentz factor γ' is used as the integration variable).
- Likewise, an electron with incident energy γ gets down-scattered to any kinematically allowed smaller energy $\gamma' < \gamma$. This results in a sink at the energy γ, which is expressed in the term 3.15.
- A PP event creates two electrons with energy γ. The resulting source term is equal to expression 3.26.

Adding up these terms with the correct sign, one obtains the total rate of change $\dot{N}(\gamma)$ of the spectral electron number density:

$$\begin{aligned}\dot{N}(\gamma) =& \dot{N}_\mathrm{i}(\gamma) - N(\gamma)\left(\frac{1}{T_\mathrm{esc\,e}(\gamma)} + \int_{\gamma'_\mathrm{IC,\,min}(\gamma,x_0)}^{\gamma} C(\gamma,\gamma')\,\mathrm{d}\gamma'\right) + \\ &+ \int_{\gamma}^{\min(\gamma_0,\,\gamma_\mathrm{IC,\,max}(\gamma,x_0))} N(\gamma')C(\gamma',\gamma)\,\mathrm{d}\gamma' + 2\int_{x_{\gamma,\,\mathrm{th}}(\gamma,x_0)}^{x_{\gamma,\,0}} n_\gamma(x_\gamma)P(x_\gamma,\gamma)\,\mathrm{d}x_\gamma\end{aligned} \tag{3.28}$$

In the course of the text, the expression within round brackets is called electron spectral loss rate. It is the sum of the spectral escape rate (first summand) and of the spectral IC down-scattering rate (second summand). The sum of the source terms in the second line of equation 3.28 is called electron spectral production rate. Notice that both the spectral injection rate and the spectral production rate have the dimension of $[\gamma]^{-1}[t]^{-1}[l]^{-3}$, while the unit of the spectral loss rate is only $[\gamma]^{-1}[t]^{-1}$.

Second, the HE photons are considered. The following sources and sinks are included to determine the rate of change $\dot{n}_\gamma(x_\gamma)$ of the spectral number density of the photons:

- There is a source at the energy x_γ due to the photon spectral injection rate $\dot{n}_{\gamma,\,\mathrm{i}}(x_\gamma)$.
- The finite escape timescale $T_\mathrm{esc\,ph}$ leads to the sink term $n_\gamma(x_\gamma)/T_\mathrm{esc\,ph}(x_\gamma)$.
- A photon with energy x_γ undergoing PP is removed from the photon distribution, causing the sink term 3.27.
- Soft photons are IC up-scattered. The corresponding source at the energy x_γ is given by the expression 3.16.

Again, the photons' kinetic equation assumes equality between the total rate of change $\dot{n}_\gamma(x_\gamma)$ of the spectral number density of the photons and of the sum of the sources and the sinks:

$$\dot{n}_\gamma(x_\gamma) = \dot{n}_{\gamma,\,\mathrm{i}}(x_\gamma) - n_\gamma(x_\gamma)\left(\frac{1}{T_\mathrm{esc\,ph}(x_\gamma)} + \int_{\gamma_\mathrm{PP,\,min}(x_\gamma,x_0)}^{\gamma_\mathrm{PP,\,max}(x_\gamma,x_0)} P(x_\gamma,\gamma)\,\mathrm{d}\gamma\right) + \dot{n}_{\gamma,\,\mathrm{IC}}(x_\gamma) \tag{3.29}$$

In the following, the part in the round brackets is named photon spectral loss rate. It is comprised of the spectral escape rate (first summand) and of the spectral pair-absorption rate (second summand). Again, one should realise that the dimensions of the spectral injection rate and of the spectral production rate are $[x_\gamma]^{-1}[t]^{-1}[l]^{-3}$, while the spectral loss rate is in units of $[x_\gamma]^{-1}[t]^{-1}$.

Now it is assumed that the system is in steady state. This means that the total rates of change of the spectral number densities can be set equal to zero in equations 3.28 and 3.29. It is possible now to solve each equation for the respective spectral number density in front of the round brackets. By this, one obtains

$$N(\gamma) = \frac{\dot{N}_\mathrm{i}(\gamma) + \int_{\gamma}^{\min(\gamma_0,\, \gamma_{\mathrm{IC,\,max}}(\gamma,x_0))} N(\gamma')C(\gamma',\gamma)\,\mathrm{d}\gamma' + 2\int_{x_{\gamma,\,\mathrm{th}}(\gamma,x_0)}^{x_{\gamma,\,0}} n_\gamma(x_\gamma)P(x_\gamma,\gamma)\,\mathrm{d}x_\gamma}{\frac{1}{T_{\mathrm{esc\,e}}(\gamma)} + \int_{\gamma'_{\mathrm{IC,\,min}}(\gamma,x_0)}^{\gamma} C(\gamma,\gamma')\,\mathrm{d}\gamma'} \tag{3.30}$$

from equation 3.28, as well as

$$n_\gamma(x_\gamma) = \underbrace{\frac{\dot{n}_{\gamma,\,\mathrm{i}}(x_\gamma)}{\frac{1}{T_{\mathrm{esc\,ph}}(x_\gamma)} + \int_{\gamma_{\mathrm{PP,\,min}}(x_\gamma,x_0)}^{\gamma_{\mathrm{PP,\,max}}(x_\gamma,x_0)} P(x_\gamma,\gamma)\,\mathrm{d}\gamma}}_{=\,n_{\gamma,\,\mathrm{i}}(x_\gamma)} + \underbrace{\frac{\dot{n}_{\gamma,\,\mathrm{IC}}(x_\gamma)}{\frac{1}{T_{\mathrm{esc\,ph}}(x_\gamma)} + \int_{\gamma_{\mathrm{PP,\,min}}(x_\gamma,x_0)}^{\gamma_{\mathrm{PP,\,max}}(x_\gamma,x_0)} P(x_\gamma,\gamma)\,\mathrm{d}\gamma}}_{=\,n_{\gamma,\,\mathrm{IC}}(x_\gamma)} \tag{3.31}$$

from equation 3.29. Here, two contributions to n_γ have been identified and denoted by $n_{\gamma,\,\mathrm{i}}$ and by $n_{\gamma,\,\mathrm{IC}}$. The upper cutoffs of $\dot{n}_{\gamma,\,\mathrm{i}}$ and of $\dot{n}_{\gamma,\,\mathrm{IC}}$ are inherited to $n_{\gamma,\,\mathrm{i}}$ and to $n_{\gamma,\,\mathrm{IC}}$, respectively. Consequently, $n_\gamma(x_\gamma)$ has an upper cutoff at

$$x_{\gamma,\,0}(\gamma_0) = \max(x_{\gamma,\,\mathrm{i},\,0},\, x_{\gamma,\,\max}(\gamma_0,x_0)). \tag{3.32}$$

Substituting for n_γ in equation 3.30 with use of equation 3.31 (and once again making an exchange of γ and γ') yields

$$N(\gamma) = \frac{\dot{N}_\mathrm{i}(\gamma) + \int_{\gamma}^{\min(\gamma_0,\, \gamma_{\mathrm{IC,\,max}}(\gamma,x_0))} N(\gamma')C(\gamma',\gamma)\,\mathrm{d}\gamma' + Q_\mathrm{PP}(\gamma)}{\frac{1}{T_{\mathrm{esc\,e}}(\gamma)} + \int_{\gamma'_{\mathrm{IC,\,min}}(\gamma,x_0)}^{\gamma} C(\gamma,\gamma')\,\mathrm{d}\gamma'} \tag{3.33}$$

with the abbreviation

$$\begin{aligned} Q_\mathrm{PP}(\gamma) = \int_{x_{\gamma,\,\mathrm{th}}(\gamma,x_0)}^{x_{\gamma,\,0}(\gamma_0)} & \left(\dot{n}_{\gamma,\,\mathrm{i}}(x_\gamma) + \int_{\gamma_{\mathrm{IC,\,th}}(x_\gamma,x_0)}^{\gamma_0} N(\gamma')C(\gamma',\gamma'-x_\gamma)\,\mathrm{d}\gamma'\right) \cdot \\ & \cdot \frac{2\,P(x_\gamma,\gamma)}{\frac{1}{T_{\mathrm{esc\,ph}}(x_\gamma)} + \int_{\gamma_{\mathrm{PP,\,min}}(x_\gamma,x_0)}^{\gamma_{\mathrm{PP,\,max}}(x_\gamma,x_0)} P(x_\gamma,\gamma')\,\mathrm{d}\gamma'}\,\mathrm{d}x_\gamma \end{aligned} \tag{3.34}$$

called spectral PP rate. The fraction in the second line of this equation will be called normalised spectral PP probability. With help of the results from section 3.1.2 and with equation 3.32 it can be realised that $Q_\mathrm{PP}(\gamma)$ is zero for $\gamma > \gamma_{\mathrm{Q},\,0}$, where the cutoff is defined by

$$\gamma_{\mathrm{Q},\,0}(\gamma_0) = \gamma_{\mathrm{PP,\,max}}(\underbrace{\max(x_{\gamma,\,\mathrm{i},\,0},\, x_{\gamma,\,\max}(\gamma_0,x_0))}_{=\,x_{\gamma,\,0}},\, x_0). \tag{3.35}$$

From the properties of the summands of the numerator of equation 3.33, it is obvious that the right-hand side of this equation has an upper cutoff at

$$\gamma_0 = \max(\gamma_{\mathrm{i},\,0},\, \gamma_0,\, \overbrace{\gamma_{\mathrm{PP,\,max}}(\underbrace{\max(x_{\gamma,\,\mathrm{i},\,0},\, x_{\gamma,\,\max}(\gamma_0,x_0))}_{=\,x_{\gamma,\,0}},\, x_0)}^{=\,\gamma_{\mathrm{Q},\,0}}). \tag{3.36}$$

3.2.2.2 Conceptual Solution Scheme

To employ such an IC pair cascade in an astrophysical context and to associate the cascaded gamma-ray emission with (a part of) the observed gamma-ray emission, the goal is now to find the steady-state photon distribution $n_\gamma(x_\gamma)$ of the cascade. This can be achieved straightforwardly via equation 3.31. The following quantities appear in the right-hand side of this equation: The HE photon energy x_γ, the photon escape timescale $T_{\mathrm{esc\,ph}}$, the electron distribution N, the photon injection rate $\dot{n}_{\gamma,\mathrm{i}}$ and the soft photon distribution n_0 (through the interaction rates C and P, see equations 3.11 and 3.24). The cutoffs x_l and x_0 are not explicitly mentioned here, because they are known as soon as n_0 has been specified. The cutoff γ_0 is not mentioned here, too, because it is a property of the function $N(\gamma)$. The functions in the integral borders are known from sections 3.1.1 and 3.1.2. Therefore, equation 3.31 can conceptually be rewritten as

$$n_\gamma(x_\gamma) = \mathcal{G}'(n_0, \dot{n}_{\gamma,\mathrm{i}}, T_{\mathrm{esc\,ph}}, N, x_\gamma) \tag{3.37}$$

where the functional $\mathcal{G}'$ was defined accordingly. The functions n_0, $\dot{n}_{\gamma,\mathrm{i}}$ and $T_{\mathrm{esc\,ph}}$ are parameters that describe the physical situation. They have to be specified a priori according to the astrophysical situation to be modelled and this will actually be a main task in chapter 5 and 6. When they are known, equation 3.37 can be shortened to

$$n_\gamma(x_\gamma) = \mathcal{G}(N, x_\gamma) \tag{3.38}$$

where again the functional $\mathcal{G}$ was defined accordingly. It is now obvious that n_γ can be computed as soon as N is known.

However, to determine N, it is necessary to solve equation 3.33. This task is far more difficult, as this integral equation has to be solved iteratively. Conceptually seen, this equation can be rewritten as

$$N(\gamma) = \mathcal{F}'(n_0, \dot{N}_\mathrm{i}, \dot{n}_{\gamma,\mathrm{i}}, T_{\mathrm{esc\,ph}}, T_{\mathrm{esc\,e}}, N, \gamma) \tag{3.39}$$

with an adequate definition of $\mathcal{F}'$. Again, the soft photon number density, the injection rates and the escape timescales have to be prescribed when the physical setting is known. Hence, they are input functions. Then, the electrons' kinetic equation reads as

$$N(\gamma) = \mathcal{F}(N, \gamma) \tag{3.40}$$

with a proper definition of $\mathcal{F}$. As no analytical solution to this equation is known, it can only be solved numerically by an iterative scheme. The idea is to "guess" an initial $N(\gamma)$, to compute the right-hand side of equation 3.40 as a function of γ and then to assign this to the next $N(\gamma)$ which then can be used in the subsequent iteration step. The right-hand side of 3.40 is determined repeatedly with help of N of the previous iteration step. The computational details of this approach are elucidated in section 4.3.

To determine $\mathcal{F}$ and $\mathcal{G}$ it is necessary to know γ_0. It is possible to determine γ_0 (and consequently $\gamma_{\mathrm{Q},0}$ and $x_{\gamma,0}$) in every iteration step via the recursive definition 3.36. This would be necessary, if the problem was time dependent with changing $x_{\gamma,\mathrm{i},0}$ and $\gamma_{\mathrm{i},0}$. In the present case, $x_{\gamma,\mathrm{i},0}$ and $\gamma_{\mathrm{i},0}$ are however constant. Consequently, the cutoffs γ_0, $\gamma_{\mathrm{Q},0}$ and $x_{\gamma,0}$ are also constant. First, for the three main cases all possible sub-cases are considered via case differentiations and second, the comprising definitions for the cases will be given:

- Case 1:
  $\dot{N}_\mathrm{i} = 0$ and $\dot{n}_{\gamma,\mathrm{i}}$ is non-vanishing. Consequently, it is $\gamma_{\mathrm{i},0} = 0$. This case has no sub-cases. The cutoffs are defined as follows:

$$x_{\gamma,0} = x_{\gamma,\mathrm{i},0} \tag{3.41a}$$

$$\gamma_{\mathrm{Q},0} = \gamma_{\mathrm{PP,max}}(x_{\gamma,\mathrm{i},0},\, x_0) \tag{3.41b}$$

$$\gamma_0 = \gamma_{\mathrm{PP,max}}(x_{\gamma,\mathrm{i},0},\, x_0) \tag{3.41c}$$

- Case 2:
  $\dot{N}_\mathrm{i}$ is non-vanishing and $\dot{n}_{\gamma,\,\mathrm{i}} = 0$. Consequently, it is $x_{\gamma,\,\mathrm{i},\,0} = 0$. This case has no sub-cases. The cutoffs are defined as follows:

$$x_{\gamma,\,0} = x_{\gamma,\,\max}(\gamma_{\mathrm{i},\,0},\, x_0) \tag{3.42a}$$
$$\gamma_{\mathrm{Q},\,0} = \gamma_{\mathrm{PP},\,\max}(x_{\gamma,\,\max}(\gamma_{\mathrm{i},\,0},\, x_0),\, x_0) \tag{3.42b}$$
$$\gamma_0 = \gamma_{\mathrm{i},\,0} \tag{3.42c}$$

- Case 3:
  Both $\dot{N}_\mathrm{i}$ and $\dot{n}_{\gamma,\,\mathrm{i}}$ are non-vanishing. Here, a case differentiation is necessary:
  - Case 3A:
    It is assumed that $\gamma_{\mathrm{PP},\,\max}(x_{\gamma,\,\mathrm{i},\,0},\, x_0) > \gamma_{\mathrm{i},\,0}$. In this case, the cutoffs are fully determined by the injected photons and consequently equal to those of case 1. Equations 3.41 are valid.
  - Case 3B:
    It is assumed that $\gamma_{\mathrm{PP},\,\max}(x_{\gamma,\,\mathrm{i},\,0},\, x_0) \leq \gamma_{\mathrm{i},\,0}$. One more case differentiation is necessary here:
    - Case 3Ba:
      It is assumed that $x_{\gamma,\,\mathrm{i},\,0} > \gamma_{\mathrm{i},\,0}$. In this case, it is:

$$x_{\gamma,\,0} = x_{\gamma,\,\mathrm{i},\,0} \tag{3.43a}$$
$$\gamma_{\mathrm{Q},\,0} = \gamma_{\mathrm{PP},\,\max}(x_{\gamma,\,\mathrm{i},\,0},\, x_0) \tag{3.43b}$$
$$\gamma_0 = \gamma_{\mathrm{i},\,0} \tag{3.43c}$$

    - Case 3Bb:
      It is assumed that $x_{\gamma,\,\mathrm{i},\,0} \leq \gamma_{\mathrm{i},\,0}$. In this case, another differentiation is necessary:
      - Case 3Bb$_\mathrm{a}$:
        It is assumed that $x_{\gamma,\,\max}(\gamma_{\mathrm{i},\,0},\, x_0) > x_{\gamma,\,\mathrm{i},\,0}$. In this case, the cutoffs are fully determined by the injected electrons and consequently equal to those of case 2. Equations 3.42 are valid.
      - Case 3Bb$_\mathrm{b}$:
        It is assumed that $x_{\gamma,\,\max}(\gamma_{\mathrm{i},\,0},\, x_0) \leq x_{\gamma,\,\mathrm{i},\,0}$. In this case, the cutoffs are equal to those of case 3Ba and equations 3.43 are valid.

All these cutoffs can easily be verified by evaluating the recursive definitions 3.32, 3.35 and 3.36 with help of the respective case assumptions as well as with help of the findings from sections 3.1.1 and 3.1.2, stating that the two functions $\gamma_{\mathrm{PP},\,\max}(x_\gamma, x)$ and $x_{\gamma,\max}(\gamma, x)$ essentially return a value that is always smaller than the function's first argument and stating that they increase monotonically with increasing first argument.

Now, by ordering $x_{\gamma,\,\mathrm{i},\,0}$, $\gamma_{\mathrm{i},\,0}$, $x_{\gamma,\,\max}(\gamma_0,\, x_0)$ and $\gamma_{\mathrm{PP},\,\max}(x_{\gamma,\,0},\, x_0)$ for the cases and sub-cases from above, they are summarised into three classes:

- Class A: Dominance of injected photons
  This class comprises cases 1 and 3A. It is $\gamma_{\mathrm{i},\,0} < \gamma_{\mathrm{PP},\,\max}(x_{\gamma,\,0},\, x_0) < x_{\gamma,\,\mathrm{i},\,0}$ and equations 3.41 are valid.
- Class B: Dominance of injected electrons
  This class comprises cases 2 and 3Bb$_\mathrm{a}$. It is $x_{\gamma,\,\mathrm{i},\,0} < x_{\gamma,\,\max}(\gamma_0,\, x_0) < \gamma_{\mathrm{i},\,0}$ and equations 3.42 are valid.

- Class C: Mixed influence
  This class comprises cases 3Ba and 3Bb$_\mathrm{b}$. It is $\max(\gamma_{\mathrm{PP,\,max}}(x_{\gamma,\,0},\,x_0),\,x_{\gamma,\,\mathrm{max}}(\gamma_0,\,x_0)) < \min(\gamma_{\mathrm{i},\,0},\,x_{\gamma,\,\mathrm{i},\,0})$ and equations 3.43 are valid.

To sum up, the cascade setting is entirely described when the following quantities have been prescribed:

- The soft photons' spectral number density $n_0(x)$ with cutoffs x_l and x_0
- The HE photons' spectral injection rate $\dot{n}_{\gamma,\,\mathrm{i}}$ with cutoffs $x_{\gamma,\,\mathrm{i},\,\mathrm{l}}$ and $x_{\gamma,\,\mathrm{i},\,0}$
- The relativistic electrons' spectral injection rate $\dot{N}_\mathrm{i}$ with cutoffs $\gamma_{\mathrm{i},\,\mathrm{l}}$ and $\gamma_{\mathrm{i},\,0}$
- The HE photons' escape timescale $T_{\mathrm{esc\,ph}}$
- The electrons' escape timescale $T_{\mathrm{esc\,e}}$

Then, the steady-state spectral densities N and n_γ can be determined via 3.40 and 3.38.

As soon as the HE photon distribution is known, the emerging spectral flux density F_casc can be determined. There are, however, several possibilities how this conversion can be done. While Zdziarski (1988) did not determine observables at all, Wendel et al. (2017) took $\dot{n}_{\gamma,\,\mathrm{IC}}$ as a starting point. They converted the photon production rate to the flux density via

$$F_\mathrm{casc}(x_\gamma) = \dot{n}_{\gamma,\,\mathrm{IC}}(x_\gamma) \cdot \frac{{r_\mathrm{S}}^3}{\Omega\, D^2\; m_\mathrm{e} c^2}. \tag{3.44}$$

This approach underlies several assumptions:

1. It assumes an emitting volume of approximate size r_S^3. This was motivated by the Schwarzschild radius being the characteristic lengthscale of an AGN centre, but nevertheless it is an arbitrary choice. Furthermore, it is in clear contradiction to the assumption of no escape ($T_{\mathrm{esc\,ph}} = T_{\mathrm{esc\,e}} = \infty$) in the kinetic equations of these authors.
2. It assumes that none of the injected photons $\dot{n}_{\gamma,\,\mathrm{i}}$ leave the interaction region unaffected and that none of the injected photons are taken into account for determining the observed spectrum. This is an unreasonable assumption, because surely the injected photons can leave the interaction region unattenuated.
3. It assumes that all the IC produced photons from the emission volume leave the interaction region and are responsible for the observed radiation. Attenuation of the IC produced photons by escape and by PP is not taken into account in determining the observed emission.
4. It assumes that all the radiation is emitted along a beam of solid angle Ω.
5. The distance between the source and the observer is D.

The $m_\mathrm{e}c^2$ in the denominator of equation 3.44 is because F_casc is in units of $\mathrm{m}^{-2}\,\mathrm{s}^{-1}\,\mathrm{J}^{-1}$, whereas $\dot{n}_{\gamma,\,\mathrm{IC}}$ is measured in $\mathrm{m}^{-3}\,\mathrm{s}^{-1}$.

The approach to determine F_casc in the present work as well as in Wendel et al. (2021b) and in Wendel, Shukla and Mannheim (2021) is more realistic. The following conversion to the flux density is used:

$$F_\mathrm{casc}(x_\gamma) = n_\gamma(x_\gamma) \cdot \frac{4\pi\, R(x_\gamma)^2}{\Omega(\phi)\, D^2\; m_\mathrm{e} c} \tag{3.45}$$

Here, the following assumptions were made:

1. In contrast to number 1 above, where the emitting volume was chosen somewhat arbitrarily, the emitting volume is now assumed to have the radial size R. As the radial size of the emitting volume might be comparable to the size of the interaction region, it is sensible to set

$$R(x_\gamma) = T_{\mathrm{esc\,ph}}(x_\gamma)\, c \qquad \text{and} \tag{3.46a}$$

$$T_{\mathrm{esc\,ph}} = T_{\mathrm{esc\,e}}. \tag{3.46b}$$

By this, the contradiction of number 1 above is resolved.

2. By using n_γ instead of $\dot{n}_{\gamma,\,\mathrm{IC}}$, also the injected photons are incorporated (in addition to the IC up-scattered photons). This is the case because according to equation 3.31 $n_{\gamma,\,\mathrm{i}}$ is also involved in the determination of n_γ via the first summand in this equation. Taking also the injected photons into account in determining the emerging flux density is more realistic than in the previous approach (number 2 above), because not all the injected photons are necessarily reprocessed via the cascade.
3. Attenuation of both the injected and the IC produced photons by losses (escape and pair absorption) is taken into account through the division of the injection and production rate (numerators of equation 3.31) by the spectral loss rate (denominators of equation 3.31). By this, the disputable assumption that all the IC produced photons contribute to the flux density is relaxed.
4. It is assumed that the radiation is emitted along a conical beam with opening angle ϕ and solid angle $\Omega = 4\pi \cdot \sin^2(\phi/4)$.
5. Same as number 5 above.

One downside of both approaches is the following inconsistency. During the consideration of the cascade, homogeneity and isotropy were assumed. This contrasts to the assumption that the radiation is emitted along a beam of solid angle $\Omega < 4\pi$. Nevertheless, the cascade scenario and the mathematical framework are valid, if the soft photons are isotropically distributed.

Chapter 4

Numerical Solution Procedure

In this chapter, the numerical code developed in the course of this work is outlined, with a focus on the iterative solution of equation 3.33 or 3.40, respectively. Computations are performed with `Python` 3.4.1 (Oliphant, 2007; Millman and Aivazis, 2011) augmented by the `SciPy` ecosystem including the `SciPy` library 0.15.1 providing e.g. numerical integration, interpolation and optimisation standards (Virtanen et al., 2020), `numpy` 1.9.1 providing e.g. vectorisation, indexing and broadcasting (Oliphant, 2015; Harris et al., 2020), as well as the `matplotlib` library 1.4.2 for visualisation (Hunter, 2007).

4.1 Overview about the Code

The `Python` code as well as several auxiliary files that are imported by the code can be found on `https://github.com/ChristophWendel/PhD-project.git`. In the code, most definitions and algorithms are described by comments and docstrings, such that the purpose of each function can be understood. Nevertheless, a rough overview about the structure of the code is provided here. The code is divided into seven `.py` files, `part1.py` till `part7.py`. In every case, `part7` has to be run to evaluate the code. It can be run either in a shell or in an interactive interpreter, preferentially with the Interactive Editor for Python by Pyzo. The file `part7` imports all six other files.

`part1` starts with loading `Python`, `numpy`, `matplotlib` and `SciPy` packages. After this, exceptions and basic auxiliary functions are defined. Especially, twelve possibilities to divide an integration range into smaller sub-ranges are defined, see subsequent section. Several tools to search, import, name, export and delete data or other files are defined. After this, physical constants and input parameters relevant for ADAF considerations are defined. Subsequently, a dictionary and a corresponding function are defined, whose purpose is to save central processing unit (CPU) hours by storing interim results once they were computed and by providing the saved results without the necessity to compute them anew as soon as they are called again. Simple physical conversions and ADAF-specific functions follow. After this, the ADAF bremsstrahlung, synchrotron and Comptonised spectral luminosities are defined according to section 2.1.2.2. After these three definitions, the composite ADAF spectrum is compiled (in several representations like e.g. spectral luminosity, number density, energy density). Thereafter, the total ADAF energy density and the total number density is computed via analytical and numerical integration. At last, several definitions to plot ADAF properties are defined.

`part2` and `part3` contain a vacuum gap AGN jet toy model and an Mrk 501 toy model, respectively. As these two toy models are not part of the present work, the content of these two files is not detailed here. The two files are, however, included into the code, because several physical definitions of `part2` and `part3` are used in `part4` to `part7`. `part4` to `part7` implement the simulation of IC pair cascades as well as an experimental simulation of synchrotron IC pair cascades.

`part4` is the beginning of the cascade simulation. At first, several parameters specifying the physics of the cascade and the details of the numerical algorithm of the iteration, are given. Functionalities to import results of previous iterations follow. Several simple BLR and jet properties are determined thereafter. The input functions $\dot{N}_{\mathrm{i}}$, $\dot{n}_{\gamma,\mathrm{i}}$ and n_0 are defined. For $\dot{N}_{\mathrm{i}}$ and $\dot{n}_{\gamma,\mathrm{i}}$, any differentiable, numerically integrable function satisfying the assumptions of section 3.2.1 can be used as well as results of previous iterations. For $\dot{n}_{\gamma,\mathrm{i}}$ it is furthermore possible to use a δ_{Dirac} function peak. For n_0 any differentiable, numerically integrable function satisfying the assumptions of section 3.2.1 as well as a set of emission lines (several δ_{Dirac} peaks) can be used. In the latter case, the energies x_i and the relative flux density contributions (line strengths) $K_{\mathrm{line},\,i}$ have to be specified via a separate `.csv` file. The emission line files used in the course of this work are also provided on `https://github.com/ChristophWendel/PhD-project.git`. Subsequently, an automated check of the validity of the input parameters is coded. The computation of the soft photons' energy density, total number density and luminosity (in the specific scenarios considered in this work) follows.

These initialisations are followed by the main part where for escape, for IC scattering and for PP all kinematic limits, interaction rates (and integrated interaction rates) and the corresponding timescales and optical depths are defined, as outlined in sections 3.1.1 and 3.1.2. The naming of these definitions is mainly based on the naming of the respective quantities by Zdziarski (1988). Furthermore, many definitions to plot the functions are defined. Additionally, various formulae (loss rate, production rate, emissivity) on synchrotron radiation are implemented, for the purpose of the experimental synchrotron IC pair cascades.

As is obvious from section 3.2.2.2, the integration borders of the integrals in the kinetic equations and the upper cutoffs of several expressions depend on the upper cutoffs of the injection rates and of the soft photon distribution. These integration borders and upper cutoffs are determined near the end of `part4`. After this, the sequence of sampling points of the Lorentz factor is compiled, the initial choice $N_{\mathrm{init}}(\gamma)$ for the electron distribution is specified and the data structure containing the results of the iteration is initialised. Finally, a function used in the experimental super-iteration to check for convergence is defined.

`part5` solves the electron kinetic equation. First, the product of $N(\gamma)$ with the electron spectral loss rate (the subtrahend in equation 3.28, which is equivalent to the second term of equation 1 by Zdziarski (1988) up to inclusion of escape, the correct integration borders and synchrotron photons as possible target photons) is computed and plotted. Second, the term 3.14 (second summand of numerator of equation 3.33, which is equivalent to the third term of equation 1 by Zdziarski (1988) up to inclusion of the correct integration borders and synchrotron photons as possible target photons) is computed and plotted. Third, the spectral photon production rate $\dot{n}_{\gamma,\mathrm{IC}}$ (expression 3.16, which is equivalent to the first summand in the squared brackets of equation 1 by Zdziarski (1988) up to inclusion of the correct integration borders and synchrotron photons as possible target photons) is computed and plotted. Fourth, the spectral PP rate Q_{PP} (expression 3.34, which is equivalent to the fourth term of equation 1 by Zdziarski (1988) up to inclusion of escape, the correct integration borders and synchrotron photons as possible target photons) is computed and plotted. This is essentially an integration along x_γ and can be done via two alternatives. The first alternative integrates the entire integrand (as it is written in equation 3.34) along x_γ. The second alternative splits the integral into a sum of two integrals, each of which has a simpler integrand. Essentially, the splitting makes use of the distributive property of the integrand of Q_{PP}. It is however found, that none of these two alternatives brings a substantial gain in computational efficiency and can reduce the CPU hours appreciably. If $\dot{n}_{\gamma,\mathrm{i}}$ is a δ_{Dirac} peak, then the second alternative is always applied. Fifth, $\mathcal{F}$ (the right-hand side of equation 3.33 or 3.40, respectively) is defined. Subsequently, the iterative scheme is implemented as explained in section 4.3. Finally, the iteration results are saved and plotted and all input values are exported into a file.

`part6` contains further definitions on synchrotron radiation, compiles the synchrotron kinetic equation and implements an experimental simulation of synchrotron IC pair cascades. In this type of cascade, the electrons spiral in a magnetic field and emit synchrotron photons, which serve as another, varying population of soft target photons in addition to the external photons. To find steady-state solutions for these cascades, the EED N and the synchrotron photon distribution have to be computed alternatingly and in several turns in an additional super-iteration, which is coded at the end of `part6`. While such cascades are not the subject of the present work, they represent an interesting topic of future research.

`part7` begins with an inefficient and thus obsolete part. It computes equation 8 of Zdziarski (1988), which is the integration of the continuity equation resulting from equation 3.33 in the deep Thomson regime (where PP is not happening any more and where the energy transfers of IC scattering events become continuous). Another obsolete routine follows. It finds N in the transition of the Thomson to the KN regime via interpolating the solution of the continuity equation (which is valid only in the deep Thomson regime) to the converged iteration (which is correct in the deep KN regime). Subsequently, the HE photon spectral number density n_γ (equation 3.31 or 3.38, respectively) is computed as well as its contributions $n_{\gamma,\mathrm{i}}$ and $n_{\gamma,\mathrm{IC}}$ (and other representations of it like the spectral energy density or integrals of these quantities). Thereafter, the conversion of n_γ to F_{casc} is performed according to equation 3.45 and the results are exported to a file. The comparison to observational data of Mrk 501 (as described in chapter 5) follows and SSC model data points are included. Thereafter, for the case of 3C 279 (as discussed in chapter 6) the simulation results are compared to observational data. The bodies of all the definitions up to here (except those making use of multi-core utilities) can be evaluated also in an interactive session. The code can, however, also be run via the shell. If multi-core computations are to be included, the code must be evaluated via a shell. For this purpose, the functions to be called as well as the identifiers, to which the objects returned by the functions are assigned, have to be specified in the very last part of `part7`.

4.2 Integrations

All integrations of this work are executed numerically with the `Python` function `scipy.integrate.quad` to compute definite integrals based on the Fortran library QUADPACK. Only in the case of the integration of the ADAF spectrum, an analytical integration is additionally performed (as described in section 2.1.2.2). Using `scipy.integrate.quad` has various advantages:

1. It can directly integrate `Python` functions without the need to discretise the functions manually. If the integrand is dependent on more than one argument, the arguments along which it is not integrated can be used as arguments of the superordinate function that calls `scipy.integrate.quad`. This makes the code easy to read and write and easily expandable.
2. `scipy.integrate.quad` has versatile routines to always achieve the requested and freely selectable relative error tolerance. This feature is widely used in this code.
3. The necessary number of sub-divisions of the integration range is automatically chosen such that also fast-changing integrands are integrated with the requested error tolerance. If this was not the case, one would have to implement self-made routines that adapt the integration mesh according to the integrand's behaviour, which would be an error-prone endeavour.

Because of these benefits, it was chosen in the early stages of this work to apply this integrator. There are, however, also three drawbacks:

1. The integrator can yield wrong results and can raise a warning, if the integration range is extending over several orders of magnitude.
2. Singularities, discontinuities or points where the integrand is not differentiable provoke wrong results together with a warning.
3. There is no easy way to parallelise the integration with `scipy.integrate.quad`.

These drawbacks are resolved or at least reduced by the following widely applicable approach.

The aim is to integrate a function $f(x)$ along x from the lower integration border b_l to the upper border b_0 with use of the `Python` function `scipy.integrate.quad`. In certain cases, this integrator raises an integration warning stating that `"the integral is probably divergent, or slowly convergent"`. Additionally, in some cases an obviously wrong result is returned. This error occurs, if the integration range is stretching over several orders of magnitude and/or if the integrand $f(x)$ is not differentiable at one or several points. This is e.g. the case for the integration of the ADAF spectrum (see section 2.1.2.2), which extends over about ten orders of magnitude with kinks at the transitions of the various spectral contributions.

To prevent this warning and to eliminate or reduce the error, the integral from b_l to b_0 is split into a sum of n integrals along the integration range:

$$\int_{b_\mathrm{l}}^{b_0} f(x)\,\mathrm{d}x = \sum_{i=1}^{n} \int_{b_i}^{b_{i+1}} f(x)\,\mathrm{d}x \tag{4.1}$$

It is $b_1 = b_\mathrm{l}$ and $b_{n+1} = b_0$. Every part integral with a correspondingly shorter integration range is then integrated with `scipy.integrate.quad` and after the numerical integrations, the sum of the results of the part integrals is determined to obtain the result of the whole integral of interest. This procedure is called the ISA.

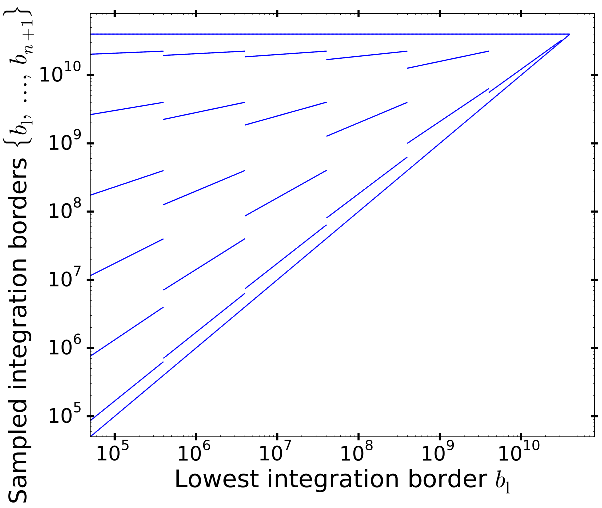

Figure 4.1: Example of spacing of sampled integration borders using `SampleIntegrationBorders11`. Here, it is $b_0 = 4 \cdot 10^{10}$ and b_l is plotted on the x-axis. On the y-axis, all sampled integration borders b_i are shown.

The result of the integral and whether a warning is raised or prevented, depends sensitively on the spacing of the values b_2 to b_n along x. An approximately logarithmic spacing is found to be reasonable for all cases of use in this work. The functions `SampleIntegrationBorders` defined in `part1` are taylored for this purpose. For example, `SampleIntegrationBorders11` is used for the ISA of Q_PP. For this case, the spacing of the integration borders is shown in figure 4.1. In this spacing, n increases about logarithmically with the difference between b_l and b_0. The integration part ranges $[b_1,\, b_2]$ and $[b_n,\, b_{n+1}]$ (ranges at the borders of the whole range) are shorter than the part ranges in the central part of the whole range. This is advisable as the integrand has substantial variations near the borders of the whole range, especially slightly above b_1. Making the part ranges arbitrarily small yields, however, a loss in computational efficiency.

By applying the ISA, drawback 1 is mitigated due to the shorter part integration ranges. Drawback 2 can also be resolved, if one includes all points where the integrand is not differentiable into the list $\{b_1,\, \ldots,\, b_{n+1}\}$ provided the respective point is located in between of b_l and b_0. This is exemplarily illustrated for the case of the normalised spectral PP probability, which is

$$\frac{2\,P(x_\gamma,\gamma)}{\frac{1}{T_{\mathrm{esc\,ph}}(x_\gamma)} + \int_{\gamma_{\mathrm{PP,\,min}}(x_\gamma,x_0)}^{\gamma_{\mathrm{PP,\,max}}(x_\gamma,x_0)} P(x_\gamma,\gamma')\,\mathrm{d}\gamma'}. \tag{4.2}$$

This term is part of the integrand of Q_PP (see equation 3.34), which is integrated along x_γ. One can realise that this term can have kinks at certain values x_γ.

First, remember from section 3.1.2 that for given γ and given x, the function $P(x_\gamma,\gamma)$ is zero below $x_\gamma = x_{\gamma,\mathrm{th}}(\gamma,x)$. If $n_0(x)$ is a continuous function non-zero up to x_0, then the lower cutoff of P is located at $x_{\gamma,\mathrm{th}}(\gamma,x_0)$. If $n_0(x)$ is a discrete spectrum, e.g. a set of δ_Dirac peaks at values x_i, then P is comprised of various contributions. Each δ_Dirac peak of n_0 causes one contribution with a lower cutoff at $x_{\gamma,\mathrm{th}}(\gamma,x_i)$. These lower cutoffs of the contributions to P cause kinks in P and in

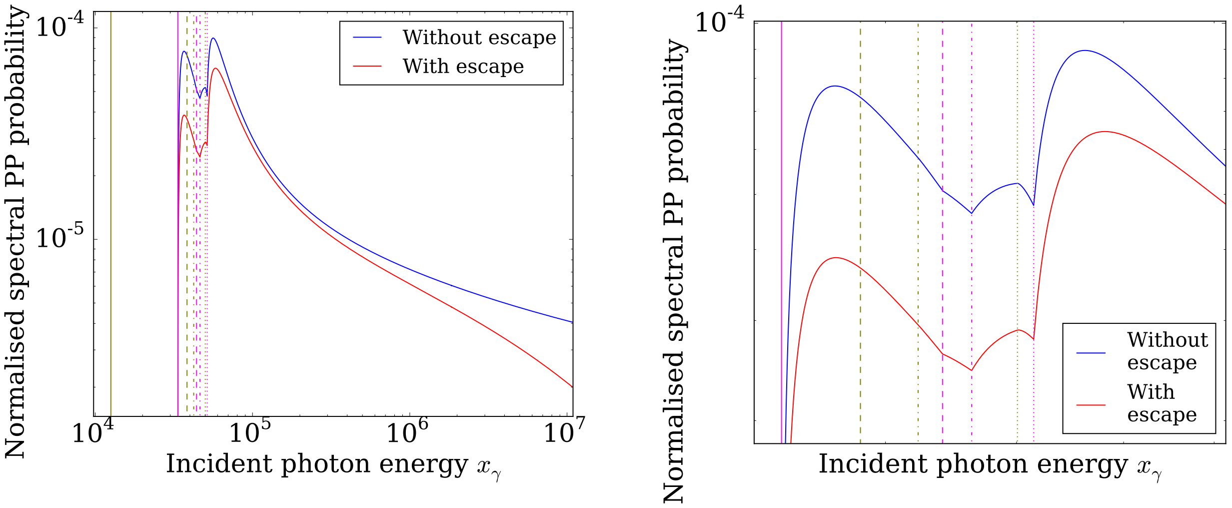

Figure 4.2: Exemplary plot of the normalised spectral PP probability for $\gamma = 3 \cdot 10^4$ and for n_0 as defined in equation 5.6. Plotted is in both panels the normalised spectral PP probability (expression 4.2 as the red line and expression 4.2 without the escape term in the denominator as the blue line) versus the energy x_γ. The pink, grey thin lines mark the values $x_\gamma = x_{\gamma,\mathrm{th}}(\gamma, x_i)$, the values $x_\gamma = 1/x_i$, respectively. The kinks due to the He II Lyman α line, the H Lyman series, the H Lyman β line, the H Lyman α line are marked by solid, dashed, dash-dotted, dotted line styles, respectively. The right-hand side panel is a zoom into the left-hand side panel.

expression 4.2. Therefore the values $x_{\gamma,\mathrm{th}}(\gamma, x_i)$ have to be specified as integration borders b_i in the ISA when Q_{PP} is to be correctly determined.

Second, consider the spectral pair-absorption rate (the second summand in the denominator of expression 4.2). It is zero, if $\gamma_{\mathrm{PP,\,max}}(x_\gamma, x_0) = \gamma_{\mathrm{PP,\,min}}(x_\gamma, x_0)$. This is the case at the PP threshold $x_\gamma = 1/x_0$. For smaller x_γ, the pair-absorption rate is vanishing. Now, let n_0 again be a set of discrete peaks at x_i, instead of being continuous. Then, P is again a sum of various contributions due to every peak in n_0. Consequently, the pair-absorption rate gets an additional contribution at every $1/x_i$. Each contribution is non-zero only above $x_\gamma = 1/x_i$ (see figure 5.3, where the spectral pair-absorption rate is shown exemplarily as a function on x_γ by the lilac line and its four contributions due to four discrete emission lines at the energies x_i are shown by the orange lines). Therefore, these values should also be included into the list of integration borders of Q_{PP}.

An exemplary course of the normalised PP probability with the kinks visible at $x_{\gamma,\mathrm{th}}(\gamma, x_i)$ and at $1/x_i$ in the case of n_0 being a set of four discrete lines is shown in figure 4.2. If the normalised PP probability (or any function that involves the normalised PP probability) is integrated along x_γ, these kinks have to be given as integration borders of the ISA, if they are located in the integration range.

This type of consideration is performed in every integration along the code. By applying the ISA and inclusion of all points where the integrand is not differentiable into the list $\{b_1, \ldots, b_{n+1}\}$ of integration borders, drawback 2 is resolved, too. Drawback 3 will partly be relaxed by multi-core implementation, which is outlined in section 4.4.

4.3 The Iterative Scheme

After being able to determine all integrations correctly, the goal is now to solve equation 3.40 by an iterative scheme and to yield steady-state solutions of $N(\gamma)$. At the end of `part4`, the iteration is prepared and it is executed in `part5`. Both of the following schemes as well as several auxiliary functions are defined in the second half of `part5`.

4.3.1 Scheme 1: Iteration as a Whole

In an early stage of this work (Wendel et al., 2017), the following iteration scheme was applied. The index j counts the iteration steps. During each iteration step, N is determined along the range of γ. At the beginning of the first iteration step, the range of γ along which the kinetic equation is to be solved is discretised into κ_0 values $\gamma_{k,\,0}$, where $k \in \{1, \ldots, \kappa_0\}$. The sequence of these sampling points is written as $(\gamma_k)_0$. Then, a starting course of $N(\gamma)$ called $N_{\mathrm{init}}(\gamma)$ is prescribed. The sequence containing the corresponding values at the sampling points is written as $(N_k)_0$. In the first step of the iteration, a new sequence $(\gamma_k)_1$ of κ_1 sampling points is compiled. Then one computes and assigns $N_{k,\,1} = \mathcal{F}((N_k)_0, \gamma_{k,\,1})$ for every k. In other words, $\mathcal{F}$ is determined with usage of $(N_k)_0$ at every point $\gamma_{k,\,1}$ and the respective result is the value of N at $\gamma_{k,\,1}$, namely $N_{k,\,1}$. When all $N_{k,\,1}$ have been determined, this iteration step is finished and one has obtained the sequence $(N_k)_1$.

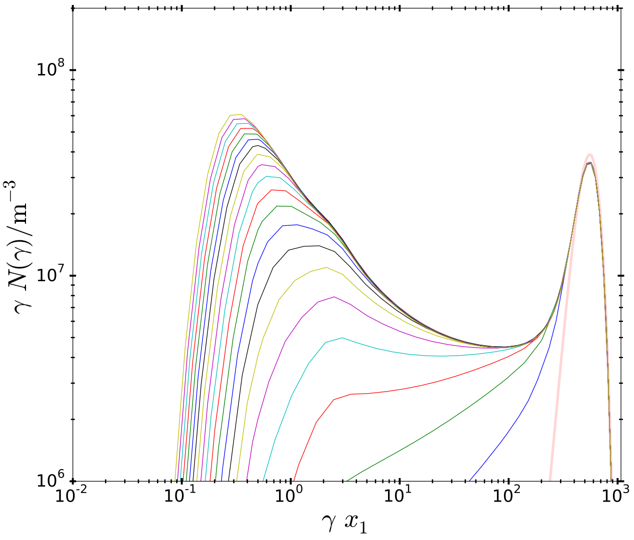

Figure 4.3: Demonstration of iterative scheme 1: EED of the IC pair cascade in Mrk 501 as described in chapter 5, compare also figure 5.2. Plotted is $\gamma\,N(\gamma)$ (the electron spectral energy density) versus $\gamma\,x_1$ (the Lorentz factor multiplied with the energy of the highest energetic emission line). The function N_{init} used as initialisation ($j = 0$) is drawn as the transparent rose line. The thin coloured lines show N for $j \in \{1, \ldots, 20\}$ (from bottom to top). The iteration was aborted after the 20. iteration step due to slow convergence.

This technique is repeated in the subsequent steps. In every iteration step a new sequence of κ_j sampling points $\gamma_{k,\,j}$ is determined as well as a new sequence of values of N is computed. The value of N at the k-th sampling point after the j-th iteration step is briefly written as $N_{k,\,j}$. In the j-th iteration step, the sequence $(N_k)_j$ is yielded via $N_{k,\,j} = \mathcal{F}((N_k)_{j-1}, \gamma_{k,\,j})$. The j-th iteration step uses the knowledge of the sequence $(N_k)_{j-1}$ of the iteration step $j-1$. The index j runs along $0, 1, 2, \ldots, j_{\mathrm{final}}$ until an appropriate convergence criterion is met after the j_{final}-th iteration step, finalising the iteration. With this iteration scheme, it is advisable to choose a small κ_j (few sampling points) for small j and to raise κ_j (make the grid denser) with increasing j. The borders of the evaluation range are however kept fix, i.e. all $\gamma_{1,\,j}$ (lowest Lorentz factor) are equal and can be chosen by the user (as long as the assumptions from section 3.2.1 are satisfied) and all $\gamma_{\kappa_j,\,j} = \gamma_0$ (highest Lorentz factor) are determined via the equations 3.41c, 3.42c or 3.43c.

For the scenario and the parameters described in chapter 5, the iteration results achieved with this scheme are shown in figure 4.3. In the KN regime, convergence is reached after very few iteration steps, but the lower γ is, the more steps are necessary until N converges. Reaching convergence along the whole range of γ would necessitate substantially more iteration steps. For the resulting runtime of this iteration scheme, see section 5.3. It is shown now, why this scheme is computationally inefficient. To see this, the following has to be recognised:

1. - First, inspect the second summand of the numerator of equation 3.33. It is immediately obvious that in order to evaluate this term at a certain $\gamma_{k',\,j}$, the function N has to be evaluated only at bigger values of γ (because the lower integration border is $\gamma_{k',\,j}$). Hence, to evaluate this term, knowledge about N at values $\gamma < \gamma_{k',\,j}$ is not necessary.

   - Second, inspect $\dot{n}_{\gamma,\,\mathrm{IC}}$ (the second summand in the round brackets in equation 3.34). Realise that in order to evaluate this term at a certain x_γ, the function N has to be evaluated only at values $\geq \gamma_{\mathrm{IC,\,th}}(x_\gamma, x_0)$ (because this is the lower integration border).

Hence, to evaluate this term, knowledge about N at values $x_\gamma < \gamma_{\mathrm{IC,\,th}}(x_\gamma, x_0)$ is not necessary.

- Third, remember from section 3.1.1 that $\gamma_{\mathrm{IC,\,th}}$ decreases with decreasing x_γ. Therefore, to evaluate Q_{PP} (defined in equation 3.34 and appearing in equation 3.33) at a given $\gamma_{k',\,j}$, the function N has to be evaluated only at values $\geq \gamma_{\mathrm{IC,\,th}}(x_{\gamma,\,\mathrm{th}}(\gamma_{k',\,j}, x_0), x_0)$ (because $x_{\gamma,\,\mathrm{th}}(\gamma_{k',\,j}, x_0)$ is the lower integration border). Hence, to evaluate Q_{PP}, knowledge about N at values $\gamma < \gamma_{\mathrm{IC,\,th}}(x_{\gamma,\,\mathrm{th}}(\gamma_{k',\,j}, x_0), x_0)$ is not necessary.
- Fourth, remember from sections 3.1.1 and 3.1.2 that it is always $x_{\gamma,\,\mathrm{th}}(\gamma_{k',\,j}, x_0) > \gamma_{k',\,j}$ and $\gamma_{\mathrm{IC,\,th}}(x_\gamma, x_0) > x_\gamma$. Then, one can write

  $$\gamma_{\mathrm{IC,\,th}}(x_{\gamma,\,\mathrm{th}}(\gamma_{k',\,j}, x_0), x_0) > \gamma_{\mathrm{IC,\,th}}(\gamma_{k',\,j}, x_0) > \gamma_{k',\,j}. \tag{4.3}$$

  Thus, one can infer that to evaluate $Q_{\mathrm{PP}}(\gamma)$ at a given $\gamma_{k',\,j}$, the function N never has to be evaluated at values $< \gamma_{k',\,j}$.

Conclusively, it is found that an evaluation of $\mathcal{F}$ at a certain point $\gamma_{k',\,j}$ does not require knowledge about N below this $\gamma_{k',\,j}$ but only at and above this $\gamma_{k',\,j}$.

2. Furthermore, in most cases, a wider integration range makes an integration computationally more demanding. Therefore, the CPU hours needed for one evaluation of $\mathcal{F}$ increase with decreasing γ due to the more extended integration ranges (especially of Q_{PP}, see equation 3.34).

   Because of these two observations, it is evident that it is a superfluous task to iterate N at low values of $\gamma_{k,\,j}$, while N at higher values has not converged yet. The error at high $\gamma_{k,\,j}$ would lead to needless inaccuracies in the evaluation of $\mathcal{F}$ at lower $\gamma_{k,\,j}$.

3. Generally, convergence is achieved slower at lower γ. While $j_{\mathrm{final}} = 3$ or 4 suffices in the extreme KN regime, j_{final} of several hundreds can be necessary to achieve convergence in the Thomson regime. This is an effect of the energy transferred in one scattering event becoming smaller as γ decreases. Therefore, the farther the interaction happens away from the extreme KN regime, the more iteration steps are necessary. This slow convergence behaviour at low γ enforces j_{final} to be very high (typically several hundreds). This results in repeated evaluations of $\mathcal{F}$ at intermediate and high γ, even though convergence was already achieved there much earlier. Hence, lots of unnecessary evaluations of $\mathcal{F}$ are enforced at medium and high γ, ensuing in an avoidable increase in the corresponding CPU hours.

Therefore, it is reasonable to uncouple the iteration along γ and to begin iterating at high $\gamma_{k,\,j}$ until convergence is achieved, and only then switch to lower $\gamma_{k,\,j}$. This is the approach of a much more efficient scheme, described in the subsequent section.

4.3.2 Scheme 2: Pointwise Iteration

In scheme 1, a whole sequence $(N_k)_j$ of κ_j values is computed in each iteration step. A more efficient scheme is explained in the following and depicted in figure 4.4. As initialisation, a fixed grid (γ_k) of κ sampling points is defined, where γ_1 can still be chosen and $\gamma_\kappa = \gamma_0$. In contrast to scheme 1, the grid stays unchanged during the course of the iteration. Then $N_{\mathrm{init}}(\gamma)$ is prescribed and the corresponding values $N_{k,\,0}$ are determined. For every k, there is a j that is a counter for the iteration step number at this γ_k. The j-th value of $N(\gamma_k)$ at the k-th sampling point is briefly written as $N_{k,\,j}$. The sequence of the values $N_{k,\,j}$ with $k \in \{1,\, 2,\, \ldots,\, \kappa\}$ and with the maximum j at each k is written as $(N_k)_{\max}$. At each point of time during the iteration, $(N_k)_{\max}$ is the best approximation of N to the yet unknown, converged N.

The iteration proceeds as follows: First, N is iterated at the highest Lorentz factor γ_κ. Precisely, the first iteration step is $N_{\kappa,\,1} = \mathcal{F}((N_k)_{\max}, \gamma_\kappa)$ and every subsequent step is $N_{\kappa,\,j} = \mathcal{F}((N_k)_{\max}, \gamma_\kappa)$. After every step, $(N_k)_{\max}$ is updated. This proceeds until convergence of $N_{\kappa,\,j}$ is achieved. This is

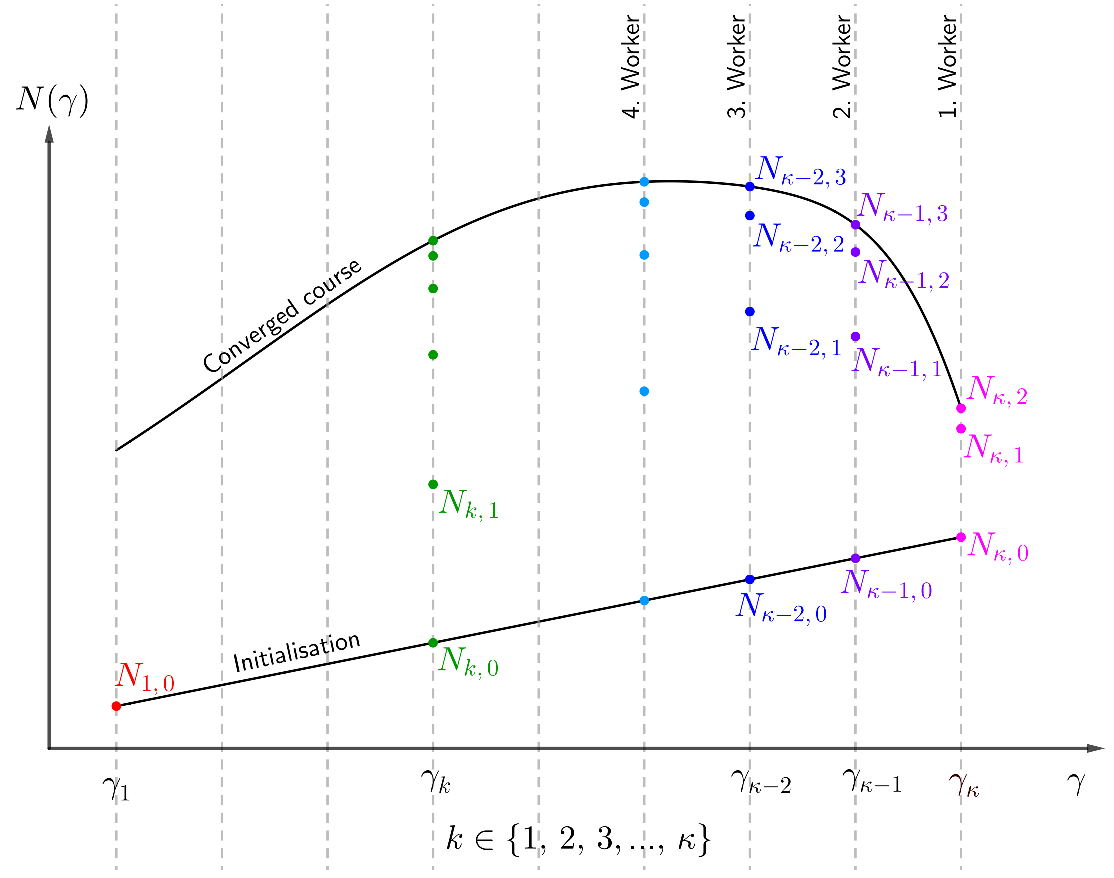

Figure 4.4: Sketch of the iteration scheme 2 to solve the electrons' kinetic equation 3.40. Plotted is the electron spectral number density N versus γ. The Lorentz factor is discretised into a total of κ values γ_k, indexed by k. It is started with iterating at $k = \kappa$, from the initialisation course of N until convergence is achieved (at $N_{\kappa,\,2}$ in this example. So, here it is $j_{\text{final},\,\kappa} = 2$). After this, it is iterated at $k = \kappa - 1$ until convergence is reached (after the iteration step $j_{\text{final},\,\kappa-1} = 3$ in this example). This goes on one k after the other (from high k downwards). If multi-core computing is applied, several workers compute in parallel. Each worker iterates at one certain k. If one worker has found convergence, it jumps to the highest k that is not processed yet and begins iterating at this sampling point.

the case if $N_{\kappa,\,j} - N_{\kappa,\,j-1}$ is smaller than a maximum error to be specified. The finally converged value of N at the k-th sampling point is called $N_{k,\,j_{\mathrm{final},\,k}}$ and the number of the corresponding iteration step is $j_{\mathrm{final},\,k}$.

After this, N is iterated at $\gamma_{\kappa-1}$. Briefly written, $N_{\kappa-1,\,j} = \mathcal{F}((N_k)_{\max}, \gamma_{\kappa-1})$ is determined and $(N_k)_{\max}$ is refreshed successively for every j at this k, until convergence is reached with the value $N_{\kappa-1,\,j_{\mathrm{final},\,\kappa-1}}$.

This proceeds for successively decreasing k. When N has converged at $k = 1$, the whole iteration is finished. Exemplary results of this iteration scheme are shown in figure 5.2 and in the left-hand side column of figure 6.3. The first big advantage of this scheme is that it is ensured that in the evaluation of $\mathcal{F}$ the converged course of N is always used. This is the case due to the finding of point 1 in section 4.3.1 and because the part of $(N_k)_{\max}$ above the certain $\gamma_{k'}$ where it is currently iterated does already contain the converged course of N. This minimises inaccuracies and therefore minimises the number of necessary iteration steps and substantially reduces the CPU hours necessary for the entire iteration. The second advantage is that at each γ_k only the minimum number of iteration steps are performed. This also reduces the total number of evaluations of $\mathcal{F}$ (in comparison to scheme 1) and correspondingly the necessary CPU hours.

4.3.3 Iterating in the Thomson Regime

As mentioned earlier, $j_{\mathrm{final},\,k}$ increases with decreasing k. More iteration steps are necessary at lower γ. On the other hand, for given x, Q_{PP} is zero at $\gamma < 1/(4x)$, because PP cannot create electrons with energies $\gamma < 1/(4x)$ (see section 3.1.2). This makes the evaluation of $\mathcal{F}$ computationally very much less expensive, because the CPU hours needed for the evaluation of $\mathcal{F}$ are dominated by Q_{PP}. Consequently, iterations below $1/(4x)$ (which is the approximate border to the Thomson regime) are substantially faster than (slightly) above $1/(4x)$. Therefore, in scheme 2 pointwise iterations as described in section 4.3.2 are also applied in the Thomson regime to determine N. For extended n_0, this border below which PP does not happen is smeared into an extended transitional range.

Pointwise iteration as described in section 4.3.2 was not used in an early stage of this work (Wendel et al., 2017). At that time, the approach by Zdziarski (1988) was pursued. For $\gamma < 1/(4x)$ (in the Thomson regime), the steady-state kinetic equation 3.28 transforms into a continuity equation in energy space with source terms represented by the injection rate and by the PP rate. This continuity equation can be solved for N. This results, however, in an additional integration of the PP rate along γ, which is computationally very expensive. This now obsolete solution of the continuity equation is implemented at the beginning of `part7`, but usage is not recommended due to inefficiency.

In an early stage of this work, N was determined in the KN regime by scheme 1 and in the Thomson regime by solving the continuity equation (Wendel et al., 2017). Both these solutions are, however, inaccurate around $1/(4x)$. Therefore, in this case, it is additionally necessary to interpolate both solutions in the transition between the Thomson and the KN regime. Such an interpolation technique is additionally implemented in `part7`, but it is obsolete due to the advantages of scheme 2.

4.4 Multi-Core Implementation

Generally, array programming makes computations more efficient, reducing the necessary CPU hours and reducing the carbon footprint (Portegies Zwart, 2020). Therefore vectorised operations with use of `numpy` arrays are applied throughout the code where possible. Additionally, it is reasonable to use logarithmic grids in most numerical computations, to prevent unnecessarily dense meshes. Despite these measures, execution of the iteration according to scheme 2 on a single CPU core takes several ten minutes for favourable input parameters and several hours for unfavourable input parameters. With respect to the needed CPU hours, n_0 is the most influential input parameter. The more extended the distribution n_0 is, the wider the integration ranges of C and P (which are the lowest level integrations in the nested integrals of equation 3.33) become, and the more CPU hours are necessary and a longer runtime ensues. To shorten the runtime by exploiting the potential of state-of-the-art CPUs, multi-core programming is implemented in the code through the `multiprocessing` (`mp`) package in two manners.

4.4.1 Multiple Workers in the Iteration

As described in section 4.3.2, in iteration scheme 2 the grid of sampling points is fixed. At each point γ_k it is iterated until convergence is achieved, starting at $k = \kappa$ and proceeding downwards. During the iteration, as soon as the latest $N_{k,\,j}$ is determined, the sequence $(N_k)_{\max}$ is updated and used for the next iteration step.

It is, however, possible to perform several iterations at different γ_k simultaneously by workers on different CPU cores, as exemplarily shown in figure 4.4 for four workers. This scheme is implemented in the code with usage of `mp.Process`, which instantiates the workers in the different CPU cores. `mp.Process` is used here instead of the easier to handle `mp.Pool` because child processes started with `mp.Process` can itself start child processes, which is done as described in the subsequent section.

A difficulty is that the workers have to be constructed such that they can communicate their results to other workers while they are still active. This is necessary because $(N_k)_{\max}$ has to be updated permanently, so that each worker can always use the best approximation of N. If this inter-process communication would not happen, it would not only be impossible to shorten the total runtime, but also the results of the pointwise iterations would be erroneous because an iteration at k' would be based on the wrong course of N at $k > k'$. To properly implement the inter-process communication, the varying data structure containing $(N_k)_{\max}$ is stored in an `mp.Manager` dictionary, which can be accessed and manipulated by the workers concurrently. The sequence (γ_k) is put into an `mp.Queue`, from which the workers retrieve the values γ_k when a new pointwise iteration is started. The `mp.Queue` and the `mp.Manager` instances as well as the conventional arguments needed by the workers have to be passed as arguments of the function `WorkerToIteratePointwise` that is evaluated by the parallel processes. The function `WorkerToIteratePointwise` running in all the child processes repeatedly retrieves the next lower γ_k from the queue and iterates at this value (via calling `IterateOnePointPointwise`) until the queue is empty (meaning that it has arrived at γ_1). The function `IterateOnePointPointwise` performs an iteration at a certain γ_k until the iteration is considered as finished through fulfilment of a corresponding criterion function `MoreIterationsNecessary`. While `MoreIterationsNecessary` returns `True`, the respective iteration is continued.

After each evaluation of $\mathcal{F}$, the result is stored in the `mp.Manager` dictionary, so that the parallel workers can build upon this. Thereby, the following caveat has to be considered. Actually, the `mp.Manager` dictionary is a dictionary of dictionaries. (This is the case to have a properly arranged and well-organised data structure.) It is, however, impossible to directly manipulate the items of the internal dictionaries via indexing. To bypass this deficiency, the internal dictionary to be manipulated has to be extracted and stored as a new dictionary. This new dictionary can then be modified, i.e. be loaded with the result of $\mathcal{F}$. After this, it is reassigned as an entry to the `mp.Manager` dictionary of dictionaries.

The function `MoreIterationsNecessary` does not only check for convergence of $N_{k',\,j}$. At first, and in any case, at least two iteration steps are performed. Then, the status of all the iterations at values $k > k'$ is checked. One or more iterations at $k > k'$ being still running, is a sufficient condition to continue the iteration at k'. As soon as all the iterations at higher k have been finished, at least one additional iteration step is done at k'. After this, several additional checks are performed, mainly concerning the accuracy of the computation of Q_{PP}. Only if all superordinate criteria are satisfied, it is checked for convergence, as described in section 4.3.2.

This parallelisation approach is, however, found to be not very efficient. The runtime does not decrease inversely proportional when the number of cores increases. The runtime with using two, three workers is only about 40 %, 47 % shorter than with using only one worker (see section 5.3), respectively. The decrease of the runtime is negligible for more than three workers. This behaviour can be understood as follows. Remember that the computation of $\mathcal{F}((N_k)_{\max}, \gamma_{k'})$ makes use of all the values of $(N_k)_{\max}$ above k'.

- For high values of k' (i.e. not far below κ), the elements of $(N_k)_{\max}$ with $k > k'$ that are still iterated by the various active workers make up the major part of the elements of $(N_k)_{\max}$ with $k > k'$. This means that the iteration at k' is almost all the time built on an inaccurate $(N_k)_{\max}$ as long as the workers at higher k are still iterating. Only if the workers at $k > k'$ have achieved convergence, the iteration at k' can achieve convergence at all. This problem is particularly severe for high k' and for a big number of parallel workers. Therefore, at high k', increasing the number of workers does not shorten the runtime.
- This issue alleviates for decreasing k'. For moderate values of k' a substantial part of the elements of $(N_k)_{\max}$ with $k > k'$ has already reached convergence at $j_{\text{final},k}$. So, the part of $(N_k)_{\max}$ at $k > k'$ already has a high degree of accuracy and consequently, the iteration at k' is built on accurate prerequisites. Hence, at intermediate k', parallelisation is reasonable.
- For still more decreasing k', the issue is exacerbated through another effect. The lower k' becomes, the nearer/deeper one comes to the Thomson regime. Here, the computation of $\mathcal{F}((N_k)_{\max}, \gamma_{k'})$ is especially dependent on those values of $(N_k)_{\max}$ with k only very slightly bigger than k' (due to the small energy transfers in the Thomson regime). As long as these values have not converged yet, the iteration at k' is using inaccurate prerequisites. Therefore, parallelisation is inefficient near/in the Thomson regime, too.

Therefore, it is not advisable to employ more than two CPU cores for the parallelised iteration. To make use of the remaining CPU cores, parallelisation is introduced at one further site in the code, described subsequently.

4.4.2 Parallelisation of Integrations

Leverage point is the function Q_{PP}, whose computation makes up the vast majority of the CPU hours needed for the computation of $\mathcal{F}$. It is therefore near to parallelise the computation of Q_{PP}, which essentially is an integration along x_γ. Parallelising an integration that is executed with `scipy.integrate.quad` can be done thanks to the ISA, which splits the integration range into shorter part ranges. These part integrals can be computed by child processes distributed to the available CPU cores. This is done with `mp.Pool`, which can instantiate asynchronous workers via `apply_async`. The respective integration borders as well as the integrand and the integrand's arguments have to be passed to the child processes. On doing so, it is not possible to pass N as an interpolated `Scipy interp1d` object. Instead, one has to take care that always only the sampling points and corresponding values are passed. Then, the interpolations to a callable function have to be performed internally by the child processes.

The decrease of the runtime by this parallelisation approach depends on the one hand on the number of available cores and on the other hand and much more sensitively on the choice of the number and the locations of the integration borders in the ISA. Also in this case, it is found that the runtime is not inversely proportional to the number of cores. Despite of thorough inspection of the integrand and proper placement of the integration borders, the reduction of the runtime when employing 32 available cores can not be pushed over 60 % with respect to only one core (see section 5.3). The reason is that some particular part integrals (usually those with strongly changing integrand) require substantially more CPU hours than most other part integrals. Dividing these CPU-hours-dominating part integrals into additional parts does not yield further reduction of the runtime.

Chapter 5

Vacuum Gap Activity in Markarian 501

In this chapter the mathematical and computational framework developed so far will be used to provide an explanation for a peculiar observational transient feature in the SED of the BL Lac object Mrk 501. The concerned observation will be addressed in section 5.1. Thereafter, the theoretical model to explain this observational feature via an electron beam inducing a cascade on emission line photons will be outlined. In section 5.3, this cascade will be computed and the simulation results will be discussed. In this chapter's fourth section, the results of the cascade simulation will be checked for consistency and arranged into the physical picture of Mrk 501 to draw consequences and inferences. Open issues will be discussed in the last section. For a concise summary of this chapter, see Wendel et al. (2021a).

5.1 Hints to a Narrow Spectral Component in Markarian 501

During a multi-wavelength campaign from March to September 2014 a two-week-long flaring period of Mrk 501 was registered in July (MAGIC Collaboration et al., 2020). The flaring state was most prominent in the X-ray regime, where the X-Ray Telescope on-board the Neil Gehrels Swift satellite detected the highest count rate ever as well as hard spectra, and in the VHE regime, covered by the Major Atmospheric Gamma-ray Imaging Cherenkov (MAGIC) telescopes, a stereoscopic system of two 17 m IACTs on the Roque de los Muchachos Observatory. All but one nightly multi-wavelength SEDs from this flaring period could be well described by an SSC scenario (MAGIC Collaboration et al., 2020).

During the night 19./20. of July 2014 (modified Julian date (MJD) 56857.98) hints to a peculiar spectral feature were detected by the MAGIC telescopes with high significance ($\approx 3\,\sigma - 4\,\sigma$). Hints to the same spectral imprint were also seen in the nights 18./19. and 20./21. of July with lower significance. The spectral feature, a narrow component centred around 3 TeV, was also present after ruling out instrumentation problems or irregularities in the data analysis in a dedicated inquiry. The narrow spectral feature was substantiated by three tests:

- Usually, the TeV spectra of blazars can be fitted with simple functions like a PL, an LP or an LP with exponential cutoff. Such standard functions could however be discarded with more than $3\,\sigma$ confidence level for the MJD 56857.98 MAGIC telescopes' spectrum.
- The VHE spectrum below 1.5 TeV was fitted by an LP, that was extrapolated to higher energies. It was found with more than $4\,\sigma$ that this extrapolation has to be rejected as a fit of the points above 1.5 TeV.
- A two-component model fit invoking a narrow LP (referred to as an eplogpar function) and a broad LP is preferred over a single LP fit at $\approx 4\,\sigma$ (for details see MAGIC Collaboration

et al., 2020). Similarly to the additional narrow LP, a Gaussian function in addition to the wide spectral component can also describe the MJD 56857.98 TeV spectrum.

Hints to similar narrow TeV components inconsistent with standard fitting functions have been found earlier in Mrk 501, but with lower significance (Abdo et al., 2011; Ahnen et al., 2017b; Ahnen et al., 2018). Four suggestions were brought forth as possible theoretical explanations for such a narrow TeV bump:

- The MAGIC Collaboration et al. (2020) provided the following scenario. Two temporally separated, mono-energetic injection periods, escape, radiative cooling and stochastic particle acceleration in a single emission region were assumed. It was found that a pileup of electrons around a certain equilibrium energy ensues (provided the respective timescales are appropriately dimensioned) and that a narrow EED (described by a relativistic Maxwellian that is attached to a PL turning into an LP) is created, which is responsible for the narrow SED feature. This model has two deficiencies: First, it cannot make statements about the origin of the injected electrons and it does not give a reason how the injection energy $\gamma \approx 10^4$ can be motivated. Second, from the parameters used for this model, one can infer that this emission region must be distinct from the SSC emission region. For example, the Doppler factors, the particle densities or the implemented processes are different in both models. Then, however, the authors give no reason why during all the July 2014 nights except MJD 56857.98 the SSC region is emitting, whereas on MJD 56857.98 the SSC region is switched off and instead the pileup emission region is active.

- A similar explanation was developed by Hu and Yan (2021). Setting up a Fokker-Planck equation and incorporating injection, escape, stochastic acceleration, shock acceleration, diffusion in energy space, electron cooling (via synchrotron radiation and IC scattering), synchrotron self absorption and pair absorption, the time-dependent EED in a single, relativistically moving emission region was numerically determined. It was found that for certain conditions (and for two temporally separated injection episodes) a peculiar EED forms that has basically two parts: One wide PL hump at lower energies and one sharp, peaky part at higher energies, which is called pileup part. This pileup part forms only if particle escape is inefficient and only if shock acceleration dominates over stochastic acceleration. This later condition is opposing to the above-mentioned pileup model by the MAGIC Collaboration et al. (2020), where only stochastic acceleration was implemented. Hu (2022) argues that the strong curvature of the LP EED used by the MAGIC Collaboration et al. (2020) is not reconcilable with a self-consistent treatment of stochastic acceleration, electron cooling and escape.

  In the scenario by Hu and Yan (2021), the synchrotron photons emitted by the PL EED part are IC up-scattered by the pileup electrons and form the narrow 3 TeV feature. Also the other nightly SEDs can be explained within this model with adjusted parameters and especially with single electron injection. A drawback of this model is that the authors do not provide a natural motivation for the origin of the seemingly fine-tuned injection times and durations necessary to explain the transient 3 TeV bump.

- Furthermore, a two-zone SSC scenario was applied by the MAGIC Collaboration et al. (2020). It invokes a large SSC region with low particle density and low D and a small SSC region (which is either co-spatial to the large region or spatially separated from it) with higher density and higher D. The small emitting region can be interpreted as a minijet in a jet-in-a-jet scenario (see section 2.4.6). It is found that the SSC emission from the large zone creates the broadband two-hump SED and that the SSC emission from the small zone causes the bump at 3 TeV. The disadvantages within this scenario are that first the large SSC region needs parameters slightly different than during the other nights of the flaring period and second that the small region needs a very narrow PL EED, whose origin is not addressed by the authors.

- The fourth explanation was presented by the MAGIC Collaboration et al. (2020) and in detail by Wendel et al. (2021b). It is the subject of this work and will be elucidated in the following.

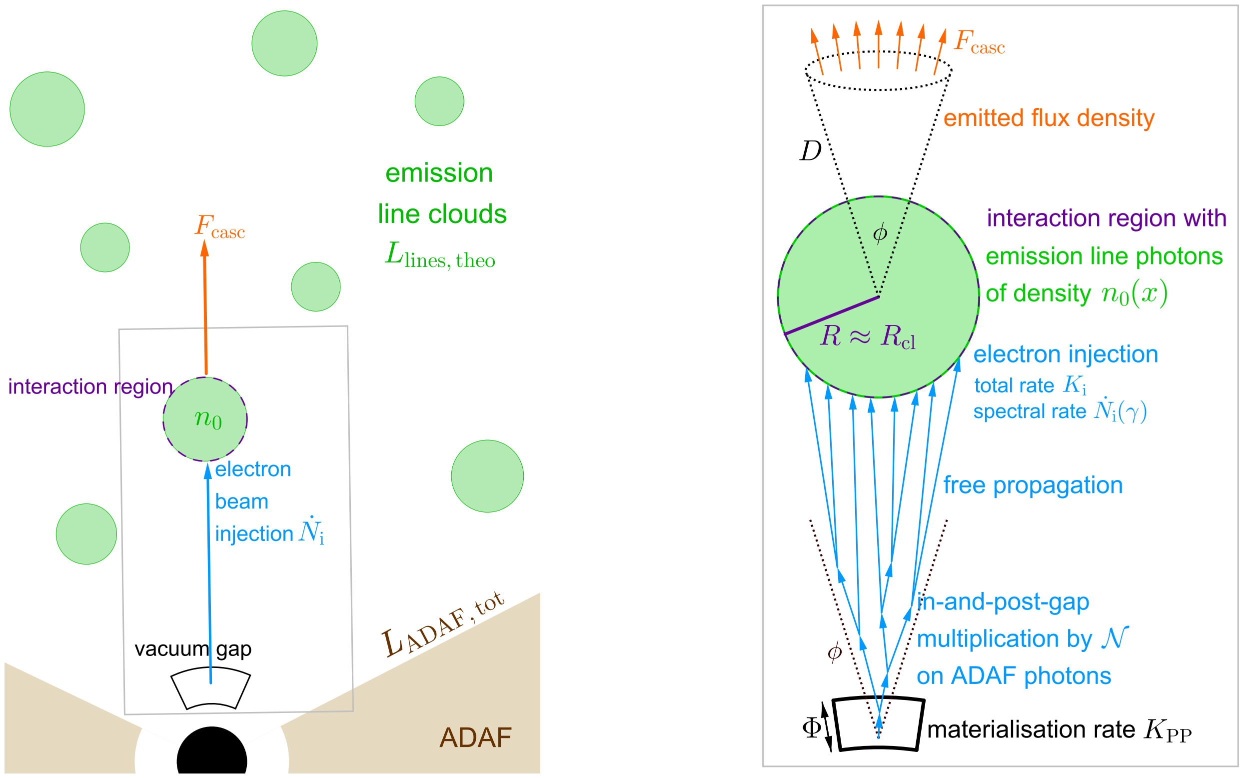

Figure 5.1: Depiction (not to scale) of the cascade model, developed to explain a narrow spectral feature in Mrk 501. The conventional SSC emitting region is thought to be located farther downstream the jet and therefore not seen in this figure. Left panel: Schematic illustration of the inner region (sub-pc scale) of Mrk 501. Right panel: Zoom into the grey box of the left panel.

5.2 Description of the Modelled Physical Setting

First, it is assumed that like on every night of the July 2014 flaring period, the SSC region is also emitting during the night MJD 56857.98. This provides an explanation of the broadband SED.

Second, to provide an explanation for the narrow bump, the model depicted in figure 5.1 and explained henceforth is applied.

Around the central SMBH of Mrk 501, an ADAF of temperature T_{e} and accretion rate $\dot{m}$ is present. All relevant quantities like the spectral luminosity, the spectral number density and the total number density are behaving according to the equations given in sections 2.1.2.2 and 2.5. The ADAF is a copious photon emitter, with two effects described in the subsequent sections.

5.2.1 An Electron Beam from a Vacuum Gap

The ADAF supplies the magnetosphere with gamma-ray photons. These photons self interact and produce electron positron pairs. The total number density of such photons above the PP threshold is given by equations 2.18 and 2.19. The resulting materialisation rate of electron positron pairs in the magnetosphere can be approximated by

$$K_{\mathrm{PP}} = 0.2\,\sigma_{\mathrm{T}}\,{n_{\mathrm{PP}}}^2\,c \qquad (5.1)$$

(e.g. Levinson and Rieger, 2011). Here, the number density n_{PP} of photons capable to undergo PP is realised either by $n_{\mathrm{PP,\,1}}(M_{\mathrm{BH}}, \dot{m}, T_{\mathrm{e}})$ or by $n_{\mathrm{PP,\,2}}(M_{\mathrm{BH}}, \dot{m})$. The PP cross section was approximated by its value $0.2\,\sigma_{\mathrm{T}}$ around the maximum.

It is furthermore assumed that a vacuum gap is open and located near the poles of the magnetosphere. The potential drop Φ of the active gap accelerates intruding charge carriers to relativistic energies. Especially, the electrons created via PP are accelerated to a maximum energy $\approx e\,\Phi$ and travel along the magnetic field lines away from the BH.

By this, an electron beam with opening angle ϕ is formed in the gap and directed approximately along the BH spin axis. As soon as the electrons have been accelerated to relativistic energies, they begin to emit synchro-curvature radiation as well as IC radiation. The latter is the result of scattering events on the ADAF photons, which are the dominating target photons in the very inner portion of the AGN. The produced gamma rays also interact with the ADAF photons and pair produce a next generation of electrons (Broderick and Tchekhovskoy, 2015; Chen and Yuan, 2020). This cascade takes place in and immediately behind the gap and it is therefore called in-and-post-gap cascade in the following. (As the exact magnetic field topology as well as the angular distribution of the anisotropic ADAF photon field is unknown in the framework of this model, this cascade cannot be treated with the measures developed in chapter 3 and is therefore only considered in a simplified way.) The in-and-post-gap cascade ceases as soon as curvature radiation emission ceases and as soon as the collision angles between the beam particles and the ADAF photons become so small (glancing collisions) that the PP threshold condition is not satisfied any more. It is assumed that during this in-and-post-gap cascade, the seed electrons are multiplied by the number $\mathcal{N}$. Meanwhile, the energy of one seed electron is distributed to all its child electrons. The rate of child electrons per unit volume is

$$K_\mathrm{i} = K_\mathrm{PP}\,\mathcal{N}. \tag{5.2}$$

and their maximum energy is $e\,\Phi/\mathcal{N}$. This electron beam propagates away from the AGN centre for several tens or hundreds of r_S. It is assumed that the beam of child electrons propagates until it encounters another region that is pervaded by a field of target photons, see section 5.2.2. In this region, another IC pair cascade will evolve. The electrons from the beam are injected into this interaction region and initiate this cascade. Therefore, they are henceforth designated as injected electrons.

In a realistic case, the injected electron distribution will not be mono-energetic. Therefore, as a first-order approximation, the spectral injection rate of electrons per unit volume is assumed to be a Gaussian function. Precisely, it is used

$$\dot{N}_\mathrm{i}(\gamma) = \begin{cases} \frac{K_\mathrm{i}}{\varsigma\sqrt{2\pi}} \cdot \exp\left(-\frac{(\gamma-\gamma_\mathrm{mean})^2}{2\,\varsigma^2}\right) & \text{if } \gamma_{\mathrm{i},1} \leq \gamma \leq \gamma_{\mathrm{i},0}, \\ 0 & \text{otherwise.} \end{cases} \tag{5.3}$$

This is a Gaussian around the mean Lorentz factor γ_mean with width ς. It has a lower cutoff at $\gamma_{\mathrm{i},1} = \gamma_\mathrm{mean} - 3.0\,\varsigma$ and an upper cutoff at $\gamma_{\mathrm{i},0} = \gamma_\mathrm{mean} + 3.0\,\varsigma$. Here, the factors 3 are chosen such that on the one hand the discontinuities in $\dot{N}_\mathrm{i}$ at the cutoffs are far away from γ_mean and on the other hand that the conditions $\gamma_{\mathrm{i},1} \gg 1$ and $\gamma\,x > 1$ (see section 3.2.1) are still satisfied for realistic values of γ_mean and ς. As mentioned above, the upper energy cutoff should be equal to the maximum energy. Therefore it is set

$$\gamma_{\mathrm{i},0}\, m_\mathrm{e} c^2 = e\,\Phi/\mathcal{N}. \tag{5.4}$$

Notice, too, that the Gaussian is normalised such that the total injection rate is indeed $\approx K_\mathrm{i}$ (up to what is neglected below $\gamma_{\mathrm{i},1}$ and above $\gamma_{\mathrm{i},0}$).

5.2.2 Emission-Line Photons from an Ionised Cloud

The second effect of the ADAF is the following. It acts as an illuminator of the BLR-like surroundings. Due to its BL Lac nature, Mrk 501 does not show a pronounced BLR. Even though, there might be gas clouds abundant in the host galaxy centre and surrounding the AGN. Such clouds can result from interstellar hydrogen and helium gas (Wilms, Allen and McCray, 2000) brought to collapse by minor galaxy merger events. When such gas clouds migrate to the AGN centre, they are photo-ionised by Mrk 501's ADAF radiation and act similarly to a BLR (see section 2.1.4). As an effect of de-excitation the clouds emit atomic lines, of which the Lyman α line has indeed been observed (see section 2.4.3.2). Expressed quantitatively, the ADAF has a total luminosity $L_{\mathrm{ADAF,\,tot}}(\dot{m}, T_\mathrm{e})$ (see

i	Designation of line	Wavelength λ_i/nm	Relative contribution $K_{\mathrm{line},\,i}$ to flux density
1	Helium II Lyman α	30.5	2.00
2	Hydrogen Lyman series	93.0	0.17
3	Hydrogen Lyman β	102.6	0.57
4	Hydrogen Lyman α	121.5	5.40

Table 5.1: The four emission lines that are taken into account in compiling the soft target photon distribution. The coefficients $K_{\mathrm{line},\,1}$ and $K_{\mathrm{line},\,2}$ are adopted from Abolmasov and Poutanen (2017), while $K_{\mathrm{line},\,3}$ and $K_{\mathrm{line},\,4}$ stem from Pian, Falomo and Treves (2005).

section 2.1.2.2). A fraction ξ (see section 2.1.4) of this luminosity is reprocessed by the gas clouds into emission lines of luminosity

$$\xi\, L_{\mathrm{ADAF,\,tot}}(\dot{m}, T_{\mathrm{e}}). \tag{5.5}$$

It is assumed that N_{cl} ionised gas clouds with a mean radius R_{cl} are present in Mrk 501 and that each cloud emits line photons. The number N_{cl} of clouds can be estimated as follows. On the one hand, there must be more than one cloud. This is the case, because a single cloud revolving around the central object cannot accomplish the broad emission line profile. The lines are broadened because the rest-frame lines of a substantial number of revolving clouds are Doppler-shifted and superposed (see section 2.1.4). On the other hand, Mrk 501 is a BL Lac object and as such it might be an evolved AGN quite starved in gas supplies (see section 2.4.1). Consequently, the BLR might only be sparsely populated by gas clouds. To reconcile these two constraints, it is assumed $N_{\mathrm{cl}} = 10$ in the following.

The spectral number density of emission line photons near a cloud is described via a set of four Delta functions located at dimensionless emission line energy x_i:

$$n_0(x) = K_{\mathrm{lines}} \cdot \sum_{i=1}^{4} \frac{K_{\mathrm{line},\,i}}{x_i} \cdot \delta_{\mathrm{Dirac}}\,(x - x_i) \tag{5.6}$$

The conversion of the emission line wavelengths is $x_i = h_{\mathrm{Pl}}/(\lambda_i\, m_{\mathrm{e}}\, c)$. The parameter K_{lines} is a measure for the number density of all the line photons. And while the numbers $K_{\mathrm{line},\,i}$ describe the i-th line's relative energy flux density contributions, the numbers $K_{\mathrm{line},\,i}/x_i$ determine the i-th line's relative number density contributions. Consequently,

$$n_{\mathrm{line},\,i} = K_{\mathrm{lines}} \cdot \frac{K_{\mathrm{line},\,i}}{x_i} \tag{5.7}$$

determines the total number density of photons of the i-th emission line and the total emission line number density is

$$n_{\mathrm{lines}} = K_{\mathrm{lines}} \cdot \sum_{i=1}^{4} \frac{K_{\mathrm{line},\,i}}{x_i}. \tag{5.8}$$

The four emission lines taken into account are the prominent lines listed in table 5.1. In this table, the lines' wavelengths are given as well as the strengths $K_{\mathrm{line},\,i}$, that are adopted from spectroscopic observations of blazars in the UV by Pian, Falomo and Treves (2005) as well as from the synthetic BLR spectra compiled by Abolmasov and Poutanen (2017) with the photo-ionisation code Cloudy. Notice that in this case it is $x_1 = x_0$ because the 1st line (the He II Lyman α line) is the highest energetic component of n_0. Furthermore, do not confuse the symbol x_1 with $x_{\mathrm{l}} = x_4$.

Equations 5.7 and 5.8 are describing the respective number densities in or very near to the ionised gas clouds. The ensemble of all the clouds is responsible for the AGN's broad emission line luminosity. So, from the number of clouds, from their typical radius and from equation 5.7, the luminosity emitted by Mrk 501 in the emission line i is obtained by

$$L_{i,\,\mathrm{theo}} = N_{\mathrm{cl}} \cdot 4\pi R_{\mathrm{cl}}^2 \cdot n_{\mathrm{line},\,i}\, x_i \cdot m_{\mathrm{e}} c^3 \tag{5.9}$$

and the total emission line luminosity is determined by

$$L_{\text{lines, theo}} = N_{\text{cl}} \cdot 4\pi R_{\text{cl}}^2 \cdot \sum_{i=1}^{4} K_{\text{lines}}\, K_{\text{line},\, i} \cdot m_{\text{e}} c^3. \tag{5.10}$$

Now, there are two expressions for the total emission line luminosity, equation 5.10 and expression 5.5, which therefore can be set equal:

$$L_{\text{lines, theo}} = \xi\, L_{\text{ADAF, tot}}(\dot{m}, T_{\text{e}}) \tag{5.11}$$

Now, the key assumption is that one such cloud moves near the electron beam emanating from the magnetosphere. In this case, the relativistic electrons penetrate into the emission line photon field of this cloud and the electrons interact with the soft target photons to initiate and sustain an IC pair cascade. Such an encounter of the electron beam with an obstacle (may it be an emission line cloud or a stellar envelope) is not implausible. It can be speculated that it actually is the cause of Mrk 501's observed jet bending (see section 2.4.3.2).

This cascade is assumed to happen in a region of typical size R. Therefore, equations 3.46 are valid, but additionally it is assumed that the radial size and the escape timescales are independent of the energies. Thus it is $T_{\text{esc e}} = T_{\text{esc ph}} = R/c$. This radial size of the interaction region should be equal or at least comparable to the size R_{cl} of the emission line photon field of one gas cloud, because the cascade cannot proceed outside of the target photon field. Therefore,

$$R \approx R_{\text{cl}} \tag{5.12}$$

has to be verified later.

The electron beam's opening angle is ϕ and the beam penetrates into the cascade region in outward direction (away from the AGN centre). Due to the prescription $1 \ll \gamma$, the IC scattering kinematics, the PP kinematics guarantee that the resulting HE photons, electrons are directed nearly parallel to the incident electron direction, the incident HE photon direction, respectively. Therefore, it is valid to set the electron beam's opening angle equal to the opening angle (used in equation 3.45) of the emerging gamma-ray photon beam, and denote both angles with the same ϕ.

In the cascade, the energy injected by the electrons is reprocessed into electrons with lower energy as well as into gamma-ray photons. In steady state, this scenario can be described by the kinetic equations developed in chapter 3. The electrons from the gap are identified with the injected electrons and the emission line photons represent the LE background photons. The task is to solve the cascade equations (as explained in chapter 4) and to check whether the emerging gamma rays can explain the observed narrow 3 TeV component.

As outlined in section 3.2.2, in order to specify the physical setting of the cascade (equation 3.39) it is also necessary to specify $\dot{n}_{\gamma,\,\text{i}}$. This quantity is obviously vanishing in the present scenario because only the relativistic electrons but no HE photons are injected into the interaction region with the emission line photons. Hence it is used $\dot{n}_{\gamma,\,\text{i}}(x_\gamma) = 0$.

For the soft target photons of the cascade, only the emission line photons (which essentially are reprocessed ADAF photons) but not the ADAF photons themselves are taken into account. It is instructive to proof the validity of this assumption via a geometrical reasoning. The ionised cloud might emit the line photons approximately isotropically. Therefore, the angular distribution of the line photons in the interaction region is isotropic, too. Consequently, the collision angles between the electron beam and the line photons should be equally distributed, with mean collision angle 90°. The situation is different for ADAF photons, because the photon source is around the jet base in this case, whereas the interaction region is above the jet base. The electrons and the ADAF photons would meet in glancing collisions with an average collision angle $< 90°$. Hence, in this case the interaction rates and the photon energies in the electron rest frame were reduced in comparison to the case with emission line photons. As a result, the ADAF photons can be neglected as target photons in the cascade considered.

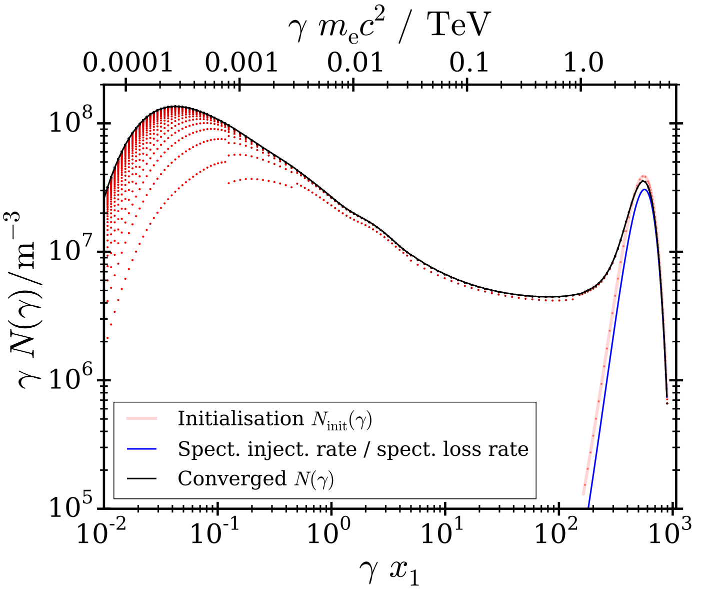

Figure 5.2: Steady-state EED of the IC pair cascade in Mrk 501, determined by iterative scheme 2. Plotted is $\gamma\, N(\gamma)$ (the electron spectral energy density) versus $\gamma\, x_1$ (the Lorentz factor multiplied with the energy of the highest energetic emission line, which is the He II Lyman α line, here). The function N_{init} used as initialisation for N is drawn as the transparent rose line. It is an approximation of the blue line, which is $\dot{N}_{\mathrm{i}}$ divided by the spectral loss rate. The points of the iteration are plotted as red dots. The converged course of N is drawn in black.

For completeness it should also be mentioned, that the interaction rates from equations 3.1.1 and 3.1.2 are valid only for isotropically distributed interaction angles and only for $x \ll 1$, which is hardly satisfied for ADAF spectra. So, if ADAF photons were to be used, one might have to use interaction rates, that are angle-dependent and not restricted to LE photons, increasing the computational effort in the solution of the kinetic equations.

To summarise, the setting is determined by the following parameters: The distance to Mrk 501 as well as the SMBH mass are fixed (see section 2.4.3.2). The accretion flow properties are then determined by the free parameters T_{e} and $\dot{m}$. The reprocessing fraction ξ is a parameter that will be assigned to two alternative values in advance. Afterwards, the model will be checked for contradictions to the choices of ξ. The quantities $K_{\mathrm{line},\,i}$, ξ and K_{lines} describe the soft photon field, but only the latter parameter is a free parameter, as the $K_{\mathrm{line},\,i}$ are chosen from the literature. The electron injection rate is specified by the free parameters K_{i}, γ_{mean} and ς. The latter two quantities fix the value of $\gamma_{\mathrm{i},\,0}$. The accretion flow parameters also fix K_{PP}. Then equation 5.2 determines $\mathcal{N}$ and equation 5.4 determines Φ, which has to be checked for plausibility. Furthermore, the geometric quantities R and ϕ are free to choose. So, T_{e}, $\dot{m}$, K_{lines}, K_{i}, γ_{mean}, ς, R and ϕ are treated as parameters free within sensible borders.

5.3 Results of the Modelling

Now, the multi-wavelength SED from MJD 56857.98 is fitted within the model described in the previous section. It is expected (from test simulations) that the cascaded emission is negligible around and below several GeV. This is because photons and electrons escape before being reprocessed to the MeV regime. Therefore, the entire SED below the VHE regime has to be due to the SSC emission from the region that is also emitting during all other nights of the flaring period. This SSC fitting was done by the MAGIC Collaboration et al. (2020) with a conventional SSC model (Tavecchio, Maraschi and Ghisellini, 1998) using a broken PL as EED. The fitting parameters are listed in table 5.2 and are very similar to the values of the other nightly SEDs. Hence, no extreme assumptions are necessary for the SSC model. The resulting flux density F_{SSC} is shown as the grey dash-dotted line in figure 5.5.

The steady-state IC pair cascade evolving through the interaction of the electron beam with the emission line photons is treated now as described in chapter 3 with the specifications from section 5.2. The ensuing kinetic equations are solved according to the approach of chapter 4, $N(\gamma)$ and $n_\gamma(x_\gamma)$ are yielded and the resulting gamma-ray flux density $F_{\mathrm{casc}}(x_\gamma)$ is determined and added to the SSC flux density F_{SSC}. The parameters that have effects on the cascaded spectrum are K_{lines}, K_{i}, γ_{mean}, ς, R, and ϕ. These values are varied until a best fit of $F_{\mathrm{casc}} + F_{\mathrm{SSC}}$ to the entire SED is achieved. The fitting procedure has to be done manually, because to keep the needed CPU hours

Quantity	Best fit value
Lorentz factor at lower cutoff	$1.0 \cdot 10^3$
Lorentz factor at PL break	$4.0 \cdot 10^5$
Lorentz factor at upper cutoff	$3.0 \cdot 10^6$
Lower PL index	2.0
Upper PL index	3.1
Radius of the SSC emission region	$2.9 \cdot 10^{13}\,\mathrm{m}$
B	$1.2 \cdot 10^{-5}\,\mathrm{T}$
Doppler factor D	20
Total electron number density	$2.1 \cdot 10^{10}\,\mathrm{m}^{-3}$

Table 5.2: Best fit values found by fitting the SSC model to the broadband SED from MJD 56857.98.

Quantity	Best fit value
K_{lines}	$9.7 \cdot 10^{12}\,\mathrm{m}^{-3}$
K_{i}	$3.3 \cdot 10^4\,\mathrm{s}^{-1}\mathrm{m}^{-3}$
γ_{mean}	$3.4 \cdot 10^{12}\,\mathrm{eV}/(m_{\mathrm{e}}c^2)$
ς	$0.23\,\gamma_{\text{mean}}$
R	$3.0 \cdot 10^{11}\,\mathrm{m}$
ϕ	$1.8°$

Table 5.3: Best fit values found by fitting the IC pair cascade model (on top of the SSC model) to the narrow spectral feature (on top of the broadband two-hump SED).

within acceptable borders, it is not possible to perform an automated run through the parameter space.

It is found possible to describe the SED from MJD 56857.98 with this approach with the input parameters listed in table 5.3. Whether these parameters are physically reasonable will be checked in the subsequent section. Now, the immediate results of the cascade simulation are discussed.

The iterative scheme to determine $N(\gamma)$ is initialised with the function $N_{\text{init}}(\gamma)$, which can in principle be arbitrarily chosen. It is of course reasonable to choose N_{init} such that it is near to the final, converged course of N. In many cases, a PL can be a reasonable choice. In the present case,

$$\dot{N}_{\text{i}}(\gamma) \Big/ \left(\frac{1}{T_{\text{esc}\,\text{e}}(\gamma)} + \int_{\gamma'_{\text{IC, min}}(\gamma,\, x_0)}^{\gamma} C(\gamma, \gamma')\,\mathrm{d}\gamma' \right) \tag{5.13}$$

is a possible choice. This function, shown as the blue line in figure 5.2, is a reasonable approximation for the final N, because at those energies not far below $\gamma_{\text{i, 0}}$, the steady-state N is dominated by the interplay of injection, escape and electron loss via IC down-scattering to lower energies, whereas the electron production rate (see equation 3.28) is not dominating here. Therefore, in expression 5.13 the injection rate is divided by the loss rate. However, in the present case and also in other cases, it is advantageous to choose

$$N_{\text{init}}(\gamma) = \frac{\dot{N}_{\text{i}}(\gamma)}{\frac{1}{2} \cdot \left(\int_{\gamma'_{\text{IC, min}}(\gamma_{\text{i, 1}},\, x_0)}^{\gamma_{\text{i, 1}}} C(\gamma_{\text{i, 1}}, \gamma')\,\mathrm{d}\gamma' + \int_{\gamma'_{\text{IC, min}}(\gamma_{\text{i, 0}},\, x_0)}^{\gamma_{\text{i, 0}}} C(\gamma_{\text{i, 0}}, \gamma')\,\mathrm{d}\gamma' \right)}. \tag{5.14}$$

This function is shown in figure 5.2 by the rose, transparent line. In expression 5.14 the injection rate is divided by the mean of the IC down-scattering rate at $\gamma_{\text{i,1}}$ and at $\gamma_{\text{i, 0}}$. This mean in the denominator is advantageous (in comparison to if the IC down-scattering rate was evaluated at every sampling point γ like in equation 5.13) because it can be determined once and saved in advance, and then reused for every γ, speeding up the evaluation of $N_{\text{init}}(\gamma)$ in the first iteration step. The escape rate is also neglected in expression 5.14 because it is not dominant in comparison to the IC down-scattering rate, here. Using equation 5.14 instead of 5.13 yields a reduction of the CPU hours by $\approx 2\,\%$. Thus, the drawback that 5.14 introduces an additional inaccuracy (difference between blue and rose line in figure 5.2) for the initialisation is overcompensated by the reduced evaluation time, and hence acceptable.

The iteration is executed with iteration scheme 2 on an Advanced Micro Devices Ryzen Threadripper 2990WX CPU with 32 cores. Each value N_k is iterated until a convergence condition is satisfied. For $\gamma_k > 10\,x_1^{-1}$, this condition is $|N_{k,\,j-1} - N_{k,\,j}|\,/N_{k,\,j} < 0.001$. In other words, the relative change between successive values has to be below 0.001. For $\gamma_k \leq 10\,x_1^{-1}$ (which is the approximate border to the Thomson regime), the condition is $|N_{k,\,j-1} - N_{k,\,j}|\,/N_{k,\,j} < 0.001 \cdot (\gamma_k x_1/10)^2$, lowering the maximum-allowed relative change quadratically with decreasing γ. This is necessary, because of

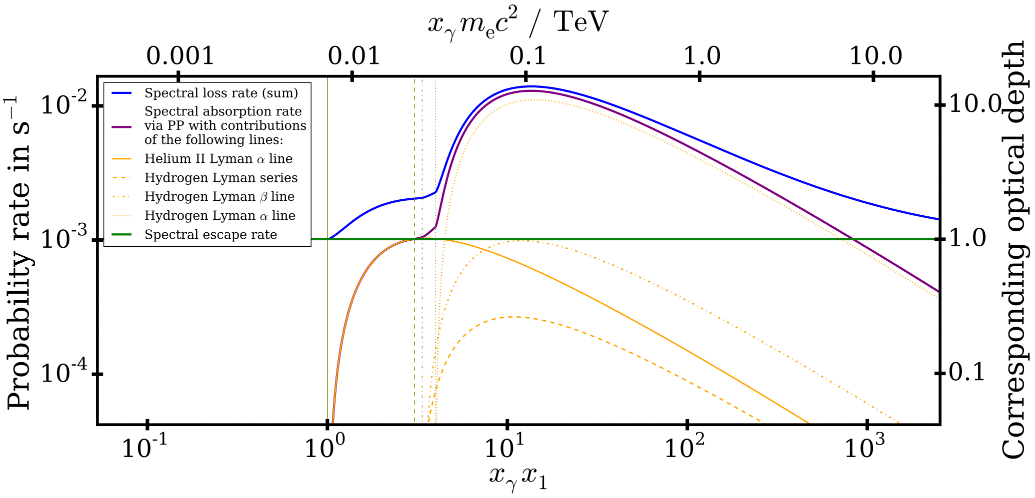

Figure 5.3: Photon loss rates of the IC pair cascade in Mrk 501. Plotted is the probability rate (and the corresponding optical depth) of the respective HE photon loss channel (pair-absorption rate in lilac, its contributions in orange, escape in green, the sum of all in blue) versus the product of the HE photon energy with the energy x_1 of the He II Lyman α line. The thin vertical lines mark the PP thresholds, i.e. the values $x_\gamma = x_i^{-1}$ for the i-th line, where the linestyle corresponds to the respective linestyle of the orange lines.

the decreasing energy transfer in one scattering event as electrons drop deeper into the Thomson regime. The relative error tolerance of `scipy.integrate.quad` is set $= 0.01$ for $j = 0$ and $= \max(0.01/j,\, 0.001)$ for all $j > 0$. Without multi-core computing used in the ISA for determining Q_{PP}, the runtime of the iteration is 2.16 h, 1.38 h and 1.14 h for one, two, three workers iterating simultaneously (as described in section 4.4.1), respectively. With multi-core computing used for determining Q_{PP} (as described in section 4.4.2), the runtime of the iteration is 0.852 h, 0.509 h and 0.449 h for one, two, three workers iterating simultaneously, respectively.

The converged course of N is depicted by the black line in figure 5.2. With decreasing γ, the number of necessary iteration steps is increasing from about $j_{\mathrm{final}} = 2$, 3 or 4 in the deep KN regime to about 100 in the Thomson regime, as can be seen by the red dots in figure 5.2.

A caveat in the choice of N_{init} should be mentioned here. It is not advisable to choose N_{init} to be (almost) equal to the final, converged course of N. If at some k', N_{init} is very near (or almost equal) to the true N, but not near to the true N away from k', then N converges to the correct value at k' after very few iteration steps, but at the next lower sampling point $k = k' - 1$ the relative change $\left|N_{k'-1,j-1} - N_{k'-1,j}\right| / N_{k'-1,j}$ is below the maximum-allowed relative change (due to the small difference between N_{init} and the true, converged N) and the iteration at $k' - 1$ is prematurely declared as finished. Hence, an error, which is small but bigger than at higher k, will be present at $k' - 1$. This will repeat at $k' - 2$, $k' - 3$, … but the errors will accumulate. This results in a final N that sticks to N_{init} along several k. Only if the error exceeds a threshold, N does not stick to N_{init} anymore and converges to the true N. This caveat can be mitigated by lowering the maximum-allowed relative change, but this also increases the necessary CPU hours. Therefore it is more reasonable to resume an iteration with a different N_{init}, if the converged N is obviously situated on N_{init} at several k.

For demonstration purpose, the same scenario is also computed with iteration scheme 1, with the results of the first 20 iteration steps shown in figure 4.3. Until the completion of the 20. iteration step, the runtime is 3.71 h, 1.46 h and 1.84 h without multi-core computing, with three workers iterating simultaneously, with multi-core computing used for determining Q_{PP}, respectively. Achieving convergence along the whole range of γ would require several hours of additional runtime. Comparing the timing properties of both iteration schemes, it becomes evident that using scheme 2 is advantageous.

As explained above and as obvious from figure 5.2, the course of N at energies $\gamma \gtrapprox 2 \cdot 10^2\, x_1^{-1}$ is dominated by $\dot{N}_\mathrm{i}$ and the IC down-scattering rate. In the range $\gamma \lessapprox 10\, x_1^{-1}$ it is about $N \sim \gamma^{-2}$. This dependence is valid in the Thomson regime for saturated cascades without escape (Zdziarski, 1988). In the present case, the smaller the electron energy becomes, the more escape dominates. Consequently, the smaller the electron energy becomes, the more N deviates from the $\sim \gamma^{-2}$ course, as is discernible around $\gamma \lessapprox 10^{-1}\, x_1^{-1}$. Due to escape, electrons cannot reach arbitrarily low energies.

In the course of N, a small bump and another very small bump is discernible at $\gamma \approx 2\, x_1^{-1}$ and at $\gamma \approx 0.5\, x_1^{-1}$, respectively. These bumps are caused by PP. Precisely, the spectral PP rate of the HE photons on the H Lyman photons (in particular on the Lyman α photons) peaks at $\gamma \approx 2\, x_1^{-1}$. The spectral PP rate on the He II Lyman α photons peaks at $\gamma \approx 0.5\, x_1^{-1}$.

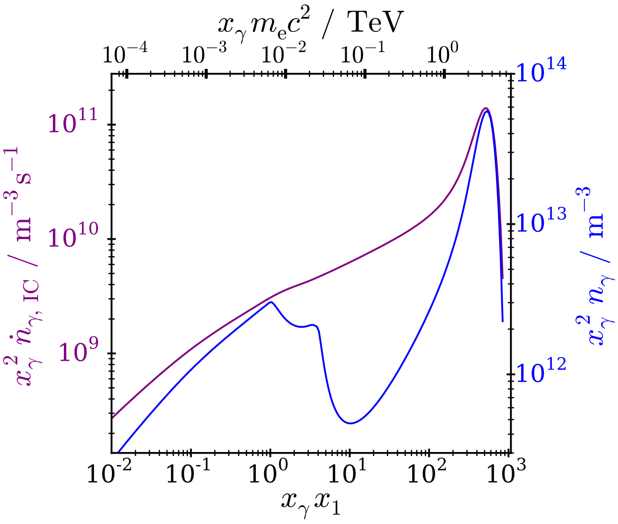

Figure 5.4: Spectra of the HE photons of the IC pair cascade in Mrk 501. Plotted is on the left y-axis (lilac) the product of the squared photon energy with the spectral production rate (given by equation 3.16) and on the right y-axis (blue) the product of the squared photon energy with the photon number density (given via equation 3.31) versus the product of the photon energy with the energy of the highest energetic emission line (which is the helium II Lyman α line, here).

Figure 5.3 shows the contributions to the spectral loss rate of the HE photons. In the range $3\, x_1^{-1} < x_\gamma < 800\, x_1^{-1}$ (equivalent to $19\,\mathrm{GeV} < \epsilon_\gamma < 5.1\,\mathrm{TeV}$), pair absorption is dominating over escape, while escape is dominating over pair absorption below and above this range. The pair-absorption rate has a maximum (caused mainly by pair absorption on H Lyman α photons) at $x_\gamma \approx 12\, x_1^{-1}$. The coefficients $K_{\mathrm{line},\,2}$ and $K_{\mathrm{line},\,3}$ are comparatively small, so that the contributions of the H Lyman β photons and of the H Lyman series is sub-dominant. Each channel of the photon loss rate can be converted to an optical depth. This is done by multiplying the escape timescale $T_{\mathrm{esc\,ph}}$ with the respective loss rate, see figure 5.3.

From N, the spectral production rate $\dot{n}_{\gamma,\,\mathrm{IC}}$ of the HE photons is easily determined via equation 3.16. It is shown by the lilac line in figure 5.4. The electron injection peak at $\approx 500\, x_1^{-1}$ causes a peak in $\dot{n}_{\gamma,\,\mathrm{IC}}$ slightly below $\approx 500\, x_1^{-1}$. This is due to the fact that in KN scatterings, the electron transfers a big fraction of its energy to the photon. The drop of N in the Thomson regime due to escape is inherited to $\dot{n}_{\gamma,\,\mathrm{IC}}$, too.

Furthermore, the spectral number density n_γ is determined via equation 3.38 or 3.31, respectively, and is shown by the blue line in figure 5.4. As there are no injected HE photons in the present setting, n_γ is represented completely by $n_{\gamma,\,\mathrm{IC}}$. Similarly to N and $\dot{n}_{\gamma,\,\mathrm{IC}}$, it shows a peak at $\approx 500\, x_1^{-1}$. It also shows a deep dip above $x_\gamma \approx 4\, x_1^{-1}$, which is a consequence of pair absorption on the H Lyman α photons. Furthermore, it shows another trough above $\approx x_1^{-1}$, which is the effect of pair absorption on the He Lyman α photons. The troughs in n_γ are consequences of the ridges in the pair-absorption rate (see figure 5.3). The edgy peak of n_γ at $\approx x_1^{-1}$ is constituted by those photons that are just below the PP threshold and consequently just not pair absorbed.

In comparison to $\dot{n}_{\gamma,\,\mathrm{IC}}$, the peak at $\approx 500\, x_1^{-1}$ is even narrower in n_γ because the spectral loss rate (the denominator of n_γ) of the photons increases with decreasing energy, which suppresses the red wing of the peak. From these findings it is evident that the distinct shape of n_γ (the edgy peak at x_1^{-1}, the first trough, the deeper trough and the narrow peak at $500\, x_1^{-1}$) is appearing as an effect of n_0 being dominated by the He and H Lyman α line and because of the injection being located just above the range where pair absorption dominates. If $n_0(x)$ was a more extended distribution or if the injection was situated in the range where pair absorption is dominant, the profile of n_γ would be more smeared and the dips and peaks would be less pronounced.

Furthermore, the HE photons' total energy density can be determined via integration of $x_\gamma\, n_\gamma$ from 0 to the upper cutoff (see limitation 3.5) of n_γ:

$$\int_0^{x_{\gamma,\,\max}(\gamma_{\mathrm{i},\,0},\,x_0)} x_\gamma\, n_\gamma(x_\gamma)\,\mathrm{d}x_\gamma \cdot m_\mathrm{e}c^2 \approx 4.5\,\mathrm{J/m^3} \tag{5.15}$$

This is slightly smaller than the soft photons' total energy density, which is given by

$$K_\mathrm{lines} \cdot \sum_{i=1}^{4} K_{\mathrm{line},\,i} \cdot m_\mathrm{e}c^2 \approx 6.5\,\mathrm{J/m^3}. \tag{5.16}$$

This comparison validates the assumption of linearity of the IC pair cascade (see section 3.2.1).

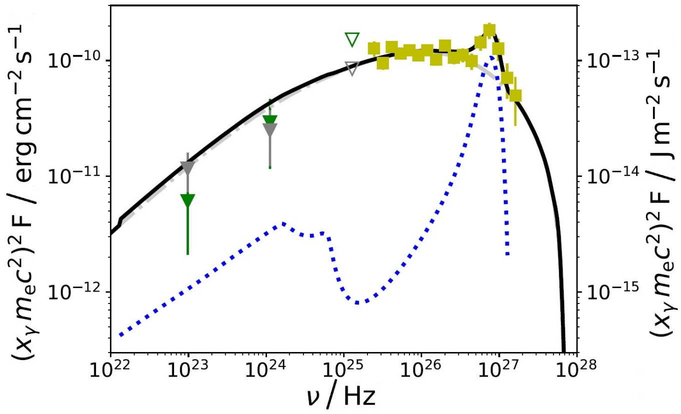

Figure 5.5: Modelled SED of Mrk 501 due to SSC and cascaded emission. The figure shows the HE hump of Mrk 501 with the narrow bump around 3 TeV. Plotted is $x_\gamma^2\, m_\mathrm{e}^2 c^4 \cdot F$, the product of the squared photon energy with the spectral flux density, versus the frequency ν. The data points are the observations from 19. of July 2014 (MJD 56857.98). The MAGIC telescopes' observations are the yellow squares, Fermi-LAT data are the grey (10-day time intervals) and green (4-day time intervals) triangles. Open markers are upper limits. The blue dotted, the light grey dash-dotted and the black solid line depict F_casc (the cascaded emission), F_SSC (the SSC emission) and $F_\mathrm{casc} + F_\mathrm{SSC}$, respectively. For details on the observational data, see MAGIC Collaboration et al. (2020).

From n_γ, the emerging flux density F_casc is determined through equation 3.45. In most SSC or EC models, relativistic electrons with an isotropic distribution are considered in an isotropically magnetised blob, which itself moves relativistically along the jet. Therefore, the escaping spectrum has to be transformed from the comoving blob frame to the AGN frame, leading to Doppler boosting. In contrast, in the present model, electrons and photons stream away from the central object along the jet. An isotropic, relativistically moving blob has not formed yet. Hence, N and n_γ are measured in the AGN frame. Therefore, no additional transformation is performed, in line with Wendel, Shukla and Mannheim (2021).

The resulting F_casc is shown by the blue dotted line in figure 5.5. As mentioned earlier, the cascaded flux density as well as F_SSC contribute to the total flux density (black line in figure 5.5). The broadband emission is explained by the SSC model and the narrow 3 TeV bump is explained by radiation from the cascade induced by the electron beam from the gap.

5.4 Inferences about the Physical Constitution of Markarian 501

Now, it is checked whether the findings of the cascade simulation that can describe the observational data are plausible and consistently fitting into the concept of Mrk 501.

5.4.1 Emission-Line Clouds in Markarian 501

It is started with using K_lines obtained from the cascade simulation to determine the total soft photon number density via equation 5.8 as well as the hydrogen Lyman α number density via equation 5.7 with $i = 4$. This yields $n_\mathrm{lines} = 3.2 \cdot 10^{18}\,\mathrm{m^{-3}}$ and $n_{\mathrm{line},\,4} = 2.6 \cdot 10^{18}\,\mathrm{m^{-3}}$. Even though the He and H Lyman α lines contribute comparably to the flux density, the H Lyman α photon number density is about one order of magnitude higher than the number densities of the other lines and makes up to major part of n_lines.

Furthermore, the Lyman α luminosity of all the clouds is determined via setting $i = 4$ in equation 5.9. This theoretically determined Lyman α luminosity has to be equal to the observational one (see section 2.4.3.2). Thus, one can set

$$L_{\mathrm{Ly}\,\alpha,\,\mathrm{obs}} \overset{!}{=} L_{4,\,\mathrm{theo}} = N_{\mathrm{cl}} \cdot 4\pi R_{\mathrm{cl}}^2 \cdot K_{\mathrm{lines}} K_{\mathrm{line},\,4}\, m_{\mathrm{e}} c^3. \tag{5.17}$$

This equality can be solved for R_{cl}, which yields $R_{\mathrm{cl}} \approx 1.8 \cdot 10^{11}\,\mathrm{m} = 0.061\, r_{\mathrm{S}}$, in agreement with R from the simulation (see table 5.3) and confirming equation 5.12. Thus, it is inferred that the BLR of Mrk 501 is comprised of $N_{\mathrm{cl}} \approx 10$ gas clouds.

5.4.2 Illumination of the Clouds by the Accretion Flow

Now, N_{cl} and the resulting R_{cl} are known. So, the total line luminosity can readily be determined via equation 5.10 to $L_{\mathrm{lines,\,theo}} = 7.8 \cdot 10^{33}\,\mathrm{W}$, which is lower than Mrk 501's BLR luminosity upper limit by a factor 5 (Celotti, Padovani and Ghisellini, 1997). Recall that $L_{\mathrm{lines,\,theo}}$ was obtained from the cascade simulation results and from equating the observed Lyman α luminosity with the theoretical one. Also recall that equation 5.11 must be satisfied. The reprocessing fraction ξ in this equation usually attains a value of 10 %. However, in evolved, gas-starved AGN like Mrk 501, it seems plausible that less ADAF radiation is reprocessed by the BLR clouds, in other words that ξ is smaller. Therefore, values $\xi = 0.1$ and $\xi = 0.01$ are pursued in the following.

Now, reasonable values for T_{e} and $\dot{m}$ are searched such that equation 5.11 is satisfied. This is done by integrating the synthetic ADAF spectrum from Mahadevan (1997) according to equation 2.11 (as described in section 2.1.2.2) for test values of T_{e} and $\dot{m}$ and then checking whether equation 5.11 is satisfied for this pair of T_{e} and $\dot{m}$. For example, in the $\xi = 0.01$ case, it has to be $L_{\mathrm{ADAF,\,tot}}(\dot{m}, T_{\mathrm{e}}) = 7.8 \cdot 10^{35}\,\mathrm{W}$. It is found that equation 5.11 is satisfied for the values listed in table 5.4 (first three rows, therein). The corresponding ADAF spectra are plotted in figure 2.2. Obviously, for given $\dot{m}$, increasing ξ from 0.01 to 0.1 necessitates a temperature decrease by about 25 %. Expressed the other way round, a hotter AF gets more luminous, leading to a smaller luminosity fraction that has to be reprocessed to provide $L_{\mathrm{lines,\,theo}}$. The found $\dot{m}$ and T_{e} agree with typical ADAF parameters, which confirms the general plausibility of the assumed scenario. Mrk 501 is surrounded by a hot, weakly accreting ADAF, which illuminates a sparse BLR. The clouds reprocess the continuum radiation into emission lines. The emission lines from one BLR cloud serve as target photons for the IC pair cascade shaping the 3 TeV bump. In the following, it is tried to discriminate between $\xi = 0.01$ and 0.1 and to rule out one case.

5.4.3 Particle Multiplication in and behind the Gap

Recall from section 5.2.1 that the effect of the ADAF is not only the illumination of the BLR but also the irradiation of the magnetosphere with gamma-ray photons that are capable to pair produce seed electrons. The number density n_{PP} of such photons is given by equations 2.18 and 2.19. The values of $n_{\mathrm{PP},\,1}$ and $n_{\mathrm{PP},\,2}$ that are yielded for the plausible values of T_{e} and $\dot{m}$ obtained in the previous section are also given in table 5.4 (fourth and fifth as well as sixth row therein). The obtained values of $n_{\mathrm{PP},\,1}$ in the $\xi = 0.1$ case are almost two orders of magnitude smaller than in the $\xi = 0.01$ case. This is because the lower temperatures in the $\xi = 0.1$ lead to fewer bremsstrahlung and Comptonised photons in the ADAF, as is obvious from figure 2.2. As $n_{\mathrm{PP},\,2}$ is independent on the temperature, its values cannot be discriminated for different cases of ξ. For low accretion rates, there is order-of-magnitude agreement between $n_{\mathrm{PP},\,1}$ in the $\xi = 0.01$ case and $n_{\mathrm{PP},\,2}$. In contrast, no agreement is found for $n_{\mathrm{PP},\,1}$ in the $\xi = 0.1$ case and $n_{\mathrm{PP},\,2}$, suggesting that the $\xi = 0.1$ case introduces inconsistencies.

The collisions of the pair-producing gamma-ray photons lead to the materialisation rate K_{PP} of electron-positron pairs per unit volume given by equation 5.1. Depending on the direction of the electric field in the vacuum gap, positrons/electrons are accelerated into the BH. The materialisation rate of electrons/positrons that are accelerated away from the BH and form the beam is therefore

		$\dot{m} = 1.0 \cdot 10^{-4}$	$\dot{m} = 2.0 \cdot 10^{-4}$	$\dot{m} = 4.0 \cdot 10^{-4}$	$\dot{m} = 8.0 \cdot 10^{-4}$
$T_\mathrm{e} \,/\, \mathrm{K}$	$\xi = 0.01$	$1.7 \cdot 10^{10}$	$1.4 \cdot 10^{10}$	$1.1 \cdot 10^{10}$	$8.4 \cdot 10^{9}$
	$\xi = 0.1$	$1.3 \cdot 10^{10}$	$1.0 \cdot 10^{10}$	$8.1 \cdot 10^{9}$	$6.4 \cdot 10^{9}$
$n_{\mathrm{PP},1} \,/\, \mathrm{m}^{-3}$	$\xi = 0.01$	$2.8 \cdot 10^{9}$	$4.6 \cdot 10^{9}$	$4.7 \cdot 10^{9}$	$3.8 \cdot 10^{9}$
	$\xi = 0.1$	$6.7 \cdot 10^{7}$	$3.8 \cdot 10^{7}$	$5.5 \cdot 10^{7}$	$6.9 \cdot 10^{7}$
$n_{\mathrm{PP},2} \,/\, \mathrm{m}^{-3}$		$1.4 \cdot 10^{9}$	$5.6 \cdot 10^{9}$	$2.2 \cdot 10^{10}$	$9.0 \cdot 10^{10}$
$K_\mathrm{PP} \,/\, \mathrm{s}^{-1}\,\mathrm{m}^{-3}$	$\xi = 0.01$	0.031	0.084	0.088	0.058
	$\xi = 0.1$	$1.8 \cdot 10^{-5}$	$5.8 \cdot 10^{-6}$	$1.2 \cdot 10^{-5}$	$1.9 \cdot 10^{-5}$
$\mathcal{N}$	$\xi = 0.01$	$1.1 \cdot 10^{6}$	$3.9 \cdot 10^{5}$	$3.8 \cdot 10^{5}$	$5.7 \cdot 10^{5}$
	$\xi = 0.1$	$1.8 \cdot 10^{9}$	$5.7 \cdot 10^{9}$	$2.8 \cdot 10^{9}$	$1.7 \cdot 10^{9}$
$\Phi \,/\, \mathrm{V}$	$\xi = 0.01$	$6.1 \cdot 10^{18}$	$2.3 \cdot 10^{18}$	$2.2 \cdot 10^{18}$	$3.3 \cdot 10^{18}$
	$\xi = 0.1$	$1.1 \cdot 10^{22}$	$3.3 \cdot 10^{22}$	$1.6 \cdot 10^{22}$	$1.0 \cdot 10^{22}$

Table 5.4: Possible values of physical quantities attained by connection of the ADAF luminosity with the emission-line luminosity as well as with the vacuum gap PP materialisation rate. The third to sixth column shows reasonable accretion rate values $\dot{m}$, as noted in the first row. The second and the third row shows the values obtained for T_e in units of K for the respective values of the reprocessing fraction ξ and of $\dot{m}$. The fourth and fifth row shows the values obtained for $n_{\mathrm{PP},1}$ in units of m^{-3} for the respective values of ξ and $\dot{m}$. The sixth row shows the values obtained for $n_{\mathrm{PP},2}$ in units of m^{-3} for the respective values of $\dot{m}$. Recall that $n_{\mathrm{PP},2}$ is not dependent on T_e, and therefore need not to be discriminated for both ξ values. The seventh and eighth row shows the obtained values of the PP materialisation rate K_PP in units of $\mathrm{s}^{-1}\,\mathrm{m}^{-3}$ for the respective values of ξ and $\dot{m}$. The ninth and tenth row shows the obtained values of $\mathcal{N}$. The eleventh and twelfth row shows the corresponding values of Φ in units of V.

also given by K_PP. Now, this seed electron materialisation rate is determined, but this is done only for $n_{\mathrm{PP},1}$. The resulting values of K_PP are given in table 5.4 (seventh and eighth row). As a result of the deviation of $n_{\mathrm{PP},1}$ between the $\xi = 0.01$ and the $\xi = 0.1$ case, K_PP in the $\xi = 0.01$ case is bigger by factor $10^3 - 10^4$ in comparison to the $\xi = 0.1$ case.

These seed electrons are multiplied during the in-and-post-gap cascade as explained in section 5.2.1. From the obtained K_PP, from equation 5.2 and from K_i obtained from the cascade simulation, the multiplication number $\mathcal{N}$ can be yielded. (Recall that the quantity K_i is the materialisation rate of the child electrons (after the in-and-post-gap cascade) and it also is the injection rate of electrons into the cascade on the emission line photons.) The resulting values are also listed in table 5.4 (ninth and tenth row). $\mathcal{N}$ in the $\xi = 0.01$ case is a factor $10^2 - 10^3$ bigger than the multiplication number obtained in the work of Broderick and Tchekhovskoy (2015). However, only the cascade behind the gap was considered by those authors. The strong impact of curvature radiation in the gap was not taken into account. For example, Levinson and Cerutti (2018) found that more than 10^6 curvature radiation photons can be emitted in an active gap by one single seed electron. Therefore, values bigger than those found by Broderick and Tchekhovskoy (2015) seem plausible.

Now, recall that during the in-and-post-gap cascade, the energy of a seed electron (attained from the vacuum gap potential drop) is distributed to all its child electrons, which is expressed in equation 5.4. This equation is now solved for the potential drop and Φ is determined via $\gamma_{\mathrm{i},0}$ (which is known from the cascade simulation) and $\mathcal{N}$. The obtained values are also listed in table 5.4 (eleventh and twelfth row). The values of Φ in the $\xi = 0.01$ case agree with estimated values (Levinson and Rieger, 2011) and with values obtained by sophisticated gap simulations (Hirotani and Pu, 2016). The values of order $10^{22}\,\mathrm{V}$ in the $\xi = 0.1$ case are, however, beyond the realistic range. Extreme values of the magnetospheric magnetic flux density and of M_BH and a wide gap extent would be necessary to achieve such a large gap voltage. As such extreme values are unrealistic, the canonical $\xi = 0.1$ case has to be discarded (as was suggested earlier in this section). A consistent framework is however present for the $\xi = 0.01$ case. A low fraction of the AF radiation is reprocessed by the ionised gas clouds into broad emission lines.

5.4.4 The Energetical Point of View

In this section, the BZ power, which is the appropriate scale to measure other powers or luminosities, is estimated. After that, the accretion power, the vacuum gap output, the cascade power and the SSC power are compared to it.

To estimate these quantities, further features of the magnetosphere have to be estimated. For jetted AGN, a high BH angular momentum $a = 0.99$ is usually assumed and also justified by spin measurements (e.g. Bambi, 2018). Assuming equipartition between the magnetic and the gas pressure, Aharonian, Barkov and Khangulyan (2017) find

$$B = 0.19 \cdot \left(\frac{10^9 \, M_\odot}{M_\mathrm{BH}} \right)^{\frac{4}{7}} \; \mathrm{T} \tag{5.18}$$

for the magnetospheric magnetic flux density in the presence of an active gap. By this, one can evaluate equation 2.17 for the BZ power. One obtains $P_\mathrm{BZ} = 3.5 \cdot 10^{36}\,\mathrm{W}$, which is about five times $L_\mathrm{ADAF,\,tot}$ in the $\xi = 0.01$ case (see section 5.4.2). The luminosity $L_\mathrm{ADAF,\,tot}$ must however not be confused with the total accretion power $\dot{M}c^2$. From section 2.1.2, one can estimate this to $\dot{M}c^2 = \dot{m} \cdot L_\mathrm{Edd}/\eta$. With the lower limit $\dot{m} = 10^{-4}$ and the upper limit $\eta = 0.1$ one attains the lower limit $\dot{M}c^2 = 1.3 \cdot 10^{37}\,\mathrm{W}$ well above all other power scales.

Aharonian, Barkov and Khangulyan (2017) also estimate the maximum power output of a gap. For that purpose, these authors estimate the maximum possible magnetospheric charge density, electric field strength and gap extension and assume these to be realised in the magnetosphere. They parametrise their result with the BH mass, the gap's polar angle extent θ and with a quantity called multiplicity κ, which describes the level of shielding of the gap, and with the variability timescale of the transient gap emission. After converting this timescale to the typical size h_gap of the gap, the gap power is

$$P_\mathrm{gap} = 4.8 \cdot 10^{37} \, \kappa \, h_\mathrm{gap} \left(\frac{M_\mathrm{BH}}{10^9 M_\odot} \right)^{\frac{6}{7}} \sin^2 \theta \; \mathrm{W}. \tag{5.19}$$

With an extent $\theta = \pi/4$ and $h_\mathrm{gap} = 0.25$ of a weakly screened gap ($\kappa = 0.1$), one obtains the maximum gap power $P_\mathrm{gap} = 6.0 \cdot 10^{35}\,\mathrm{W}$, about an order of magnitude smaller than the BZ power.

The power that is actually tapped in the gap is (after the redistribution during the in-and-post-gap cascade) finally injected into the cascade on the emission line photons. This power injected by electrons into the interaction region can easily be determined through

$$P_\mathrm{i} = \frac{4}{3}\pi R^3 \cdot \int_{\gamma_{\mathrm{i},1}}^{\gamma_{\mathrm{i},0}} \gamma \, m_\mathrm{e} c^2 \, \dot{N}_\mathrm{i}(\gamma) \, \mathrm{d}\gamma = 1.9 \cdot 10^{33}\,\mathrm{W}. \tag{5.20}$$

Furthermore, Wendel et al. (2021b) determined the power which is emitted by the electrons in the SSC model to $P_\mathrm{SSC} = 4.4 \cdot 10^{36}\,\mathrm{W}$.

Written in a compact form, it was found that

$$0.27 \, \dot{M}c^2 = 0.80 \, P_\mathrm{SSC} = P_\mathrm{BZ} = 4.5 \, L_\mathrm{ADAF,\,tot} = 5.8 \, P_\mathrm{gap} = 1800 \, P_\mathrm{i}. \tag{5.21}$$

The first relation $0.27 \, \dot{M}c^2 = \ldots$ denotes that the accretion power sustains the entire AGN. The accreted energy is partly released via electromagnetic radiation of the AF and partly dumped into the SMBH.

The second equality $0.80 \, P_\mathrm{SSC} = P_\mathrm{BZ}$ may seem inconsistent at first glance, because given that the SSC region and its power output are essentially driven by the jet and therefore also driven by the BZ mechanism, one could expect that the SSC power must not be higher than the BZ power. This view is, however, too simplified. First, one has to consider that the SSC region is not located in the direct vicinity of the magnetosphere. It is located farther downstream the jet and therefore it is a tracer of the BZ activity of an earlier time. In this earlier magnetospheric state, the accretion rate could have been higher, such that equation 5.18 is not a valid approximation any more. The magnetic flux density would have been higher, as it would have been the BZ power. Second, the jet could also have been powered by the Blandford-Payne mechanism in addition to the BZ mechanism. Because of these two reasons, it is not necessarily implausible that $P_{\mathrm{SSC}} > P_{\mathrm{BZ}}$.

The relation $\ldots = 4.5\, L_{\mathrm{ADAF,\,tot}}$ shows that the ADAF's electromagnetically emitted luminosity is substantially smaller than the accretion power, a typical feature of the radiatively inefficient ADAF. It is even smaller than the energy extracted from the spinning BH, underlining the relevance of the BZ mechanism for recycling the rotational BH energy.

The fourth comparison $P_{\mathrm{BZ}} = 5.8\, P_{\mathrm{gap}}$ is a result that makes the estimates by Aharonian, Barkov and Khangulyan (2017) reasonable. It shows that a fraction of the BZ power can be converted to relativistic particles in an active vacuum gap under advantageous conditions.

The relation $P_{\mathrm{BZ}} = 1800\, P_{\mathrm{i}}$ shows that during the event leading to the 3 TeV spectral bump, a fraction 0.0031 of the maximum possible gap power was actually generated. The magnetospheric conditions during this concrete event have not been as favourable as assumed in the derivation of equation 5.19. This estimate is in agreement with findings by Chen and Yuan (2020), Kisaka, Levinson and Toma (2020) and Levinson and Cerutti (2018). In particular, Levinson and Cerutti (2018) find that a fraction $\approx 0.001\, P_{\mathrm{BZ}}$ is tapped in a sporadically active gap during a time span $\approx 7\, r_{\mathrm{S}}/(2\, c) \approx 9.6\,\mathrm{h}$ after an initiating spark event. This time span is in agreement with the duration of the narrow 3 TeV bump (of about one night).

5.5 Discussion

In the adopted scenario, a typical ADAF of $T_{\mathrm{e}} \approx 10^{10}\,\mathrm{K}$ surrounds the SMBH. The ADAF illuminates the few ambient clouds, which are therefore ionised and emit broad atomic lines. The reprocessing fraction ξ of the ADAF radiation into emission-line photons was found to be of the order 10^{-2}, in accordance with the observed luminosity of the hydrogen Lyman α line. Furthermore, the ADAF gamma-ray photons pair produce seed electrons which are accelerated in a vacuum gap and multiplied afterwards with a multiplication number $\mathcal{N}$ found to be several 10^5 to 10^6. These electrons inject a power of $\approx 0.06\,\%$ of the BZ power into a region where interaction with the emission-line photons from one cloud takes place. It was shown that the evolving cascade creates a peculiar imprint in the VHE spectrum. It was found that in addition to the SSC emitting region farther away from the AGN centre, which is responsible for the broadband SED, a cascade initiated by an electron beam from a vacuum gap can cause the narrow 3 TeV bump from MJD 56857.98 and that this scenario is consistent within the assumed simplifications. Gap activity and an ensuing IC pair cascade as one possible realisation of emission mechanisms beyond conventional SSC scenarios can therefore manifest in observable fine structure of blazar SEDs.

In this consideration, the in-and-post-gap cascade was treated only in a simplified manner, via the electron multiplication and energy redistribution. The relation between K_{PP} and K_{i} is however not only determined by the multiplication. It is also affected by the spreading of the electron bunch while it propagates along the beam in a divergent magnetic field. A spatial expansion of the electron bunch would reduce the electron number density and correspondingly K_{i}. To take effects like this into account, it is however necessary to perform sophisticated particle-in-cell simulations involving the trajectories of the electrons propagating in the curved magnetic field, synchro-curvature radiation effects, IC scattering and PP in the anisotropic AF photon field.

One could argue that the cascade model from chapter 3, which explicitly assumes steady state, must not be applied to the transient 3 TeV feature of Mrk 501. The timescale of the TeV bump can be estimated to several hours (one night). In comparison, the escape timescales of the concretely considered cascade are $R/c = 990\,\mathrm{s}$ according to equations 3.46, meaning that a quasi-steady state is indeed present.

The present model substantiated the presence of a small number of emission line clouds in Mrk 501. From this scarcity of clouds, one can infer that an encounter between the electron beam and an emission line cloud might not happen very often, making it understandable that the narrow TeV feature was not observed some other time in Mrk 501. As emission line clouds are usually thought to move on Keplerian orbits around the central object, such encounter events should recur with the cloud's orbital period. This presumes however that the electron beam is persistent, which might not be the case if it originates from a vacuum gap. Therefore, an encounter event (and the consequent emission of the narrow spectral feature) can only recur on timescales that are an integer multiple of the orbital period. Of course, it is possible that several clouds have their orbit crossing the electron beam, making such encounter events more frequent.

Despite the finding that gaps are inherently intermittent phenomena, a longer-lasting electron beam does not seem entirely improbable. Broderick and Tchekhovskoy (2015) found that a vacuum gap can be extended in width (perpendicular to the magnetic field lines) farther than in height (direction along field lines). In this case, the whole gap consists of several tubes that are extended along the field lines and arranged next to each other in direction perpendicular to the field lines. The neighboured tubes do however have no (or very weak) causal connection and therefore operate independently of each other. Then, the electron beam results from a superposition of the output of many independent gap tubes and consequently the intermittent behaviour is averaged.

Chapter 6

A Peculiar Gamma-Ray Spectrum of 3C 279 from the Broad-Line Region

In this chapter, an IC pair cascade in the BLR of 3C 279 is applied to explain another peculiar SED feature. Thereby, the problem of the gamma-ray emitting region in FSRQs (see section 2.4.6) will be addressed.

Data of a flaring state of 3C 279 obtained through the Fermi LAT were analysed by Wendel, Shukla and Mannheim (2021). The `pass8` data of 3C 279 from MJD 58129 to MJD 58150 (11. of January 2018 until 1. of February 2018) were generated using Science Tools version `v10r0p5` with parameters as described by these authors. The flux density values obtained by these authors are shown by the green markers in figure 6.4. The LAT spectrum shows a peculiar dip at several 10 GeV, deviating from simple model fits. For example, a PL with exponential cutoff fit and an LP fit with three fitting parameters each and with eleven degrees of freedom each yield $\chi^2_{\mathrm{red}} = 3.3$ and $= 1.2$, respectively. While these fits need not to be necessarily rejected, it is tried in the following to provide a physically motivated and robust interpretation of the data and in particular it is tried to judge about the emission region.

6.1 A Cascade on Broad-Line Region Photons

To provide an explanation for these Fermi-LAT data, a model involving IC pair cascades similar to the model used in chapter 5 is evoked. It is assumed that electrons and/or HE photons with non-thermal spectra are injected into the plasma of the inner jet of 3C 279. Such non-thermal spectra can result from a multitude of processes like shock acceleration, stochastic acceleration, magnetoluminescence, shear acceleration or vacuum gap acceleration (see e.g. Blandford, Meier and Readhead, 2019; Matthews, Bell and Blundell, 2020; Wendel, Shukla and Mannheim, 2021, and references therein). If direct electron acceleration is impossible as a consequence of growing energy losses, HE electrons can nevertheless result from the decay of ultra-relativistic protons (Lovelace, 1976; Mannheim, 1993; Mastichiadis and Kirk, 1995).

The injected particles interact with the BLR photon field and initiate an IC pair cascade. This scenario is considered in two cases, each having several sub-cases. In case 1, relativistic electrons and/or gamma rays are injected inside of the BLR, hence in the very inner portion of the AGN. The reprocessing takes place on the strong BLR photon field with spectral number density n_0 and the emerging gamma rays emanate from the outer edge of the BLR. The lengthscale of the cascade region is l, as sketched in the left-hand side panel of figure 6.1. In case 2, the injection site is not in the AGN centre. The injection takes place near the outer border of the BLR. The cascading happens in the diluted BLR photon field outside of the BLR, as sketched in the right-hand side panel of figure 6.1. The cascade in this diluted photon field is described by using a photon density reduced by a factor 0.25 in comparison to case 1 and by using the same lengthscale l. The factor 0.25

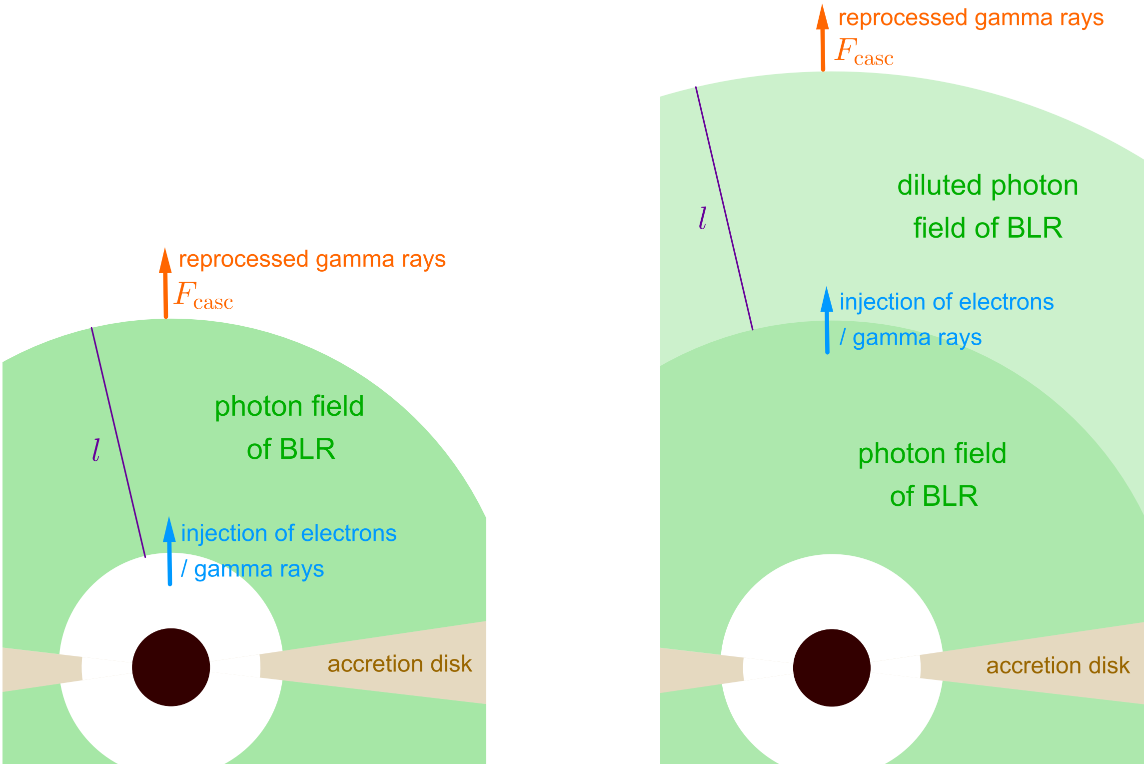

Figure 6.1: Depiction (not to scale) of the model to explain the gamma-ray spectrum of 3C 279. Left-hand side panel: Setting for cases 1a, 1b and 1c. Right-hand side panel: Setting for case 2.

is motivated by assuming that the mean distance of the spherical shell of the diluted photon field is double the mean distance of the spherical shell of the undiluted photon field. With the number density dilution being $\sim r^{-2}$, this makes the factor 0.25 plausible. To examine whether the observed gamma-ray radiation is formed in the BLR or outside of it, it is checked whether case 1 or case 2 is better suited to fit the Fermi-LAT spectrum of 3C 279.

Additionally to the discrimination between the cases 1 and 2 (cascading in versus outside of the BLR), case 1 is sub-divided into cases with differing injection. In case 1a, 1b, 1c PL-distributed photons and Gaussian-distributed electrons, LP-distributed photons, PL electrons and Gaussian electrons are injected. Purpose of this discrimination into three sub-cases is the examination of the influence of the different acceleration mechanisms on the emerging spectrum. Precisely, the following injection rates are used:

- In case 1a and 2, HE photons from the AGN centre are injected with the rate

$$\dot{n}_{\gamma,\mathrm{i}}(x_\gamma) = \begin{cases} K_{\mathrm{P}} \left(\frac{x_\gamma}{x_{\gamma,\mathrm{i},1}}\right)^{\alpha} & \text{if } x_{\gamma,\mathrm{i},1} \leq x_\gamma \leq x_{\gamma,\mathrm{i},0} \\ 0 & \text{otherwise.} \end{cases} \tag{6.1}$$

  In contrast to chapter 5, $\dot{n}_{\gamma,\mathrm{i}}$ is non-vanishing here. Additionally and completely in line with equation 5.3, electrons from a presumed vacuum gap are injected with the rate

$$\dot{N}_{\mathrm{i}}(\gamma) = \begin{cases} \frac{K_{\mathrm{i}}}{\varsigma\sqrt{(2\pi)}} \cdot \exp\left(-\frac{(\gamma-\gamma_{\mathrm{mean}})^2}{2\,\varsigma^2}\right) & \text{if } \gamma_{\mathrm{i},1} \leq \gamma \leq \gamma_{\mathrm{i},0}, \\ 0 & \text{otherwise.} \end{cases} \tag{6.2}$$

  Again, γ_{mean} and ς are the mean electron Lorentz factor and the spread of the Gaussian, respectively. K_{i} is the total electron injection rate.

- In case 1b, $\dot{N}_{\mathrm{i}}$ is zero, while the HE photon injection rate is described by

$$\dot{n}_{\gamma,\,\mathrm{i}}(x_\gamma) = \begin{cases} K_{\mathrm{P}} \left(\frac{x_\gamma}{x_{\gamma,\,\mathrm{i},\,1}}\right)^{\alpha+\beta \log_{10}(x_\gamma/x_{\gamma,\,\mathrm{i},\,1})} & \text{if } x_{\gamma,\,\mathrm{i},\,1} \le x_\gamma \le x_{\gamma,\,\mathrm{i},\,0} \\ 0 & \text{otherwise.} \end{cases} \tag{6.3}$$

- In case 1c, there is no HE photon injection. The electron injection rate is

$$\dot{N}_{\mathrm{i}}(\gamma) = \begin{cases} K_{\mathrm{P}}\, \gamma^\alpha + \frac{K_{\mathrm{i}}}{\varsigma\sqrt{(2\pi)}} \cdot \exp\left(-\frac{(\gamma-\gamma_{\mathrm{mean}})^2}{2\,\varsigma^2}\right) & \text{if } \gamma_{\mathrm{i},1} \le \gamma \le \gamma_{\mathrm{i},\,0}, \\ 0 & \text{otherwise.} \end{cases} \tag{6.4}$$

  Here, K_{i} is not the total electron injection rate but only the total one from the Gaussian distribution.

The BLR photon field is, in analogy to chapter 5, described as a set of δ_{Dirac} functions at the energies x_i. Independent of the cases, it is

$$n_0(x) = K_{\mathrm{lines}} \cdot \sum_{i=1}^{11} \frac{K_{\mathrm{line},\,i}}{x_i} \cdot \delta_{\mathrm{Dirac}}\,(x - x_i) \tag{6.5}$$

in line with equation 5.6. For all cases, the most prominent emission lines from the mid-UV to the soft-X-ray regime are included. In table 6.1, the used lines are listed along with the references of the observational BLR or simulated photo-ionisation spectra that indicate the presence and strength of the respective line. If in these literature spectra two or more lines are prominent and separated in x by $10\,\%$ or less, these lines are treated in the code as only one line. Again, $K_{\mathrm{line},\,i}$ is the relative contribution of the i-th line. K_{lines} parametrises the total number density of the emission line photons.

Like in chapter 5, energy-independent escape of the photons and electrons is included in all considered cases. Equations 3.46a and 3.46b are assumed to be valid and l is written instead of R for the escape lengthscale. While R was the radius of a spherical interaction region, l is the thickness of the spherical-shell-like interaction region. In case 1 (and its sub-cases), l is nearly equal to the BLR radial size because the injection takes place in the interior of the BLR, see left-hand side panel of figure 6.1.

The approach pursued in the subsequent sections is as follows. As described in chapter 3, the injection rates, n_0 and the escape timescales fully determine the IC pair cascade. All prerequisites, assumptions and approximations stated in that chapter are adopted here, unless otherwise stated. The coupled, steady-state kinetic equations will be solved with the numerical techniques described in chapter 4. In cases 1, after the cascading takes place along the distance l, the gamma rays leave the BLR without further reprocessing or absorption in the r^{-2}-diluted photon field. Also, absorption in the external photon field from the equatorial torus and in the extragalactic background light is not taken into account (MAGIC Collaboration et al., 2008). So, the gamma sphere is associated with the outer edge of the BLR (Blandford and Levinson, 1995). In case 2, the injection site is located near the BLR outer edge and the cascading takes place along a distance l in the diluted BLR photon field. In both cases, the observable flux density F_{casc} is determined via equation 3.45 from n_γ, with $R = l$, with $\Omega(\phi)$ being the solid angle of the beam and with D from section 2.4.3.1. In all cases, F_{casc} is fit to the Fermi LAT data. First, the cases 1a, 1b and 1c are fit to the data points by varying the respective fitting parameters of the injection rates, by varying the numbers $K_{\mathrm{line},\,i}$ within borders compatible with reasonable broad emission line spectra and by varying K_{lines}, ϕ and l. Second, F_{casc} in case 2 is fit to the data points. As argued above, to model the reprocessing in the diluted BLR photon field outside of the BLR, the values for $K_{\mathrm{line},\,i}$ and l in case 2 are kept the same as in case 1a. The value K_{lines} in case 2 is a factor 0.25 smaller than the one used in case 1a. The reason for this is, as mentioned above, that the spherical target photon shell in case 2 is located at double a distance and is therefore a factor 2^{-2} smaller.

i	Designation of line	Wavelength λ_i/nm	Relative contribution $K_{\mathrm{line},\,i}$ to flux density Case 1a	Case 1b	Case 1c
1	O VII [e, a, d]	2.20	5.90	4.80	5.20
2	C V [e, a]	4.05	3.55	4.25	3.45
3	Fe XVIII [a, d]	9.39	4.70	5.75	5.05
4	Fe XXIII [a, d]	13.3	3.95	2.90	3.80
5	He II Lyman continuum [e]	22.8	0.75	0.45	0.70
6	He II Lyman α [e, a, d]	30.5	3.70	2.90	3.50
7	He I [e, a, d]	58.4	4.80	4.75	5.30
8	H I Lyman continuum[c]	93.0	1.75	1.60	1.75
9	H I Lyman α [e, a, d, b, c]	122	4.35	1.70	4.35
10	C IV [e, a, d, b, c]	155	1.85	0.70	1.90
11	Mg II [a, d, b, c]	280	0.55	0.20	0.60

Table 6.1: The eleven emission lines that are taken into account in compiling the soft target photon distribution. The lower-case letters indicate that the respective line is prominent in the respective reference:
a: Atomic and molecular physics database by R. L. Kelly from Harvard-Smithsonian Center for Astrophysics available at `https://lweb.cfa.harvard.edu/ampcgi/kelly.pl`,
b: Telfer et al. (2002),
c: Pian, Falomo and Treves (2005),
d: Chianti atomic database for astrophysical spectroscopy by Dere et al. (1997) and Landi et al. (2012),
e: Abolmasov and Poutanen (2017)

6.2 Results of the Modelling

For the cases described in the previous section, the cascade is simulated for the respectively given set of input parameters and the emerging spectra are determined. As convergence criteria, for $\gamma_k > 10\,x_1^{-1}$ it is required that $|N_{k,\,j-1} - N_{k,\,j}|\,/N_{k,\,j} < 0.01$. For $\gamma_k \leq 10\,x_1^{-1}$ the convergence condition is $|N_{k,\,j-1} - N_{k,\,j}|\,/N_{k,\,j} < 0.01 \cdot (\gamma_k x_1/10)^{0.5}$. For each case, the fitting parameters of the injection functions and the coefficients $K_{\mathrm{line},\,i}$ are varied until the Fermi LAT data can be described by the respective model. In all three cases 1a, 1b and 1c, it is possible to meet the LAT data points by the modelled spectra. The used $K_{\mathrm{line},\,i}$ are given in table 6.1 and the fitting parameters found are listed in table 6.2. The corresponding χ^2_{red} (as well as the number of degrees of freedom and the number of fitting parameters) are also reported in this table. The χ^2_{red} are determined with 14 data points each, i.e. the upper limits are left out. To count the number of the fitting parameters, the coefficients $K_{\mathrm{line},\,i}$ are not taken into account because these values have been varied away only slightly from the literature values. Furthermore, the cutoffs $x_{\gamma,\,\mathrm{i},\,1}$, $x_{\gamma,\,\mathrm{i},\,0}$, $\gamma_{\mathrm{i},\,1}$ and $\gamma_{\mathrm{i},\,0}$ are not taken as fitting parameters, because they have been chosen before the fitting procedure to lie below and above the LAT energy range.

In figure 6.2, the contributions to the spectral photon loss rate and the optical depths are shown exemplarily for case 1a. The corresponding figures for the other cases appear qualitatively very similar and are therefore not shown. In comparison to the optical depth obtained by Liu and Bai (2006, see the dashed line of figure 8 therein) under the assumption that the emitting region is located at the inner BLR border, the pair-absorption optical depth obtained in the present work in the energy range $\approx 10\,\mathrm{GeV} - 90\,\mathrm{GeV}$ is only very slightly larger. In the range $\approx 30\,\mathrm{GeV} - 90\,\mathrm{GeV}$, the present-work optical depth is comparable to the optical depth determined by the H. E. S. S. Collaboration et al. (2019) for gamma-ray emission slightly inside of a BLR with shell geometry (see cyan lines in figure 5's left-hand side panel in that reference) as well as for gamma-ray emission from the deep interior of a BLR with ring geometry (see blue lines in figure 5's right-hand side panel in that reference).

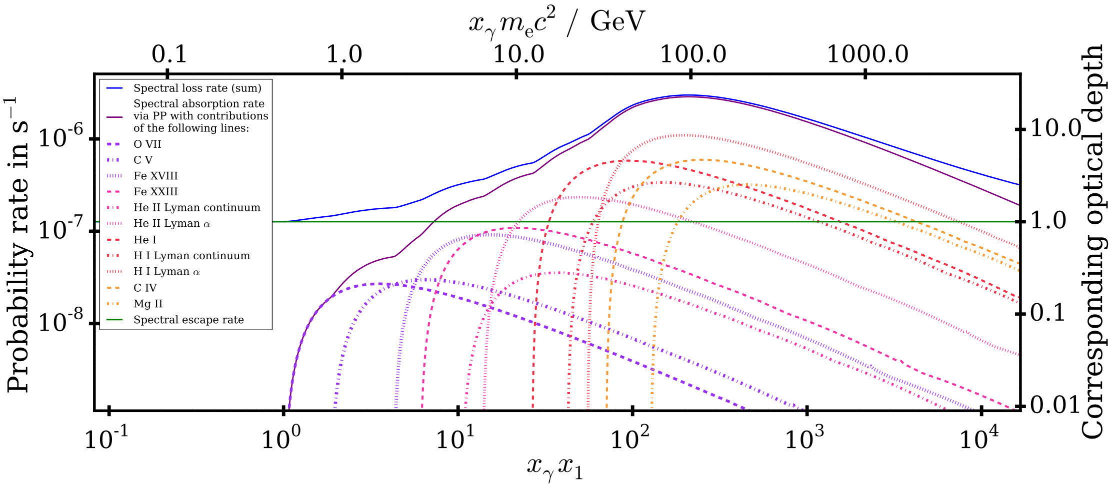

Figure 6.2: Photon loss rate channels in case 1a of the 3C 279 model. On the left-hand, right-hand side y-axis the various contributions to the loss rate, the corresponding optical depths of an HE photon are shown for case 1a, respectively. The quantities are plotted along the HE photon energy. On the lower, upper x-axis the product of the dimensionless HE photon energy with the dimensionless energy of the O VII emission line, the dimensioned photon energy is plotted, respectively.

Quantity	Best fit value		
	Case 1a	Case 1b	Case 1c
$x_{\gamma,\mathrm{i},1}\, m_\mathrm{e} c^2 \,/\, \mathrm{eV}$	$1.0 \cdot 10^{8}$	$1.0 \cdot 10^{11}$	
$x_{\gamma,\mathrm{i},0}\, m_\mathrm{e} c^2 \,/\, \mathrm{eV}$	$5.0 \cdot 10^{11}$	$5.0 \cdot 10^{11}$	
$\gamma_{\mathrm{i},1}$	$\gamma_\mathrm{mean} - 3\,\varsigma$		$5.0 \cdot 10^{7}\ \mathrm{eV}/(m_\mathrm{e}c^2)$
$\gamma_{\mathrm{i},0}$	$\gamma_\mathrm{mean} + 3\,\varsigma$		$5.0 \cdot 10^{11}\ \mathrm{eV}/(m_\mathrm{e}c^2)$
$\phi \,/\, {}^\circ$	2.0	2.0	2.0
$l \,/\, \mathrm{m}$	$2.4 \cdot 10^{15}$	$2.4 \cdot 10^{15}$	$2.4 \cdot 10^{15}$
$K_\mathrm{lines} \,/\, \mathrm{m}^{-3}$	$1.2 \cdot 10^{9}$	$1.1 \cdot 10^{9}$	$1.2 \cdot 10^{9}$
$K_\mathrm{i} \,/\, \mathrm{s}^{-1}\mathrm{m}^{-3}$	$5.8 \cdot 10^{-3}$		$6.5 \cdot 10^{-3}$
$K_\mathrm{P} \,/\, \mathrm{s}^{-1}\mathrm{m}^{-3}$	0.012	0.014	$8.9 \cdot 10^{3}$
$\gamma_\mathrm{mean}\, m_\mathrm{e} c^2 \,/\, \mathrm{eV}$	$2.0 \cdot 10^{11}$		$2.0 \cdot 10^{11}$
$\varsigma \,/\, \gamma_\mathrm{mean}$	0.20		0.20
α	-2.1	-2.2	-2.3
β		0.068	
Number of degrees of freedom	7	9	7
Number of fitting parameters	7	5	7
χ^2_red	0.90	0.62	0.83
$L_\mathrm{lines,\,theo} \,/\, \mathrm{W}$	$7.4 \cdot 10^{37}$	$5.7 \cdot 10^{37}$	$7.3 \cdot 10^{37}$
$L_\mathrm{UV,\,theo} \,/\, \mathrm{W}$	$4.5 \cdot 10^{37}$	$2.9 \cdot 10^{37}$	$4.5 \cdot 10^{37}$
$r_\mathrm{BLR} \,/\, \mathrm{m}$	$4.9 \cdot 10^{14}$	$4.0 \cdot 10^{14}$	$4.9 \cdot 10^{14}$

Table 6.2: Values found for the input parameters by fitting the IC pair cascade model in the various cases to the Fermi LAT spectrum. The obtained χ^2_red are also given for each case. Luminosity measures of the BLR and the corresponding C IV time-lag radius are presented, too.

While most authors (like e.g. Liu and Bai, 2006; H. E. S. S. Collaboration et al., 2019) do not include extreme-UV and soft-X-ray lines into their BLR spectra (because observational evidence for their existence is weak due to the intergalactic medium being opaque at these wavelengths (see e.g. Wilms, Allen and McCray, 2000)), such emission lines are included in the present work (because synthetic photo-ionisation spectra indicate the existence of atomic emission lines up to the X-ray regime), causing the pair-absorption optical depth to be non-zero down to slightly below 1 GeV. For example, Tavecchio and Ghisellini (2012) assumed a BLR with shell geometry, used an illuminating AF luminosity similar to the present work and obtained an optical depth that is comparable to the present-work optical depth above $\approx 10\,\mathrm{GeV}$, but smaller at lower energies.

As a result of the neglecting of near-UV and optical emission lines, the present-work optical depth decreases with increasing photon energy $\gtrapprox 90\,\mathrm{GeV}$. Including near-UV and optical emission lines into the BLR spectrum (like e.g. Tavecchio and Mazin, 2009; H. E. S. S. Collaboration et al., 2019) would make the BLR optically thick at energies above $\approx 100\,\mathrm{GeV}$ and consequently the gamma-ray photons observed by the LAT around 100 GeV could not be explained within this framework.

Realistic BLR spectra would not only consist of a set of emission lines, but also of a continuum, which is a reflected fraction of the AF and the coronal emission illuminating the BLR. In this work's approach, the continuum contribution to the BLR spectrum is not implemented separately, but it is included into the coefficients $K_{\mathrm{line},\,i}$. This makes it understandable why the $K_{\mathrm{line},\,i}$ at soft-X-ray energies are comparable to the $K_{\mathrm{line},\,i}$ at UV wavelengths (see table 6.1).

The obtained EEDs are shown in the left-hand side column of figure 6.3. Cases 1a and 1c are almost equal at high energies, because here the Gaussian injection dominates in forming the EED. The additional PL electron injection in case 1c becomes influential at lower energies, where it compensates the escape that is dominating in case 1a at low energies. The kink of N in case 1c is due to the cutoff $\gamma_{\mathrm{i},1}$. Case 1b is similar to case 1a except for the Gaussian peak contribution.

For the cases 1a, 1b and 1c, the photon injection rate, the production rate and their sum $\dot{n}_{\gamma,\mathrm{i}} + \dot{n}_{\gamma,\mathrm{IC}}$ are shown by the lilac curves in the right-hand side panels of figure 6.3. In case 1a, new photons with energies below 0.3 GeV are mainly due to injection, while the IC up-scattering is responsible for the majority of new photons above 0.3 GeV. In case 1b, injection dominates below 1 GeV and above 100 GeV due to the curvature of the LP spectral injection rate. In case 1c, the entire photon population is due to IC up-scattering, but the photon production rate is very similar to $\dot{n}_{\gamma,\mathrm{i}} + \dot{n}_{\gamma,\mathrm{IC}}$ of case 1a. Due to the cascading, the emerging gamma-ray spectra have no memory about the type of injected particles.

For the cases 1a, 1b and 1c, the photon number densities and their two contributions are shown by the blue curves in the right-hand side panels of figure 6.3. As described in chapter 3 (and in particular by equation 3.31), the number density is the result of the interplay of the injection rate, the IC production rate and the loss rate. This is reflected in the blue lines being formed not only by the course of $\dot{n}_{\gamma,\mathrm{i}}$ and/or $\dot{n}_{\gamma,\mathrm{IC}}$, but also by the contributions of the photon loss rate. The various dips in the number densities ensue from the more or less pronounced bumps in the loss rate, controlled by the $K_{\mathrm{line},\,i}$. The strongest absorption feature at several 10 GeV is due to the He, H and C IV lines and causes the dip in the LAT data, as can be seen in figure 6.4. There, the obtained flux densities for the cases 1a (blue), 1b (pink) and 1c (also blue) are compared to the observational points (green). The spectral bump above $\approx 70\,\mathrm{GeV}$ is resulting on the one hand from the Gaussian electron injection in case 1a and 1c and from the curvature of the LP gamma-ray injection in case 2 and on the other hand from the moderate optical depth at these energies.

6.3 Inferences about the Location of the Gamma-Ray Emission

All sub-cases of case 1 provide a satisfying fit of the observational data irrespective of the nature of the injected particles. This supports the possibility that case 1 is a valid and robust model and correspondingly that the detected gamma rays emanate from the outer BLR border after being

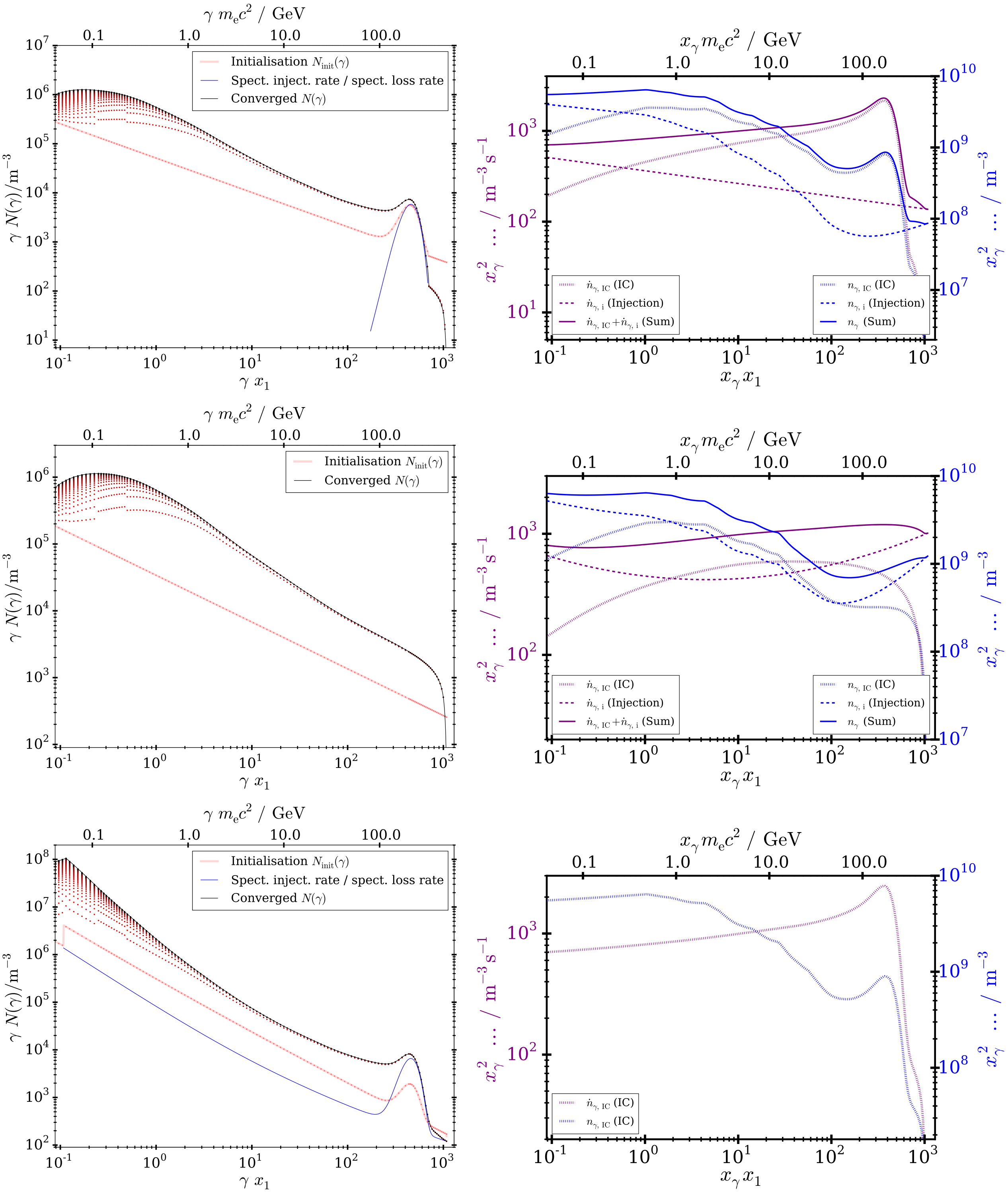

Figure 6.3: Steady-state EEDs and gamma-ray photon spectra of the IC pair cascades in 3C 279. For what is shown in the panels in the left-hand side column, see the caption of figure 5.2. The colour scale of the iterated points is an equidistant transition from pure red at $j = 0$ to pure black at $j = j_{\mathrm{final},\,k}$. In all panels, x_1 is the energy of the O VII line at 2.2 nm. In the panels in the right-hand side column, on the left-hand side y-axis (lilac), the product of the squared photon energy with the spectral production rate $\dot{n}_{\gamma,\,\mathrm{IC}}$ (dotted), with the spectral injection rate $\dot{n}_{\gamma,\,\mathrm{i}}$ (dashed) and with $\dot{n}_{\gamma,\,\mathrm{IC}} + \dot{n}_{\gamma,\,\mathrm{i}}$ (solid) is plotted versus the product of the dimensionless photon energy with x_1 (bottom x-axis). On the right-hand side y-axis (blue), the product of the squared photon energy with the photon number density (given via equation 3.31, solid line) and with its two contributions $n_{\gamma,\,\mathrm{i}}$ (dashed) and $n_{\gamma,\,\mathrm{IC}}$ (dotted) is plotted. The panels in the first, second, third row are for the case 1a, 1b, 1c, respectively. The top x-axis shows the dimensional electron/photon energy in GeV.

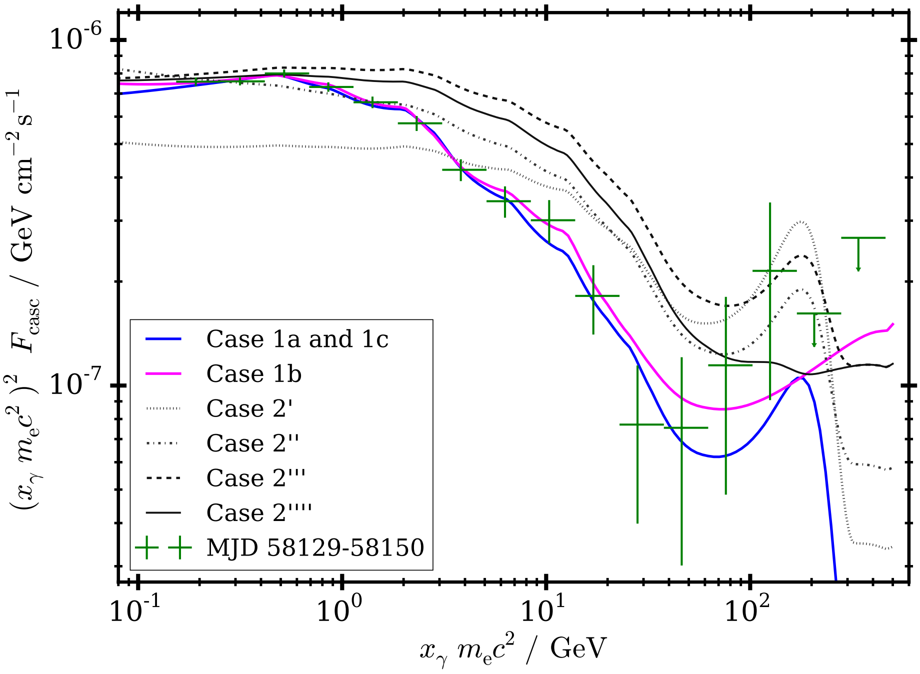

Figure 6.4: Modelled cascade spectra of 3C 279 and the Fermi-LAT data points. Plotted is the energy flux density versus the photon energy. The green data points are the LAT detections / upper limits as analysed by Wendel, Shukla and Mannheim (2021). The coloured, grey lines correspond to cascades in the BLR (cases 1), in the diluted photon field outside of the BLR (cases 2), respectively. The modelled spectra of case 1a and 1c are almost indistinguishable within plotting accuracy.

reprocessed by a cascade in the BLR.

It is straightforward to determine the total BLR luminosity, now. In analogy to equation 5.10, it is

$$L_{\mathrm{lines,\,theo}} = 4\pi l^2 \cdot \sum_{i=1}^{11} K_\mathrm{lines}\, K_{\mathrm{line},\,i} \cdot m_\mathrm{e}c^3. \tag{6.6}$$

Leaving the emission lines with $\lambda_i < 10\,\mathrm{nm}$ aside and adding up the lines from $i = 4$ to 11, the UV luminosity $L_{\mathrm{UV,\,theo}}$ of the BLR is obtained. From this UV luminosity, the BLR's radial size r_BLR can be estimated via equation 2.16. The resulting values are shown in table 6.2. When applying equation 2.16, the 135 nm luminosity $L_{135\,\mathrm{nm}}$ is to be used, which however cannot be directly determined from the BLR spectrum used in this work. To determine $L_{\mathrm{UV,\,theo}}$, all emission lines down to 10 nm were used, with the justification that $L_{135\,\mathrm{nm}}$ is generally considered as a proxy for the UV luminosity. If only lines between $135\,\mathrm{nm} - 135/2\,\mathrm{nm} = 67.5\,\mathrm{nm}$ and $135\,\mathrm{nm} + 135/2\,\mathrm{nm} = 202.5\,\mathrm{nm}$ are used, the radii will be about half of those given in table 6.2. Using equation 2.15 instead of equation 2.16, the values of r_BLR are smaller by a factor ≈ 0.9. Taking additionally into account that there is still uncertainty in the normalisations of radius luminosity relations throughout the literature (Ghisellini and Tavecchio, 2008; Kilerci Eser et al., 2015), the values found for r_BLR can be considered to agree with l as obtained from the cascade simulations (see table 6.2). This validates the assumption that the BLR photon field is the target photon field of the cascade.

Now, the cascade simulation of case 2 is considered to examine the possibility of cascading and radiation production outside of the BLR, at double a distance compared to cases 1. Case 2 has the HE photon and electron injection rate functions 6.1 and 6.2 in common with case 1a. Case 2 has also the parameters $K_{\mathrm{line},\,i}$ in common with case 1a, because the relative line strengths do not change with the dilution of the photon density. However, the value of K_lines is taken to be a factor 0.25 times the one obtained in case 1a (as stated in table 6.2), while the escape lengthscale l in case 2 is equal to case 1a, see figure 6.1. By this, a cascade with lower influence of PP and IC scattering and correspondingly with increased influence of escape is emulated. To begin with, the injection function parameters K_P, K_i, α, γ_mean, ς and ϕ are also kept equal to the ones presented for case 1a in table 6.2. The cascade simulation is executed and the emerging spectrum is shown (by the grey dotted curve labelled $2'$) in figure 6.4 and yields $\chi^2_\mathrm{red} = 106$. The injection function parameters and ϕ are not necessarily required to be equal from case 1a to case 2 but they are fitting parameters in case 2. Therefore, varying K_P, K_i, α, γ_mean, ς and ϕ, it is tried to fit the case 2 model to the LAT data points. If it is possible to find a set of the fitting parameters that can describe the observational data with the reduced K_lines, the possibility of gamma-ray production outside of the BLR is validated.

A satisfactory fit can, however, not be found. Why this is the case, can be understood as follows. The reduction of K_lines by a factor 0.25 causes less pair absorption and a stronger influence of escape. This leads to an increased flux density above $\approx 4\,\mathrm{GeV}$ and to a decreased flux density below $4\,\mathrm{GeV}$ (as obvious from the case $2'$ curve in figure 6.4). Then, to meet the data points below $4\,\mathrm{GeV}$, the normalisation K_P has to be increased. This as well as a gentle decrease of K_G to not overshoot the points around $100\,\mathrm{GeV}$ is done in the case $2''$ (see dash-dotted curve in figure 6.4), yielding $\chi^2_\mathrm{red} = 12.8$. However, this leads to an increasing contribution of $\dot{n}_{\gamma,\mathrm{i}}$ to the flux density, resulting in too soft a slope below $\approx 0.6\,\mathrm{GeV}$. This can be mitigated by increasing α, which is performed in case $2'''$ (see figure 6.4), where the slope below $0.6\,\mathrm{GeV}$ is in agreement with the data. However, the increased α also increases the flux density in the range around $10\,\mathrm{GeV}$ far over the observational points (as obvious from the case $2'''$ curve). To meet these points again, two possibilities remain. First, one can almost entirely remove the electron injection and thus reduce $\dot{n}_{\gamma,\mathrm{IC}}$ at energies above several $10\,\mathrm{GeV}$. In case $2''''$, the electron injection is lowered by a factor ≈ 0.1, but still the points around $10\,\mathrm{GeV}$ are overshot. If the points around $10\,\mathrm{GeV}$ were to be met, one would have to reduce the injection above $10\,\mathrm{GeV}$ even more. But then, the data points around $100\,\mathrm{GeV}$ could not be met any more, ruling out this possibility. Second, one could increase the pair absorption around $10\,\mathrm{GeV}$ by increasing the corresponding $K_{\mathrm{line},\,i}$. This would however raise the BLR luminosity over reasonable values and it would contravene the assumption of constant $K_{\mathrm{line},\,i}$. Hence, cascading and emission outside of the BLR cannot be reconciled with the Fermi LAT data from MJD 58129 to MJD 58150 within the model presented here.

6.4 Discussion

Lepto-hadronic or pure leptonic models like SSC and EC models involving relativistically moving blobs can explain non-thermal SEDs of blazars like 3C 279 consisting of a synchrotron hump and an HE hump. However, short-time gamma-ray variability with high amplitudes as well as spectral sub-structure in the SED is indicative for additional radiation processes (Shukla and Mannheim, 2020; Wendel et al., 2021b). One example is the considered period of high activity from 3C 279 from MJD 58129 to MJD 58150. It was shown that emission from an IC pair cascade induced by relativistic electrons and/or HE photons in or near the BLR can account for the spectral sub-structure (in particular for the pair-absorption dip around several $10\,\mathrm{GeV}$) in the Fermi LAT data. Three sub-cases (cases 1a, 1b and 1c) were considered, differing in the particle composition and in the concrete spectral shape of the injection rate. The three sub-cases have in common that the cascade happens in the BLR (case 1). In all three sub-cases, the numerically determined emerging spectrum can describe the data points, even though the contributions of the injected photons (attenuated through pair absorption) and of the IC-produced photons to the total spectrum vary between the sub-cases. This insensitivity of the model fit to the concrete injection rate underlines the robustness of the finding that the HE gamma rays emanate from BLR distances. The escape length (which is equal to the cascade region size and approximately equal to the BLR radius) was found to be $2.4 \cdot 10^{15}\,\mathrm{m}$ and agrees with a radius estimate based on the 135 nm luminosity of the BLR. Furthermore, this finding agrees with the gamma-sphere radius around $1\,\mathrm{GeV}$ as estimated by Blandford and Levinson (1995).

A cascade on target photons from outside of the BLR was modelled with usage of a lowered soft photon density and the same size (escape timescale) of the interaction region (case 2). Within these prerequisites, finding reasonable fits to the data was not possible. This substantiates the finding that the gamma rays detected by the LAT emanate from the BLR outer edge.

Below $\approx 0.1\,\mathrm{GeV}$, the emission of the considered cascade decreases with decreasing energy. This is because of the limitation of radiation reprocessing in this energy regime due to the dominating impact of escape. Therefore, this model cannot account for emission below several $10\,\mathrm{MeV}$. Still, SSC and/or EC emission is necessary to account for the broadband two-hump blazar SED. Hence, the present model is no substitute of common SSC or EC models but an addendum to account for the fine structure on top of the beamed jet emission. In the consideration of Mrk 501 in chapter 5, the total theoretical SED was yielded as a superposition of SSC emission and cascaded emission. This adding of SSC or EC emission from a blob farther downstream the jet was not done in the case of 3C 279. This is justified because in the limited Fermi LAT energy range the SSC or EC emission is a featureless PL (possibly with cutoff) or an LP. Adding a PL or an LP to the cascaded spectra would alter the fitting parameters of the injection rates, but it would not introduce a difference between case 1 and case 2 and therefore it would not change the findings concerning the spatial origin of the radiation.

Of course, the finding that the emission region is located at BLR scales in this certain activity phase of 3C 279 can neither be generalised to other periods or objects, nor does it invalidate the findings about the location of the gamma-ray emission region discussed in section 2.4.6. In AGN jets, multiple emitting regions can exist simultaneously and can propagate along the jet (Stern and Poutanen, 2011; Stern and Poutanen, 2014; Aleksić et al., 2014b; Lei and Wang, 2015; Finke, 2016; Rani et al., 2018; Patiño-Álvarez et al., 2019; Shukla and Mannheim, 2020; Acharyya, Chadwick and Brown, 2021). Thus, evidence for a certain emission location does not exclude emission at one or more different locations, especially during different times or for other objects.

Chapter 7

Conclusion

The aim of this work was to develop a radiation emission scenario, that can provide explanations for observed, spectral or temporal peculiar features of blazar SEDs. The concatenated interaction of IC scattering and PP is presenting such an emission process beyond conventional leptonic models.

7.1 Radiation Processes beyond Conventional Models

Linear IC pair cascades with escape terms were mathematically described by two coupled kinetic equations. The chosen approach incorporates several differences and improvements in comparison to previous works but also has drawbacks and offers starting points for further refinement.

In this work, the interaction region was assumed to be spatially confined, meaning that the escape timescales are finite. Thus, the region can be optically thick or thin and the cascade is not necessarily saturated as it was the case in the works of Zdziarski (1988) and Wendel et al. (2017). This broadens the field of astrophysical applications of this type of cascade.

Furthermore, in the cascade simulation, the region and the particle densities were assumed to be homogeneous and isotropic. The homogeneity together with the finite escape timescale implies sharp borders with unphysical jump discontinuities. The setting would be really self-consistent and even more versatile, if a radial coordinate was introduced, along which the densities and accordingly the interaction rates as well as consequential quantities can vary. Such an approach, similar to the work by Gould (1979) who however dealt with an SSC-like process with fixed emission coefficients and without PP and who consequently did not take cascading into account, can be pursued in future work, if the additional coordinate does not raise the computational effort over acceptable borders. Likewise, the introduction of a time coordinate would broaden the applicability of the model, but it would also increase the computational effort.

The isotropy and spherical symmetry assumed in the cascade modelling is contrasting with the assumption of beamed injection, cascade and emission. Nevertheless, this geometric inconsistency does not invalidate the assumptions and the used mathematical description of the radiation processes as long as the target photon distribution is isotropic, which was shown to be the case in chapters 5 and 6.

The differences of the radiation processes involved in the present work to those of conventional SSC or EC models are as follows.

- In conventional models, like e.g. in the model by Tavecchio, Maraschi and Ghisellini (1998) used by the MAGIC Collaboration et al. (2020), the EED is chosen and fixed without deeper trials to give a motivation or a justification for the choice. In the present work, the EED is determined self-consistently by taking into account the balance between injection, PP, energy losses via IC down-scattering and escape. This is a more realistic treatment in comparison to conventional SSC or EC models.

- In the present work, the steady-state electron and HE photon distributions are determined self-consistently as soon as the injection rates have been specified. To get reasonable results via this approach, the injection energies must be quite high meaning that pre-acceleration is implicitly assumed to have taken place before the electrons enter the interaction region. Nevertheless, the injection rates have to be chosen arbitrarily. It would be an improvement, that should be addressed in future work, to also include acceleration mechanisms in addition to injection into the electrons' kinetic equation (like e.g. in the work of Hu and Yan, 2021).

- The process of PP is consistently taken into account, not only through absorption of gamma-ray photons (pair absorption) but also through electron production. This leads to the cascading and to the evolution of further generations of gamma rays and electrons and to the repeated IC and PP processes. This approach complies with the suggestion by Marcowith, Henri and Pelletier (1995) and Vuillaume, Henri and Petrucci (2018) to not only pair-absorb an incident/injected spectrum by an exponential term but to allow for radiation production in the whole source.

- Synchro-curvature radiation is not incorporated in the present work. For the scenarios considered in chapters 5 and 6, this neglect is valid because of the following arguments. First, the momentum of the seed electrons perpendicular to the magnetic field is lost via synchrotron radiation briefly after the electrons are created in the vacuum gap (Viganò et al., 2015). Further acceleration in the gap and propagation behind it take place only along the magnetic field. Therefore the pitch angle rapidly becomes small and stays small due to the IC scattering and PP kinematics. Correspondingly, synchrotron emission might be negligible in the cascade on the emission-line photons. Second, the interaction regions with the line photons are located at BLR distances in this work. At such distances, the magnetic field lines' curvature radius is big enough that curvature radiation is negligible, too. These two reasonings presume that the magnetic field is still uniformly ordered and has not been isotropised yet. This assumption might be valid at BLR distances, but it is invalid farther downstream the jet. Therefore, in order to apply the IC pair cascade to emission regions at much smaller or greater distances, inclusion of synchro-curvature radiation seems indispensable.

As argued in section 3.2.2, the way of determining the emerging gamma-ray spectrum is more realistic than in the work of Wendel et al. (2017). Both the injected gamma rays diminished by losses (pair absorption and escape) and the IC-produced gamma rays diminished by losses are taken into account. This makes the simulated scenario applicable to cascades in both the optically thick and thin regime.

Further radiation processes can be relevant in certain astrophysical environments. For example, elastic scattering of HE photons on the cosmic microwave background (photon-photon scattering) can be relevant in the early universe at $z > 100$ (Zdziarski and Svensson, 1989). Moreover, triplet PP can be important in cascades in pulsar outer gaps with respect to particle multiplication and as an energy-loss mechanism (Wendel, 2013). Therefore, additionally to the above-mentioned implementation of synchro-curvature radiation, other radiation processes could be incorporated into the code to allow the scrutiny of cascade processes in a broader range of astrophysical scenarios.

Another powerful improvement would be to extend the cascades to non-linear ones. In this case, the photons created in the cascade would act as targets, too. This would necessitate two demanding tasks. First, the restriction of the target photon energies $x \ll 1$ has to be released, as the strict division between soft target photons and HE photons gets blurred. This would mean that the full interaction rates inferred by Jones (1968) are necessary, raising the computational effort considerably. Second, the target photon distribution is not fixed anymore, but is resulting from the electron distribution, which again is resulting from the target photon distribution. This problem could be computationally solved by implementing a superordinate iteration, an iteration of iterations. This would be an additional iterative algorithm that alternatingly determines the photon distribution and the electron distribution until both distributions converge.

Based on the two examples of Mrk 501 and 3C 279, observed spectral components, that challenge the pure two-humped SEDs as explained by SSC and EC models, are attributed to theoretically determined emission features from IC pair cascades. In the case of Mrk 501, an electron beam accelerated in a magnetospheric vacuum gap near a rotating SMBH initiates an electromagnetic cascade on emission-line photons from an ionised gas cloud. The gamma rays leaving the cascade region manifest as a narrow peak at 3 TeV in accordance with tentative evidence for such a feature in MAGIC telescopes data. Parameters (like the ADAF's electron temperature, the accretion rate and the number of clouds as well as their reprocessing fraction) necessary within this model are found to be plausible. The transient character of gap activity in connection with the randomness of an encounter event of a cloud with the electron beam can account for the intermittency of the spectral bump.

A similar cascade is computed for 3C 279. Various functions are used for the injection rate initiating the IC pair cascade. When cascading in the BLR photon field is considered, the reprocessed gamma-ray spectrum displays a trough around several 10 GeV, irrespective of the spectral form of the injection rate. The spectrum from this cascade in the BLR can explain the Fermi-LAT data from MJD 58129 - 58150. A cascade in the diluted photon field outside of the BLR cannot satisfactorily fit these data. The reason for this is that the ratio of escape to reprocessing in the weak photon field is such that the resulting spectrum is so hard that the trough around several 10 GeV cannot be reproduced.

7.2 Drawbacks and Advantages of the Numerical Approach

A robust numerical code was developed for the purpose of iteratively solving for the steady-state EEDs and SEDs.

The iteration scheme (scheme 2, see section 4.3.2) used to solve the electrons' kinetic equation iterates pointwise from high γ towards lower values. By this, in every iteration step the best-possible approximation of N can be used, making the iteration scheme much more efficient than the scheme in which the whole sampling range is iterated at once (scheme 1, see section 4.3.1 as applied by Wendel et al., 2017). The iteration can be performed down into the Thomson regime without additional computational methods like solving the continuity equation and interpolating in the Thomson-to-KN transition as done by Zdziarski (1988) and Wendel et al. (2017).

The code is parallelised at two sites:

- The iteration can be performed not only at one sampling point at a time, but at several points simultaneously, as outlined in section 4.4.1. These parallel iterations are distributed to several workers on separate CPU cores. The capability to reduce the runtime via this approach is however limited. For increasing number of iterating workers, inaccuracies occur and accumulate because of the ignorance of the course of N due to the not-finished-yet simultaneous iterations.
- In addition to the parallelisation of the iteration, the computation of the term Q_{PP} is parallelised by making use of the ISA and distributing the part integrals to available cores (see section 4.4.2). The capability of this approach to reduce the runtime is limited, too. This has two reasons: First, it is impossible to divide the integration range in such a way that all the part integrals have an (almost) equal amount of CPU hours. Second, even if this was possible, the following would be the case. If the number of part integrals was increased over a certain number (i.e. if the integration ranges of the part integrals were reduced below a certain width), the CPU hours of the single part integrals would not decrease any more.

Using iteration scheme 2, the runtime of one complete determination of N can be reduced by a factor ≈ 0.2 through these parallelisation techniques (see section 5.3).

These findings with respect to parallelisation possibilities are valid if all integrations are executed with `scipy.integrate.quad`, which is the case in this work. The advantage of using `scipy.integrate.quad` is that it is a robust, versatile and widely approved, adaptive integration algorithm, especially to integrate fast-changing integrands and integrands with sharp features. Error tolerances can be specified and actual error estimates are supplied. A disadvantage of `scipy.integrate.quad` is that, as described above, the parallelisation potential is limited, because the CPU hours needed for one integration cannot be evenly distributed to arbitrarily many cores. Another drawback is the following: In the determination of C and P (equation 3.11 and 3.24), the integrand has to be evaluated very often. To shorten the evaluation time, it would be possible to evaluate the integrand once and for all along the three independent variables and to store the results in a multi-dimensional grid. Then, the integration algorithm could retrieve the stored values, which can yield a time gain. This approach is, however, not feasible together with `scipy.integrate.quad`. The multi-dimensional grid containing the values of the integrand would essentially be a multivariate piecewise-constant function with a large number of discontinuities between the constant parts. These discontinuities would disturb the algorithm of `scipy.integrate.quad` and would cause long integration times and possibly raise errors.

Integrations through self-taylored integrators can possibly resolve these problems. First, they can be parallelised more effectively, as the summation can be concurrently performed by an arbitrary number of workers. Second, together with a self-taylored integration algorithm, a stored piecewise-constant function can be used instead of the lengthy integrand. The implementation of self-taylored integrators and the use of multi-dimensional grids storing the results of the actual integrand can be working points for future improvements of the code, if an additional decrease of the CPU hours and/or higher parallelisation are desirable.

7.3 Outlook

The observations presented in this work challenge conventional models. Therefore, a radiation model incorporating emission from an IC pair cascade was developed and it was examined whether this model complies with the observations. The findings underline that the full radiation reprocessing and correct radiation transport are indispensable in theoretical models that aim to produce realistic gamma-ray spectra of AGN jets, especially if the radiation originates from optically thick regions.

As explained above, the incorporation of synchrotron radiation is a step towards a more realistic and more versatile model of radiation production in AGN jets. In synchrotron IC pair cascades, the electrons lose energy by the emission of synchrotron photons, which typically have energies in the IR-to-X-ray regime (see section 2.4.2). Consequently, they act as soft target photons in addition to the external soft photons. The external photon population is assumed to be a fixed input function. However, the synchrotron photon population ensues from the electron distribution, which itself is influenced by the synchrotron target photons. This is a similar problem as in the case of non-linear cascades mentioned above. It can be addressed by repeatedly determining the electron distribution (via a common iteration as described in section 4.3.2) and the resulting synchrotron photon distribution. This results in a superordinate iteration. In every iteration step, the electron distribution and the synchrotron distribution are determined anew and the latter is included (in addition to the external photon distribution) in the soft target photon distribution in the subsequent iteration step. Such a cascade is actually not a linear one. It is however distinct from the above-mentioned non-linear cascade, in which IC-produced gamma-ray photons serve as targets.

This extension of the IC pair cascade to a synchrotron IC pair cascade was indeed performed, as mentioned in chapter 4. Performing one complete superordinate iteration is however computationally demanding. The problem is not the evaluation of the synchrotron emissivity via integrating over the modified Bessel function. This evaluation of the synchrotron emissivity is causing very few CPU hours. From the synchrotron emissivity, the number density is determined. The latter is evaluated at several sampling points. Between the sampling points the number density is interpolated by a piecewise-linear function, whose advantage is that it can be evaluated much faster than the integral over the modified Bessel function. The problem is, that typical synchrotron distributions extend over five to ten orders of magnitude along energy. Using such broad distributions in C and P (equation 3.11 and 3.24), strongly increases the CPU hours in comparison to the use of δ_{Dirac} peaks as in the present work. Together with the need for an iteration of iterations, this raises the runtime of one superordinate iteration up to several 10 h. Therefore, this type of synchrotron IC pair cascades is experimental and not ready for application to astrophysical problems yet. If a higher degree of parallelisation can be achieved through the implementation of a self-taylored integrator (see preceding section), synchrotron IC pair cascades can be computed. This would widen the range of applications of the code and it would raise the model to a refined SSC + EC model, that can not only account for the broadband blazar SEDs but also explain narrow spectral features.

Such a theoretical model, will be an ideal complement of the Cherenkov Telescope Array (CTA). This is a currently built set of instruments comprised out of two arrays of next-generation IACTs. More than 100 telescopes of varying size will be deployed by the international collaboration at two observational sites, one on the island of La Palma in immediate vicinity to the MAGIC telescopes to cover the northern hemisphere of the sky, and the other in Chile in the Atacama dessert near to the Very Large Telescope to observe the southern hemisphere. The CTA will have superior specifications in comparison to contemporary IACTs. In particular, the sensitivity will be ten times stronger than the one of current IACTs. Together with a larger collection area and a higher energy resolution, this will enable improved assessment of short-time variability as well as more precise characterisation of fine structure in observational spectra. If the narrow 3 TeV feature tentatively found in Mrk 501 was real and not only a one-time event but a recurrent one, the CTA will substantiate the evidence for such spectral peculiarities and will thus provide a deeper glimpse into the anatomy of AGN jets. This will allow theoretical models of gamma-ray emission from AGN jets to be falsified and stimulate further refinements. Together with improved abilities to explore the time domain of emission processes and in conjunction with dense multi-wavelength or multi-messenger coverage due to additional detectors, our knowledge about the most powerful persistent engines will be enhanced. In the course of this, a multitude of new questions will open up and call for sophisticated answers. To avoid the impression that this ongoing search is a futile or desperate endeavour, it is inspiring to recall the words of the astrophysicist, scientist and author Carl Sagan:

> "We make our world significant by the courage of our questions and the depth of our answers."
>
> Sagan, Tyson and Druyan (2013)

List of Physical Constants, Quantities and Variables

This is a list of all the physical and mathematical symbols that are used throughout the text. If one designator is used for different quantities, it is listed separately for each meaning.

Sign	**Description**	**Unit**
a	Dimensionless angular momentum of a BH	
A	Mean Comptonisation amplification factor	
A_{ADAF}	Surface area of an ADAF	m^2
b_i	The i-th integration border used in the ISA; Here, it is $i \in \{1, 2, \ldots, n, n+1\}$	same as the integration variable's unit
b_{l}	Lower integration border of a definite integral	same as the integration variable's unit
b_0	Upper integration border of a definite integral	same as the integration variable's unit
B	Magnetic flux density	T
c	Velocity of light in vacuum	$\mathrm{m\,s^{-1}}$
C	Spectral IC scattering interaction rate; Probability per unit time and per unit final energy for an electron with incident energy γ to get the final energy γ' in an IC scattering event	$\mathrm{s^{-1}}$
D	Relativistic Doppler factor	
D	Luminosity distance of a source	m
e	Elementary charge; Electric charge of the proton	C
E_1	Exponential integral defined in equation 5.1.1 of Abramowitz and Stegun (1968)	
E_{IC}	Abbreviation used in the IC scattering kinematics of equation 3.2	
E_{PP}	Abbreviation used in the PP kinematics of equation 3.18	
f	Arbitrary function to be integrated	same as the unit of the quantity f stands for
F	Auxiliary function for the spectral bremsstrahlung luminosity $L_{\mathrm{ADAF,\,brems}}$ of an ADAF; Equation 28 by Mahadevan (1997)	
F	Spectral flux density; Number of streaming photons per unit area, per unit time and per unit (dimensioned) energy interval	$\mathrm{m^{-2}\,s^{-1}\,J^{-1}}$
F_{casc}	Spectral flux density emerging from the cascade interaction region; Number of streaming photons per unit area, per unit time and per unit (dimensioned) energy interval	$\mathrm{m^{-2}\,s^{-1}\,J^{-1}}$
F_{SSC}	Spectral flux density emerging from the SSC region; Number of streaming photons per unit area, per unit time and per unit (dimensioned) energy interval	$\mathrm{m^{-2}\,s^{-1}\,J^{-1}}$

Sign	**Description**	**Unit**
$\mathcal{F}$	Auxiliary functional for concisely writing equation 3.33 with the unknown quantity N and its independent variable as arguments, i.e. without the input quantities as arguments	m^{-3}
$\mathcal{F}'$	Auxiliary functional for concisely writing equation 3.33 with all unknown quantities and the independent variable as arguments	m^{-3}
G	Newtonian constant of gravitation	$\mathrm{m}^3\,\mathrm{kg}^{-1}\,\mathrm{s}^{-2}$
$\mathcal{G}$	Auxiliary functional for concisely writing equation 3.31 with the unknown quantity N and its independent variable as arguments, i.e. without the input quantities as arguments	m^{-3}
$\mathcal{G}'$	Auxiliary functional for concisely writing equation 3.31 with all unknown quantities and the independent variable as arguments	m^{-3}
h	Height of an AF; Complete diameter in vertical direction	m
h_{gap}	Height of a vacuum gap; Extent along the radial coordinate	r_{S}
i	Index of summation; Running or counting index	
j	Running index for counting the iteration steps; In scheme 1 it is $j \in \{0, 1, \ldots, j_{\mathrm{final}}\}$ irrespective of k; In scheme 2 it is $j \in \{0, 1, \ldots, j_{\mathrm{final},\,k}\}$ at the k-th sampling point; Therefore, in context of scheme 2 it would be mathematically correct to always write j_k instead of just j, but this is omitted for the sake of readability	
j_{final}	Total number of iteration steps in the iteration scheme 1	
$j_{\mathrm{final},\,k}$	Total number of iteration steps used at the k-th sampling point $\gamma_{k,\,j}$ in the iteration scheme 2	
J	Angular momentum	$\mathrm{m}^2\,\mathrm{kg}\,\mathrm{s}^{-1}$
k	Running index, used for numbering of the sampled Lorentz factors $\gamma_{k,\,j}$; In scheme 2 it is $k \in \{1, 2, \ldots, \kappa\}$ irrespective of j; In scheme 1 it is $k \in \{1, 2, \ldots, \kappa_j\}$ in the j-th iteration step; Therefore, in context of scheme 1 it would be mathematically correct to always write k_j instead of just k, but this is omitted for the sake of readability	
k'	A certain reference value of k meaning the value of k, where N is actually evaluated or considered	
K_{i}	Total electron injection rate per unit volume (in form of the Gaussian-distributed electrons); The total number of electrons that are injected (in form of the Gaussian-distributed electrons) into the cascade per unit time and per unit volume	$\mathrm{m}^{-3}\,\mathrm{s}^{-1}$
$K_{\mathrm{line},\,i}$	Ratio of the energy flux density of the i-th emission line to the energy flux density of the (hypothetical) hydrogen Balmer β line; Proxy for the strength of line i	
K_{lines}	Coefficient of the spectral number density of emission line photons; Proxy for the emission line photons' total number density	m^{-3}
K_{PP}	Pair materialisation rate per unit volume; Number density of electron positron pairs that are created in the magnetosphere per unit time	$\mathrm{m}^{-3}\,\mathrm{s}^{-1}$
K_{P}	Coefficient of the PL or LP spectral injection rate per unit volume	$\mathrm{m}^{-3}\,\mathrm{s}^{-1}$
l	Length; In context of the cascade in 3C 279, this is the escape length of the interaction region	m
$L_{135\,\mathrm{nm}}$	Monochromatic continuum luminosity at a wavelength of 135 nm multiplied by 135 nm; Proxy for the continuum luminosity centred around 135 nm	W

Sign	**Description**	**Unit**
L_{ADAF}	Spectral luminosity of an ADAF	$\mathrm{W\,Hz^{-1}}$
$L_{\mathrm{ADAF,\,brems}}$	Bremsstrahlung contribution to the spectral luminosity of an ADAF	$\mathrm{W\,Hz^{-1}}$
$L_{\mathrm{ADAF,\,IC}}$	IC contribution to the spectral luminosity of an ADAF	$\mathrm{W\,Hz^{-1}}$
$L_{\mathrm{ADAF,\,sync}}$	Synchrotron contribution to the spectral luminosity of an ADAF	$\mathrm{W\,Hz^{-1}}$
$L_{\mathrm{ADAF,\,sync,\,1}}$	Synchrotron contribution to the spectral luminosity of an ADAF from inside of the radius $r_{\mathrm{ADAF,\,out}}$	$\mathrm{W\,Hz^{-1}}$
$L_{\mathrm{ADAF,\,sync,\,2}}$	Synchrotron contribution to the spectral luminosity of an ADAF from outside of the radius $r_{\mathrm{ADAF,\,out}}$	$\mathrm{W\,Hz^{-1}}$
$L_{\mathrm{ADAF,\,tot}}$	Total luminosity of an ADAF	W
L_{Edd}	Eddington luminosity	W
$L_{i,\,\mathrm{theo}}$	Luminosity in the emission line i of the entire BLR, determined theoretically	W
$L_{\mathrm{lines,\,theo}}$	Total emission-line luminosity of the entire BLR, determined theoretically	W
$L_{\mathrm{Ly}\,\alpha,\,\mathrm{obs}}$	Observed Lyman α emission-line luminosity of the entire BLR	W
$L_{\mathrm{UV,\,theo}}$	Luminosity of the entire BLR in UV emission lines, determined theoretically	W
L_ν	Spectral luminosity	$\mathrm{W\,Hz^{-1}}$
$\dot{m}$	Dimensionless accretion rate	
$\dot{m}_{\mathrm{crit}}$	Critical dimensionless accretion rate	
m_{e}	Mass of the electron	kg
m_{p}	Mass of the proton	kg
$\dot{M}$	Absolute accretion rate	$\mathrm{kg\,s^{-1}}$
M_{BH}	Mass of a BH	kg
$\dot{M}_{\mathrm{Edd}}$	Eddington accretion rate	$\mathrm{kg\,s^{-1}}$
$M_\odot$	Mass of the Sun	kg
n	Number of part integrals used in the ISA	
n_0	Generally the spectral number density of LE photons; In particular the spectral number density of emission-line photons	$\mathrm{m^{-3}}$
n_{ADAF}	Spectral number density of ADAF photons	$\mathrm{m^{-3}\,J^{-1}}$
$n_{\mathrm{ADAF,\,tot}}$	Total number density of ADAF photons	$\mathrm{m^{-3}}$
$n_{\mathrm{line},\,i}$	Total number density of photons from emission line i	$\mathrm{m^{-3}}$
n_{lines}	Total number density of all emission-line photons	$\mathrm{m^{-3}}$
n_{PP}	Total number density of ADAF photons able to self interact via PP	$\mathrm{m^{-3}}$
$n_{\mathrm{PP,\,1}}$	Total number density of ADAF photons able to self interact via PP; Determined based on the ADAF spectrum obtained by Mahadevan (1997)	$\mathrm{m^{-3}}$
$n_{\mathrm{PP,\,2}}$	Total number density of MeV ADAF photons able to self interact via PP; Determined based on an approximation from Levinson and Rieger (2011)	$\mathrm{m^{-3}}$
n_γ	Spectral number density of HE photons	$\mathrm{m^{-3}}$
$\dot{n}_\gamma$	Spectral change rate of HE photons per unit space volume; Number of HE photons, that are removed or inserted per unit space volume, per unit time and per unit (dimensionless) energy interval	$\mathrm{m^{-3}\,s^{-1}}$
$n_{\gamma,\,\mathrm{i}}$	Contribution to the HE photons' spectral number density, that ensues through the balance of injection, escape and absorption	$\mathrm{m^{-3}}$
$\dot{n}_{\gamma,\,\mathrm{i}}$	Spectral injection rate of HE photons per unit space volume; Number of HE photons, that are injected per unit space volume, per unit time and per unit (dimensionless) energy interval	$\mathrm{m^{-3}\,s^{-1}}$

Sign	Description	Unit
$n_{\gamma,\,\mathrm{IC}}$	Contribution to the HE photons' spectral number density, that ensues through the balance of production via IC up-scattering, escape and absorption	$\mathrm{m^{-3}}$
$\dot{n}_{\gamma,\,\mathrm{IC}}$	Spectral production rate of HE photons per unit space volume via IC scattering; Number of HE photons, that are IC produced per unit space volume, per unit time and per unit (dimensionless) energy interval	$\mathrm{m^{-3}\,s^{-1}}$
N	Spectral number density of electrons (or positrons)	$\mathrm{m^{-3}}$
$\dot{N}$	Spectral change rate of electrons per unit space volume; Number of electrons, that are removed or inserted per unit space volume, per unit time and per unit (dimensionless) energy interval	$\mathrm{m^{-3}\,s^{-1}}$
N_{cl}	Number of clouds in a BLR	
$\dot{N}_{\mathrm{i}}$	Spectral injection rate of electrons per unit space volume; Number of electrons, that are injected per unit space volume, per unit time and per unit (dimensionless) energy interval	$\mathrm{m^{-3}\,s^{-1}}$
N_{init}	Choice for the spectral number density of electrons used for the initialisation of the iteration	$\mathrm{m^{-3}}$
$N_{k,\,j}$	Value of the electron spectral number density determined at the k-th sampling point $\gamma_{k,\,j}$ during iteration step j	$\mathrm{m^{-3}}$
$(N_k)_{\mathrm{max}}$	Sequence containing for every γ_k the latest value (in other words the value with the highest j) of the electron spectral number density during the proceeding of the iteration via scheme 2	$\mathrm{m^{-3}}$
$\mathcal{N}$	Multiplication number of the electrons in the in-and-post-gap cascade	
P	Spectral PP interaction rate; Probability per unit time and per unit electron energy for an HE photon with energy x_γ to create an electron with energy γ (as well as its anti particle with energy $x_\gamma - \gamma$) in a PP event	$\mathrm{s^{-1}}$
P_{BZ}	BZ power	W
P_{gap}	Maximum power extractable from a magnetospheric vacuum gap	W
P_{i}	Power that is injected into the cascade interaction region	W
P_{SSC}	Power that is emitted by all electrons in the SSC emission region	W
Q	Electric charge	C
Q_{PP}	Spectral PP rate of electrons due to the interaction of injected and IC up-scattered HE photons with the soft target photons per unit space volume; Number of electrons, that are pair produced per unit space volume, per unit time and per unit (dimensionless) energy interval	$\mathrm{m^{-3}\,s^{-1}}$
r	Radius in a spherical coordinate system; Radius from the central BH	m
$r_{\mathrm{ADAF,\,in}}$	Radius of the inner border of an ADAF	m
$r_{\mathrm{ADAF,\,out}}$	Radius of the outer border of an ADAF	m
r_{BLR}	Radius of the BLR	m
r_{h}	Radius of the BH event horizon	m
r_{IC}	Abbreviation defined in equation 3.12 and used in the IC scattering interaction rate	
r_{ISCO}	Radius of the ISCO	m
r_{PP}	Abbreviation defined in equation 3.25 and used in the PP interaction rate	
r_{stat}	Radial distance of the static limit from the BH singularity	m
r_{S}	Schwarzschild radius	m

Sign	**Description**	**Unit**
R	Radius of some spherical object in the AGN surroundings; Radius of an emission region; Radius of a blob	m
R_{cl}	Typical radius of ionised gas clouds in Mrk 501	m
s_1	Dimensionless quantity describing the self-similar ADAF solution by Narayan and Yi (1995) and Mahadevan (1997)	
s_2	Dimensionless quantity describing the self-similar ADAF solution by Narayan and Yi (1995) and Mahadevan (1997)	
t	Time	s
T_{e}	Electron temperature in an ADAF	K
T	Temperature	K
$T_{\mathrm{esc\,e}}$	Escape timescale of the electrons	s
$T_{\mathrm{esc\,ph}}$	Escape timescale of the HE photons	s
T_{p}	Proton temperature in an ADAF	K
x	Dimensionless soft photon energy $\epsilon/(m_{\mathrm{e}}c^2)$	
x	Arbitrary independent variable in the context of numerical integration and the ISA	same as the unit of the quantity x stands for
x_0	Dimensionless upper cutoff energy of n_0; The distribution n_0 is vanishing above this energy	
x_i	Dimensionless soft photon energy of emission line i; Location of the i-th δ_{Dirac} peak in the case of n_0 being a discrete spectrum; Be careful not to confuse x_i with $i = 1$ and the quantity x_{l}	
x_{l}	Dimensionless lower cutoff energy of n_0; The distribution n_0 is vanishing below this energy; Be careful not to confuse this quantity with the sign x_i with $i = 1$	
x_γ	Dimensionless HE photon energy $\epsilon_\gamma/(m_{\mathrm{e}}c^2)$; In the context of an IC scattering event, this denotes the photon energy after the scattering event; In the context of a PP event, this is the energy of the incident HE photon	
$x_{\gamma,\,\mathrm{i},\,0}$	Upper cutoff of $\dot{n}_{\gamma,\,\mathrm{i}}$; The distribution $\dot{n}_{\gamma,\,\mathrm{i}}$ is zero above this dimensionless energy	
$x_{\gamma,\,0}$	Upper cutoff of n_γ; The distribution n_γ is zero above this dimensionless energy	
$x_{\gamma,\,\mathrm{i},\,\mathrm{l}}$	Lower cutoff of $\dot{n}_{\gamma,\,\mathrm{i}}$; The distribution $\dot{n}_{\gamma,\,\mathrm{i}}$ is zero below this dimensionless energy	
$x_{\gamma,\,\mathrm{max}}$	Maximum possible dimensionless HE photon energy after an IC scattering event	
$x_{\gamma,\,\mathrm{th}}$	Lowest possible dimensionless HE photon energy before a PP event	
z	Argument of the exponential integral E_1	Hz^{-1}
z	Redshift	
α	Viscosity of an AF	
α	PL index of BLR size-luminosity relations	
α	PL index of the spectral injection rate	
β	Ratio of gas pressure in an AF to total pressure	
β	Velocity of a moving blob relative to the velocity of light c	
β	Curvature parameter of an LP	
γ	Electron (or positron) Lorentz factor; In the context of an IC scattering event, this denotes the Lorentz factor before the scattering event; In the context of a PP event, this is one lepton's final Lorentz factor	

Sign	**Description**	**Unit**
γ_0	Upper cutoff of N; The distribution N is zero above this Lorentz factor	
$\gamma_{\mathrm{i},0}$	Upper cutoff of $\dot{N}_\mathrm{i}$; The distribution $\dot{N}_\mathrm{i}$ is zero above this Lorentz factor	
$\gamma_{\mathrm{i},\mathrm{l}}$	Lower cutoff of $\dot{N}_\mathrm{i}$; The distribution $\dot{N}_\mathrm{i}$ is zero below this Lorentz factor	
$\gamma_{\mathrm{IC},\max}$	Upper limit of the Lorentz factor for an incident electron undergoing IC scattering	
$\gamma_{\mathrm{IC},\mathrm{th}}$	Threshold Lorentz factor for an incident electron undergoing IC scattering	
$\gamma_{k,j}$	In the iteration scheme 1, Lorentz factor of the k-th sampling point during the j-th iteration step	
γ_k	In the iteration scheme 2, Lorentz factor of the k-th sampling point	
γ_{mean}	Mean Lorentz factor of the normal-distributed electron injection rate	
$\gamma_{\mathrm{PP},\max}$	Maximum Lorentz factor of an electron created in a PP event	
$\gamma_{\mathrm{PP},\min}$	Minimum Lorentz factor of an electron created in a PP event	
$\gamma_{\mathrm{Q},0}$	Upper cutoff of Q_{PP}; The function Q_{PP} is zero above this Lorentz factor	
γ'	Final electron Lorentz factor after an IC scattering event; Final Lorentz factor of the second lepton produced in a PP event; In the context of the electrons' kinetic equation of a cascade, this Lorentz factor is the integration variable	
$\gamma'_{\mathrm{IC},\min}$	Lowest possible final electron Lorentz factor after an IC scattering event	
Γ	Bulk Lorentz factor	
δ_{Dirac}	Dirac delta distribution	the reciprocal of its argument's unit
ϵ	Photon energy; In the consideration of photon interactions this denotes the soft photon's energy, in contrast to ϵ_γ	J
$\epsilon_{\mathrm{ADAF},0}$	Upper cutoff energy of ADAF spectra	J
$\epsilon_{\mathrm{ADAF},\mathrm{th}}$	Threshold energy for ADAF photons undergoing PP self interactions	J
$\epsilon_{\mathrm{trans}}$	Transition energy between self-absorbed and optically thin ADAF synchrotron radiation	J
ϵ_γ	An HE photon's energy	J
η	Efficiency of an AF to convert mass energy into kinetic or electromagnetic energy	
θ	Polar angle in a spherical coordinate system; Co-latitude; Angle towards the rotation axis of the central object; Viewing angle of an AGN	rad
κ	Number of Lorentz factor sampling points used in the iteration scheme 2	
κ	Vacuum gap multiplicity, describing how much the gap is screened by the magnetospheric plasma	
κ_j	Number of Lorentz factor sampling points $\gamma_{k,j}$ used in the j-th step of the iteration scheme 1	
λ_i	Wavelength of the i-th emission line	m
ν	Frequency of an electromagnetic wave	Hz

Sign	**Description**	**Unit**
ξ	Reprocessing fraction of the AF luminosity into the BLR luminosity	
σ	Standard deviation of a normal distribution as quantification of a confidence level	same as the corresponding random variable
σ_T	Thomson cross section	m^2
ς	Standard deviation (width) of the normal-distributed electron injection rate	
τ	Optical depth	
Φ	Voltage (potential drop) of an electrostatic vacuum gap	V
ϕ	Opening angle of both the injected beam and of the photon beam emitted from the cascade region	rad
χ^2_red	Chi-square per degree of freedom; Reduced chi-square	
Ω	Solid angle of the injected particles and of the photon beam emitted from the cascade region	sr

List of Abbreviations

3C the Third Cambridge Catalogue of Radio Sources

ADAF advection-dominated accretion flow

AF accretion flow

AGILE Astro-Rivelatore Gamma a Immagini Leggero (Italian for Lightweight Gamma Imaging Astro Detector); Web presence: `http://agile.iasf-roma.inaf.it/`

AGN active galactic nucleus

BH black hole

BL Lac BL Lacertae

BLR broad-line region

BZ Blandford-Znajek

CPU central processing unit

CTA Cherenkov Telescope Array; Web presence: `https://www.cta-observatory.org/`

EC external-Compton

EED electron energy distribution

FACT First Geiger-mode Avalanche Photodiodes Cherenkov Telescope; Web presence: `https://fact-project.org/`

FSRQ flat-spectrum radio quasar

GJ Goldreich-Julian

HE high-energy; depending on the context, this can specifically denote the $100\,\mathrm{MeV} - 100\,\mathrm{GeV}$ energy range, or in a broader connection the energy range above $m_\mathrm{e}c^2$

IACT imaging atmospheric Cherenkov telescope

IC inverse-Compton

IR infrared

ISA integral splitting approach

ISCO innermost stable circular orbit

KN Klein-Nishina

LAT Large Area Telescope; Web presence: `https://fermi.gsfc.nasa.gov/science/instruments/lat.html`

LE low-energy; in the context of IC pair cascades this denotes the energy range well below $m_\mathrm{e}c^2$

LP log parabola (noun); log-parabolic (compound adjective)

MAGIC Major Atmospheric Gamma-ray Imaging Cherenkov; Web presence: `https://magic.mpp.mpg.de/`

MJD modified Julian date

mp multiprocessing

Mrk Markarian

NLR narrow-line region

PKS Parkes catalogue of radio sources

PL power law (noun); power-law (compound adjective)

PP pair production (noun); pair-production (compound adjective)

quasar quasi-stellar radio source

SAS société par actions simplifiée (French for simplified joint stock company)

SED spectral energy distribution

SMBH supermassive black hole

SSC synchrotron-self-Compton

TANAMI Tracking Active Galactic Nuclei with Austral Milliarcsecond Interferometry, a multi-wavelength monitoring program of AGN observable from the southern sky with focus on employing VLBI; Web presence: `https://pulsar.sternwarte.uni-erlangen.de/tanami/`

TXS the catalogue of the Texas survey, an interferometric survey of discrete radio sources

UV ultraviolet

VHE very high energy; specifically denoting the 100 GeV − 100 TeV energy range

VLBI very long baseline interferometry

References

Abbott, R. et al. (Apr. 2021). 'GWTC-2: Compact Binary Coalescences Observed by LIGO and Virgo during the First Half of the Third Observing Run'. In: *Physical Review X* 11.2, 021053, p. 021053. URL: `https://ui.adsabs.harvard.edu/abs/2021PhRvX..11b1053A`.

Abdo, A. A. et al. (June 2010). 'The Spectral Energy Distribution of Fermi Bright Blazars'. In: *ApJ* 716.1, pp. 30–70. URL: `https://ui.adsabs.harvard.edu/abs/2010ApJ...716...30A`.

Abdo, A. A. et al. (Feb. 2011). 'Insights into the High-energy γ-ray Emission of Markarian 501 from Extensive Multifrequency Observations in the Fermi Era'. In: *ApJ* 727.2, 129, p. 129. URL: `https://ui.adsabs.harvard.edu/abs/2011ApJ...727..129A`.

Abdollahi, S. et al. (Mar. 2020). 'Fermi Large Area Telescope Fourth Source Catalog'. In: *ApJS* 247.1, 33, p. 33. URL: `https://ui.adsabs.harvard.edu/abs/2020ApJS..247...33A`.

Abolmasov, P. and Poutanen, J. (Jan. 2017). 'Gamma-ray opacity of the anisotropic stratified broad-line regions in blazars'. In: *MNRAS* 464.1, pp. 152–169. URL: `https://ui.adsabs.harvard.edu/abs/2017MNRAS.464..152A`.

Abramowitz, M. and Stegun, I. A. (1968). *Handbook of mathematical functions with formulas, graphs and mathematical tables.* URL: `https://ui.adsabs.harvard.edu/abs/1968hmfw.book.....A`.

Acciari, V. A. et al. (June 2021). 'Multiwavelength variability and correlation studies of Mrk 421 during historically low X-ray and γ-ray activity in 2015-2016'. In: *MNRAS* 504.1, pp. 1427–1451. URL: `https://ui.adsabs.harvard.edu/abs/2021MNRAS.504.1427A`.

Acharyya, A., Chadwick, P. M. and Brown, A. M. (Jan. 2021). 'Locating the gamma-ray emission region in the brightest Fermi-LAT flat-spectrum radio quasars'. In: *MNRAS* 500.4, pp. 5297–5321. URL: `https://ui.adsabs.harvard.edu/abs/2021MNRAS.500.5297A`.

Ackermann, M. et al. (June 2016). 'Minute-timescale >100 MeV γ-Ray Variability during the Giant Outburst of Quasar 3C 279 Observed by Fermi-LAT in 2015 June'. In: *ApJ* 824.2, L20, p. L20. URL: `https://ui.adsabs.harvard.edu/abs/2016ApJ...824L..20A`.

Agaronyan, F. A., Atoyan, A. M. and Nagapetyan, A. M. (Apr. 1983). 'Photoproduction of Electron-Positron Pairs in Compact X-Ray Sources'. In: *Astrophysics* 19, pp. 187–194. URL: `https://ui.adsabs.harvard.edu/abs/1983Ap.....19..187A`.

Aharonian, F. et al. (Aug. 2007). 'An Exceptional Very High Energy Gamma-Ray Flare of PKS 2155-304'. In: *ApJ* 664, pp. L71–L74. URL: `https://ui.adsabs.harvard.edu/abs/2007ApJ...664L..71A`.

Aharonian, F. A., Barkov, M. V. and Khangulyan, D. (May 2017). 'Scenarios for Ultrafast Gamma-Ray Variability in AGN'. In: *ApJ* 841.1, 61, p. 61. URL: `https://ui.adsabs.harvard.edu/abs/2017ApJ...841...61A`.

Aharonian, F. A. and Plyasheshnikov, A. V. (July 2003). 'Similarities and differences between relativistic electron-photon cascades developed in matter, photon gas and magnetic field'. In: *Astroparticle Physics* 19.4, pp. 525–548. URL: `https://ui.adsabs.harvard.edu/abs/2003APh....19..525A`.

Ahnen, M. L. et al. (July 2017a). 'First multi-wavelength campaign on the gamma-ray-loud active galaxy IC 310'. In: *A&A* 603, A25, A25. URL: `https://ui.adsabs.harvard.edu/abs/2017A&A...603A..25A`.

Ahnen, M. L. et al. (July 2017b). ‘Multiband variability studies and novel broadband SED modeling of Mrk 501 in 2009’. In: *A&A* 603, A31, A31. URL: `https://ui.adsabs.harvard.edu/abs/2017A&A...603A..31A`.

Ahnen, M. L. et al. (Dec. 2018). ‘Extreme HBL behavior of Markarian 501 during 2012’. In: *A&A* 620, A181, A181. URL: `https://ui.adsabs.harvard.edu/abs/2018A&A...620A.181A`.

Akharonian, F. A., Kririllov-Ugriumov, V. G. and Vardanian, V. V. (Oct. 1985). ‘Formation of Relativistic Electron-Photon Showers in Compact X-Ray Sources’. In: *Ap&SS* 115.2, pp. 201–225. URL: `https://ui.adsabs.harvard.edu/abs/1985Ap&SS.115..201A`.

Albert, J. et al. (Nov. 2007). ‘Variable Very High Energy γ-Ray Emission from Markarian 501’. In: *ApJ* 669, pp. 862–883. URL: `https://ui.adsabs.harvard.edu/abs/2007ApJ...669..862A`.

Aleksić, J. et al. (Nov. 2014a). ‘Black hole lightning due to particle acceleration at subhorizon scales’. In: *Science* 346, pp. 1080–1084. URL: `http://ads.ari.uni-heidelberg.de/abs/2014Sci...346.1080A`.

Aleksić, J. et al. (July 2014b). ‘MAGIC observations and multifrequency properties of the flat spectrum radio quasar 3C 279 in 2011’. In: *A&A* 567, A41, A41. URL: `https://ui.adsabs.harvard.edu/abs/2014A&A...567A..41A`.

Alexander, T. and Netzer, H. (Feb. 1997). ‘Bloated stars as AGN broad-line clouds: the emission-line profiles’. In: *MNRAS* 284.4, pp. 967–980. URL: `https://ui.adsabs.harvard.edu/abs/1997MNRAS.284..967A`.

Antonucci, R. R. J. and Miller, J. S. (Oct. 1985). ‘Spectropolarimetry and the nature of NGC 1068.’ In: *ApJ* 297, pp. 621–632. URL: `https://ui.adsabs.harvard.edu/abs/1985ApJ...297..621A`.

Antonucci, R. (Jan. 1993). ‘Unified models for active galactic nuclei and quasars.’ In: *ARA&A* 31, pp. 473–521. URL: `https://ui.adsabs.harvard.edu/abs/1993ARA&A..31..473A`.

Atwood, W. B. et al. (June 2009). ‘The Large Area Telescope on the Fermi Gamma-Ray Space Telescope Mission’. In: *ApJ* 697.2, pp. 1071–1102. URL: `https://ui.adsabs.harvard.edu/abs/2009ApJ...697.1071A`.

Baade, W. and Minkowski, R. (Jan. 1954a). ‘Identification of the Radio Sources in Cassiopeia, Cygnus A, and Puppis A.’ In: *ApJ* 119, p. 206. URL: `https://ui.adsabs.harvard.edu/abs/1954ApJ...119..206B`.

– (Jan. 1954b). ‘On the Identification of Radio Sources.’ In: *ApJ* 119, p. 215. URL: `https://ui.adsabs.harvard.edu/abs/1954ApJ...119..215B`.

Balbus, S. A. and Hawley, J. F. (July 1991). ‘A Powerful Local Shear Instability in Weakly Magnetized Disks. I. Linear Analysis’. In: *ApJ* 376, p. 214. URL: `https://ui.adsabs.harvard.edu/abs/1991ApJ...376..214B`.

Bambi, C. (June 2018). ‘Astrophysical Black Holes: A Compact Pedagogical Review’. In: *Annalen der Physik* 530.6, p. 1700430. URL: `https://ui.adsabs.harvard.edu/abs/2018AnP...53000430B`.

Bardeen, J. M. and Petterson, J. A. (Jan. 1975). ‘The Lense-Thirring Effect and Accretion Disks around Kerr Black Holes’. In: *ApJ* 195, p. L65. URL: `https://ui.adsabs.harvard.edu/abs/1975ApJ...195L..65B`.

Bardeen, J. M., Press, W. H. and Teukolsky, S. A. (Dec. 1972). ‘Rotating Black Holes: Locally Nonrotating Frames, Energy Extraction, and Scalar Synchrotron Radiation’. In: *ApJ* 178, pp. 347–370. URL: `https://ui.adsabs.harvard.edu/abs/1972ApJ...178..347B`.

Barkov, M. V., Aharonian, F. A. and Bosch-Ramon, V. (Dec. 2010). ‘Gamma-ray Flares from Red Giant/Jet Interactions in Active Galactic Nuclei’. In: *ApJ* 724.2, pp. 1517–1523. URL: `https://ui.adsabs.harvard.edu/abs/2010ApJ...724.1517B`.

Barth, A. J., Ho, L. C. and Sargent, W. L. W. (Feb. 2002). ‘Stellar Velocity Dispersion and Black Hole Mass in the Blazar Markarian 501’. In: *ApJ* 566, pp. L13–L16. URL: `https://ui.adsabs.harvard.edu/abs/2002ApJ...566L..13B`.

Barthel, P. D. (Jan. 1989). ‘Is Every Quasar Beamed?’ In: *ApJ* 336, p. 606. URL: `https://ui.adsabs.harvard.edu/abs/1989ApJ...336..606B`.

Becerra Gonzalez, J. et al. (July 2019). ‘Study of the Variable Broadband Emission of Markarian 501 during the Most Extreme Swift X-ray Activity’. In: *36th International Cosmic Ray Conference*

(ICRC2019). Vol. 36. International Cosmic Ray Conference, 554, p. 554. URL: `https://ui.adsabs.harvard.edu/abs/2019ICRC...36..554B`.

Becerra González, J. et al. (July 2021). 'Optical spectral characterization of the gamma-ray blazars S4 0954+65, TXS 1515-273, and RX J0812.0+0237'. In: *MNRAS* 504.4, pp. 5258–5269. URL: `https://ui.adsabs.harvard.edu/abs/2021MNRAS.504.5258B`.

Beckmann, V. and Shrader, C. R. (2012). *Active Galactic Nuclei*. Wiley-VCH GmbH. URL: `https://ui.adsabs.harvard.edu/abs/2012agn..book.....B`.

Bentz, M. C. et al. (Oct. 2021). 'A Detailed View of the Broad-line Region in NGC 3783 from Velocity-resolved Reverberation Mapping'. In: *ApJ* 920.2, 112, p. 112. URL: `https://ui.adsabs.harvard.edu/abs/2021ApJ...920..112B`.

Beskin, V. S., Istomin, Y. N. and Parev, V. I. (Dec. 1992). 'Filling the Magnetosphere of a Supermassive Black-Hole with Plasma'. In: *Soviet Ast.* 36, p. 642. URL: `https://ui.adsabs.harvard.edu/abs/1992SvA....36..642B`.

Blandford, R. D. and Levinson, A. (Mar. 1995). 'Pair Cascades in Extragalactic Jets. I. Gamma Rays'. In: *ApJ* 441, p. 79. URL: `https://ui.adsabs.harvard.edu/abs/1995ApJ...441...79B`.

Blandford, R. D. and Payne, D. G. (June 1982). 'Hydromagnetic flows from accretion disks and the production of radio jets.' In: *MNRAS* 199, pp. 883–903. URL: `https://ui.adsabs.harvard.edu/abs/1982MNRAS.199..883B`.

Blandford, R. D. and Rees, M. J. (Jan. 1978). 'Some comments on radiation mechanisms in Lacertids.' In: *BL Lac Objects*. Ed. by A. M. Wolfe, pp. 328–341. URL: `https://ui.adsabs.harvard.edu/abs/1978bllo.conf..328B`.

Blandford, R. D. and Znajek, R. L. (May 1977). 'Electromagnetic extraction of energy from Kerr black holes.' In: *MNRAS* 179, pp. 433–456. URL: `https://ui.adsabs.harvard.edu/abs/1977MNRAS.179..433B`.

Blandford, R., Meier, D. and Readhead, A. (Aug. 2019). 'Relativistic Jets from Active Galactic Nuclei'. In: *ARA&A* 57, pp. 467–509. URL: `https://ui.adsabs.harvard.edu/abs/2019ARA&A..57..467B`.

Blumenthal, G. R. and Gould, R. J. (Jan. 1970). 'Bremsstrahlung, Synchrotron Radiation, and Compton Scattering of High-Energy Electrons Traversing Dilute Gases'. In: *Reviews of Modern Physics* 42.2, pp. 237–271. URL: `https://ui.adsabs.harvard.edu/abs/1970RvMP...42..237B`.

Boettcher, M., Harris, D. E. and Krawczynski, H. (2012). *Relativistic Jets from Active Galactic Nuclei*. URL: `https://ui.adsabs.harvard.edu/abs/2012rjag.book.....B`.

Bosco, F. et al. (Sept. 2021). 'Spatially Resolving the Kinematics of the $\lesssim$100 μas Quasar Broad-line Region Using Spectroastrometry. II. The First Tentative Detection in a Luminous Quasar at z = 2.3'. In: *ApJ* 919.1, 31, p. 31. URL: `https://ui.adsabs.harvard.edu/abs/2021ApJ...919...31B`.

Böttcher, M. and Dermer, C. D. (Jan. 2002). 'An Evolutionary Scenario for Blazar Unification'. In: *ApJ* 564.1, pp. 86–91. URL: `https://ui.adsabs.harvard.edu/abs/2002ApJ...564...86B`.

Böttcher, M. et al. (May 2013). 'Leptonic and Hadronic Modeling of Fermi-detected Blazars'. In: *ApJ* 768.1, 54, p. 54. URL: `https://ui.adsabs.harvard.edu/abs/2013ApJ...768...54B`.

Böttcher, M. and Els, P. (Apr. 2016). 'Gamma-Gamma Absorption in the Broad Line Region Radiation Fields of Gamma-Ray Blazars'. In: *ApJ* 821.2, 102, p. 102. URL: `https://ui.adsabs.harvard.edu/abs/2016ApJ...821..102B`.

Boyer, R. H. and Lindquist, R. W. (Feb. 1967). 'Maximal Analytic Extension of the Kerr Metric'. In: *Journal of Mathematical Physics* 8.2, pp. 265–281. URL: `https://ui.adsabs.harvard.edu/abs/1967JMP.....8..265B`.

Brandenburg, A. et al. (June 1995). 'Dynamo-generated Turbulence and Large-Scale Magnetic Fields in a Keplerian Shear Flow'. In: *ApJ* 446, p. 741. URL: `https://ui.adsabs.harvard.edu/abs/1995ApJ...446..741B`.

Britto, R. J. G., Razzaque, S. and Lott, B. (Feb. 2015). 'Spectral Studies of Flaring FSRQs at GeV Energies Using Pass 8 Fermi-LAT Data'. In: *arXiv e-prints*, arXiv:1502.07624. URL: `https://ui.adsabs.harvard.edu/abs/2015arXiv150207624B`.

Broderick, A. E. and Tchekhovskoy, A. (Aug. 2015). ‘Horizon-scale Lepton Acceleration in Jets: Explaining the Compact Radio Emission in M87’. In: *ApJ* 809.1, 97, p. 97. URL: `https://ui.adsabs.harvard.edu/abs/2015ApJ...809...97B`.

Burtscher, L. et al. (Oct. 2013). ‘A diversity of dusty AGN tori. Data release for the VLTI/MIDI AGN Large Program and first results for 23 galaxies’. In: *A&A* 558, A149, A149. URL: `https://ui.adsabs.harvard.edu/abs/2013A&A...558A.149B`.

Carter, B. (Feb. 1971). ‘Axisymmetric Black Hole Has Only Two Degrees of Freedom’. In: *Phys. Rev. Lett.* 26.6, pp. 331–333. URL: `https://ui.adsabs.harvard.edu/abs/1971PhRvL..26..331C`.

Celotti, A., Padovani, P. and Ghisellini, G. (Apr. 1997). ‘Jets and accretion processes in active galactic nuclei: further clues’. In: *MNRAS* 286.2, pp. 415–424. URL: `https://ui.adsabs.harvard.edu/abs/1997MNRAS.286..415C`.

Cerruti, M. et al. (July 2021). ‘The Blazar Hadronic Code Comparison Project’. In: *arXiv e-prints*, arXiv:2107.06377. URL: `https://ui.adsabs.harvard.edu/abs/2021arXiv210706377C`.

Chen, A. Y. and Yuan, Y. (June 2020). ‘Physics of Pair Producing Gaps in Black Hole Magnetospheres. II. General Relativity’. In: *ApJ* 895.2, 121, p. 121. URL: `https://ui.adsabs.harvard.edu/abs/2020ApJ...895..121C`.

Chen, A. Y., Yuan, Y. and Yang, H. (Aug. 2018). ‘Physics of Pair Producing Gaps in Black Hole Magnetospheres’. In: *ApJ* 863.2, L31, p. L31. URL: `https://ui.adsabs.harvard.edu/abs/2018ApJ...863L..31C`.

Cheng, K. S., Ho, C. and Ruderman, M. (Jan. 1986). ‘Energetic Radiation from Rapidly Spinning Pulsars. II. VELA and Crab’. In: *ApJ* 300, p. 522. URL: `http://adsabs.harvard.edu/abs/1986ApJ...300..522C`.

Collin, S. and Huré, J. .-. (June 2001). ‘Size-mass-luminosity relations in AGN and the role of the accretion disc’. In: *A&A* 372, pp. 50–58. URL: `https://ui.adsabs.harvard.edu/abs/2001A&A...372...50C`.

Crinquand, B. et al. (Apr. 2020). ‘Multidimensional Simulations of Ergospheric Pair Discharges around Black Holes’. In: *Phys. Rev. Lett.* 124.14, 145101, p. 145101. URL: `https://ui.adsabs.harvard.edu/abs/2020PhRvL.124n5101C`.

Curtis, H. D. (Jan. 1918). ‘Descriptions of 762 Nebulae and Clusters Photographed with the Crossley Reflector’. In: *Publications of Lick Observatory* 13, pp. 9–42. URL: `https://ui.adsabs.harvard.edu/abs/1918PLicO..13....9C`.

Czerny, B. (Dec. 2019). ‘Modelling broad emission lines in active galactic nuclei’. In: *Open Astronomy* 28.1, pp. 200–212. URL: `https://ui.adsabs.harvard.edu/abs/2019OAst...28..200C`.

Davidson, K. and Netzer, H. (Oct. 1979). ‘The emission lines of quasars and similar objects’. In: *Reviews of Modern Physics* 51.4, pp. 715–766. URL: `https://ui.adsabs.harvard.edu/abs/1979RvMP...51..715D`.

de Jager, O. C. (Aug. 1999). ‘Central black hole mass estimates for Mkn 501 from shot noise-like X-Ray and TeV flares during 1997’. In: *26th International Cosmic Ray Conference (ICRC26), Volume 3.* Vol. 3. International Cosmic Ray Conference, p. 346. URL: `https://ui.adsabs.harvard.edu/abs/1999ICRC....3..346D`.

Decarli, R., Dotti, M. and Treves, A. (May 2011). ‘Geometry and inclination of the broad-line region in blazars’. In: *MNRAS* 413.1, pp. 39–46. URL: `https://ui.adsabs.harvard.edu/abs/2011MNRAS.413...39D`.

Dere, K. P. et al. (Oct. 1997). ‘CHIANTI - an atomic database for emission lines’. In: *A&AS* 125, pp. 149–173. URL: `https://ui.adsabs.harvard.edu/abs/1997A&AS..125..149D`.

Dermer, C. D., Schlickeiser, R. and Mastichiadis, A. (Mar. 1992). ‘High-energy gamma radiation from extragalactic radio sources.’ In: *A&A* 256, pp. L27–L30. URL: `https://ui.adsabs.harvard.edu/abs/1992A&A...256L..27D`.

Dermer, C. D. et al. (Feb. 2014). ‘Equipartition Gamma-Ray Blazars and the Location of the Gamma-Ray Emission Site in 3C 279’. In: *ApJ* 782.2, 82, p. 82. URL: `https://ui.adsabs.harvard.edu/abs/2014ApJ...782...82D`.

Dermer, C. D. and Giebels, B. (June 2016). ‘Active galactic nuclei at gamma-ray energies’. In: *Comptes Rendus Physique* 17.6, pp. 594–616. URL: `https://ui.adsabs.harvard.edu/abs/2016CRPhy..17..594D`.

Donea, A.-C. and Protheroe, R. J. (Jan. 2003). ‘Radiation fields of disk, BLR and torus in quasars and blazars: implications for /γ-ray absorption’. In: *Astroparticle Physics* 18.4, pp. 377–393. URL: `https://ui.adsabs.harvard.edu/abs/2003APh....18..377D`.

Dorner, D. et al. (Feb. 2015). ‘FACT - Monitoring Blazars at Very High Energies’. In: *arXiv e-prints*, arXiv:1502.02582. URL: `https://ui.adsabs.harvard.edu/abs/2015arXiv150202582D`.

Esin, A. A., McClintock, J. E. and Narayan, R. (Nov. 1997). ‘Advection-Dominated Accretion and the Spectral States of Black Hole X-Ray Binaries: Application to Nova Muscae 1991’. In: *ApJ* 489.2, pp. 865–889. URL: `https://ui.adsabs.harvard.edu/abs/1997ApJ...489..865E`.

Event Horizon Telescope Collaboration et al. (Apr. 2019). ‘First M87 Event Horizon Telescope Results. I. The Shadow of the Supermassive Black Hole’. In: *ApJ* 875.1, L1, p. L1. URL: `https://ui.adsabs.harvard.edu/abs/2019ApJ...875L...1E`.

Fabian, A. C. and Miniutti, G. (July 2005). ‘The X-ray spectra of accreting Kerr black holes’. In: *arXiv e-prints*, astro-ph/0507409. URL: `https://ui.adsabs.harvard.edu/abs/2005astro.ph..7409F`.

Fanaroff, B. L. and Riley, J. M. (May 1974). ‘The morphology of extragalactic radio sources of high and low luminosity’. In: *MNRAS* 167, 31P–36P. URL: `https://ui.adsabs.harvard.edu/abs/1974MNRAS.167P..31F`.

Ferland, G. J. et al. (Oct. 2017). ‘The 2017 Release Cloudy’. In: *Rev. Mexicana Astron. Astrofis.* 53, pp. 385–438. URL: `https://ui.adsabs.harvard.edu/abs/2017RMxAA..53..385F`.

Fian, C. et al. (Sept. 2021). ‘Microlensing of the broad emission lines in 27 gravitationally lensed quasars. Broad line region structure and kinematics’. In: *A&A* 653, A109, A109. URL: `https://ui.adsabs.harvard.edu/abs/2021A&A...653A.109F`.

Finke, J. D. (Oct. 2016). ‘External Compton Scattering in Blazar Jets and the Location of the Gamma-Ray Emitting Region’. In: *ApJ* 830.2, 94, p. 94. URL: `https://ui.adsabs.harvard.edu/abs/2016ApJ...830...94F`.

Ford, A. L., Keenan, B. D. and Medvedev, M. V. (Sept. 2018). ‘Electron-positron cascade in magnetospheres of spinning black holes’. In: *Phys. Rev. D* 98, 063016, p. 063016. URL: `https://ui.adsabs.harvard.edu/abs/2018PhRvD..98f3016F`.

Foschini, L. et al. (July 2013). ‘Fermi/LAT detection of extraordinary variability in the gamma-ray emission of the blazar PKS 1510-089’. In: *A&A* 555, A138, A138. URL: `https://ui.adsabs.harvard.edu/abs/2013A&A...555A.138F`.

Foschini, L. (July 2017). ‘What we talk about when we talk about blazars?’ In: *Frontiers in Astronomy and Space Sciences* 4, 6, p. 6. URL: `https://ui.adsabs.harvard.edu/abs/2017FrASS...4....6F`.

Fossati, G. et al. (Sept. 1998). ‘A unifying view of the spectral energy distributions of blazars’. In: *MNRAS* 299.2, pp. 433–448. URL: `https://ui.adsabs.harvard.edu/abs/1998MNRAS.299..433F`.

Frank, J., King, A. and Raine, D. J. (2002). *Accretion Power in Astrophysics: Third Edition.* URL: `https://ui.adsabs.harvard.edu/abs/2002apa..book.....F`.

Fromerth, M. J. and Melia, F. (Mar. 2001). ‘The Formation of Broad-Line Clouds in the Accretion Shocks of Active Galactic Nuclei’. In: *ApJ* 549.1, pp. 205–214. URL: `https://ui.adsabs.harvard.edu/abs/2001ApJ...549..205F`.

Ghisellini, G., Maraschi, L. and Tavecchio, F. (June 2009). ‘The Fermi blazars’ divide’. In: *MNRAS* 396.1, pp. L105–L109. URL: `https://ui.adsabs.harvard.edu/abs/2009MNRAS.396L.105G`.

Ghisellini, G. and Tavecchio, F. (July 2008). ‘The blazar sequence: a new perspective’. In: *MNRAS* 387.4, pp. 1669–1680. URL: `https://ui.adsabs.harvard.edu/abs/2008MNRAS.387.1669G`.

Ghisellini, G. et al. (Dec. 1998). ‘A theoretical unifying scheme for gamma-ray bright blazars’. In: *MNRAS* 301.2, pp. 451–468. URL: `https://ui.adsabs.harvard.edu/abs/1998MNRAS.301..451G`.

Ghisellini, G. et al. (July 2011). 'The transition between BL Lac objects and flat spectrum radio quasars'. In: *MNRAS* 414.3, pp. 2674–2689. URL: `https://ui.adsabs.harvard.edu/abs/2011MNRAS.414.2674G`.

Ghisellini, G. et al. (Nov. 2014). 'The power of relativistic jets is larger than the luminosity of their accretion disks'. In: *Nature* 515.7527, pp. 376–378. URL: `https://ui.adsabs.harvard.edu/abs/2014Natur.515..376G`.

Ghisellini, G. et al. (July 2017). 'The Fermi blazar sequence'. In: *MNRAS* 469.1, pp. 255–266. URL: `https://ui.adsabs.harvard.edu/abs/2017MNRAS.469..255G`.

Ghisellini, G. (Jan. 2012). 'Jetted Active Galactic Nuclei'. In: *International Journal of Modern Physics Conference Series*. Vol. 8. International Journal of Modern Physics Conference Series, pp. 1–12. URL: `https://ui.adsabs.harvard.edu/abs/2012IJMPS...8....1G`.

– (2013). *Radiative Processes in High Energy Astrophysics*. Vol. 873. Springer. URL: `https://ui.adsabs.harvard.edu/abs/2013LNP...873.....G`.

Giannios, D. (May 2013). 'Reconnection-driven plasmoids in blazars: fast flares on a slow envelope'. In: *MNRAS* 431.1, pp. 355–363. URL: `https://ui.adsabs.harvard.edu/abs/2013MNRAS.431..355G`.

Giannios, D., Uzdensky, D. A. and Begelman, M. C. (Mar. 2010). 'Fast TeV variability from misaligned minijets in the jet of M87'. In: *MNRAS* 402.3, pp. 1649–1656. URL: `https://ui.adsabs.harvard.edu/abs/2010MNRAS.402.1649G`.

Giommi, P. et al. (Mar. 2012). 'A simplified view of blazars: clearing the fog around long-standing selection effects'. In: *MNRAS* 420.4, pp. 2899–2911. URL: `https://ui.adsabs.harvard.edu/abs/2012MNRAS.420.2899G`.

Giroletti, M. et al. (Jan. 2004). 'Parsec-Scale Properties of Markarian 501'. In: *ApJ* 600.1, pp. 127–140. URL: `https://ui.adsabs.harvard.edu/abs/2004ApJ...600..127G`.

Glawion, D. and Wierzcholska, A. (Aug. 2021). 'Is PKS 0625-354 another variable TeV active galactic nucleus?' In: *arXiv e-prints*, arXiv:2108.01331. URL: `https://ui.adsabs.harvard.edu/abs/2021arXiv210801331G`.

Glawion, D. E. et al. (Jan. 2017). 'Black hole lightning of IC 310 and the days after'. In: *6th International Symposium on High Energy Gamma-Ray Astronomy*. Vol. 1792. American Institute of Physics Conference Series, 050003, p. 050003. URL: `https://ui.adsabs.harvard.edu/abs/2017AIPC.1792e0003G`.

Goad, M. R., Korista, K. T. and Ruff, A. J. (Nov. 2012). 'The broad emission-line region: the confluence of the outer accretion disc with the inner edge of the dusty torus'. In: *MNRAS* 426.4, pp. 3086–3111. URL: `https://ui.adsabs.harvard.edu/abs/2012MNRAS.426.3086G`.

Goad, M. and Koratkar, A. (Mar. 1998). 'Broad Emission Line Variability as a Constraint upon the Physical Conditions within the Broad Emission Line Region of NGC 5548'. In: *ApJ* 495.2, pp. 718–739. URL: `https://ui.adsabs.harvard.edu/abs/1998ApJ...495..718G`.

Gokus, A. et al. (May 2021). 'The first GeV flare of the radio-loud narrow-line Seyfert 1 galaxy PKS 2004-447'. In: *A&A* 649, A77, A77. URL: `https://ui.adsabs.harvard.edu/abs/2021A&A...649A..77G`.

Goldreich, P. and Julian, W. H. (Aug. 1969). 'Pulsar Electrodynamics'. In: *ApJ* 157, p. 869. URL: `https://ui.adsabs.harvard.edu/abs/1969ApJ...157..869G`.

Gould, R. J. (July 1979). 'Compton and synchrotron processes in spherically-symmetric non-thermal sources.' In: *A&A* 76, pp. 306–311. URL: `https://ui.adsabs.harvard.edu/abs/1979A&A....76..306G`.

Gravity Collaboration et al. (Apr. 2021). 'The central parsec of NGC 3783: a rotating broad emission line region, asymmetric hot dust structure, and compact coronal line region'. In: *A&A* 648, A117, A117. URL: `https://ui.adsabs.harvard.edu/abs/2021A&A...648A.117G`.

H. E. S. S. Collaboration et al. (July 2019). 'Constraints on the emission region of 3C 279 during strong flares in 2014 and 2015 through VHE γ-ray observations with H.E.S.S.' In: *A&A* 627, A159, A159. URL: `https://ui.adsabs.harvard.edu/abs/2019A&A...627A.159H`.

Haardt, F., Maraschi, L. and Ghisellini, G. (Sept. 1994). 'A Model for the X-Ray and Ultraviolet Emission from Seyfert Galaxies and Galactic Black Holes'. In: *ApJ* 432, p. L95. URL: `https://ui.adsabs.harvard.edu/abs/1994ApJ...432L..95H`.

Harris, C. R. et al. (Sept. 2020). 'Array programming with NumPy'. In: *Nature* 585.7825, pp. 357–362. URL: `https://ui.adsabs.harvard.edu/abs/2020Natur.585..357H`.

Hartman, R. C. et al. (Jan. 1992). 'Detection of High-Energy Gamma Radiation from Quasar 3C 279 by the EGRET Telescope on the Compton Gamma Ray Observatory'. In: *ApJ* 385, p. L1. URL: `https://ui.adsabs.harvard.edu/abs/1992ApJ...385L...1H`.

Harvey, A. L. W., Georganopoulos, M. and Meyer, E. T. (Oct. 2020). 'Powerful extragalactic jets dissipate their kinetic energy far from the central black hole'. In: *Nature Communications* 11, 5475, p. 5475. URL: `https://ui.adsabs.harvard.edu/abs/2020NatCo..11.5475H`.

Hayashida, M. et al. (July 2015). 'Rapid Variability of Blazar 3C 279 during Flaring States in 2013-2014 with Joint Fermi-LAT, NuSTAR, Swift, and Ground-Based Multiwavelength Observations'. In: *ApJ* 807.1, 79, p. 79. URL: `https://ui.adsabs.harvard.edu/abs/2015ApJ...807...79H`.

Hirotani, K. (Jan. 2005). 'High energy emission from pulsars: Outer gap scenario'. In: *Advances in Space Research* 35, pp. 1085–1091. URL: `https://ui.adsabs.harvard.edu/abs/2005AdSpR..35.1085H`.

Hirotani, K. and Okamoto, I. (Apr. 1998). 'Pair Plasma Production in a Force-free Magnetosphere around a Supermassive Black Hole'. In: *ApJ* 497.2, pp. 563–572. URL: `https://ui.adsabs.harvard.edu/abs/1998ApJ...497..563H`.

Hirotani, K. and Pu, H.-Y. (Feb. 2016). 'Energetic Gamma Radiation from Rapidly Rotating Black Holes'. In: *ApJ* 818, 50, p. 50. URL: `https://ui.adsabs.harvard.edu/abs/2016ApJ...818...50H`.

Hirotani, K. et al. (Dec. 2016). 'Lepton Acceleration in the Vicinity of the Event Horizon: High-energy and Very-high-energy Emissions from Rotating Black Holes with Various Masses'. In: *ApJ* 833.2, 142, p. 142. URL: `https://ui.adsabs.harvard.edu/abs/2016ApJ...833..142H`.

Hirotani, K. et al. (Aug. 2017). 'Lepton Acceleration in the Vicinity of the Event Horizon: Very High Energy Emissions from Supermassive Black Holes'. In: *ApJ* 845.1, 77, p. 77. URL: `https://ui.adsabs.harvard.edu/abs/2017ApJ...845...77H`.

Hirotani, K. et al. (Feb. 2021). 'Two-dimensional Particle-in-cell Simulations of Axisymmetric Black Hole Magnetospheres'. In: *ApJ* 908.1, 88, p. 88. URL: `https://ui.adsabs.harvard.edu/abs/2021ApJ...908...88H`.

Hu, W. (Jan. 2022). Private communication via e-mail correspondence.

Hu, W. and Yan, D. (Dec. 2021). 'On the narrow spectral feature at 3 TeV in the MAGIC spectrum of Mrk 501'. In: *MNRAS* 508.3, pp. 4038–4046. URL: `https://ui.adsabs.harvard.edu/abs/2021MNRAS.508.4038H`.

Hunter, J. D. (May 2007). 'Matplotlib: A 2D Graphics Environment'. In: *Computing in Science and Engineering* 9.3, pp. 90–95. URL: `https://ui.adsabs.harvard.edu/abs/2007CSE.....9...90H`.

IceCube Collaboration et al. (July 2018). 'Multimessenger observations of a flaring blazar coincident with high-energy neutrino IceCube-170922A'. In: *Science* 361, eaat1378, eaat1378. URL: `https://ui.adsabs.harvard.edu/abs/2018Sci...361.1378I`.

Israel, W. (Sept. 1968). 'Event horizons in static electrovac space-times'. In: *Communications in Mathematical Physics* 8.3, pp. 245–260. URL: `https://ui.adsabs.harvard.edu/abs/1968CMaPh...8..245I`.

Jarvis, M. J. and McLure, R. J. (June 2006). 'Orientation dependency of broad-line widths in quasars and consequences for black hole mass estimation'. In: *MNRAS* 369.1, pp. 182–188. URL: `https://ui.adsabs.harvard.edu/abs/2006MNRAS.369..182J`.

Jones, F. C. (Mar. 1968). 'Calculated Spectrum of Inverse-Compton-Scattered Photons'. In: *Physical Review* 167, pp. 1159–1169. URL: `https://ui.adsabs.harvard.edu/abs/1968PhRv..167.1159J`.

Kaspi, S. et al. (Apr. 2007). 'Reverberation Mapping of High-Luminosity Quasars: First Results'. In: *ApJ* 659.2, pp. 997–1007. URL: `https://ui.adsabs.harvard.edu/abs/2007ApJ...659..997K`.

Kaspi, S. et al. (July 2021). 'Taking a Long Look: A Two-decade Reverberation Mapping Study of High-luminosity Quasars'. In: *ApJ* 915.2, 129, p. 129. URL: `https://ui.adsabs.harvard.edu/abs/2021ApJ...915..129K`.

Kato, S., Fukue, J. and Mineshige, S. (2008). *Black-Hole Accretion Disks — Towards a New Paradigm —*. URL: `https://ui.adsabs.harvard.edu/abs/2008bhad.book.....K`.

Katsoulakos, G. and Rieger, F. M. (June 2020). 'Gap-type Particle Acceleration in the Magnetospheres of Rotating Supermassive Black Holes'. In: *ApJ* 895.2, 99, p. 99. URL: `https://ui.adsabs.harvard.edu/abs/2020ApJ...895...99K`.

Katsoulakos, G., Rieger, F. M. and Reville, B. (Aug. 2020). 'Constraining Cosmic-Ray Acceleration in the Magnetospheric Gaps of Sgr A*'. In: *ApJ* 899.1, L7, p. L7. URL: `https://ui.adsabs.harvard.edu/abs/2020ApJ...899L...7K`.

Keenan, M. et al. (Aug. 2021). 'The relativistic jet dichotomy and the end of the blazar sequence'. In: *MNRAS* 505.4, pp. 4726–4745. URL: `https://ui.adsabs.harvard.edu/abs/2021MNRAS.505.4726K`.

Kerr, R. P. (Sept. 1963). 'Gravitational Field of a Spinning Mass as an Example of Algebraically Special Metrics'. In: *Phys. Rev. Lett.* 11.5, pp. 237–238. URL: `https://ui.adsabs.harvard.edu/abs/1963PhRvL..11..237K`.

Kilerci Eser, E. et al. (Mar. 2015). 'On the Scatter in the Radius-Luminosity Relationship for Active Galactic Nuclei'. In: *ApJ* 801.1, 8, p. 8. URL: `https://ui.adsabs.harvard.edu/abs/2015ApJ...801....8K`.

Kim, J.-Y. et al. (Aug. 2020). 'Event Horizon Telescope imaging of the archetypal blazar 3C 279 at an extreme 20 microarcsecond resolution'. In: *A&A* 640, A69, A69. URL: `https://ui.adsabs.harvard.edu/abs/2020A&A...640A..69K`.

King, A. R. and Pringle, J. E. (Sept. 2021). 'Can the Blandford-Znajek Mechanism Power Steady Jets?' In: *ApJ* 918.1, L22, p. L22. URL: `https://ui.adsabs.harvard.edu/abs/2021ApJ...918L..22K`.

Kisaka, S., Levinson, A. and Toma, K. (Oct. 2020). 'Comprehensive Analysis of Magnetospheric Gaps around Kerr Black Holes Using 1D GRPIC Simulations'. In: *ApJ* 902.1, 80, p. 80. URL: `https://ui.adsabs.harvard.edu/abs/2020ApJ...902...80K`.

Konigl, A. and Kartje, J. F. (Oct. 1994). 'Disk-driven Hydromagnetic Winds as a Key Ingredient of Active Galactic Nuclei Unification Schemes'. In: *ApJ* 434, p. 446. URL: `https://ui.adsabs.harvard.edu/abs/1994ApJ...434..446K`.

Krauß, F. et al. (June 2014). 'TANAMI blazars in the IceCube PeV-neutrino fields'. In: *A&A* 566, L7, p. L7. URL: `https://ui.adsabs.harvard.edu/abs/2014A&A...566L...7K`.

Landi, E. et al. (Jan. 2012). 'CHIANTI—An Atomic Database for Emission Lines. XII. Version 7 of the Database'. In: *ApJ* 744.2, 99, p. 99. URL: `https://ui.adsabs.harvard.edu/abs/2012ApJ...744...99L`.

Lawrence, A. (Oct. 1991). 'The relative frequency of broad-lined and narrow-lined active galactic nuclei : implications for unified schemes.' In: *MNRAS* 252, p. 586. URL: `https://ui.adsabs.harvard.edu/abs/1991MNRAS.252..586L`.

Lei, M. and Wang, J. (Aug. 2015). 'Location of gamma-ray flaring region in quasar 4C +21.35'. In: *PASJ* 67.4, 79, p. 79. URL: `https://ui.adsabs.harvard.edu/abs/2015PASJ...67...79L`.

Levinson, A. (July 2000). 'Particle Acceleration and Curvature TeV Emission by Rotating, Supermassive Black Holes'. In: *Phys. Rev. Lett.* 85.5, pp. 912–915. URL: `https://ui.adsabs.harvard.edu/abs/2000PhRvL..85..912L`.

Levinson, A. and Cerutti, B. (Sept. 2018). 'Particle-in-cell simulations of pair discharges in a starved magnetosphere of a Kerr black hole'. In: *A&A* 616, A184, A184. URL: `https://ui.adsabs.harvard.edu/abs/2018A&A...616A.184L`.

Levinson, A. and Rieger, F. (Apr. 2011). 'Variable TeV Emission as a Manifestation of Jet Formation in M87?' In: *ApJ* 730.2, 123, p. 123. URL: `https://ui.adsabs.harvard.edu/abs/2011ApJ...730..123L`.

Levinson, A. and Segev, N. (Dec. 2017). ‘Existence of steady gap solutions in rotating black hole magnetospheres’. In: *Phys. Rev. D* 96.12, 123006, p. 123006. URL: `https://ui.adsabs.harvard.edu/abs/2017PhRvD..96l3006L`.

Liao, N.-h. (July 2018). ‘Fast γ-ray Variability: A Common Feature and Powerful Probe for Jetted AGNs’. In: *Galaxies* 6, p. 68. URL: `http://adsabs.harvard.edu/abs/2018Galax...6...68L`.

Liodakis, I. (Aug. 2018). ‘Toy model for the acceleration of blazar jets’. In: *A&A* 616, A93, A93. URL: `https://ui.adsabs.harvard.edu/abs/2018A&A...616A..93L`.

Liska, M., Tchekhovskoy, A. and Quataert, E. (May 2020). ‘Large-scale poloidal magnetic field dynamo leads to powerful jets in GRMHD simulations of black hole accretion with toroidal field’. In: *MNRAS* 494.3, pp. 3656–3662. URL: `https://ui.adsabs.harvard.edu/abs/2020MNRAS.494.3656L`.

Liu, H. T. and Bai, J. M. (Dec. 2006). ‘Absorption of 10-200 GeV Gamma Rays by Radiation from Broad-Line Regions in Blazars’. In: *ApJ* 653.2, pp. 1089–1097. URL: `https://ui.adsabs.harvard.edu/abs/2006ApJ...653.1089L`.

Longair, M. S. (2011). *High Energy Astrophysics.* URL: `https://ui.adsabs.harvard.edu/abs/2011hea..book.....L`.

Lovelace, R. V. E. (Aug. 1976). ‘Dynamo model of double radio sources’. In: *Nature* 262.5570, pp. 649–652. URL: `https://ui.adsabs.harvard.edu/abs/1976Natur.262..649L`.

Lovelace, R. V. E., MacAuslan, J. and Burns, M. (Nov. 1979). ‘Particle acceleration in double radio sources’. In: *Particle Acceleration Mechanisms in Astrophysics.* Ed. by J. Arons, C. McKee and C. Max. Vol. 56. American Institute of Physics Conference Series, pp. 399–415. URL: `https://ui.adsabs.harvard.edu/abs/1979AIPC...56..399L`.

Lynden-Bell, D. (Aug. 1969). ‘Galactic Nuclei as Collapsed Old Quasars’. In: *Nature* 223.5207, pp. 690–694. URL: `https://ui.adsabs.harvard.edu/abs/1969Natur.223..690L`.

MacLachlan, G. A. et al. (June 2013). ‘Minimum variability time-scales of long and short GRBs’. In: *MNRAS* 432.2, pp. 857–865. URL: `https://ui.adsabs.harvard.edu/abs/2013MNRAS.432..857M`.

MAGIC Collaboration et al. (June 2008). ‘Very-High-Energy gamma rays from a Distant Quasar: How Transparent Is the Universe?’ In: *Science* 320.5884, p. 1752. URL: `https://ui.adsabs.harvard.edu/abs/2008Sci...320.1752M`.

MAGIC Collaboration et al. (Sept. 2018). ‘Gamma-ray flaring activity of NGC1275 in 2016-2017 measured by MAGIC’. In: *A&A* 617, A91, A91. URL: `https://ui.adsabs.harvard.edu/abs/2018A&A...617A..91M`.

MAGIC Collaboration et al. (May 2020). ‘Study of the variable broadband emission of Markarian 501 during the most extreme Swift X-ray activity’. In: *A&A* 637, A86, A86. URL: `https://ui.adsabs.harvard.edu/abs/2020A&A...637A..86M`.

MAGIC Collaboration et al. (Nov. 2021). ‘Investigation of the correlation patterns and the Compton dominance variability of Mrk 421 in 2017’. In: *A&A* 655, A89, A89. URL: `https://ui.adsabs.harvard.edu/abs/2021A&A...655A..89M`.

Mahadevan, R. (Mar. 1997). ‘Scaling Laws for Advection-dominated Flows: Applications to Low-Luminosity Galactic Nuclei’. In: *ApJ* 477, pp. 585–601. URL: `https://ui.adsabs.harvard.edu/abs/1997ApJ...477..585M`.

Mannheim, K. (Mar. 1993). ‘The proton blazar.’ In: *A&A* 269, pp. 67–76. URL: `https://ui.adsabs.harvard.edu/abs/1993A&A...269...67M`.

Mannheim, K. and Biermann, P. L. (Jan. 1992). ‘Gamma-ray flaring of 3C 279 : a proton-initiated cascade in the jet ?’ In: *A&A* 253, pp. L21–L24. URL: `https://ui.adsabs.harvard.edu/abs/1992A&A...253L..21M`.

Mao, P. et al. (June 2016). ‘A Comprehensive Statistical Description of Radio-through-Gamma-Ray Spectral Energy Distributions of All Known Blazars’. In: *ApJS* 224.2, 26, p. 26. URL: `https://ui.adsabs.harvard.edu/abs/2016ApJS..224...26M`.

Maraschi, L., Ghisellini, G. and Celotti, A. (Sept. 1992). ‘A Jet Model for the Gamma-Ray–emitting Blazar 3C 279’. In: *ApJ* 397, p. L5. URL: `https://ui.adsabs.harvard.edu/abs/1992ApJ...397L...5M`.

Marcowith, A., Henri, G. and Pelletier, G. (Nov. 1995). ‘Gamma-ray emission of blazars by a relativistic electron-positron beam’. In: *MNRAS* 277.2, pp. 681–699. URL: https://ui.adsabs.harvard.edu/abs/1995MNRAS.277..681M.

Markowitz, A. G., Krumpe, M. and Nikutta, R. (Apr. 2014). ‘First X-ray-based statistical tests for clumpy-torus models: eclipse events from 230 years of monitoring of Seyfert AGN’. In: *MNRAS* 439.2, pp. 1403–1458. URL: https://ui.adsabs.harvard.edu/abs/2014MNRAS.439.1403M.

Marziani, P. et al. (May 1996). ‘Comparative Analysis of the High- and Low-Ionization Lines in the Broad-Line Region of Active Galactic Nuclei’. In: *ApJS* 104, p. 37. URL: https://ui.adsabs.harvard.edu/abs/1996ApJS..104...37M.

Mastichiadis, A. and Kirk, J. G. (Mar. 1995). ‘Self-consistent particle acceleration in active galactic nuclei.’ In: *A&A* 295, p. 613. URL: https://ui.adsabs.harvard.edu/abs/1995A&A...295..613M.

Matthews, J. H., Bell, A. R. and Blundell, K. M. (Sept. 2020). ‘Particle acceleration in astrophysical jets’. In: *New A Rev.* 89, 101543, p. 101543. URL: https://ui.adsabs.harvard.edu/abs/2020NewAR..8901543M.

Meyer, E. T. et al. (Oct. 2011). ‘From the Blazar Sequence to the Blazar Envelope: Revisiting the Relativistic Jet Dichotomy in Radio-loud Active Galactic Nuclei’. In: *ApJ* 740.2, 98, p. 98. URL: https://ui.adsabs.harvard.edu/abs/2011ApJ...740...98M.

Meyer, M., Petropoulou, M. and Christie, I. M. (May 2021). ‘The Observability of Plasmoid-powered γ-Ray Flares with the Fermi Large Area Telescope’. In: *ApJ* 912.1, 40, p. 40. URL: https://ui.adsabs.harvard.edu/abs/2021ApJ...912...40M.

Meyer, M., Scargle, J. D. and Blandford, R. D. (May 2019). ‘Characterizing the Gamma-Ray Variability of the Brightest Flat Spectrum Radio Quasars Observed with the Fermi LAT’. In: *ApJ* 877.1, 39, p. 39. URL: https://ui.adsabs.harvard.edu/abs/2019ApJ...877...39M.

Michell, J. (Jan. 1784). ‘On the Means of Discovering the Distance, Magnitude, &c. of the Fixed Stars, in Consequence of the Diminution of the Velocity of Their Light, in Case Such a Diminution Should be Found to Take Place in any of Them, and Such Other Data Should be Procured from Observations, as Would be Farther Necessary for That Purpose. By the Rev. John Michell, B. D. F. R. S. In a Letter to Henry Cavendish, Esq. F. R. S. and A. S.’ In: *Philosophical Transactions of the Royal Society of London Series I* 74, pp. 35–57. URL: https://ui.adsabs.harvard.edu/abs/1784RSPT...74...35M.

Millman, K. J. and Aivazis, M. (Mar. 2011). ‘Python for Scientists and Engineers’. In: *Computing in Science and Engineering* 13.2, pp. 9–12. URL: https://ui.adsabs.harvard.edu/abs/2011CSE....13b...9M.

Moles, M., Masegosa, J. and del Olmo, A. (Nov. 1987). ‘Two Elliptical Galaxies with Active Nuclei: NGC 6212 and MKN 501’. In: *AJ* 94, p. 1143. URL: https://ui.adsabs.harvard.edu/abs/1987AJ.....94.1143M.

Mücke, A. and Protheroe, R. J. (Mar. 2001). ‘A proton synchrotron blazar model for flaring in Markarian 501’. In: *Astroparticle Physics* 15.1, pp. 121–136. URL: https://ui.adsabs.harvard.edu/abs/2001APh....15..121M.

Narayan, R., Mahadevan, R. and Quataert, E. (Jan. 1998). ‘Advection-dominated accretion around black holes’. In: *Theory of Black Hole Accretion Disks.* Ed. by M. A. Abramowicz, G. Björnsson and J. E. Pringle, pp. 148–182. URL: https://ui.adsabs.harvard.edu/abs/1998tbha.conf..148N.

Narayan, R. and Yi, I. (June 1994). ‘Advection-dominated Accretion: A Self-similar Solution’. In: *ApJ* 428, p. L13. URL: https://ui.adsabs.harvard.edu/abs/1994ApJ...428L..13N.

– (Oct. 1995). ‘Advection-dominated Accretion: Underfed Black Holes and Neutron Stars’. In: *ApJ* 452, p. 710. URL: https://ui.adsabs.harvard.edu/abs/1995ApJ...452..710N.

Netzer, H. (Jan. 1990). ‘AGN emission lines.’ In: *Active Galactic Nuclei.* Ed. by R. D. Blandford et al., pp. 57–160. URL: https://ui.adsabs.harvard.edu/abs/1990agn..conf...57N.

Novikov, I. D. and Thorne, K. S. (Jan. 1973). ‘Astrophysics of black holes.’ In: *Black Holes (Les Astres Occlus)*, pp. 343–450. URL: https://ui.adsabs.harvard.edu/abs/1973blho.conf..343N.

Oliphant, T. E. (Jan. 2007). ‘Python for Scientific Computing’. In: *Computing in Science and Engineering* 9.3, pp. 10–20. URL: `https://ui.adsabs.harvard.edu/abs/2007CSE.....9c..10O`.

– (2015). *Guide to NumPy*. 2nd. North Charleston, SC, USA: CreateSpace Independent Publishing Platform. ISBN: 151730007X.

Onken, C. A. et al. (Aug. 2020). ‘A thirty-four billion solar mass black hole in SMSS J2157-3602, the most luminous known quasar’. In: *MNRAS* 496.2, pp. 2309–2314. URL: `https://ui.adsabs.harvard.edu/abs/2020MNRAS.496.2309O`.

Padovani, P. (Aug. 2017). ‘On the two main classes of active galactic nuclei’. In: *Nature Astronomy* 1, 0194, p. 0194. URL: `https://ui.adsabs.harvard.edu/abs/2017NatAs...1E.194P`.

Patiño-Álvarez, V. M. et al. (Oct. 2019). ‘Is there a non-stationary γ-ray emission zone 42 pc from the 3C 279 core?’ In: *A&A* 630, A56, A56. URL: `https://ui.adsabs.harvard.edu/abs/2019A&A...630A..56P`.

Penrose, R. (Jan. 1969). ‘Gravitational Collapse: the Role of General Relativity’. In: *Nuovo Cimento Rivista Serie* 1, p. 252. URL: `https://ui.adsabs.harvard.edu/abs/1969NCimR...1..252P`.

Peterson, B. M. (2006). ‘The Broad-Line Region in Active Galactic Nuclei’. In: *Physics of Active Galactic Nuclei at all Scales*. Ed. by D. Alloin. Vol. 693, p. 77. URL: `https://ui.adsabs.harvard.edu/abs/2006LNP...693...77P`.

Peterson, B. M. et al. (Oct. 2005). ‘Multiwavelength Monitoring of the Dwarf Seyfert 1 Galaxy NGC 4395. I. A Reverberation-based Measurement of the Black Hole Mass’. In: *ApJ* 632.2, pp. 799–808. URL: `https://ui.adsabs.harvard.edu/abs/2005ApJ...632..799P`.

Petropoulou, M., Giannios, D. and Sironi, L. (Nov. 2016). ‘Blazar flares powered by plasmoids in relativistic reconnection’. In: *MNRAS* 462.3, pp. 3325–3343. URL: `https://ui.adsabs.harvard.edu/abs/2016MNRAS.462.3325P`.

Pian, E., Falomo, R. and Treves, A. (Aug. 2005). ‘Hubble Space Telescope ultraviolet spectroscopy of blazars: emission-line properties and black hole masses’. In: *MNRAS* 361.3, pp. 919–926. URL: `https://ui.adsabs.harvard.edu/abs/2005MNRAS.361..919P`.

Pittori, C. et al. (Apr. 2018). ‘The Bright γ-ray Flare of 3C 279 in 2015 June: AGILE Detection and Multifrequency Follow-up Observations’. In: *ApJ* 856.2, 99, p. 99. URL: `https://ui.adsabs.harvard.edu/abs/2018ApJ...856...99P`.

Portegies Zwart, S. (Sept. 2020). ‘The ecological impact of high-performance computing in astrophysics’. In: *Nature Astronomy* 4, pp. 819–822. URL: `https://ui.adsabs.harvard.edu/abs/2020NatAs...4..819P`.

Poutanen, J. and Stern, B. (July 2010). ‘GeV Breaks in Blazars as a Result of Gamma-ray Absorption Within the Broad-line Region’. In: *ApJ* 717.2, pp. L118–L121. URL: `https://ui.adsabs.harvard.edu/abs/2010ApJ...717L.118P`.

Ptitsyna, K. and Neronov, A. (Aug. 2016). ‘Particle acceleration in the vacuum gaps in black hole magnetospheres’. In: *A&A* 593, A8, A8. URL: `https://ui.adsabs.harvard.edu/abs/2016A&A...593A...8P`.

Punch, M. et al. (Aug. 1992). ‘Detection of TeV photons from the active galaxy Markarian 421’. In: *Nature* 358.6386, pp. 477–478. URL: `https://ui.adsabs.harvard.edu/abs/1992Natur.358..477P`.

Quinn, J. et al. (Jan. 1996). ‘Detection of Gamma Rays with E $>$ 300 GeV from Markarian 501’. In: *ApJ* 456, p. L83. URL: `https://ui.adsabs.harvard.edu/abs/1996ApJ...456L..83Q`.

Rani, B. et al. (May 2018). ‘Exploring the Connection between Parsec-scale Jet Activity and Broadband Outbursts in 3C 279’. In: *ApJ* 858.2, 80, p. 80. URL: `https://ui.adsabs.harvard.edu/abs/2018ApJ...858...80R`.

Reimer, A. (Aug. 2007). ‘The Redshift Dependence of Gamma-Ray Absorption in the Environments of Strong-Line AGNs’. In: *ApJ* 665.2, pp. 1023–1029. URL: `https://ui.adsabs.harvard.edu/abs/2007ApJ...665.1023R`.

Rieger, F. M. and Mannheim, K. (Jan. 2003). ‘On the central black hole mass in Mkn 501’. In: *A&A* 397, pp. 121–125. URL: `https://ui.adsabs.harvard.edu/abs/2003A&A...397..121R`.

Rieger, F. (Jan. 2019). ‘Gamma-Ray Astrophysics in the Time Domain’. In: *Galaxies* 7.1, p. 28. URL: `https://ui.adsabs.harvard.edu/abs/2019Galax...7...28R`.

Rieger, F. M. (Jan. 2017). ‘Gamma-rays from non-blazar AGN’. In: *6th International Symposium on High Energy Gamma-Ray Astronomy*. Vol. 1792. American Institute of Physics Conference Series, 020008, p. 020008. URL: `https://ui.adsabs.harvard.edu/abs/2017AIPC.1792b0008R`.

Romero, G. and Gutiérrez, E. (July 2020). ‘The Origin of Matter at the Base of Relativistic Jets in Active Galactic Nuclei’. In: *Universe* 6.7, p. 99. URL: `https://ui.adsabs.harvard.edu/abs/2020Univ....6...99R`.

Roos, N. (Jan. 1992). ‘Gas Clouds from Tidally Disrupted Stars in Active Galactic Nuclei’. In: *ApJ* 385, p. 108. URL: `https://ui.adsabs.harvard.edu/abs/1992ApJ...385..108R`.

Rybicki, G. B. and Lightman, A. P. (1979). *Radiative processes in astrophysics*. URL: `https://ui.adsabs.harvard.edu/abs/1979rpa..book.....R`.

– (1986). *Radiative Processes in Astrophysics*. URL: `https://ui.adsabs.harvard.edu/abs/1986rpa..book.....R`.

Sagan, C., Tyson, N. and Druyan, A. (2013). *Cosmos*. The Random House Publishing Group. ISBN: 9780307800985.

Salpeter, E. E. (Aug. 1964). ‘Accretion of Interstellar Matter by Massive Objects.’ In: *ApJ* 140, pp. 796–800. URL: `https://ui.adsabs.harvard.edu/abs/1964ApJ...140..796S`.

Sandage, A. (May 1965). ‘The Existence of a Major New Constituent of the Universe: the Quasistellar Galaxies.’ In: *ApJ* 141, p. 1560. URL: `https://ui.adsabs.harvard.edu/abs/1965ApJ...141.1560S`.

Sbarrato, T. et al. (Sept. 2021). ‘Jetted radio-quiet quasars at z>5’. In: *arXiv e-prints*, arXiv:2109.08156. URL: `https://ui.adsabs.harvard.edu/abs/2021arXiv210908156S`.

Scheuer, P. A. G. and Readhead, A. C. S. (Jan. 1979). ‘Superluminally expanding radio sources and the radio-quiet QSOs’. In: *Nature* 277, pp. 182–185. URL: `https://ui.adsabs.harvard.edu/abs/1979Natur.277..182S`.

Schmidt, M. (Mar. 1963). ‘3C 273 : A Star-Like Object with Large Red-Shift’. In: *Nature* 197.4872, p. 1040. URL: `https://ui.adsabs.harvard.edu/abs/1963Natur.197.1040S`.

Schweitzer, A., Günzler, C. and Zürcher, J. (2017). *Die Weltanschauung der Ehrfurcht vor dem Leben. Kulturphilosophie III: Dritter und vierter Teil*. C.H.Beck. ISBN: 9783406704796.

Scoville, N. and Norman, C. (Sept. 1988). ‘Broad Emission Lines From the Mass-Loss Envelopes of Giant Stars in Active Galactic Nuclei’. In: *ApJ* 332, p. 163. URL: `https://ui.adsabs.harvard.edu/abs/1988ApJ...332..163S`.

Seyfert, C. K. (Jan. 1943). ‘Nuclear Emission in Spiral Nebulae.’ In: *ApJ* 97, p. 28. URL: `https://ui.adsabs.harvard.edu/abs/1943ApJ....97...28S`.

Shah, Z. et al. (Apr. 2019). ‘Study on temporal and spectral behaviour of 3C 279 during 2018 January flare’. In: *MNRAS* 484.3, pp. 3168–3179. URL: `https://ui.adsabs.harvard.edu/abs/2019MNRAS.484.3168S`.

Shakura, N. I. and Sunyaev, R. A. (June 1973). ‘Reprint of 1973A&A....24..337S. Black holes in binary systems. Observational appearance.’ In: *A&A* 500, pp. 33–51. URL: `https://ui.adsabs.harvard.edu/abs/1973A&A....24..337S`.

Shlosman, I., Vitello, P. A. and Shaviv, G. (July 1985). ‘Active galactic nuclei - Internal dynamics and formation of emission clouds’. In: *ApJ* 294, pp. 96–105. URL: `https://ui.adsabs.harvard.edu/abs/1985ApJ...294...96S`.

Shukla, A. and Mannheim, K. (Aug. 2020). ‘Gamma-ray flares from relativistic magnetic reconnection in the jet of the quasar 3C 279’. In: *Nature Communications* 11, 4176, p. 4176. URL: `https://ui.adsabs.harvard.edu/abs/2020NatCo..11.4176S`.

Shukla, A. et al. (Feb. 2018). ‘Short-timescale γ-Ray Variability in CTA 102’. In: *ApJ* 854.2, L26, p. L26. URL: `https://ui.adsabs.harvard.edu/abs/2018ApJ...854L..26S`.

Song, Y. et al. (Oct. 2017). ‘Enhanced gamma radiation towards the rotation axis from the immediate vicinity of extremely rotating black holes’. In: *MNRAS* 471.1, pp. L135–L139. URL: `https://ui.adsabs.harvard.edu/abs/2017MNRAS.471L.135S`.

Stern, B. E. and Poutanen, J. (Oct. 2011). 'Variation of the $\gamma\gamma$ opacity by the He II Lyman continuum constrains the location of the γ-ray emission region in the blazar 3C 454.3'. In: *MNRAS* 417.1, pp. L11–L15. URL: `https://ui.adsabs.harvard.edu/abs/2011MNRAS.417L..11S`.

– (Oct. 2014). 'The Mystery of Spectral Breaks: Lyman Continuum Absorption by Photon-Photon Pair Production in the Fermi GeV Spectra of Bright Blazars'. In: *ApJ* 794.1, 8, p. 8. URL: `https://ui.adsabs.harvard.edu/abs/2014ApJ...794....8S`.

Stocke, J. T., Danforth, C. W. and Perlman, E. S. (May 2011). 'Broad Lyα Emission from Three Nearby BL Lacertae Objects'. In: *ApJ* 732, 113, p. 113. URL: `https://ui.adsabs.harvard.edu/abs/2011ApJ...732..113S`.

Svensson, R. (July 1982). 'Electron-Positron Pair Equilibria in Relativistic Plasmas'. In: *ApJ* 258, p. 335. URL: `https://ui.adsabs.harvard.edu/abs/1982ApJ...258..335S`.

Svensson, R. (July 1987). 'Non-thermal pair production in compact X-ray sources : first-order Compton cascades in soft radiation fields.' In: *MNRAS* 227, pp. 403–451. URL: `https://ui.adsabs.harvard.edu/abs/1987MNRAS.227..403S`.

Swanenburg, B. N. et al. (Sept. 1978). 'COS B observation of high-energy γ radiation from 3C273'. In: *Nature* 275.5678, p. 298. URL: `https://ui.adsabs.harvard.edu/abs/1978Natur.275..298S`.

Tadhunter, C. (Aug. 2008). 'An introduction to active galactic nuclei: Classification and unification'. In: *New A Rev.* 52.6, pp. 227–239. URL: `https://ui.adsabs.harvard.edu/abs/2008NewAR..52..227T`.

Tan, C. et al. (June 2020). 'The Physical Properties of Fermi-4LAC Flat Spectrum Radio Quasars'. In: *ApJS* 248.2, 27, p. 27. URL: `https://ui.adsabs.harvard.edu/abs/2020ApJS..248...27T`.

Tavecchio, F. and Ghisellini, G. (Sept. 2012). '"Flat" broad line region and gamma-ray absorption in blazars'. In: *arXiv e-prints*, arXiv:1209.2291. URL: `https://ui.adsabs.harvard.edu/abs/2012arXiv1209.2291T`.

Tavecchio, F., Maraschi, L. and Ghisellini, G. (Dec. 1998). 'Constraints on the Physical Parameters of TeV Blazars'. In: *ApJ* 509.2, pp. 608–619. URL: `https://ui.adsabs.harvard.edu/abs/1998ApJ...509..608T`.

Tavecchio, F. and Mazin, D. (Jan. 2009). 'Intrinsic absorption in 3C 279 at GeV-TeV energies and consequences for estimates of the extragalactic background light'. In: *MNRAS* 392.1, pp. L40–L44. URL: `https://ui.adsabs.harvard.edu/abs/2009MNRAS.392L..40T`.

Tchekhovskoy, A., Narayan, R. and McKinney, J. C. (Nov. 2011). 'Efficient generation of jets from magnetically arrested accretion on a rapidly spinning black hole'. In: *MNRAS* 418.1, pp. L79–L83. URL: `https://ui.adsabs.harvard.edu/abs/2011MNRAS.418L..79T`.

Telfer, R. C. et al. (Feb. 2002). 'The Rest-Frame Extreme-Ultraviolet Spectral Properties of Quasi-stellar Objects'. In: *ApJ* 565.2, pp. 773–785. URL: `https://ui.adsabs.harvard.edu/abs/2002ApJ...565..773T`.

The Nobel Committee for Physics (2021a). *Scientific Background on the Nobel Prize in Physics 2019 – PHYSICAL COSMOLOGY AND AN EXOPLANET ORBITING A SOLAR-TYPE STAR.* Advanced information. NobelPrize.org. Nobel Prize Outreach AB 2021. URL: `https://www.nobelprize.org/prizes/physics/2019/advanced-information/`.

– (2021b). *Scientific Background on the Nobel Prize in Physics 2020 – THEORETICAL FOUNDTION FOR BLACK HOLES AND THE SUPERMASSIVE COMPACT OBJECT AT THE GALACTIC CENTRE.* Advanced information. NobelPrize.org. Nobel Prize Outreach AB 2021. URL: `https://www.nobelprize.org/prizes/physics/2020/advanced-information/`.

Thorne, K. S. (July 1974). 'Disk-Accretion onto a Black Hole. II. Evolution of the Hole'. In: *ApJ* 191, pp. 507–520. URL: `https://ui.adsabs.harvard.edu/abs/1974ApJ...191..507T`.

Tursunov, A. et al. (May 2020). 'Supermassive Black Holes as Possible Sources of Ultrahigh-energy Cosmic Rays'. In: *ApJ* 895.1, 14, p. 14. URL: `https://ui.adsabs.harvard.edu/abs/2020ApJ...895...14T`.

Urry, C. M. and Padovani, P. (Sept. 1995). 'Unified Schemes for Radio-Loud Active Galactic Nuclei'. In: *PASP* 107, p. 803. URL: `https://ui.adsabs.harvard.edu/abs/1995PASP..107..803U`.

Véron-Cetty, M. .-. and Véron, P. (July 2010). 'A catalogue of quasars and active nuclei: 13th edition'. In: *A&A* 518, A10, A10. URL: `https://ui.adsabs.harvard.edu/abs/2010A&A...518A..10V`.

Vietri, G. et al. (Dec. 2020). 'SUPER. III. Broad line region properties of AGNs at z $\sim$ 2'. In: *A&A* 644, A175, A175. URL: `https://ui.adsabs.harvard.edu/abs/2020A&A...644A.175V`.

Viganò, D. et al. (Feb. 2015). 'Compact formulae, dynamics and radiation of charged particles under synchro-curvature losses'. In: *MNRAS* 447.2, pp. 1164–1172. URL: `https://ui.adsabs.harvard.edu/abs/2015MNRAS.447.1164V`.

Vilkoviskij, E. Y. and Czerny, B. (June 2002). 'The role of the central stellar cluster in active galactic nuclei. I. Semi-analytical model'. In: *A&A* 387, pp. 804–817. URL: `https://ui.adsabs.harvard.edu/abs/2002A&A...387..804V`.

Vincent, S. and Lebohec, S. (Dec. 2010). 'Monte Carlo simulation of electromagnetic cascades in black hole magnetosphere'. In: *MNRAS* 409.3, pp. 1183–1194. URL: `https://ui.adsabs.harvard.edu/abs/2010MNRAS.409.1183V`.

Virtanen, P. et al. (2020). 'SciPy 1.0: Fundamental Algorithms for Scientific Computing in Python'. In: *Nature Methods* 17, pp. 261–272. URL: `https://rdcu.be/b08Wh`.

Vuillaume, T., Henri, G. and Petrucci, P. .-. (Dec. 2018). 'A stratified jet model for AGN emission in the two-flow paradigm'. In: *A&A* 620, A41, A41. URL: `https://ui.adsabs.harvard.edu/abs/2018A&A...620A..41V`.

Wagner, S. M. et al. (Oct. 2021). 'Statistical properties of flux variations in blazar light curves at GeV and TeV energies'. In: *arXiv e-prints*, arXiv:2110.14797. URL: `https://ui.adsabs.harvard.edu/abs/2021arXiv211014797W`.

Wakely, S. P. and Horan, D. (Jan. 2008). 'TeVCat: An online catalog for Very High Energy Gamma-Ray Astronomy'. In: *International Cosmic Ray Conference*. Vol. 3. International Cosmic Ray Conference, pp. 1341–1344. URL: `https://ui.adsabs.harvard.edu/abs/2008ICRC....3.1341W`.

Wald, R. M. (Sept. 1974). 'Black hole in a uniform magnetic field'. In: *Phys. Rev. D* 10.6, pp. 1680–1685. URL: `https://ui.adsabs.harvard.edu/abs/1974PhRvD..10.1680W`.

Wendel, C. (2013). 'Bestimmung des hochenergetischen Spektrums des Crab-Pulsars anhand eines Outer Gap-Modells'. Diplomarbeit. Julius-Maximilians-Universität Würzburg. URL: `https://doi.org/10.25972/OPUS-25719`.

Wendel, C., Shukla, A. and Mannheim, K. (Aug. 2021). 'Pair Cascades at the Edge of the Broad-line Region Shaping the Gamma-Ray Spectrum of 3C 279'. In: *ApJ* 917.1, 32, p. 32. URL: `https://ui.adsabs.harvard.edu/abs/2021ApJ...917...32W`.

Wendel, C. et al. (Jan. 2017). 'Simulating electromagnetic cascades in magnetospheres of active galactic nuclei'. In: *6th International Symposium on High Energy Gamma-Ray Astronomy*. Vol. 1792. American Institute of Physics Conference Series, 050026, p. 050026. URL: `https://ui.adsabs.harvard.edu/abs/2017AIPC.1792e0026W`.

Wendel, C. et al. (Aug. 2021a). 'Gamma-ray signatures from pair cascades in recombination-line radiation fields'. In: *arXiv e-prints*, arXiv:2108.02649. URL: `https://ui.adsabs.harvard.edu/abs/2021arXiv210802649W`.

Wendel, C. et al. (Feb. 2021b). 'Electron-beam interaction with emission-line clouds in blazars'. In: *A&A* 646, A115, A115. URL: `https://ui.adsabs.harvard.edu/abs/2021A&A...646A.115W`.

Wilms, J., Allen, A. and McCray, R. (Oct. 2000). 'On the Absorption of X-Rays in the Interstellar Medium'. In: *ApJ* 542, pp. 914–924. URL: `http://adsabs.harvard.edu/abs/2000ApJ...542..914W`.

Woltjer, L. (July 1959). 'Emission Nuclei in Galaxies.' In: *ApJ* 130, p. 38. URL: `https://ui.adsabs.harvard.edu/abs/1959ApJ...130...38W`.

Zajacek, M. and Tursunov, A. (Dec. 2019). 'The Electric Charge of Black Holes: Is It Really Always Negligible'. In: *The Observatory* 139, pp. 231–236. URL: `https://ui.adsabs.harvard.edu/abs/2019Obs...139..231Z`.

Zajaček, M. et al. (Nov. 2018). 'On the charge of the Galactic centre black hole'. In: *MNRAS* 480.4, pp. 4408–4423. URL: `https://ui.adsabs.harvard.edu/abs/2018MNRAS.480.4408Z`.

Zdziarski, A. A. (Dec. 1988). 'Saturated Pair-Photon Cascades on Isotropic Background Photons'. In: *ApJ* 335, p. 786. URL: https://ui.adsabs.harvard.edu/abs/1988ApJ...335..786Z.

Zdziarski, A. A. and Svensson, R. (Sept. 1989). 'Absorption of X-Rays and Gamma Rays at Cosmological Distances'. In: *ApJ* 344, p. 551. URL: https://ui.adsabs.harvard.edu/abs/1989ApJ...344..551Z.

Zel'dovich, Y. B. (Sept. 1964). 'The Fate of a Star and the Evolution of Gravitational Energy Upon Accretion'. In: *Soviet Physics Doklady* 9, p. 195. URL: https://ui.adsabs.harvard.edu/abs/1964SPhD....9..195Z.

Acknowledgements

I thank Prof. Dr. Karl Mannheim for his support, for guidance during the past years, for helpful ideas and for taking time to discuss issues even when other urgent tasks were pressing. I also thank him for taking seriously the responsibility for societal issues and problems facing humanity beyond astrophysics. I am no less thankful to Dr. Josefa Becerra González and to Dr. Amit Shukla for their scientific support, for their kind collaboration and for a lot of clarifying explanations.

Moreover, I thank Dr. Dorit Glawion, Katja Meier and Dr. David Paneque for fruitful discussions on various astrophysical topics. Advice on coding problems by Alexander Kappes also turned out to be really valuable, what I am very thankful about. Furthermore, I am grateful to Dr. Daniela Dorner and Marcus Langejahn for helpful instructions on a number of technical problems.

I also acknowledge organisational support by Karin Kuhns, Sandra Mölter, Bernd Mölter, Dr. Jana Bauer and Susanne Groth as well as financial support by the Universität Würzburg and by the project "Promotion inklusive" set up by the Universität zu Köln and the German Bundesministerium für Arbeit und Soziales.

I am deeply thankful to my parents and my brother for their support in any form during all my life. Finally, I thank all those people who have been supportive, benevolent or kind to me.

Publications in Context with this Work

Peer-Reviewed Papers with Major Contribution:

MAGIC Collaboration et al. (May 2020). 'Study of the variable broadband emission of Markarian 501 during the most extreme Swift X-ray activity'. In: *A&A* 637, A86, A86. URL: `https://ui.adsabs.harvard.edu/abs/2020A&A...637A..86M`

C. Wendel et al. (Feb. 2021b). 'Electron-beam interaction with emission-line clouds in blazars'. In: *A&A* 646, A115, A115. URL: `https://ui.adsabs.harvard.edu/abs/2021A&A...646A.115W`

C. Wendel, A. Shukla and K. Mannheim (Aug. 2021). 'Pair Cascades at the Edge of the Broad-line Region Shaping the Gamma-Ray Spectrum of 3C 279'. In: *ApJ* 917.1, 32, p. 32. URL: `https://ui.adsabs.harvard.edu/abs/2021ApJ...917...32W`

Peer-Reviewed Papers with Minor Contribution and Proceedings:

M. L. Ahnen et al. (July 2017a). 'First multi-wavelength campaign on the gamma-ray-loud active galaxy IC 310'. In: *A&A* 603, A25, A25. URL: `https://ui.adsabs.harvard.edu/abs/2017A&A...603A..25A`

C. Wendel et al. (Jan. 2017). 'Simulating electromagnetic cascades in magnetospheres of active galactic nuclei'. In: *6th International Symposium on High Energy Gamma-Ray Astronomy.* Vol. 1792. American Institute of Physics Conference Series, 050026, p. 050026. URL: `https://ui.adsabs.harvard.edu/abs/2017AIPC.1792e0026W`

D. E. Glawion et al. (Jan. 2017). 'Black hole lightning of IC 310 and the days after'. In: *6th International Symposium on High Energy Gamma-Ray Astronomy.* Vol. 1792. American Institute of Physics Conference Series, 050003, p. 050003. URL: `https://ui.adsabs.harvard.edu/abs/2017AIPC.1792e0003G`

A. Shukla et al. (Feb. 2018). 'Short-timescale γ-Ray Variability in CTA 102'. In: *ApJ* 854.2, L26, p. L26. URL: `https://ui.adsabs.harvard.edu/abs/2018ApJ...854L..26S`

J. Becerra Gonzalez et al. (July 2019). 'Study of the Variable Broadband Emission of Markarian 501 during the Most Extreme Swift X-ray Activity'. In: *36th International Cosmic Ray Conference (ICRC2019).* Vol. 36. International Cosmic Ray Conference, 554, p. 554. URL: `https://ui.adsabs.harvard.edu/abs/2019ICRC...36..554B`

C. Wendel et al. (Aug. 2021a). 'Gamma-ray signatures from pair cascades in recombination-line radiation fields'. In: *arXiv e-prints*, arXiv:2108.02649. URL: `https://ui.adsabs.harvard.edu/abs/2021arXiv210802649W`

Statutory Declaration of Authorship

I ensure that this PhD thesis was written autonomously by myself. Likewise, I declare that the work is my own and was performed solely with the stated aids and sources and with the instructions of the acknowledged collaborators, above all with the guidance of Prof. Dr. Karl Mannheim. In particular, I affirm that I have not had and do not have any contact with persons or organisations that support the production of dissertations in a commercial manner or for money. When I used published results of other scientists, I always signified this by citing the correct reference. Moreover, I have marked all quotations appropriately. All the presented work was done during my PhD candidature at the Julius-Maximilians-Universität Würzburg. I complied with and respect the university's guidelines for good practice in science. This work has not been presented in any other field of education or examination.

Würzburg, the 25th February 2022